Michael Brockamp

Massive Black Holes in Galaxies

Massive Black Holes in Galaxies

Dissertation

zur

Erlangung des Doktorgrades (Dr. rer. nat.)

der

Mathematisch-Naturwissenschaftlichen Fakultät

der

Rheinischen Friedrich-Wilhelms-Universität Bonn

vorgelegt von

Michael Brockamp

aus

Gütersloh

Bonn, Juli 2014

Angefertigt mit Genehmigung der Mathematisch-Naturwissenschaftlichen Fakultät
der Rheinischen Friedrich-Wilhelms-Universität Bonn

1. Gutachter:
Prof. Dr. Pavel Kroupa

2. Gutachter:
Prof. Dr. Holger Baumgardt

Tag der Promotion: 29.9.2014

Erscheinungsjahr: 2014

Erklärung

Ich versichere, daß ich die von mir vorgelegte Dissertation selbstständig angefertigt, die benutzten Quellen und Hilfsmittel vollständig angegeben und die Stellen der Arbeit - einschließlich Tabellen, Karten und Abbildungen -, die anderen Werken im Wortlaut oder dem Sinn nach entnommen sind, in jedem Einzelfall als Entlehnung kenntlich gemacht habe; daß diese Dissertation noch keiner anderen Fakultät oder Universität zur Prüfung vorgelegen hat; daß sie - abgesehen von unten angegeben Erstautor-Publikationen - noch nicht veröffentlicht worden ist sowie, daß ich eine solche Veröffentlichung vor Abschluß des Promotionsverfahrens nicht vornehmen werde. Die Bestimmungen dieser Promotionsordnung sind mir bekannt. Die von mir vorgelegte Dissertation ist von Prof. Dr. Pavel Kroupa betreut worden.

Bonn, Datum ———————— , ———————————— (Michael Brockamp)

Erstautor-Publikationen

Brockamp, M., Baumgardt, H., & Kroupa, P. 2011, MNRAS, 418, 1308
(Kapitel 3 in dieser Dissertation)

Brockamp, M., Küpper, A. H. W., Thies, I., Baumgardt, H., & Kroupa, P. 2014,
MNRAS, 441, 150
(Kapitel 4 in dieser Dissertation)

Weitere Publikationen

Mieske, S., Küpper, A. H. W., & Brockamp, M. 2014, A&A, 565, L6

Peuten, M., Brockamp, M., Küpper, A. H. W., & Kroupa, P. 2014, ApJ, in press

Zusammenfassung

Die vorliegende Doktorarbeit handelt von supermassereichen schwarzen Löchern (SMSL), ihrem Wachstum und dem Einfluss, den sie auf ihre Wirtsgalaxien und deren Kugelsternhaufensysteme ausüben. Um die geleistete Arbeit in einen umfassenden wissenschaftlichen Kontext einordnen zu können, werden im ersten Teil dieser Doktorarbeit die relevanten wissenschaftlichen Grundlagen dargelegt. Gleichzeitig wird ein umfangreicher Überblick über den gegenwärtigen Stand der Forschung schwarzer Löcher vermittelt. Zunächst wird im Rahmen der allgemeinen Relativitätstheorie die Physik dieser Objekte betrachtet (Kapitel 1). Dabei wird auf eine aktuelle Arbeit von Andrew Hamilton Bezug genommen. Diese gestattet es, Eigenschaften schwarzer Löcher anschaulich und zugleich mathematisch korrekt zu erläutern. Im Anschluss werden alle möglichen Bahnen in einer Schwarzschild Metrik diskutiert auf denen sich Objekte bewegen können. So wird eine Verbindung zwischen der Physik schwarzer Löcher und den Prozessen, die zu ihrem Wachstum führen, hergestellt. Diverse SMSL Wachstumsprozesse werden erläutert (Kapitel 2), nachdem auf beobachtbare Skalierungsrelationen eingegangen wurde. So enthält die Steigung, aber auch die statistische Streuung dieser empirischen SMSL Skalierungsrelationen, wertvolle Informationen über den Ursprung und das Wachstum schwarzer Löcher.

Im zweiten Teil dieser Doktorarbeit (Kapitel 3) stehen die Ergebnisse der eigenen Forschung im Vordergrund. Zunächst wird ein Wachstumsprozess betrachtet, bei dem Sterne durch Relaxation im Drehimpulsraum zu Trajektorien hin diffundieren, welche letztendlich im unmittelbaren Einflussbereich des SMSL münden. Die Sterne werden dabei von Gezeitenkräften zerrissen und ein Teil der stellaren Materie wird akkretiert. Bei der verwendeten Methode handelt es sich um direkte N-Körperrechnungen. Es wird gezeigt, dass die Einfallrate von Sternen nicht hoch genug ist, um das Wachstum sehr massereicher schwarzer Löcher signifikant zu beeinflussen. Dennoch können von SMSL zerrupfte Sterne einen erheblichen Anteil am Wachstum schwarzer Löcher im unteren Massenbereich von 10^4-$10^5 M_\odot$ beigetragen haben. Interessanterweise scheint die Masse des SMSL keinen großen Einfluss auf die Einfallrate von Sternen zu haben. Die Ergebnisse wurden im MNRAS Journal publiziert.

Im darauf folgenden Kapitel 4 wird eine selbstentwickelte Software vorgestellt, welche den Einfluss von Galaxien, zentralen schwarzen Löchern und weiteren Effekten auf die Erosionsrate von Kugelsternhaufensystemen untersucht. Zum ersten Mal konnte eine weitreichende Verallgemeinerung der dynamischen Reibungsformel von Chandrasekhar eingebaut werden. Diese basiert nicht mehr auf der Annahme einer Maxwellschen Geschwindigkeitsverteilung. Des Weiteren berücksichtigt sie, dass der Beschleunigungsvektor der dynamischen Reibung nicht anti-parallel zum

Geschwindigkeitsvektor stehen muss. Bereits in den ersten Rechnungen mit dieser Software haben sich Hinweise auf eine neue Phase in der Entwicklung von Kugelsternhaufensystemen finden lassen. So wird anfänglich eine große Anzahl von Kugelsternhaufen durch starke Gezeitenschocks innerhalb der Galaxie zerstört. Der Einfluss massereicher schwarzer Löcher auf die zeitliche Erosionsrate und Gesamtanzahl zerstörter Kugelsternhaufen wird diskutiert. Darüberhinaus lassen sich die flachen Anzahldichteprofile von Kugelsternhaufensystemen in elliptischen Galaxien, sowie das Nichtvorhandensein von Kugelsternhaufen in der kompakten Zwerggalaxie M 32, einer Satellitengalaxie der Andromedagalaxie, erklären. Die Ergebnisse wurden in einem zweiten Artikel im MNRAS Journal veröffentlicht.

Im dritten und letzten Teil dieser Doktorarbeit wird zunächst die numerische Implementierung eines schwarzen Loches inklusive voll relativistischer Einfangbedingungen erläutert. Anhand der relativistischen Perihel-Präzession des Merkurs und dem Verschmelzungsprozess zweier schwarzer Löcher getestet, wird die Strategie zur Durchführung eines weiteren, zukünftigen Projektes mit dieser Software vorgestellt. Dabei geht es um das Wachstum massereicher schwarzer Löcher durch stellare Trümmerteile von erodierten Sternhaufen. Schlussendlich wird auch noch die Bedeutung bereits gewonnener Erkenntnisse für die sogenannte spezifische Frequenz von Kugelsternhaufen in elliptischen Galaxien diskutiert.

Summary

The main subjects of the underlying PhD study are supermassive black holes (SMBHs), their growth and the influence they exert on vast globular cluster systems. In the first part of this work I provide a comprehensive overview of black hole related research. In this way the own findings can be connected to a broader scientific background. Simultaneously, the current state of SMBH research is summarized. The physics behind black holes will be presented first (Chapter 1). This is done by introducing a fully general relativistic concept for visualizing black holes. It was developed by Andrew Hamilton. Afterwards, I will discuss all possible trajectories in a non-rotating Schwarzschild metric. In this way the link between the physics of black holes and various SMBH growth processes, which belong to the domain of astrophysics, can be established. However, before summarizing different growth scenarios, the most important scaling relations are described (Chapter 2). The slope and intrinsic scatter of these empirical correlations contain information about the SMBH growth history.

In the second part of this PhD study I focus on my own results. In Chapter 3, I will investigate the flux of stars which enter loss cone trajectories through angular momentum diffusion. The inferred results are based on direct N-body computations which are presented in Brockamp et al. (2011). Depending on the mass of the central SMBH, stars on loss cone orbits can either be swallowed as a whole, or tidally disrupted. In the latter case some fraction of the unbounded star becomes accreted. It is found that the tidal disruption rate of stars is nearly independent of the SMBH mass. Angular momentum diffusion is not sufficient to fuel the growth of the most massive black holes. However, it can influence the growth history of SMBHs in the lowest mass range spanning 10^4-$10^5 \mathrm{M}_\odot$.

In the following Chapter 4 I present a newly developed computer code, which is called MUESLI. It numerically integrates the equation of motion of individual globular clusters (GCs) in elliptical galaxies by taking GC disruption processes into account. MUESLI thus evaluates the erosion rate of whole globular cluster systems. Several aspects which influence the GC erosion rate like the tidal field of the host galaxy, SMBHs and dynamical friction (DF) are considered. For the first time an extensive generalization of Chandrasekhar's dynamical friction formula is implemented into N-body software. It does not only handle non-Maxwellian velocity distributions, but can also treat dynamical friction forces which are not anti-parallel to the velocity vector. Already the first computations indicated a new phase in the evolution of whole globular cluster systems. Depending on the strength of the tidal field of the host galaxy, a huge fraction of GCs is destroyed rapidly through tidal shocking. The influence of the central SMBH on the fraction of destroyed GCs is discussed. Additionally, the

performed computations naturally explain the central shallow number density profiles of GCs systems as well as the non existence of GCs around the compact dwarf galaxy M 32, which is a satellite of the Andromeda galaxy. The presented results are based on Brockamp et al. (2014).

The implementation of a relativistic SMBH with fully general relativistic capture conditions into the MUESLI code is treated in the last part of this PhD study. After testing it by means of reproducing the precession rate of Mercury as well as by computing a binary black hole inspiral, the basic strategy for realizing a further loss cone project is described. Finally, I present first results which were obtained with MUESLI for the shaping of the GC specific frequency versus the absolute galaxy luminosity.

Acknowledgements

Contents

List of Abbreviations

ADAF . . . . Advection Dominated Accretion Flow
AGN . . . . Active Galactic Nucleus
BCG . . . . Brightest Cluster Galaxy
DF . . . . Dynamical Friction
dSph . . . . Dwarf Spheroidal (Galaxy)
GC . . . . Globular Cluster
GCS . . . . Globular Cluster System
GPU . . . . Graphics Processing Unit
HST . . . . Hubble Space Telescope
IDW . . . . Inverse Distance Weighting
IMBH . . . . Intermediate-Mass Black Hole
Lambda-CDM . . . . . . Lambda-Cold Dark Matter
MASER . . . . Microwave Amplification by Stimulated Emission of Radiation
MNP . . . . Modified-Newtonian Potential
MNRAS . . . . Monthly Notices of the Royal Astronomical Society
MUESLI . . . . M̲ulti-Purpose E̲lliptical Galaxy S̲CF + Time-Transformed L̲eapfrog I̲ntegrator
PN . . . . Post-Newtonian
SCF . . . . Self-Consistent Field (Method)
SDSS . . . . Sloan Digital Sky Survey
SEV . . . . Stellar Evolution
SMBH . . . . Supermassive Black Hole
SMSL . . . . Supermassereiches Schwarzes Loch
SPODYR . . . . Stellar Populations and Dynamics Research (Group)
TDDP . . . . Tidal Disruption Dominated Phase
TDE . . . . Tidal Disruption Event
TTL . . . . Time-Transformed Leapfrog (Scheme)
UMBH . . . . Ultramassive Black Hole
WISE . . . . Wide-Field Infrared Survey Explorer

Part I

Introduction & Scientific Context

Chapter 1

General Black Hole Dynamics

1.1. Black Holes

"Abandon hope, all ye who enter here."

Dante Alighieri (1265-1321), The Divine Comedy

Black holes are the most powerful objects which are known, capable of swallowing light and matter without the chance of a recurrence. The first ideas concerning astrophysical objects which appear dark were presented by the geologist John Michell in 1784. Based on a Newtonian treatment of the propagation of light, Michell (1784) calculated that objects with a given mass, $M_\bullet$, and critical size, r_s, which satisfy the relation:

$$r_s = \frac{2GM_\bullet}{c^2} \approx 3\left(\frac{M_\bullet}{M_\odot}\right) \text{km}, \tag{1.1}$$

would appear invisible for external observers. This is due to an escape velocity which equals the velocity of light. Although Michell's model of a dark star is frequently used for educational purposes and reproduces some features of black holes, it has actually nothing in common with a realistic black hole whose interior is physically disconnected from the outside. It is a pure mathematical coincidence that Michell's critical radius corresponds to the Schwarzschild radius of a (non rotating) black hole.

The actual concept behind black holes as solutions to Einsteins field equations was pioneered by Karl Schwarzschild during his military service on the Eastern Front in the First World War. Schwarzschild (1916) found the solution of a non-rotating black hole, although his model was frequently dismissed as physically irrelevant (even by Einstein himself) due to a divergence of physical quantities at the locus of the Schwarzschild radius. In 1958, David Finkelstein introduced a method which allowed to remove these (unphysical) divergences at r_s through a coordinate transformation (Finkelstein, 1958). Five years later, Roy Kerr generalized the Schwarzschild solution to rotating black holes (Kerr, 1963) and in the year 1964 John Wheeler introduced the name *black hole* during a public lecture. Before that lecture, black holes were termed *frozen stars*.

Apart from increasing observational evidence for the existence of black holes, i.e. the discovery of quasars (Schmidt, 1963), the next milestones in theoretical black hole

research were initiated by Jacob Bekenstein and Stephen Hawking. Bekenstein (1973) and Hawking (1974) established a fundamental relation between the area, $A = 4\pi r_s^2$, and the entropy of a black hole $S = kA/\left(4l_p^2\right)$, where k is the Boltzmann constant and l_p the Planck length. This insight offers first clues about deep fundamental relations between the nature of gravity, thermodynamics, geometry, and quantum mechanics. It has been recognized that there are no objects which can store more entropy than a black hole of equal size and that the maximal amount of entropy scales with the surface and not the volume.

Today, black holes are the cornerstones in the search for a united theory of gravity and quantum mechanics. Recent approaches (e.g. van Raamsdonk (2010); Papadodimas & Raju (2013); Maldacena & Susskind (2013)) yield deep insights into the emergence of space-time itself and the interaction between gravity and quantum mechanics under the extreme conditions within a black hole.

In the following discussion the physics behind non-rotating black holes will be explained by making use of the *river* or *waterfall* model for black holes which was developed by Hamilton & Lisle (2008). It is based on a coordinate transformation of the Schwarzschild metric into Gullstrand-Painlevé coordinates. Its generalization to rotating black holes will not be discussed in detail here but can also be found in Hamilton & Lisle (2008). This model explains all essential aspects of black holes like the apparent freeze of time at the horizon, the membrane like nature of the horizon, tidal forces and the inevitability of a central singularity.

The great benefit of the *river model for black holes* is that it treats space as a fluid (i.e. the *river*) on a flat background spacetime. However, the flat background spacetime can not be experienced by observers which are moving in the river. These observers can only measure distances, angles and time scales relative to objects which are also part of the river. The river itself can stretch and posses a curl or twist vector at each point. The space i.e. the river drains into the black hole and the objects within this reference frame obey the laws of special relativity.

Following Hamilton & Lisle (2008), the metric of a non-rotating black hole in Schwarzschild coordinates is

$$ds^2 = -\left(1 - \frac{2M_\bullet}{r}\right)dt^2 + \frac{dr^2}{1 - \frac{2M_\bullet}{r}} + r^2\left(d\theta^2 + \sin\theta^2 d\phi^2\right), \tag{1.2}$$

where ds is the line element and the constants c and G are set to one. $M_\bullet$ is the mass of the black hole. Evidently, at scales of the Schwarzschild radius, $r_s = 2M_\bullet$, the metric exhibits a coordinate singularity as the second term diverges. Schwarzschild coordinates are defined in such a way that the "observer" remains at rest far outside the black hole. She/he only records events which were made by local probes and which sent her/him all the information. Obviously, she/he does not receive (useful) information from a probe which has fallen into a black hole. By the coordinate transformation:

$$t_{ff} = t - \int_r^\infty \frac{\beta\left(r'\right)}{1 - \beta\left(r'\right)^2}dr', \ \tilde\theta = \theta, \ \tilde\phi = \phi, \ \tilde r = r \tag{1.3}$$

4

the Schwarzschild metric in Schwarzschild coordinates can be converted into Gullstrand-Painlevé coordinates:

$$ds^2 = -dt_{ff}^2 + (\beta(r)\, dt_{ff})^2 + 2\beta(r)\, dt_{ff} dr + dr^2 + r^2 d\theta^2 + r^2 \sin\theta^2 d\phi^2. \qquad (1.4)$$

The function

$$\beta(r) = \left(\frac{2M_\bullet}{r}\right)^{\frac{1}{2}} \qquad (1.5)$$

is the velocity of radially infalling space (in units of $G = c = 1$) as measured from the flat background spacetime. Obviously, an observer in the flat background spacetime and which is decoupled from the radial inflow of space is purely fictitious and has no meaning in reality. Nevertheless, his/her observations yield useful information for the visualization and understanding of the physics of black holes, especially within their horizons. In the following discussion we take the role of this omniscient watcher. An analogous black hole river model with a physically meaningful reference frame can be found in Braeck & Grøn (2013). As can be seen from Equation 1.4, the spatial part of the metric is nothing else than the flat metric of spherical coordinates. The Schwarzschild spacetime is well defined within the Schwarzschild radius i.e. the event horizon of the black hole. At the position of the Schwarzschild radius, r_s, the velocity of the infalling space is $\beta(r_s) = 1$, i.e. it corresponds to the speed of light.

Within this picture, non-rotating black holes can be easily explained[1]. See also Figure 1.1 for an illustrative model of the river model of non-rotating black holes. The event horizon (Schwarzschild radius) is the ultimate boundary of a black hole. Everything can enter the event horizon of a black hole, but nothing can escape. This behaviour is reminiscent of a one-way membrane. The event horizon is the place where the velocity of infalling space equals the speed of light. At the horizon, a photon with zero angular momentum and which is radially directed outwards might be trapped forever owing to compensating velocities. However, the tiniest perturbation would cause its plunge into the hole. Observers which are part of the space river will never see how accreted matter passes the horizon. Instead, all inflowing material (apparently) seems to freeze in time owing to a diverging photon recovery timescale at the horizon. Photons which are emitted very close to the horizon need longer and longer to reach distant observer because they have to move against the accelerating space-river. This generates the impression of time which asymptotically freezes at the horizon. It is often claimed that in return the infalling probe sees the whole (infinite) future of the universe in an instant of time. This claim is completely wrong. Only if the probe manages to stay at the horizon at the speed of light it would see the infinite future of the universe according to the laws of special relativity. However, with such a kind of engine at hand it would not require a black hole for doing so.

The infalling probe passes the event horizon without realizing it and in finite time. The situation is similar to a fish which crosses a critical distance just before the threshold of a turbine shaft where the flowing water exceeds his maximal speed of

---

[1]Space does not spiral inwards as one might suggest for the case of a rotating black hole. Instead, the infalling space possesses a twist vector at each point which induces a shear moment on any object.
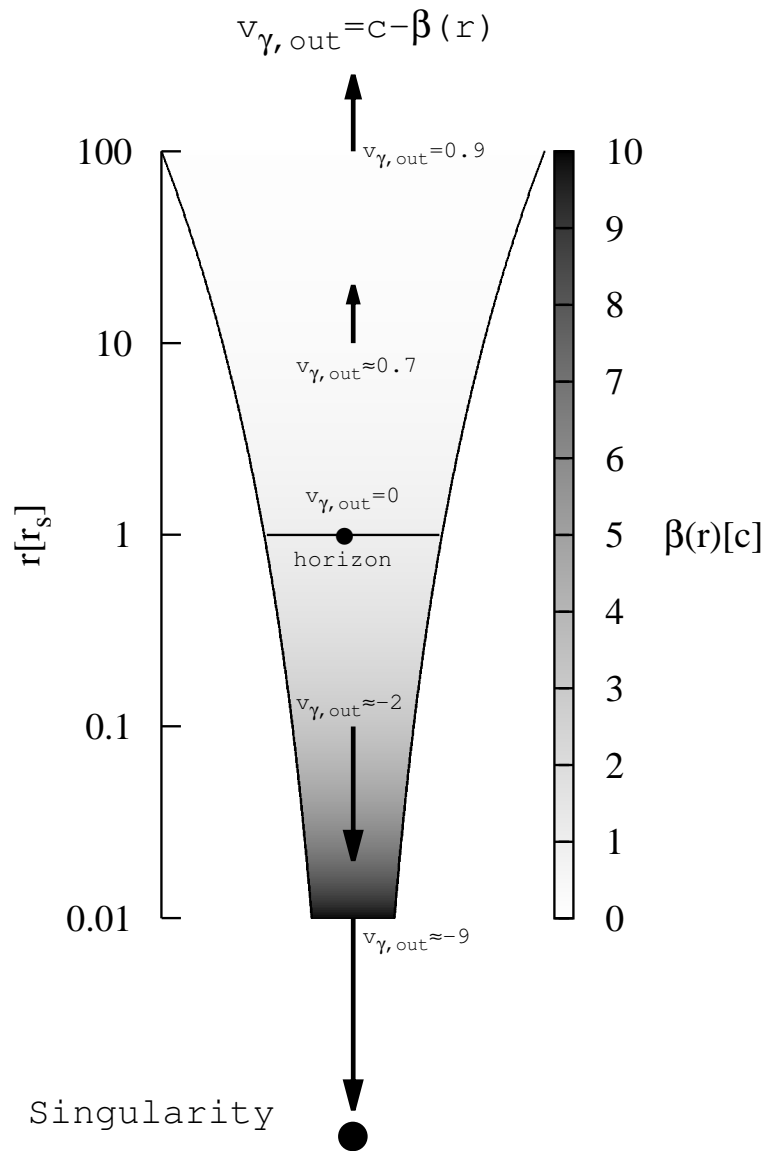
Figure 1.1. In the reference frame of the flat background spacetime (in units of $G = c = 2M_\bullet = 1$) the color coded infall velocity of space, $\beta(r)$, is plotted as a function of the radius. Below r_s, even photons are swept away by the infalling space. An outgoing ray at the exact position of the horizon will never reach an observer at save distances. This explains why all forms of infalling matter seem to freeze in time when approaching the horizon of a black hole. The parabolic form has no physical meaning and is used for illustrative purposes only. In reality space falls radially inwards from all directions.

movement. The fish would not be able to detect anything special at the point of no return.

Below r_s, $\beta(r)$ exceeds the speed of light and everything is rushed deeper into the hole. Although the velocity of infalling space is greater than c (as measured from the flat background spacetime), the infalling probe does not measure superluminal

motions since it is part of the river itself. The probe itself can neither stay at rest nor escape as this would require superluminal speeds in contradiction to the laws of special relativity. From its perspective, the sphere of darkness (i.e. the so called illusory horizon) grows during infall since material in front of it becomes increasingly redshifted (Hamilton & Lisle, 2008; Hamilton, 2012). The probe will never see how material in front of it crashes onto the singularity. Simultaneously, the sphere of causal contact which is the region from which information can still reach the infalling probe (i.e. its own particle horizon) decreases continuously. This means that even quantum communication breaks down on even smaller length scales during infall, in a process which is termed "asymptotic silence" (Andersson et al., 2005).

Finally, at the position of the central singularity the infalling probe "unites" with the illusory horizon. Everything is crushed out of existence at the singularity/illusory horizon as space collapses arbitrarily fast ($\lim_{r \to 0} \beta(r) = \infty$). There is nothing which can prevent this form of ultimate collapse as the transmission speed of forces required to generate a repulsive force/pressure are always limited by the speed of light. Once inside a black hole, the infall into the singularity is inevitable as the progression of time itself.

1.2. Trajectories around Black Holes

1.2.1. $1/r$ Potential

After having introduced the physical concept behind a black hole in § 1.1, the possible types of trajectories around these objects will be summarized in this section. In this manner a link between the physics of black holes itself and their gravitational influence on their surrounding (i.e. relevance to astrophysics) can be established. As a by-product, a simple but fully relativistic capture criterion for particles (e.g. stars) by non-rotating Schwarzschild black holes can be derived (§ 1.2.3). Its generalization to rotating Kerr black holes can be found elsewhere (e.g. Novikov & Frolov 1989; Will 2012).

In order to illustrate the uniqueness of trajectories in a Schwarzschild metric, it is useful to first discuss all allowed trajectories in a static Keplerian ($V(r) \propto -1/r$) potential. By writing the total energy E of a particle of mass m in polar coordinates as:

$$E = \frac{m}{2}\dot{r}^2 + V(r) + \frac{m}{2}r^2\dot{\phi}^2, \tag{1.6}$$

where $mr^2\dot{\phi}^2/2 = L^2/(2mr^2)$ is the centrifugal potential and $L = mr^2\dot{\phi}$ is the angular momentum, one can define the sum

$$V_{\text{eff}} = V(r) + L^2/(2mr^2) \tag{1.7}$$

as the effective potential. Depending on the total energy E of a particle, one discriminates four different trajectories, sketched as $T_0 - T_3$. The situation is illustrated in Figure 1.2.
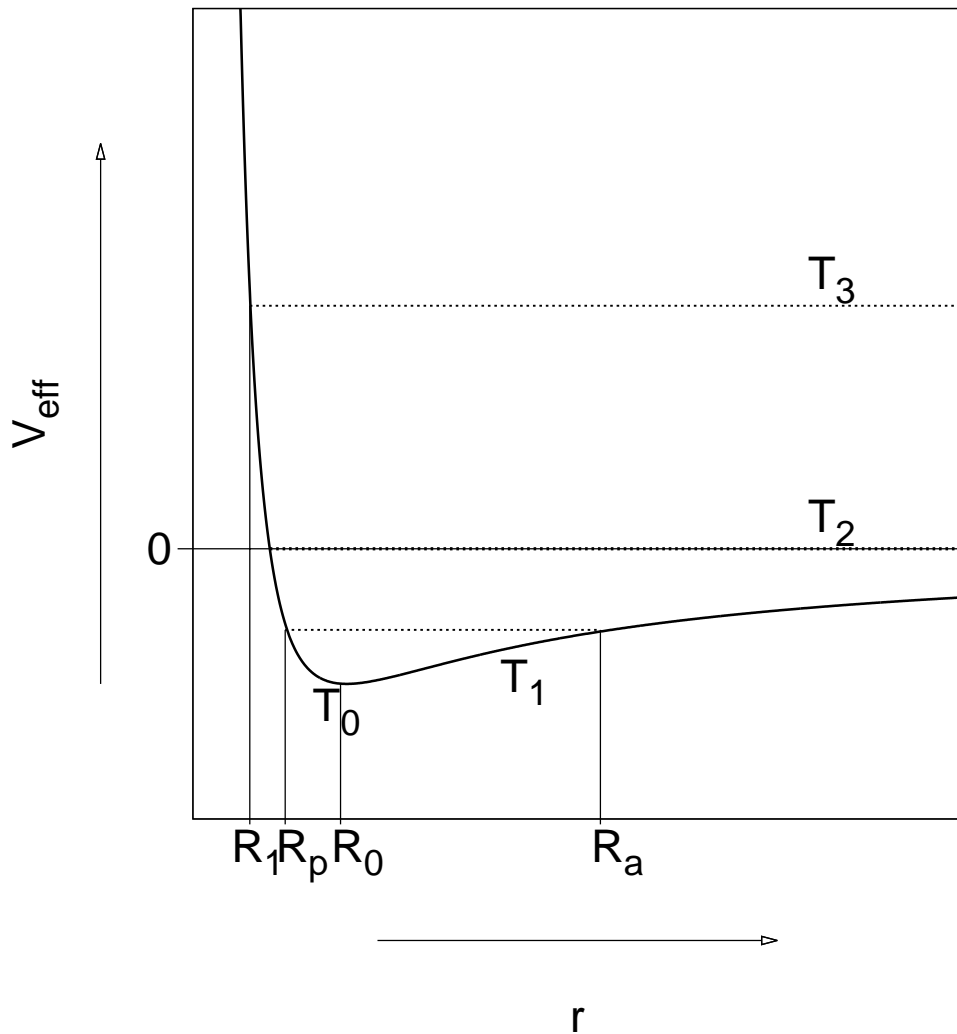
Figure 1.2. Effective potential for a Keplerian point potential. No particle with finite angular momentum can pass the angular momentum barrier as $V_{\text{eff}} \to \infty$ for $r \to 0$.

- T_0: $V_{\text{eff}} = E < 0$ The minimum energy is given by the criterion $\dot{r} = -\sqrt{\frac{2(E-V_{\text{eff}})}{m}} = 0$ and thus $r = $ const. The particle revolves on a circular orbit with fixed radius R_0.

- T_1: $V_{\text{eff}} < E < 0$ The particle is bound and moves on an elliptical orbit. The minimal distance R_P is called pericenter while the maximal distance R_a is known as the apocenter. All bound orbits are closed[2].

- T_2: $E = 0$ The intersection between bound and unbound orbits. The form of the orbit corresponds to a parabola.

---

[2] There exist only two potentials, the Keplerian and the harmonic oscillator potential $V(r) \propto r^2$, where all bound trajectories are generally closed.

- T_3: $E > 0$ A particle on a hyperbolic trajectory reaches the minimal radius R_1 and then recedes back to infinity.

For positive $L > 0$ and $r \to 0$, the centrifugal potential grows unlimited and prevents particles from reaching $r = 0$.

1.2.2. Schwarzschild Black Hole Potential

An impassable angular momentum barrier is absent in general relativistic black hole potentials. The plunge of a particle into the central singularity of a black hole is inescapable, once the angular momentum of the particle is less than a given (but always finite) threshold scale. This criterion is derived in detail below but can also be found in several textbooks (e.g. Misner et al. 1973; Novikov & Frolov 1989).

The gravitational field of a non-rotating black hole is spherically symmetric and the trajectory of a nearby particle can be assumed to lie on a plane specified by the co-ordinates r and ϕ. The emission of gravitational waves is not taken into account. Furthermore, it is assumed that infalling particles induce no back-reaction on the Schwarzschild metric i.e. by turning it into a Kerr metric. Following Novikov & Frolov (1989), the equation of motions of particles around a non-rotating black hole have the form:

$$\left(\frac{\mathrm{d}r}{c\mathrm{d}t} \right)^2 = \frac{\left(1 - \frac{r_s}{r} \right)^2 \left[\tilde{E}^2 - \left(1 - \frac{r_s}{r} \right) \left(1 + \tilde{L}^2 \frac{r_s^2}{r^2} \right) \right]}{\tilde{E}^2} \tag{1.8}$$

$$\left(\frac{\mathrm{d}\phi}{c\mathrm{d}t} \right) = \frac{\left(1 - \frac{r_s}{r} \right) \tilde{L} r_s}{\tilde{E} r^2}. \tag{1.9}$$

The parameters $\tilde{E} = E / \left(mc^2 \right)$ and $\tilde{L} = L / \left(m r_s \right)$ correspond to the specific total energy and angular momentum of the particle. The Schwarzschild radius $r_s = 2GM_\bullet / c^2$ is proportional to the mass $M_\bullet$ of the black hole. When particles approach the pericenter or apocenter of a black hole, the first time derivative of the radius has to be zero, i.e. $\frac{\mathrm{d}r}{\mathrm{d}t} = 0$. At these extremal points, $\tilde{E}^2 - \left(1 - \frac{r_s}{r} \right) \left(1 + \tilde{L}^2 \frac{r_s^2}{r^2} \right) = 0$. The function

$$V_{\mathrm{eff}}(r) = \left(1 - \frac{r_s}{r} \right) \left(1 + \tilde{L}^2 \frac{r_s^2}{r^2} \right) \tag{1.10}$$

is often called the effective potential. It allows to characterize all classes of trajectories for free floating test particles, analogous to the Newtonian case (§ 1.2.1). The specific energy and angular momentum of the particle are conserved quantities as the Schwarzschild metric is invariant under angular coordinate and time transformations. All allowed trajectories ($T_0 - T_5$) are illustrated in Figure 1.3 for particles with different specific energies but the same specific angular momentum $\tilde{L} = 2.6$. They are summarized below:

- T_0 & T_1 represent stable classes of bound orbits. They are not closed and are subject to orbital precession. A particle at the exact location of the local minimum (T_0) has a circular motion.
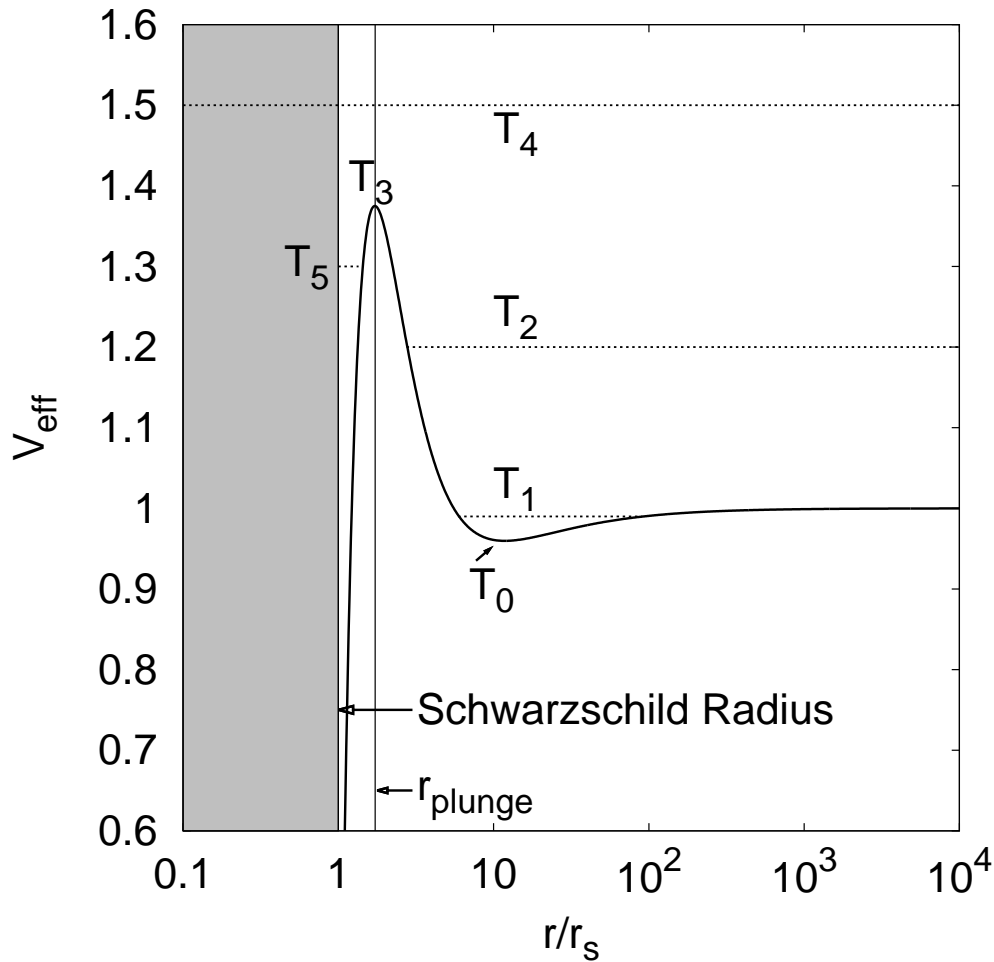
Figure 1.3. In this figure the effective potential with specific angular momentum $\tilde{L} = 2.6$ is plotted as a function or r/r_s. As long as $\tilde{L} \geq \sqrt{3}$, there are several classes of allowed trajectories in a Schwarzschild space-time ($T_0 - T_5$). Approaching particles with (squared) specific energies above the global maximum of $V_{\text{eff}}(r)$ at T_3 will be swallowed by the black hole.

- T_2 symbolizes unbound orbits with a hyperbolic shape.

- T_3 represents a unique class of unstable circular orbits at the global maximum of V_{eff}. An arbitrary small perturbation will either send the particle into the singularity of the black hole or expel it to infinity. These orbits do not occur in Newtonian physics.

- Particles above the maximum of the effective potential (T_4) will either be swallowed or escape forever. These trajectories are also impossible in Newtonian physics.

- Trajectories of particles which are generated at the Schwarzschild radius and which are later swallowed by the black hole correspond to class T_5.

Particles on a path towards the black hole and which have crossed the plunge radius,
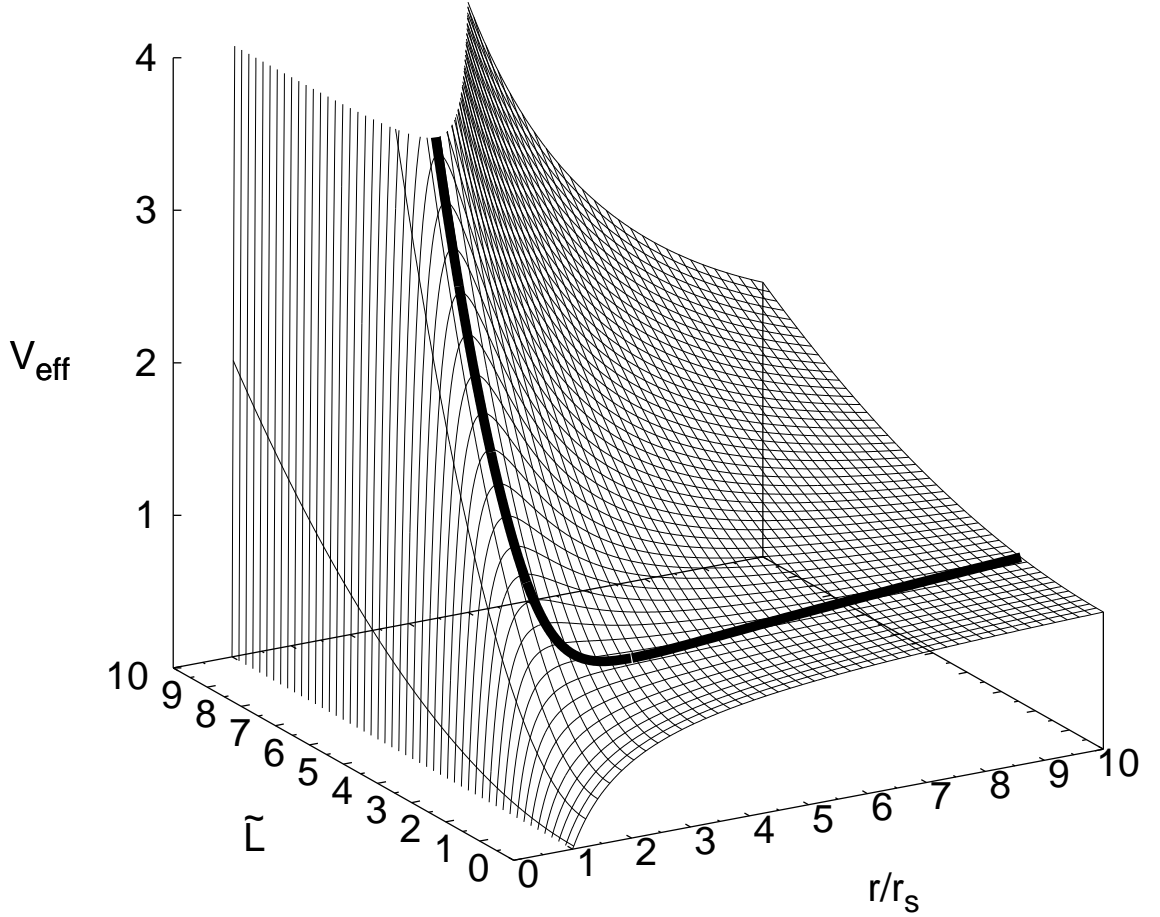
Figure 1.4. The effective potential $V_{\text{eff}}(r)$ plotted as a function of $\tilde{L}$. The plunge radius converges to $r_{\text{plunge}} = 1.5r_s$ if $\tilde{L} \to \infty$. Stable circular orbits can only exist for $r \geq 3r_s$ and $\tilde{L} \geq \sqrt{3}$. The thick black curve traces the maximum of the effective potential. If the specific angular momentum is smaller than $\tilde{L} < \sqrt{3}$, the effective potential becomes monotonic and particle trajectories either end inside the black hole or have to point towards infinity.

r_{plunge}, will inevitably be absorbed by the horizon. The effective potential, $V_{\text{eff}}(r)$, has its global maximum at r_{plunge}. A 3D phase space plot (Figure 1.4) illustrates the shape of the effective potential as a function of r and $\tilde{L}$. The plunge radius is obtained by solving:

$$\frac{\mathrm{d}V_{\text{eff}}}{\mathrm{d}r} = 0 = r^2 - 2\tilde{L}^2 r_s r + 3\tilde{L}^2 r_s^2. \tag{1.11}$$

The two solutions $r_{\pm} = r_s \left[\tilde{L}^2 \pm \tilde{L}\sqrt{\tilde{L}^2 - 3} \right]$ represent the global maximum of $V_{\text{eff}}(r)$ at $r_- = r_{\text{plunge}}$ (black thick line in Fig. 1.4) and the local minimum of the curve at r_+. Unstable circular orbits exist only for $r_- > 1.5r_s$ and $\tilde{L} > \sqrt{3}$ since $\lim_{\tilde{L} \to \infty} (r_{\text{plunge}}) = 1.5r_s$. Circular orbits which are stable can only exist for $r_+ > 3r_s$ and $\tilde{L} > \sqrt{3}$. The maximal conversion efficiency, ϵ, of gravitational binding energy into heat/radiation of an almost circular accretion flow ($\tilde{L}(r) \propto \sqrt{r}$) around a non-rotating black hole is

therefore restricted by the limit[3]:

$$\epsilon = \Delta E / \left(mc^2\right) = \left.\sqrt{V_{\text{eff}}}\right|_{r\to\infty} - \left.\sqrt{V_{\text{eff}}}\right|_{r=3r_s,\tilde{L}=\sqrt{3}}$$

$$= 1 - \sqrt{\left(1 - \frac{r_s}{3r_s}\right)\left(1 + 3\frac{r_s^2}{9r_s^2}\right)} \approx 0.06. \qquad (1.12)$$

Accreted matter on circular orbits which passes this limit will enter the unstable regime. From then on, gravitational binding energy can no longer be converted into heat/radiation as the matter plunges within a light crossing timescale r_s/c into the black hole. The innermost stable circular orbit (ISCO), which also marks the inner boundary of the accretion disk, can be (indirectly) inferred via X-ray spectroscopy of accreting black holes (see e.g. Reynolds 2013; Brenneman 2013 and references for a review on this topic).

Particles which approach the black hole with a specific angular momentum less than $\tilde{L} = \sqrt{3}$ will always be captured. In this case the effective potential becomes a monotonic decreasing function (see Figure 1.4) and there are no stable orbits altogether.

1.2.3. Loss Cone Trajectories

The plunge radius, r_{plunge}, which is always larger than 1.5 times the Schwarzschild radius can therefore be used in SMBH growth studies as the effective boundary of the black hole i.e. as a general capture criterion. As discussed in § 1.2.2, there is no way a particle (without self propulsion) can prevent its final infall, once it passed r_{plunge} in the direction of the black hole i.e. $r < r_{\text{plunge}}$. Given the case that $\tilde{L} < \sqrt{3}$, one only has to check whether the particle is moving in direction of the black hole. The parameter r_{plunge} depends on the velocity and position vectors $\vec{r}$ and $\vec{v}$ of each particle. A general relativistic capture criterion can be defined as:

$$\begin{cases} r < r_{\text{plunge}} = r_s\left[\tilde{L}^2 - \tilde{L}\sqrt{\tilde{L}^2 - 3}\right], \quad \tilde{L} = \left|\frac{m\vec{r}\times\vec{v}}{mr_s}\right| = \frac{1}{r_s}\left|\vec{r}\times\vec{v}\right| \quad : \quad \tilde{L} \geq \sqrt{3} \\ \vec{r}\cdot\vec{v} < 0 \qquad\qquad\qquad\qquad\qquad\qquad\qquad\qquad\qquad\qquad\qquad\quad : \quad \tilde{L} < \sqrt{3} \end{cases} \qquad (1.13)$$

However, nature is complex and the usage of point particles and Equation 1.13 in numerical investigations must be considered carefully. In reality, a Sun like or red giant star would be tidally disrupted outside the Schwarzschild radius (or even outside the plunge radius, r_{plunge}) of a $M_\bullet < 10^8 M_\odot$ black hole. Significant amounts of mass can be blown away in such tidal disruption events (TDEs) and the observed energy release is enormous (Zauderer et al., 2011). In addition to that a star might become gravitationally unbound close to a black hole without being on a trajectory of the kind T_4

---

[3]The amount of extractable energy (measured at infinity) for maximal rotating black holes lies between $\Delta E / \left(mc^2\right) \approx 0.04$ (retrograde motion in the equatorial plane) and $\Delta E / \left(mc^2\right) \approx 0.4$ (prograde motion in the equatorial plane) (Novikov & Frolov, 1989). High resolution sub-mm VLBI observations of M87 revealed that a retrograde accretion flow is not compatible with observations subject to a source size of $5.5r_s$. This is smaller than the innermost stable circular orbit for retrograde accretion when corrected for gravitational lensing effects (Doeleman et al., 2012). A spinning black hole with a prograde accretion disk seems to match the observations.

(§ 1.2.2). In general, the physics behind TDEs are complex. Their occurrence depends on many parameters (e.g. $M_\bullet$, its spin, stellar structure) (MacLeod et al., 2012). The usage of a disruption radius $r_{\rm dis} > r_{\rm plunge} > r_s$ instead of the general relativistic criterion (Equation 1.13) might be a more reasonable strategy for numerical tidal disruption investigations of solar like stars around black holes less massive than $M_\bullet < 10^8 M_\odot$. The disruption radius is defined as:

$$r_{\rm dis} = g r_\star \left(\frac{M_\bullet}{M_\star} \right)^{\frac{1}{3}}, \tag{1.14}$$

where $r_\star$ is the radius and $M_\star$ the mass of the star. The parameter g accounts for several physical effects like the spin of the black hole (Kochanek, 1992; Lai et al., 1994; Ivanov & Chernyakova, 2006). In a first order approximation, $g = 1$. The situation changes when treating compact remnants and/or very massive black holes in excess of $10^8 M_\odot$. In this case the tidal disruption radius, $r_{\rm dis}$, lies within the event horizon of the black hole and Equation 1.13 instead of Equation 1.14 should be used. The relevant radius, $r_{\rm cap}$, where the object becomes either swallowed or tidally unbound has to be defined in consideration of the numerical problem.

Regardless of the exact fate of the stars around SMBHs (i.e. if they are disrupted or swallowed as a whole) one can introduce the concept of the loss cone. The loss cone defines a special region in velocity space which is defined by the loss cone angle, θ_{lc}. The symmetry axis of θ_{lc} points in direction of the SMBH and a particle on a loss cone trajectory will either be disrupted, swallowed or scattered onto a different orbit (if there is a binary SMBH) within one orbital timescale, i.e. crossing time $T_{\rm cross} = r/v$. The concept behind the loss cone is illustrated in Figure 1.5.
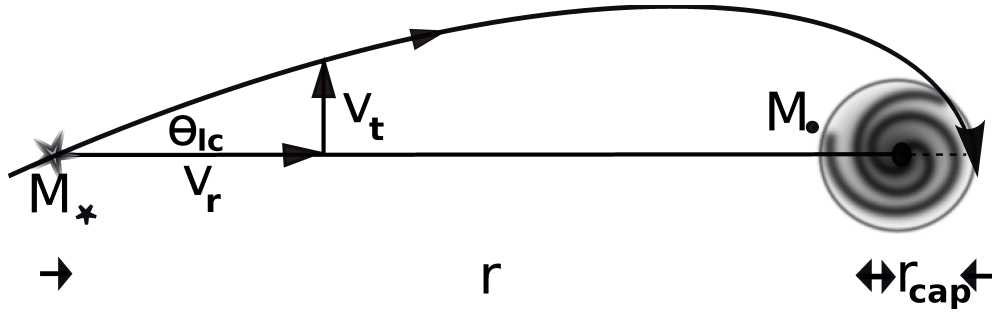
Figure 1.5. The concept of the loss cone. A star of mass $M_\star$ will be swallowed as a whole or tidally destroyed when crossing a characteristic radius, $r_{\rm cap}$. Depending on the mass of the black hole, $r_{\rm cap}$ can either be the plunge radius, $r_{\rm plunge}$, from which the plunge into the black hole is inescapable (Equation 1.13), or the tidal disruption radius, $r_{\rm dis}$ (Equation 1.14). The figure is taken from Brockamp et al. (2011).

One great challenge in astrophysics is the understanding of the related evolution of cosmic structures and massive black holes. It is important (i) to uncover all processes which are responsible for the refilling of the black hole loss cone and (ii) to understand how growing black holes affect their environment. Finally (iii), to quantify the amount

of mass on loss cone orbits in different cosmic environments. In Section 2.1 empirical scaling relations between the properties of galaxies (§ 2.1.1) and the mass of their central SMBHs (§ 2.1.2) will be introduced. Black hole scaling relations yield important observational constraints on all proposed SMBH growth mechanisms. Afterwards, some of the proposed black hole growth processes are summarized in Section 2.2. This allows to place the results of the underlying PhD study in the broader picture of black hole growth processes.

Chapter 2

SMBH Scaling Relations
& Growth Processes

2.1. SMBH Scaling Relations

One of the most important discoveries concerning the related evolution of galaxies and their central black holes was made once high resolution telescopes, e.g. the Hubble Space Telescope (HST), became operational. The observed correlations between SMBHs and galaxies contain informations about their common evolution. In the following sections, basic properties of galaxies (§ 2.1.1) and SMBH mass measurement methods (§ 2.1.2) will be presented before summarizing several important SMBH scaling relations (§ 2.1.3).

2.1.1. Galaxies

Definition

The answer to the question "what defines a galaxy" is anything but trivial. Following the suggestions by Kroupa (1998) and Forbes & Kroupa (2011), it is assumed for the sake of this PhD study that a galaxy is a bound and dynamically stable stellar system with a two-body relaxation timescale, $T_{\rm rel}$, greater than one Hubble time, H_0^{-1}. $T_{\rm rel}$ is the time until the memory of initial conditions are lost by gravitational deflections between field stars. The smoother the potential of a galaxy, the longer is the relaxation timescale. As a first order approximation, $T_{\rm rel}$ can be defined as:

$$T_{\rm rel} \approx \frac{0.1N}{\ln{(N)}} T_{\rm cross},$$

(2.15)

where N is the number of stars and $T_{\rm cross} = R/v$ is the typical crossing timescale of the galaxy. The derivation of Equation 2.15 can be found in numerous textbooks, e.g. Binney & Tremaine (2008). Merging or interacting stellar systems out of the equilibrium state are called "interacting/merging galaxies" if their progenitors fulfilled these conditions.

General Properties

Galaxies cover a huge range of masses and sizes, from dwarf elliptical galaxies with $M_{\mathrm{gal}} = 10^7 M_\odot$ and effective radii $R_e \approx 100\mathrm{pc}$ up to brightest cluster galaxies (BCG) with masses approaching $M_{\mathrm{gal}} = 10^{13} M_\odot$ (e.g. the BCG inside Abell 3827, see Carrasco et al. 2010) and R_e up to several dozen kpc. The effective radius R_e is the projected (2D) radius within which half of the optical light is emitted. Galaxies are composed of stars and stellar remnants. Depending on their type they also contain an interstellar medium (ISM) in several physical states, from a dusty and cold molecular phase up to a hot X-ray emitting plasma. Their metallicity content is positively correlated to the galaxy mass. Another very important component of a galaxy is an entity which is called "dark matter (DM)". Dark matter within galaxies and even larger structures should be defined as the discrepancy between the expected gravitational dynamics derived from the total baryonic mass content and actual observations. Up to now there is no general consensus whether the nature of DM should be explained by (i) weakly interacting particles (WIMPs) (Feng, 2010), (ii) condensed galaxy sized scalar fields from the early universe (Magaña & Matos, 2012), or (iii) a modification of the known laws of gravity in the weak curvature regime (Milgrom, 1983; Kroupa, 2012). Apart from that, galaxies often contain star formation regions, star clusters, spatially extended globular clusters systems (Harris et al., 2013) and supermassive black holes at their centers (Magorrian et al., 1998).

Galaxies can be classified into three morphology types (elliptical, spiral/disk and irregular) which themselves can be divided into several subclasses (Hubble sequence). Most galaxies in the universe with stellar masses above $M_{\mathrm{gal}} = 10^{10} M_\odot$ are rotationally supported disk galaxies (Kroupa, 2014). Nevertheless, the main focus of this PhD study lies on elliptical galaxies, hence the physical properties of spiral and irregular galaxies will not be the subject of this discussion.

Elliptical Galaxies

Elliptical galaxies are commonly observed in high density environments like galaxy clusters. Only at first glance, elliptical galaxies seem to be featureless stellar systems with old stellar populations. Indeed, they have a complex internal structure and often display shells or ripples (Malin & Carter, 1980) revealing their turbulent formation and interaction history. Contrary to spiral galaxies, the present-day star formation rate in elliptical galaxies is strongly reduced. Spectacular exceptions are some of the brightest cluster galaxies inside cooling flow clusters (e.g. the Phönix cluster, see McDonald et al. 2012) with huge reservoirs of molecular gas (Edge, 2001), star formation rates as high as $10^2 - 10^3 M_\odot yr^{-1}$ (Hicks & Mushotzky, 2005; McDonald et al., 2012) and filamentary structures around them (Fabian et al., 2008). The "typical" elliptical galaxy does not contain significant amounts of cold gas but is often embedded within an X-ray emitting halo. The integrated X-ray emission stems from discrete stellar sources like low-mass X-ray binaries (LMXBs) and hot gas. In the most massive elliptical galaxies, a corona of hot plasma is responsible for the majority of the total X-ray luminosity (Brown & Bregman, 2001).

Observations of elliptical galaxies also reveal a correlation between the effective radius, R_e, total luminosity, L, and line of sight velocity dispersion, $\sigma_{||}$. The line of sight velocity dispersion is measured from Doppler broadened spectral lines. The line broadening is mainly subject to the motion of stars in the gravitational potential of the galaxy and due to numerous orbiting binary stars within these galaxies. Following Jorgensen et al. (1996), this empirical relation has the form:

$$
\begin{aligned}
\log_{10}\left(\frac{R_e}{\text{kpc}}\right) = (1.24 \pm 0.07)\log_{10}\left(\frac{\sigma_{||}}{\text{km/s}}\right) - \\
(0.82 \pm 0.02)\log_{10}\left(\frac{\langle I\rangle_e}{\text{L}_\odot/\text{pc}^2}\right) + \zeta,
\end{aligned} \tag{2.16}
$$

where instead of L, the mean surface brightness, $\langle I\rangle_e \equiv 0.5L/\left(\pi R_e^2\right)$ (Binney & Tremaine, 2008), is often used. The parameter ζ is a calibration constant. Elliptical galaxies populate a plane within a 3D coordinate system with axes $\log_{10} R_e, \log_{10}\sigma_{||}$ and $\log_{10}\langle I\rangle_e$. This plane is known as the fundamental plane of elliptical galaxies and is defined in Equation 2.16. The fundamental plane and some of its 2D projections (such that the projected plane resembles a line) allow to evaluate physical quantities of elliptical galaxies by only measuring a few parameters. The most famous 2D projections are the Faber-Jackson and Kormendy relation. From the Faber-Jackson relation, which correlates $\sigma_{||}$ and L, one can obtain the total luminosity of the galaxy from spectral line broadening, i.e. $\sigma_{||}$. It is particularly important for inferring galaxy distances. The Kormendy relation correlates the surface brightness, $I_e\left(R = R_e\right)$, to the half light radius, R_e.

Elliptical galaxies have different shapes $E\kappa$, where $\kappa = 10 \cdot (1 - b/a)$, a is the semi-major axis and b is the semi-minor axis. The deprojected 3D shape can be symmetric, axis-symmetric (prolate or oblate) or triaxial. Very massive elliptical galaxies often have a triaxial structure (Bak & Statler, 2000; Fasano et al., 2010).

There are several ways how the overall (2D) surface brightness profiles of elliptical galaxies can be approximated by analytical regressions. Among them are the Sérsic and the Nuker law. Following Sersic (1968) and Ciotti & Bertin (1999), the Sérsic profile has the form:

$$
I_n(R) = I_e \exp\left\{-b_n\left[\left(\frac{R}{R_e}\right)^{\frac{1}{n}} - 1\right]\right\}. \tag{2.17}
$$

The Sérsic index, n, specifies the optical light concentration towards the center of the galaxy. It has typical values in the range $1 < n < 10$. The parameter b_n is a dimensionless normalization quantity which is defined in such a way that the emitted light within R_e contributes half of the total luminosity. I_e corresponds to the surface brightness at R_e. Alternatively, the surface brightness profile can also be well approximated by the Nuker profile (see e.g. Lauer et al. 1995, 2007). The Nuker profile is based on a power-law regression with inner and outer slope parameters, γ and β, as well as a parameter α controlling the sharpness of the transition (Lauer et al., 1995):

$$
I(R) = 2^{(\beta-\gamma)/\alpha}I_b\left(\frac{R_b}{R}\right)^\gamma\left[1 + (R/R_b)^\alpha\right]^{(\gamma-\beta)/\alpha} \tag{2.18}
$$

The break radius, R_b, is located at the intersection of both profiles where the curvature of the brightness profile is maximized. I_b is the brightness at R_b. Depending on α, β, γ and the break radius, R_b, one can introduce another characteristic radius, the so called cusp radius, R_γ. It is relevant for e.g. black hole related research and is defined to be:

$$R_\gamma \equiv R_b \left(\frac{\frac{1}{2} - \gamma}{\beta - \frac{1}{2}} \right)^{\frac{1}{\alpha}}. \tag{2.19}$$

In spite of these very general properties of elliptical galaxies, there are distinctions between low and high mass elliptical galaxies. Low mass elliptical galaxies which are fainter than $M_V > -20.5$ typically have disky isophotal shapes and steeply rising density profiles towards the center as given by Equation 2.17 or by Equation 2.18 in form of an unresolved break radius. They are also subject to rotation with dimensionless rotation parameters $v_{\mathrm{rot}}/\sigma_\parallel \geq 0.51$ (Kormendy & Bender, 1996; Faber et al., 1997). The more massive and luminous elliptical galaxies ($M_V < -22$) have a boxy appearance, i.e. their isophotes (=lines of constant brightness) resemble rectangles. These elliptical galaxies are mostly pressure-supported, i.e. "hot" stellar systems without significant rotation (Faber et al., 1997). The stars move along trajectories without a common sense of rotation. Often there is a pronounced transition or break in the overall surface-brightness profile $I(r)$ at a certain radius R_{break} (Trujillo et al., 2004; Lauer et al., 2007; Kormendy & Bender, 2009) when compared to Equation 2.17. The break radius can also be determined by using a Nuker law (Equation 2.18). Usually, the size of the break radius corresponds to a few percent of R_e. The brightness profile within R_{break} resembles a plateau and is much flatter than that of the outer stellar halo. If the central stellar light profile within R_{break} becomes shallower than a power-law profile, $I(R) \propto R^{-\gamma}$, with index $\gamma < 0.3$, the galaxy is termed to be a core-type galaxy (Lauer et al., 1995). Break radii of galaxies like M87 or M60 are of the order of a few 100 pc (Lauer et al., 2007). In some brightest cluster galaxies R_{break} can reach several kpc in size (McNamara et al., 2009; Postman et al., 2012), up to 10-20kpc in the most extreme brightest cluster galaxies like IC 1101 (Dressler, 1979) and Holm 15A (Lopez-Cruz et al., 2014). The difference in total luminosity which can be obtained by subtracting the measured light profile from the outer profile being extrapolated inwards, is called the light deficit, L_{def}. A cored density profile of a real galaxy is shown in Figure 2.6. It is taken from Postman et al. (2012)[4]. The break radius which can be either obtained from a core-Sérsic fit (Trujillo et al., 2004) or a Nuker law fit (Lauer et al., 1995) should not be confused with the cusp radius, R_γ, which lies inside R_{break} and which is defined in Equation 2.19. For the sake of this study the core radius is defined to be the cusp radius as long as the inner power-law profile is flatter than $I(R) \propto R^{-0.3}$. Most famous core formation scenarios involve binary or multiple SMBH evolution processes (Makino 1997; Merritt & Poon 2004; Kulkarni & Loeb 2012, § 2.2.3). Elliptical galaxies with the largest cores are therefore promising candidates for hosting the most massive SMBHs in the universe, sometimes with masses exceeding $10^{10} M_\odot$ (McNamara et al., 2009; McConnell et al., 2011; Hlavacek-Larrondo et al., 2012) and maybe even $10^{11} M_\odot$ (Lopez-Cruz et al., 2014).

---

[4]Source downloaded from the arXiv preprint server.
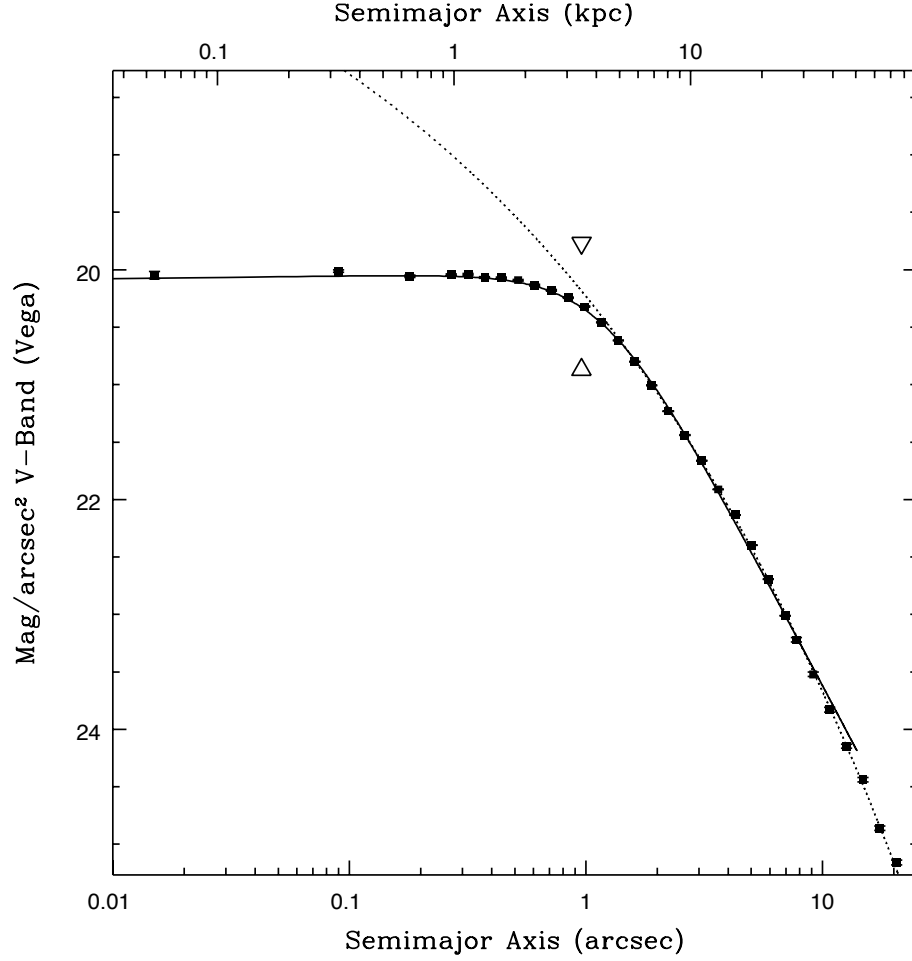
Figure 2.6. The cored density profile (black dots) of the brightest cluster galaxy inside the Abell 2261 galaxy cluster. The thin dotted line represents a Sérsic n=4 profile given by Equation 2.17. The arrows mark the position of the break radius. The area between the thin dotted profile which is obtained from a Sérsic fit of the stellar envelope and the measured brightness profile (solid black line) corresponds to the light deficit, $L_{\mathrm{def}} \approx 2 \cdot 10^{10} L_{\odot}$. The figure is taken from Postman et al. (2012).

2.1.2. SMBH Mass Measurements

All direct SMBH mass measurements rely on the temporal/kinematical properties of luminous matter close to the black hole. From the inferred velocities, these methods apply Newton's laws of gravity to infer the central SMBH mass. A complete description of all existing SMBH mass determination techniques is far beyond the scope of this PhD thesis. Hence, only the three most important methods are briefly mentioned.

- **MASERs:** Under the right circumstances (e.g. a radio continuum emitting AGN and the presence of particular molecules), some SMBHs are surrounded by circumnuclear disks containing MASERs. A MASER is a molecular cloud with stimulated spectral line emission at a particular frequency. The characteristic

frequency of these MASERs becomes shifted by the Doppler effect due to their motions around the black hole. In this way one can constrain the central potential/SMBH mass and in some cases the geometry of the disk itself. In the galaxy NGC 4258 (M 106) several MASERs orbit a $M_\bullet = 3.79 \, (\pm 0.01) \cdot 10^7 M_\odot$ black hole (Herrnstein et al., 2005). The disk which contains these MASERs is not flat but warped (Herrnstein et al., 2005). MASER spectroscopy belongs to the most precise SMBH mass measurement techniques.

- **Gas Dynamics:** Although elliptical galaxies are usually depleted of significant amounts of dust and molecular gas, roughly 20% of them (Tran et al., 2001) harbor nuclear dusty disks within their central regions (e.g. M 87 or NGC 4261). Even without MASERs, such tori can be used as tracers of the gravitational potential and allow to determine the mass of the central dark object. This is done by finding the model which reproduces the spectroscopically inferred kinematics most accurately. In these models the central SMBH mass and disk inclination are treated as free parameters. The density profile (required to evaluate the gravitational contribution from surrounding matter) is obtained from the observed surface brightness profile. Dust/gas disks are well suited for spectroscopic measurements due to their high surface brightness. Furthermore, their kinematics can be probed to small scale distances (e.g. 40 pc for M87, Walsh et al. 2013) where the Keplerian contribution of the black hole potential strongly dominates over the enclosed stellar/gas mass. The measurement of the Keplerian rise in the rotation velocity is one reason why this technique belongs to the most robust black hole mass determinations. However, the kinematics might be influenced by non-gravitational forces and in- or outflowing gas complicates the interpretation of the measurements.

- **Stellar Dynamics:** The motion of a star is governed by the overall gravitational potential. In the Galactic Center, where the nearest SMBH is located, the study of individual stellar Keplerian orbits allows to constrain the central black hole mass to be $M_\bullet = 4.31 \, (\pm 0.06 \pm 0.36) \cdot 10^6 M_\bullet$ (Gillessen et al., 2009). The second (larger) error value results from distance uncertainties. SMBH mass measurements at extragalactic distances become more challenging as individual stellar orbits can not be resolved. Instead, these measurements have to rely on the velocity dispersion profile which is obtained from broadened spectral lines. Secure SMBH mass determinations based on stellar dynamics can only be performed if the resolution scale is significantly smaller than the sphere of influence, $R_{\mathrm{infl}} \equiv GM_\bullet / \sigma_{||}^2$. This radius marks the projected distance where the circular velocity equals the line of sight velocity dispersion, $\sigma_{||}$. Only deep within R_{infl}, the Keplerian $r^{-0.5}$ rise in the velocity profile becomes evident. Merritt (2013) suggests that a resolution scale of at least $0.1 R_{\mathrm{infl}}$ is required in order to detect the Keplerian rise in the velocity profile caused by the central black hole. SMBH mass measurements based on stellar dynamics become even more ambitious in very massive core-type elliptical galaxies. Here, the low central surface brightness complicates efforts to obtain spectral information because stars deep within R_{infl} contribute much less to the line of sight velocities. If the Keplerian rise in velocity is not evident in the data, the contribution of the SMBH mass has to be

disentangled from the rest of the galactic matter. In this case additional factors must be included in the modeling: (i) The velocity distribution in cored density profiles can be tangentially biased (Quinlan & Hernquist, 1997; McConnell et al., 2012) i.e. dominated by circular orbits which reduces the observed line of sight velocity dispersion. (ii) In anisotropic and triaxial host galaxies the radial velocity dispersion depends on the line of sight and stars occupy different orbits (van den Bosch & de Zeeuw, 2010). Finally (iii), the extended matter distribution might also display a varying mass to light ratio, Y, along r (Gebhardt & Thomas, 2009; McConnell et al., 2013). In some cases stellar dynamical mass determinations differ from those obtained from gas dynamical methods. The central SMBH mass inside M87 ranges from $M_\bullet = 3.5 \pm_{0.7}^{0.9} \cdot 10^9 M_\odot$ (gas dynamics) (Walsh et al., 2013) up to $M_\bullet = 6.6 \pm_{0.6}^{0.6} \cdot 10^9 M_\bullet$ (stellar dynamics) (Gebhardt et al., 2011).

SMBH mass measurements which are based on pure general relativistic effects instead of conventional Newtonian based potential calculations will become feasible in the near future. Intercontinental sub-mm interferometry (also known as the "Event Horizon Telescope") will open an independent mass measurement method from direct size constraints of the SMBH shadow for a few particular cases of nearby and radio loud sources (Doeleman et al., 2009; Johannsen et al., 2012). The shadow of a black hole corresponds to the last stable orbit for massless particles (i.e. $1.5 r_s$, Section 1.2.2) and appears as a dark silhouette within the bright accretion disk. It is related to the mass and spin of the black hole and appears enlarged by gravitational lensing effects.

2.1.3. SMBH Demographics

$M_\bullet - L, \sigma, M_{\text{bulge}}$ Relations

Empirical SMBH scaling relations yield valuable information on the mutual evolution histories of galaxies and their central SMBHs. One of the first SMBH scaling relations was reported by Kormendy & Richstone (1995). They discovered that central SMBH masses positively correlate with the absolute B-band bulge magnitude. Follow-up work not only increased the sample of SMBH measurements but also demonstrated that other wavelength bands, especially the K-band, are much better suited for the usage in luminosity-SMBH scaling relations. In the K-band, the (red) bulge component can be disentangled from the bluish disk structure and the scatter in $M_\bullet - L_K$ becomes smaller than in the empirical $M_\bullet - L_B$ relation (Marconi & Hunt, 2003; Ferrarese & Ford, 2005). This also means that the central SMBH mass correlates more closely with the bulge component of a galaxy.

Of similar impact as $M_\bullet - L$ is a different scaling relation which was discovered in the year 2000 by Ferrarese & Merritt (2000) and Gebhardt et al. (2000). It is known as the $M_\bullet - \sigma$ relation and was continuously updated in the following years by several studies, e.g. Tremaine et al. (2002); Ferrarese & Ford (2005); Gültekin et al. (2009); Schulze & Gebhardt (2011); McConnell & Ma (2013). According to McConnell & Ma
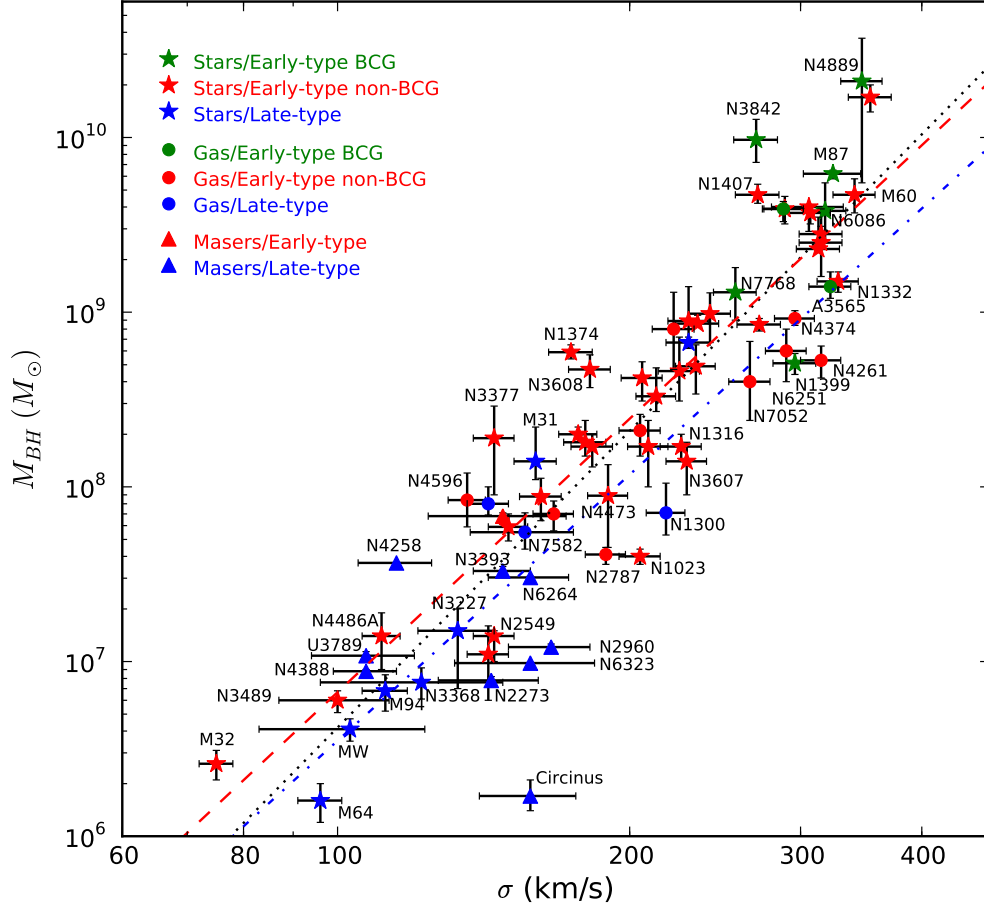
Figure 2.7. The figure is taken from McConnell & Ma (2013). It shows the most recent compilation of galaxies used for the $M_\bullet - \sigma$ relation including disk galaxies (blue), elliptical galaxies (red) and brightest cluster galaxies (green). Evidently, BCGs contain the most massive black holes. The individual data points are also labeled with respect to the used SMBH mass measurement method. As can be seen, SMBH masses obtained from the MASER spectroscopy technique (red and blue triangles) have the smallest y-error values (§ 2.1.2).

(2013), the effective velocity dispersion, σ, can be defined as:

$$\sigma^2 = \frac{\int_{R_{\min}}^{R_e} I(r) \left(v^2(r) + \sigma_{||}^2(r) \right) \mathrm{d}r}{\int_{R_{\min}}^{R_e} I(r) \mathrm{d}r}, \tag{2.20}$$

where the radial velocity, $v(r)$, and the line of sight velocity dispersion, $\sigma_{||}(r)$, are integrated from $R_{\min}$ out to the effective radius, R_e. There is no general consensus whether to use $R_{\min} = 0$ or $R_{\min} = R_{\text{infl}}$ (McConnell & Ma, 2013). In the former case, σ might be strongly biased by the high central velocities in the immediate vicinity of the black hole. $I(r)$ is the surface brightness profile. The most recent $M_\bullet - \sigma$ power-law regression (McConnell & Ma, 2013), including late and early type galaxies and by using

$R_{\mathrm{min}} = R_{\mathrm{infl}}$, is given by:

$$\log_{10}\left(\frac{M_\bullet}{\mathrm{M}_\odot}\right) = 8.32\,(\pm 0.05) + 5.64\,(\pm 0.32)\log_{10}\left(\frac{\sigma}{\mathrm{km/s}}\right). \qquad (2.21)$$

This relation is also shown in Figure 2.7. Figure 2.7 is taken from McConnell & Ma (2013). Inasmuch as the velocity dispersion σ and total luminosity are tracers of the total bulge mass, a direct relation between M_{bulge} and $M_\bullet$ is also reasonable. McLure & Dunlop (2002); Marconi & Hunt (2003); Häring & Rix (2004) found that the central SMBH mass constitutes $\approx 0.0012 - 0.002$ of the total bulge mass.

Scaling relations like $M_\bullet - L, \sigma, M_{\mathrm{bulge}}$ point to a common evolution scenario of both central black holes and galaxies. Nowadays, there exist several different explanations for the origin of these empirical relations. They range from self-regulated-gas-accretion models (Silk & Rees, 1998), scenarios where the tidal disruption of stars drive the growth of massive black holes (Zhao et al., 2002) up to mass assembly via hierarchical merger events in cold dark matter halos (Malbon et al., 2007; Jahnke & Macciò, 2011). In the latter scenario even extreme mass ratios, $M_\bullet / M_{\mathrm{bulge}}$, average out and the mean becomes similar to the observed scaling relations. However, there is evidence against these Lambda-CDM based hierarchical merger models (McConnell & Ma, 2013). They generically predict a decreasing amount of scatter towards the high mass end of the SMBH/galaxy population (subject to an enhanced merger rate) whereas observations indicate a constant scatter (McConnell & Ma, 2013). See also Shannon et al. (2013) for constraints on the gravitational wave background from pulsar timing. The obtained limits seem to be incompatible with Lambda-CDM based predictions. SMBH growth processes will be investigated in more detail in Section 2.2. Additionally, § 2.2 establishes the relationship to the work presented in this PhD thesis.

$M_\bullet - L_{\mathbf{def}}, R_{\mathbf{break}}, N_{\mathbf{GC}}$ Relations

Besides the $M_\bullet - L, \sigma, M_{\mathrm{bulge}}$ relations, there are other empirical correlations which yield insights into the interaction between galaxies and their central SMBHs. Scaling relations between $M_\bullet$ and properties of the galactic centers were reported by Kormendy & Bender (2009) and Rusli et al. (2013). Several of their results were also discussed in previous studies, e.g. Lauer et al. (2007). These scaling relation correlate $M_\bullet$ with the light deficit, L_{def}, the size of the break radius, R_{break}, or the (core-)cusp radius, R_γ (§ 2.1.1). In one popular scenario the observed shallow core profiles of massive galaxies are carved out by binary or multiple SMBH coalescence after merger events of whole galaxies. The SMBHs reduce first their angular momentum relative to each other by dynamical friction forces when moving through an entity of field stars. Once the orbital speeds of the black holes become larger than the velocity dispersion of their host galaxy, they enter the second phase, sometimes called the ejection driven phase. In this phase the two black holes form a hard binary which ejects stars (preferentially on eccentric orbits) and carves out a central stellar mass deficit. Finally, gravitational wave emission becomes dominant and causes the black holes to coalesce. Remaining stars move preferentially on circular orbits (Quinlan & Hernquist, 1997). More detailed

information on SMBH merging processes are presented in Section 2.2.3. Therefore, indirect evidence for black hole merging processes comes from core-type galaxies with a tangentially biased velocity distribution (= dominated by circular orbits) within their inner most center. An impressive example is the 800pc core of NGC 4889 with a tangentially biased velocity dispersion and a $M_\bullet \approx (2.1\pm^{1.6}_{1.5}) \cdot 10^{10} M_\odot$ black hole (McConnell et al., 2012). The galaxy experiences further dynamical heating in its core if the kick velocity of the merged black hole, through the anisotropic emission of gravitational waves, is large. The central light/mass deficit as well as the core size becomes even larger (Boylan-Kolchin et al., 2004; Merritt & Poon, 2004). The $M_\bullet - L_{\mathrm{def}}$, $M_\bullet - R_\gamma$ and $M_\bullet - R_{\mathrm{break}}$ relations will play a role in constraining merger histories of galaxies which can then be confronted with predictions of cosmological simulations. However, it should be noted that there are additional processes which might also contribute in the shaping of the observed shallow light profiles of very massive elliptical galaxies. These involve strong quasar feedback, quenching the star formation rate during the early evolution of elliptical galaxies (Martizzi et al., 2012) and star-accreting SMBHs (Merritt & Vasiliev, 2011). Due to its relevance for the underlying PhD thesis, the last aspect will be discussed in more detail in § 2.2.2.

Another empirical scaling relation with high significance for this work was unveiled by Burkert & Tremaine (2010) and Harris & Harris (2011). Their discovery was a linear relationship between the total number of globular clusters, N_{GC}, and the mass of the central black hole. There is ongoing debate, whether $M_\bullet$ and N_{GC} are indirectly related through the bulge mass of their host galaxies (Rhode, 2012) or if GCs contribute directly to SMBH feeding processes (Capuzzo-Dolcetta & Vicari, 2005; Gnedin et al., 2014). Globular clusters belong to the oldest fossils of galaxies. They represent the tip of the iceberg of an ancient population of star clusters which have been eroded since then and which formed the halo star population (see e.g. Kroupa & Boily 2002 and Chapter 4). The temporal evolution of these cluster systems, particularly in relation to different galactic environments and SMBH masses, will be presented in Chapter 4 of this PhD study.

2.2. SMBH Growth Processes

The most massive black holes must have grown quickly. Optical and infrared surveys like the Sloan Digital Sky Survey (SDSS) have uncovered the existence of quasars with accretion disc luminosities $L_D > 10^{13} L_\odot$ up to redshifts of $z \approx 7$. The current record holder is the quasar ULASJ1120+0641 with a luminosity of $L_D = 6 \cdot 10^{13} L_\odot$ at redshift $z = 7.1$ (Mortlock et al., 2011). The mass of its central black hole can be independently estimated by using the Eddington limit[5]:

$$L_{\mathrm{Edd}} = 1.3 \cdot 10^{38} \left(\frac{M_\bullet}{M_\odot} \right) \mathrm{erg/s} \approx 33000 \left(\frac{M_\bullet}{M_\odot} \right) L_\odot \qquad (2.22)$$

---

[5] At the Eddington limit the radiation force (i.e. pressure force of the photons) counterbalances the gravitational force of the black hole. The Eddington limit applies to spherical symmetric cases.

as well as by applying a technique which bases on the measured MgII line width. Emission lines like MgII are broadened due to high velocities ($\approx 0.01c$) in the immediate vicinity of the SMBH and can be used as tracers of its mass. Both methods predict a central SMBH mass of $M_\bullet = 2 \cdot 10^9 M_\odot$ at a time when the universe was only 770 Myr old (Mortlock et al., 2011). However, the exact age depends on the cosmological parameters which are assumed to be $\Omega_m = 0.26$, $\Omega_\Lambda = 0.74$, $H_0 = 72 \text{km/s/Mpc}$. Massive black holes like the one in ULASJ1120+0641 pose a challenge to all proposed SMBH formation scenarios owing to a Salpeter timescale which is difficult to reconcile with initial seed black holes of only a few solar masses. This is the typical remnant mass of an O-star. The Salpeter timescale (Salpeter, 1964; Ghisellini et al., 2013):

$$t_s = 450 \left(\frac{\epsilon_D}{1 - \epsilon} \right) \left(\frac{L_{\text{Edd}}}{L_D} \right) \text{Myr}, \tag{2.23}$$

is the time until the black hole doubles its mass through gas accretion. Following Ghisellini et al. (2013), $\epsilon = \epsilon_B + \epsilon_D$ is the total efficiency parameter. It consists of a disk component, ϵ_D, i.e. the energy conversion efficiency within the accretion disk and a magnetic component, ϵ_B, which is the energy conversion efficiency of gravitational binding energy into magnetic fields/jets. By assuming $\epsilon = \epsilon_D = 0.1$, a $M_\bullet = 10 M_\odot$ seed black hole as well as Eddington limited gas accretion, the black hole would need 27-28 Salpeter timescales ($1.4 \cdot 10^9$ years) to grow up to $M_\bullet = 2 \cdot 10^9 M_\odot$. This is twice as much as its estimated age. Either, the initial seed black hole was much more massive (of the order of $10^5 M_\bullet$), the energy conversion factor is very low ($\epsilon < 0.1$), or a significant amount of gravitational binding energy is dissipated away in form of channelized magnetic outflows ($\epsilon_B \geq \epsilon_D$) (Fabian et al., 2014). Rapidly rotating black holes complicate this problem owing to efficiency parameters which can in principle rise up to $\epsilon = 0.4$. However, they may also be efficient in converting a significant amount of accretion disc energy into magnetic fields/jets and thus decrease the Salpeter timescale. If e.g. $\epsilon = 0.1$ is equally distributed into ϵ_B and ϵ_D, the Salpeter timescale is sufficiently short to grow up billion solar mass black holes very rapidly.

In addition, there are studies which claim to explain the emergence of massive ($M_\bullet > 10 M_\odot$) initial seed black holes. Massive seeds would facilitate the growth of black holes up to $10^9 M_\odot$ in the highly redshifted universe. The most famous ideas are: (i) black hole remnants from quasistars or population III stars (Dotan et al., 2011; Latif et al., 2013), (ii) runaway mergers in dense stellar systems (Portegies Zwart et al., 2004; Devecchi & Volonteri, 2009) and (iii) the direct collapse of protogalactic gas clouds (Latif et al., 2013).

In the following sections I will not continue to focus on specific formation theories of initial seed black holes but instead on SMBH growth processes in general. There exists a variety of different physical processes capable of refilling empty loss cone trajectories with different forms of matter. Several of these mechanisms act in combination but their efficiency also depends on their astrophysical environment. They can be grouped into three different regimes: Gas accretion, tidal disruption of stars and SMBH merging processes. The forth section (§ 2.2.4) summarizes two new ideas related to the growth of SMBHs. These concepts, still at the very earliest stages of development,

were uncovered by the author of this thesis. Only one of these ideas is published in Brockamp et al. (2014). The following sections provide the link between my own results and how these outcomes have to be related to a broader scientific context.

2.2.1. Gas Accretion

Bondi Accretion of Hot Gas

The simplest forms of gas accretion models were already developed in the forties, at this time they aimed to explain the growth of stars instead of black holes. Pioneered by Bondi & Hoyle (1944) and Bondi (1952), these spherical symmetric accretion flows are also known as Bondi-Hoyle accretion models. They quantify the accretion rate onto a compact object embedded within a non-rotating gas atmosphere which is stabilized by pressure. Nowadays, Bondi-Hoyle accretion models are also applied to SMBHs located in the central and densest parts of the hot ($10^{6-8}K$) gaseous environment of elliptical galaxies, galaxy groups or even whole galaxy clusters. The gaseous atmosphere has a variable sound velocity, $v_s(r)$, and satisfies the equation of state, $p/p_\infty = (\rho/\rho_\infty)^\lambda$ (Bondi, 1952). Here p_∞ and ρ_∞ are the pressure and density at large distances away from the compact object and λ is a positive constant. By assuming steady state conditions such that the accretion rate does not influence the gravitational field of the compact object, the amount of inflowing mass is $\dot{M} = 4\pi r_s^2 \rho(r_s)v(r_s)$ (Bondi, 1952). The radius r_s is the sonic point at which the ingoing flow turns from sub- to supersonic speeds. Once the gas passes this sonic point, its plunge into the central object is unavoidable as long as one neglects additional heating processes like SMBH jets. By combining the equation of state with Bernoulli's equation for fluid dynamics, explicit expressions for $v_s(r_s)$, $\rho(r_s)$, r_s and $\dot{M}$ can be derived[6]:

$$\dot{M} = 4\pi c(\lambda)\frac{\rho_\infty G^2 M_\bullet^2}{v_{s,\infty}^3}. \tag{2.24}$$

Here, $c(\lambda)$ is a function depending solely on λ (e.g. $c(5/3) = 1/4$)) and $v_{s,\infty}$ is the sound velocity at large distances. As pressure and temperature are related over the ideal gas equation, the Bondi accretion rate can also be expressed in terms of gas temperature. The characteristic radius where the gravitational escape velocity exceeds the ambient sound velocity is known as the Bondi radius, $r_b \equiv 2GM_\bullet/v_{s,\infty}^2$. Inside r_b, physical gas properties like density and sound velocity increase. The Bondi radius is related to the sonic point by $r_s/r_b = (5-3\lambda)/8$. For a few particular cases of very massive and nearby black holes, the Bondi radius, being of the order of approx. 100 pc, can be resolved with the Chandra telescope (e.g. inside NGC 3115, Wong et al. 2011).

The concept behind Bondi accretion becomes complicated when considering rotating gas atmospheres. Generally, the overall accretion rate becomes affected

---

[6]A detailed derivation of the Bondi accretion rate can be found in the lecture notes "Radiative Gas Dynamics (Winter Quarter 2011)" from B. Ryden, Ohio State University. The following equations concerning (hot) Bondi accretion are taken from there.

(Narayan & Fabian, 2011), and depending on the gas viscosity a central torus or accretion disk might develop due to the angular momentum barrier (see Narayan & Fabian 2011 and references for more details). While the occurrence of luminous and radiatively efficient accretion discs around SMBHs is suppressed, jet formation is favored (Fabian & Rees, 1995; Allen et al., 2006). Nuclear X-ray luminosities are often orders of magnitude below their theoretical maximal allowed values. See Wong et al. (2011) for the peculiar case of NGC 3115. These are the typical characteristics of Advection Dominated Accretion Flows (ADAFs). ADAFs exist in two states. In this first regime which is relevant for the physics of active galactic nuclei (AGNs) in the local universe, the gaseous medium is optically thin and the cooling time of the gas exceeds the infall timescale. In the second regime the gas is optically thick and the photon diffusion time is much shorter than the inflow timescale. In both cases a large fraction of thermal energy is advected. Black holes with their event horizons (i.e. negative heat capacities) are the only objects capable of swallowing (kinetic) energy without any visible signs in contrast to objects whose interiors are not disconnected from our spacetime (Narayan & McClintock, 2008).

However, even though ADAFs are radiatively inefficient, they are capable of generating powerful jets. The observed jet powers correlate with Bondi accretion rates obtained from observations of the gas temperature, density and SMBH mass (Allen et al., 2006). It is therefore believed that radio loud elliptical galaxies with massive central SMBHs are fed by Bondi accretion from a hot gaseous atmosphere. However, it is under debate whether Bondi accretion is also sufficient enough to power jets of the most energetic radio galaxies ($P_{\mathrm{jet}} \approx 10^{46}$erg/s) in the local universe. These radio galaxies are often associated with brightest cluster galaxies. The most extreme known representative is MS0735 (McNamara et al., 2005) which hosts an energetic radio outburst with a total energy of $E_{\mathrm{tot}} \approx 10^{62}$erg. This release of energy during one AGN outburst is similar to the total energy of 10^{11} type 1a supernovae and corresponds to the rest mass energy $m = E/c^2 = 6 \cdot 10^7 \mathrm{M}_\odot$. While Rafferty et al. (2006) and McNamara et al. (2011) claim that Bondi accretion from the hot component of the ISM can not fuel the most powerful jets inside BCGs and that instead they must be generated from cold gas accretion, Fabian (2012) points out a different view. The efficiency of Bondi accretion depends on $M_\bullet^2$. The usage of the locally calibrated SMBH scaling relations like $M_\bullet - L$ and $M_\bullet - \sigma$ (§ 2.1.3) to evaluate SMBH masses in BCGs as done by Rafferty et al. (2006) and McNamara et al. (2011) might systematically yield too small values (Hlavacek-Larrondo et al., 2012).

Cold Gas Accretion

While Bondi accretion from the hot ISM continuously increases black hole masses and powers radio loud AGNs in the local universe, its role during the formation and growth of initial seed black holes in the highly redshifted universe (e.g. $z > 15$) is debated (Volonteri & Rees 2005; Rees & Volonteri 2007 and references therein). Instead, it is commonly believed that accretion from cold gas reservoirs must have been responsible for the dominant part of SMBH mass gain. Gas is assumed to be in the *cold* state

as long as its temperature is below the virial temperature $T_{\mathrm{vir}} \propto GM(< r)m/(rk_B)$, where k_B is the Boltzmann constant and m the mean mass of the gas particles. The virial gas temperature can be derived by relating the potential energy to the thermal energy. If the gas is *cold* i.e. $T < T_{\mathrm{vir}}$, it has to be rotationally supported, otherwise it would fall directly into the galactic nucleus.

Most of the SMBH mass gain by cold gas accretion occurs during the luminous quasar phase at high redshifts (Di Matteo et al., 2012). The optical light of some quasars is sometimes obscured by cold gas and dust clouds within their host galaxies and one has to use infrared telescopes in order to identify them. By assuming a constant mass to energy conversion efficiency (e.g. $\epsilon = 10\%$), the quasar luminosity function can be integrated in order to obtain the SMBH mass density (Soltan, 1982; Kelly & Merloni, 2012). The inferred SMBH mass density from integration of the quasar luminosity function can than be compared with the local SMBH mass function evaluated from the $M_\bullet - \sigma$ relation, measured stellar velocity dispersions and the spatial distribution of galaxies (see Kelly & Merloni 2012 for a review). Both SMBH mass densities are similar to each other indicating that cold gas accretion during the initial quasar phase was a dominant driver of SMBH mass growth. However, there are several caveats in this argument which will be addressed later.

The quasar luminosity function and hence the active phase of the most massive black holes peaked in the early universe (Hasinger et al., 2005; Kelly & Shen, 2013) at times when galaxies were gas rich. Less-powerful active galactic nuclei (AGNs) like Seyfert galaxies peaked at successively lower redshifts. This is known as cosmic downsizing of the AGN activity. A quasar is the most energetic representative of a broad class of active galactic nuclei. In some cases the gas accretion rate of the central SMBH reaches several earth masses per second. This corresponds to an increase of its event horizon by several centimeter per second. Their corresponding luminosities, sometimes of the order $P \approx 10^{48}\mathrm{erg/s}$ (Ghisellini et al., 2009), are produced in accretion discs comparable in size to that of the solar system. Upper limits on the size can be obtained from changes in the disk luminosity, i.e. by relating luminosity fluctuations to the light crossing timescale of the source, i.e. $\Delta r = \Delta t \cdot c$.

Accretion discs of quasars are very thin and radiatively efficient. Typical thickness to size ratios are of the order of 0.1-3% (Narayan & Quataert, 2005). Thin and radiatively efficient accretion discs form when thermal energy is radiated away on timescales which are smaller than the advection timescale (Narayan & Quataert, 2005). This is the characteristic timescale in which matter becomes advected into the black hole. Only thin and radiatively efficient accretion discs are able to convert significant amounts of potential energy into radiation. The matter to energy conversion efficiency reaches up to $\epsilon = 40\%$ for prograde motion around a maximal rotating black hole (§ 1.2.2). Matter loses angular momentum by friction forces. These forces are also responsible for the conversion of potential energy into heat/radiation. However, the exact details of angular momentum redistribution processes within accretion discs around black holes are complicated. Their modeling requires to combine several physical processes simultaneously. These are GR effects (e.g. frame dragging), magnetic fields, turbulent

cells, radiation and heat transport and outflows/jets (Abramowicz & Fragile, 2013). In order to power quasar like luminosities, the accretion discs must be continuously replenished by new matter. According to orientation-based unified models of AGNs (Urry & Padovani, 1995), the accretion discs are fed from surrounding tori of molecular gas and dust. Typical tori have sizes between $1 - 10^2$ pc (Tristram & Schartmann, 2011). Depending on the line of sight, the active galactic nucleus appears as a Type 1 quasar or Seyfert galaxy (broad emission lines, center visible), Type 2 quasar/Seyfert galaxy (narrow emission lines, central broad-line-region blocked from view through dust) or blazar (line of sight points towards jet). However, the orientation-based unified AGN model was recently challenged by an analysis of 170.000 AGNs which were observed with the Wide-field Infrared Survey Explorer (WISE) satellite (Donoso et al., 2013). The new findings indicate that Type 2 AGNs preferentially inhabit denser galactic environments. The simple unification picture of AGNs which is solely based on the orientation parameter only is incompatible with these observations and it is suggested that more complex processes are involved.

Accretion flows which do not radiate away most of their thermal energy are much thicker (and hotter) and more reminiscent of radiatively inefficient accretion flows (Section 2.2.1). They usually operate at low accretion rates well below the maximal allowed Eddington limit, $L_{\text{Edd}} = 1.3 \cdot 10^{38} \left(\frac{\text{M}_\bullet}{\text{M}_\odot} \right) \text{erg/s}$.

Feedback Processes and Constraints on the SMBH Growth History

One crucial test for investigating whether gas accretion processes are the dominant driver of SMBH mass growth is to confront gas accretion model predictions with actual observed SMBH demographics (§ 2.1.3). In the picture proposed by Silk & Rees (1998), the so called co-evolution picture, accreting black holes produce large amounts of energy in form of radiation, jets and outflows. This stimulates star formation by compressing molecular clouds which then collapse and form new stars. Active galactic nuclei are often associated with star forming galaxies (Mullaney et al., 2012). On the other hand, once the black hole becomes massive and powerful enough, its activity also suppresses star formation and its own supply of matter. Strong AGN activity overheats the gas such that it does not collapse into stars or the central galactic nucleus. In this way, SMBHs self-regulate their own growth and that of their host galaxies. Without energetic feedback from central AGN, elliptical galaxies would have quite different properties than observed (Dubois et al., 2013). Recent observations confirm that AGNs above a given X-ray threshold luminosity of $L_X \approx 10^{44} \text{erg/s}$ start to suppress star formation efficiently (Page et al., 2012).

Gas accretion/feedback processes can explain the emergence of tightly coupled relations between properties of the host galaxy like mass, velocity dispersion or (more generally) binding energy of the bulge and $M_\bullet$ (Silk & Rees, 1998; King, 2003). However, additional challenges arise from the complexity of nature. Dynamical processes like galaxy interactions and mergers must also be taken into consideration when trying to explain these empirical relations (Di Matteo et al., 2005; Hopkins et al., 2007; Younger et al., 2008). Nevertheless, while gas accretion/feedback scenarios seem

to be the most promising ansatz for establishing the strongly coupled galaxy-SMBH relations, several open questions remain.

There is growing evidence (i) for deviations or at least significant scatter from empirical scaling relations at the high mass end of the SMBH mass function (McConnell & Ma, 2013). (ii) Furthermore, Kormendy & Ho (2013) found that SMBH masses scale differently with varying galaxy constituents. (iii) Hlavacek-Larrondo et al. (2012) claim that $M_\bullet - L$ or $M_\bullet - \sigma$ based mass estimates in BCGs which are located in cool core galaxy clusters systematically underestimate the true SMBH mass by a factor of ten. (iv) This is supported by independent studies from Mathews & Guo (2011). They calculated the injected AGN energy into the gaseous atmospheres of galaxy clusters by comparing the gas profiles with those obtained from cluster formation models without feedback. Mathews & Guo (2011) found that the central SMBHs within massive galaxy clusters like Abell 478 and Abell 1413 released $E_{\text{tot}} \approx 3 \cdot 10^{63}$erg of energy during ≈ 7 billion years of cluster lifetime. Such an enormous release of energy corresponds to the equivalent (chemical) energy of $5 \cdot 10^7$ Milky Way masses of bituminous coal and must be related to black holes much more massive than any SMBH observed so far in our cosmic neighbourhood. SMBHs of enormous proportions, sometimes exceeding $M_\bullet = 10^{11} \text{M}_\odot$, must also be present in some core-type BCGs like Holm 15A (Lopez-Cruz et al., 2014) if their central stellar light deficits were carved out by binary or multiple black hole evolution in the past. Other studies like Ghisellini et al. (2009); McNamara et al. (2009); Kelly & Shen (2013); Walker et al. (2014); Trakhtenbrot (2014) also indicate the existence of an extremely heavy population of black holes.

(v) Finally, van den Bosch et al. (2012) presented evidence that even small galaxies can contain black holes with masses much above the prediction from any scaling relation. They claimed that the putative black hole within the compact and fast rotating galaxy NGC 1277 contains a $M_\bullet = 17 \cdot 10^9 \text{M}_\odot$ black hole which corresponds to 70% of the bulge mass and 20% of the total mass of the galaxy. This is a factor of one hundred above the prediction of the $M_{\text{bulge}} - M_\bullet$ relation. While some astrophysicists cast doubt on the inferred black hole mass in NGC 1277 (Emsellem, 2013), others explain it by a black hole which was ejected during a merger event within the central brightest cluster galaxy NGC 1275 and was then captured by the much smaller galaxy NGC 1277 (Shields & Bonning, 2013). However, van den Bosch et al. (2012) claims that NGC 1277 might only represent the tip of an iceberg of a population of extremely massive black holes within small galaxies. They also found several galaxies with similar physical properties like NGC 1277 which might also host ultramassive black holes. Fabian et al. (2013) already speculates that such a population of UMBHs would not be compatible with number density counts of bright quasars and would imply a major challenge to all existing SMBH growth and formation theories.

As a matter of fact all SMBH growth channels must be taken into account in order to understand the evolution of SMBHs. There are at least two different concepts which do not depend on gas accretion scenarios but which also claim to explain empirical scaling relations. They are discussed in the following sections. Furthermore, two new ideas related to SMBH growth processes are presented in this thesis. One idea is presented

in Brockamp et al. (2014). The other idea might naturally explain SMBH masses much in excess of the prediction of any scaling relation as it postulates that under given circumstances (which have to be constrained in follow up studies) a SMBH might enter a non regulated growth mode[7].

2.2.2. Stellar Accretion

The feeding of SMBHs do not only proceed via gas accretion and SMBH merging processes, but also by tidal disruption or the swallowing of stars and compact remnants. There are three principle ways the loss cone (§ 1.2.3) of a massive black hole can be refilled with stellar mass objects. These mechanisms will be described in the following (subsub-)sections.

Relaxation

Stars exchange energy and angular momentum during gravitational two-body deflections. If one of the participatory stars loses enough energy its orbit will shrink such that it reaches the tidal disruption radius where the star becomes gravitationally unbound due to tidal forces. Alternatively, if the central black hole is very massive and/or the star is very compact (e.g. a white dwarf) it will plunge deep into the relativistic regime where it will finally be swallowed by the black hole (§ 1.2.3). The dynamics which govern the refill of the loss cone by (pure) relaxation processes are highly complicated as they depend on numerous aspects: (i) The mass and spin of the black hole (Wang & Merritt, 2004; Kesden, 2012), (ii) the graininess of the stellar distribution within the influence radius of the black hole (i.e. the relaxation timescale), (iii) the central slope of the galactic density profile which can also change with time (Baumgardt et al., 2004a; Brockamp et al., 2011), (iv) the mass spectrum of the stars (Baumgardt et al., 2004b) and (v) dynamical heating (Baumgardt et al., 2004a; Brockamp et al., 2011).

The basics behind relaxation driven loss cone refilling by equal mass stars are explained below. A more detailed study of tidal disruption rates based on numerical investigations is carried out in Chapter 3. The didactic structure of this paragraph (subsub-section) is based on Brockamp et al. (2011) and equations concerning the angular momentum diffusion concept which was developed in Frank & Rees (1976) are taken from Brockamp et al. (2011), i.e. Chapter 3.

If a stars has a pericenter distance which is smaller than the capture radius of the black hole, it will be swallowed or tidally disrupted within one crossing timescale. Obviously, the velocity vectors of all stars which move on such loss cone orbits are grouped together in a very narrow region which is known as the loss cone. The loss cone as well as the loss cone angle, θ_{lc}, are graphically illustrated in Figure 1.5. Accord-

---

[7]David Merritt pointed out in private communication that he had similar ideas before this PhD thesis was written. Ideas related to runaway black hole growth were also discussed in Hernandez & Lee (2010) and in a different context involving a Compton-cooled runaway growth in Walker et al. (2014).

ing to Frank & Rees (1976), θ_{lc} is defined within the sphere of influence (of the SMBH), r_H, as:

$$\theta_{lc} \propto \left(\frac{r_{cap}}{r} \right)^{\frac{1}{2}}.$$

(2.25)

Without a mechanism which changes the angular momentum vectors of stars, a fully occupied loss cone would be depleted quickly. This would happen on a dynamical timescale, t_{cross}. Afterwards, the capture rate would drop to zero. However, one mechanism which permanently changes the angular momentum distribution of stellar mass objects is two body relaxation. According to Frank & Rees (1976), the velocity vector of a star is shifted by the amount:

$$\theta_{Diff} \propto \left(\frac{t_{cross}}{t_{rel}} \right)^{\frac{1}{2}},$$

(2.26)

per dynamical timescale through accumulated gravitational interactions. At a particular radius which is called the critical radius, r_{crit}, angular momentum driven diffusion changes the velocity vectors of stars by amounts which are comparable to the loss cone angle, θ_{lc}, itself:

$$\left. \frac{\theta_{lc}}{\theta_{Diff}} \right|_{r=r_{crit}} = 1.$$

(2.27)

Within r_{crit}, $\theta_{lc} > \theta_{Diff}$, and stars are diffusively deflected onto loss cone trajectories. It takes several orbits to reduce their angular momentum until they enter such a loss cone trajectory. Therefore, the loss cone within r_{crit} stays empty most of the time. For this reason it is called the *empty loss cone regime*. At distances larger than r_{crit}, $\theta_{lc} < \theta_{Diff}$, and stars exchange so much angular momentum that they typically drift in- and outwards the loss cone during one crossing timescale (Frank & Rees, 1976). An additional enhancement of relaxation through e.g. the presence of massive perturbers would not increase the stellar capture rate. This regime is called the *full loss cone-* or sometimes *pinhole regime*. Most captures have their origin in the empty loss cone regime and thus they are expected to have huge binding energies.

The simplifying assumption is made that all stars have the same mass and that they follow a power-law number density profile, $n(r) = n_c \left(\frac{r}{r_H} \right)^\alpha \equiv n_0 r^\alpha$, inside the gravitational influence radius of the black hole. Here, α is the negative slope parameter and n_c is the number density at r_H. The critical radius can be calculated by making use of Eq. 2.25 and Eq. 2.26 which are inserted into Eq. 2.27:

$$r_{crit} \propto \left(\frac{r_{cap} M_\bullet^2}{M_\star^2 n_0} \right)^{\frac{1}{4+\alpha}}.$$

(2.28)

For t_{rel}, which appears in Eq. 2.26, I used the relaxation time from Spitzer & Harm (1958); Spitzer (1987). Finally, the flux of stars onto loss cone orbits can now be obtained from Equation 17 from Frank & Rees (1976) and by exchanging the velocity dispersion,

$\sigma(r)$, with $\frac{r}{t_{\text{cross}}}$:

$$\dot{C} \propto \left.\frac{\theta_{\text{lc}}^2 r^3 n(r)}{t_{\text{cross}}}\right|_{r=r_{\text{crit}}} = \left.\frac{\theta_{\text{Diff}}^2 r^3 n(r)}{t_{\text{cross}}}\right|_{r=r_{\text{crit}}}. \tag{2.29}$$

$\dot{C}$ can be further specified by substituting $r = r_{\text{crit}}$ and by using the power law density profile, $n(r \le r_{\text{crit}}) = n_0 r^\alpha$:

$$\dot{C} \propto G^{\frac{1}{2}} M_\bullet^{\frac{1}{2}} r_{\text{cap}} n_0 r_{\text{crit}}^{0.5+\alpha}. \tag{2.30}$$

However, if the central black hole mass exceeds $M_\bullet = 10^7 M_\odot$, the derived Equation 2.30 should not be used any longer to predict the stellar loss cone flux. In this case there are huge numbers of stars around and within the influence radius of the black hole and the overall potential is very smooth. The critical radius becomes larger than the gravitational influence radius of the SMBH and the velocity distribution within r_{crit} does not longer follow a Keplerian one.

If the black hole mass exceeds $M_\bullet = 10^7 M_\odot$, a different loss cone angle, $\theta_{\text{lc}}^2 \approx \frac{r_{\text{cap}} r_H}{r^2}$, has to be used (Frank & Rees, 1976). Furthermore, the capture radius is of the order of the Schwarzschild-radius, i.e. $r_{\text{cap}} \approx r_s = \frac{2GM_\bullet}{c^2}$. This formalism can now be applied to a concrete example of growing black holes inside isothermal $\rho(r) = \frac{\sigma^2}{2\pi G r^2}$ density profiles as done by Zhao et al. (2002). From Equation 2.29 one obtains the mass accretion rate:

$$\dot{M} = \langle m \rangle \dot{C} \propto \frac{\theta_{\text{lc}}^2 r^3 \langle m \rangle n(r)}{t_{\text{cross}}} = \rho(r) r^2 \sigma \theta_{\text{lc}}^2 \approx \frac{\sigma^5}{Gc^2} \cdot \left(\frac{r_H}{r}\right)^2, \tag{2.31}$$

where $r_H = \frac{GM_\bullet}{\sigma^2}$ is used for the influence radius and $\rho(r) = \langle m \rangle n(r)$ is the stellar mass density. By assuming that the majority of loss cone stars emerges from the black hole influence radius, r_H, the ratio r_H/r in Eq. 2.31 neutralizes and the integrated final black hole mass (after the time t_f) becomes:

$$M_\bullet(t_f) = \int_{t=0}^{t=t_f} \dot{M}(r = r_H) \mathrm{d}t \approx 10^8 M_\odot \cdot \left(\frac{\sigma}{200 \text{kms}^{-1}}\right)^5 \left(\frac{t_f}{H_0^{-1}}\right). \tag{2.32}$$

This expression closely follows the $M_\bullet - \sigma$ relation. However, it must be noted that there exist alternative analytical approaches to derive the flux of loss cone stars per unit time in isothermal cusps (see e.g. Chapter 6.1.3 in Merritt 2013) which yield smaller values. Firstly, in the derivation of Equation 2.32, stars were assumed to be swallowed as a whole. Secondly, the loss cone is assumed to be permanently replenished and the isothermal cusp is immune to dynamical heating. In Chapter 3 the relaxation driven approach for the origin of the $M_\bullet - \sigma$ relation is confronted with results obtained in direct N-body experiments. At least for a Sérsic ($n = 4$) density profile it is found that the relaxation driven refill of the loss cone is far too inefficient to establish the $M_\bullet - \sigma$ relation. See also § 2.2.1 & § 2.2.3 for alternative ways to explain this empirical relation.

Centrophilic Orbits

In perfectly spherical and homogeneous galaxies there are only two principle ways how stars can be swallowed by the central SMBH. They can enter loss cone trajectories

through diffusion in energy or angular momentum space (§ 2.2.2) or they might have occupied such orbits early on. In a process called *orbit draining* such stars would be destroyed within one crossing timescale. By neglecting initial *orbit draining* and relaxation driven diffusion which becomes anyway inefficient for cases of very massive galaxies with central cores, the loss cone would not be replenished (Wang & Merritt, 2004; Brockamp et al., 2011). This is related to the fact that all components of the angular momentum vector $\vec{L}$ of a star are conserved because the force $\vec{F}(\vec{r}) = F(r)\frac{\vec{r}}{r}$ depends only on radius.

The situation is different in axis-symmetric galaxies where torques from the anisotropic potential induce changes in two of the three components of the angular momentum vector of a star. If one assumes that the galaxy is symmetric around the z-axis, the Hamiltonian can be written as:

$$H = 0.5 \left(p_r^2 + p_z^2 + \frac{p_\phi^2}{r^2} \right) + \Phi(r, z), \qquad (2.33)$$

where $p_r = \dot{r}, p_z = r^2\dot{\phi}, p_\phi = \dot{z}$ are the momenta and $\Phi(r, z)$ is the potential (Binney & Tremaine, 2008). From Hamilton's equations it follows that the quantity $\dot{p}_\phi = -\frac{\partial H}{\partial \phi}$ has to be zero as Equation 2.33 does not depend on ϕ. The z-component, $L_z = p_\phi$, is therefore a conserved quantity while the other two components are not.

If one assumes a population of stars with low angular momentum, L_z, such that the L_z component alone is smaller than the critical angular momentum of a loss cone trajectory (or even zero), these stars might be destroyed after some time by the black hole. They would fulfill oscillations in the other two components of the angular momentum vector (while still preserving L_z) and enter loss cone trajectories (Merritt, 2013). Such orbits are called centrophilic orbits.

In the case of a triaxial galaxy which is even less symmetric, significant numbers of stars are on centrophilic orbits i.e. orbits which do not avoid the galactic center and where all components of the angular momentum vector change sign. The exact details of the orbital families in triaxial galaxies are complex. The dominant factors which contribute are the radial distance, shape and density profile of the elliptical galaxy as well as the presence of a central SMBH. The latter can also destroy the triaxial shape over time (Merritt & Quinlan, 1998; Holley-Bockelmann et al., 2002). In the special case of a perfect ellipsoid, i.e. separable Stäckel model, there are tube and regular box orbits (de Zeeuw, 1985). These regular box orbits have a non-vanishing probability density at the center and they can come arbitrarily close to a central SMBH. They are centrophilic. The unique characteristics of box orbit stars are that they have no fixed sense of rotation, they come to rest for an instant of time at a given equipotential surface and their trajectories fill the interior of these surfaces uniformly in a time averaged manner. The triaxial shape is maintained by box orbits and they occupy a large fraction of all orbits (of the order O(1)). In my own triaxial galaxy computations the angular momentum vectors of 25% of all particles change sign. In cuspy triaxial mass distributions, particles/stars become trapped by resonant orbits which fulfill linear relations

between their fundamental frequencies ν_x, ν_y, ν_z of the form $n\nu_x + l\nu_y + m\nu_z = 0$ with $n, l, m \in \mathbb{N}$ (Merritt & Valluri, 1999). The time averaged particle trajectories become restricted to membrane like structures. Overlapping resonances give rise to irregular (chaotic) motions. The angular momentum vectors of particles on chaotic orbits are not preserved as well. However, the motions of particles within the gravitational influence radius of the black hole are generally regular. Trajectories within the influence radius that do not preserve any component of the angular momentum vector are called pyramid orbits (Merritt & Vasiliev, 2011; Merritt, 2013). Pyramid orbits have a significant influence on the black hole feeding rate (Merritt & Vasiliev, 2011).

The flux of stars onto loss cone trajectories in triaxial galaxies is strongly enhanced compared to spherical (where it is zero) and axis-symmetrical galaxies (a stellar capture every $10^3 - 10^6$, see Vasiliev & Merritt 2013) due to their low symmetry state. While angular momentum diffusion is the main source for loss cone refill in spherical galaxies, it might be of secondary relevance in triaxial galaxies or galaxies with otherwise strongly reduced symmetries. However, quantitative predictions are extremely difficult to obtain and the full problem can only be tackled with numerical studies. In the pioneering work of Merritt & Vasiliev (2011) it was found that the swallowing rate of a several billion solar mass black hole in a triaxial galaxy might be as high as one star every few years.

This might significantly contribute to the formation of shallow core profiles of elliptical galaxies (§ 2.1.1). The accretion rate of stars in giant elliptical galaxies might also be used to probe the nature of the dark massive objects sitting at the centers of these galaxies itself. Every other compact object than a black hole without a spacetime separating horizon, less entropy and a positive heat capacity would not be able to swallow the kinetic impact energy, $E = z (1 + z)^{-1} M_\odot c^2 \approx 10^{54}$erg, of a solar like star (being of the order of its rest mass when measured at infinity) without any noticeable outburst.

Here z is the gravitational redshift at the surface and the photon recovery timescale (i.e. the time it takes until emission from the putative surface reaches the distant observer) diverges only with $\ln(z + 1)$. In a related study Narayan & McClintock (2008) excluded the existence of a surface on SgrA* by showing that its expected surface luminosity would be too dim given its current gas accretion rate. Thus Narayan & McClintock (2008) found indirect evidence for the existence of an event horizon.

Massive Perturbers

Orbital draining from centrophilic orbits and relaxation driven loss cone refilling processes are complicated by the presence of massive perturbers. It makes sense to separate the treatment of massive perturbers into two different regimes. In the first regime perturber masses M_{mp} are much smaller than the mass of the galactic nucleus, M_{nc}, whereas in the second regime $M_{mp} \approx M_{nc}$.

First, some concepts behind the $M_{mp} << M_{nc}$ regime will be presented: All ob-

jects inside a galactic nucleus being more massive than the typical field star population ($\langle m \rangle \approx 0.5\,\mathrm{M}_\odot$) are massive perturbers. Such objects are stellar remnants, gas and molecular clouds, star clusters, globular clusters or even intermediate mass black holes (IMBHs). In § 2.2.2 the concept behind the relaxation driven loss cone refill was introduced. A crucial quantity in the diffusion theory is θ_{Diff} (Equation 2.26) which itself depends on the relaxation timescale T_{rel}. The relaxation timescale becomes modified (smaller) by the presence of massive perturbers. Following Merritt (2013), the relaxation timescale of a multi component mass distribution is given by:

$$T_{\mathrm{rel}} = \frac{0.34\sigma^3}{G^2 \rho\tilde{m} \ln \Lambda}, \tag{2.34}$$

where σ is the one dimensional velocity dispersion, $\ln \Lambda$ the Coulomb logarithm and

$$\rho\tilde{m} = \rho\frac{\int n(m)m^2\,\mathrm{d}m}{\int n(m)m\,\mathrm{d}m} = \int n(m)m^2\,\mathrm{d}m. \tag{2.35}$$

Here $n(m)\,\mathrm{d}m$ refers to the total number of objects within the mass interval m to $m + \mathrm{d}m$. $\rho\tilde{m}$ can be separated into a field star and massive perturber component i.e.

$$\rho\tilde{m} = \rho\tilde{m}\big|_{\mathrm{stars}} + \rho\tilde{m}\big|_{\mathrm{mp}}. \tag{2.36}$$

Scattering processes (and loss cone refilling by diffusion) are dominated by massive perturbers as long as $\rho\tilde{m}\big|_{\mathrm{mp}} > \rho\tilde{m}\big|_{\mathrm{stars}}$ (Merritt, 2013).

The situation is complicated by additional aspects: (i) The diffusive refill of the loss cone through angular momentum transfer is most efficient within the critical radius, but r_{crit} itself depends on the existence of massive perturbers. (ii) In galactic nuclei with similar properties to that of the Milky Way, the number of massive perturbers like globular clusters or giant molecular clouds is effectively zero at distances of the order of the critical radius $r_{\mathrm{crit}} \approx 2 - 3\,\mathrm{pc}$ (Merritt, 2013). Outside r_{crit} and within the *pinhole regime* an enhanced relaxation rate owing to the presence of massive perturbers does not increase the capture rate. This is related to a loss cone which is already full. However, massive perturbers within the inner most $100\,\mathrm{pc}$ strongly enhance the binary star - SMBH interaction and thus contribute indirectly to the ejection of hypervelocity stars (Perets et al., 2007). (iii) Scattering processes by massive perturbers become less efficient if they are extended (e.g. gas clouds). The Coulomb logarithm, $\ln \Lambda$, for extended bodies with half mass radii, R_H, is defined by Binney & Tremaine (2008) as:

$$\ln \Lambda = \ln \frac{b_{\mathrm{max}}}{\max\left(R_H, Gm_{\mathrm{mp}}/v_{\mathrm{typ}}^2\right)}, \tag{2.37}$$

where the maximum impact parameter b_{max} can be approximated by the galactocentric distance r. Assuming $b_{\mathrm{max}} = 2R_H = 3\,\mathrm{pc}$, $v_{\mathrm{typ}} = 200\,\mathrm{km/s}$, the corresponding Coulomb logarithm, $\ln \Lambda \approx 0.7$, is small compared to that of much more compact objects. In conclusion, the stellar accretion rate is expected to be modestly influenced by the presence of massive perturbers in galactic nuclei similar to that of the Milky

Way (Perets et al., 2007; Merritt, 2013).

However, stellar accretion rates can be significantly increased by massive perturbers which have masses comparable to that of the nucleus itself (Liu & Chen, 2013). The loss cone refilling timescale decreases by a factor of up to 10^2 (compared to isolated galaxies) during galaxy mergers, close encounters between galaxies or the presence of a secondary SMBH close to the galactic nucleus (see § 2.2.3). This proceeds via two mechanisms (Liu & Chen, 2013). Relaxation driven diffusion within r_{crit} becomes enhanced by changes of the angular momentum distribution and the overall reduction of the symmetry leads to the formation of centrophilic orbits.

2.2.3. SMBH Merging

While there exists indisputable proof for SMBH growth via gas accretion (§ 2.2.1) and strong evidence for the occurrence of tidal disruption events (e.g. Komossa 2002; van Velzen et al. 2011; Cenko et al. 2012, § 2.2.2), the third postulated SMBH growth channel via SMBH merging is less well established. Nevertheless, indications for the occurrence of SMBH mergers exists: (i) The longevity and stability of cosmic jets with sizes of kpc up to Mpc scales (Machalski et al., 2008) is maintained by the huge angular momentum $J_{\bullet} = jGM_{\bullet}^2/c$ of rotating SMBHs, where $j \in [0,1]$ is the dimensionless spin parameter. The rotational energy of the black hole is extracted via the Blandford and Znajek mechanism (Blandford & Znajek, 1977)[8]. However, some galaxies display X-shaped jets which change their direction almost instantaneously. Such a sudden change in jet direction signalizes a spin flip of the central black hole during an SMBH merger (Merritt & Ekers, 2002; Komossa, 2003). (ii) Luminous elliptical galaxies have central shallow cores (§ 2.1.1) which are believed to result from SMBH-SMBH merging. These scenarios will be investigated in more detail below. (iii) By timing analysis of the OJ287 blazar light curve a model was established which postulates two orbiting SMBHs with a 12 year orbital period in our rest frame (Valtonen et al., 2008). Every time the secondary black hole intersects the accretion disc of the more massive primary black hole, it generates an optical outburst. This model predicted the timing of the last outburst in September 2007 with an accuracy of 1 day (Valtonen et al., 2008). If this model holds up, the eccentric black hole binary inside OJ287 will merge within the next 10^4 years.

In this section the overcome of the black hole angular momentum barrier is investigated. The starting point are two separated SMBHs in two previously merged galaxies. Under ordinary circumstances ($M_{\bullet} << M_{\mathrm{GAL}}$) the processes which reduce the angular momentum of these black holes can be divided into three overlapping regimes. In the first regime, SMBHs reduce their angular momentum by drag forces in viscous gas rich environments and/or dynamical friction (DF). For the sake of this paragraph gas physics are neglected and "dry" mergers of galaxies are considered.

---

[8]Within the ellipsoidal shaped ergosphere, spacetime is forced to move around the black hole and spin energy can be extracted from magnetic fields which are wound up and amplified.

A moving black hole induces a density perturbation in the stellar distribution behind its path. This perturbation which is sometimes called a wake, gravitationally attracts the SMBH and reduces its orbital energy and angular momentum. This process is called dynamical friction (Chandrasekhar, 1943). The black hole gradually spirals inwards. In its most simple form, the de-acceleration by DF is given by Chandrasekhar's (standard) dynamical friction formula for a Maxwellian velocity distribution (Binney & Tremaine, 2008):

$$\vec{a} = -\frac{4\pi G^2 M_\bullet \rho\left(\vec{r}\right) \ln\left(\Lambda\right)}{v^3} \left[\mathrm{erf}\left(X\right) - \frac{2X}{\sqrt{(\pi)}} \exp(-X^2)\right] \vec{v},$$ (2.38)

where $X = v/(\sqrt{2}\sigma)$, σ is the one dimensional velocity dispersion and $\vec{v}$ is the velocity of the black hole. Following Binney & Tremaine (2008), the inspiral timescale T_{inspiral} can be derived for the idealized situation of a spherical homogeneous galaxy with an isotropic velocity distribution[9]. The de-acceleration force is anti-parallel to the SMBH velocity vector and Equation 2.38 can be applied to derive the equation of motion:

$$\frac{\mathrm{d}L}{\mathrm{d}t} = -Fr = -rM_\bullet \left|\vec{a}\right|.$$ (2.39)

Assuming an isothermal density profile $\rho(r) = v_c^2/\left(4\pi G r^2\right)$ for the galactic density profile, where $v_c = \sqrt{2}\sigma$ is independent of the radial coordinate as well as a constant Coulomb logarithm, the equation of motion can be further simplified by using $L = M_\bullet rv$. By integrating Equation 2.39, the following expression for the inspiral time of SMBHs on circular orbits can be derived:

$$T_{\mathrm{inspiral}} \approx \frac{4\,\mathrm{Gyr}}{\ln \Lambda} \left(\frac{r\left(t=0\right)}{10\,\mathrm{kpc}}\right)^2 \left(\frac{10^9\,\mathrm{M_\odot}}{M_\bullet}\right) \left(\frac{\sigma}{100\,\mathrm{km/s}}\right)$$ (2.40)

The inspiral timescale for a SMBH of mass $M_\bullet = 10^9\,\mathrm{M_\odot}$ at $r\left(t=0\right) = 10\,\mathrm{kpc}$ into the galactic nucleus of a galaxy with $\sigma = 200\,\mathrm{km/s}$ is of the order of one billion years (assuming $\ln\left(\Lambda\right) = 6$).

However, this treatment of DF serves only as a coarse estimate for the timescale until a SMBH reaches the galactic center. Most astrophysical applications require a more detailed treatment of DF due to the following reasons: (i) Elliptical galaxies, especially those which are undergoing mergers, are not spherical. (ii) The velocity distribution is anisotropic, preferentially tangential biased at small radii and radially biased at large radii. Henceforth, the direction of acceleration by DF is not anti-parallel to the velocity vector of the SMBH. Consequently, Equation 2.38 has to be replaced by a 3D generalization (see Chapter 4). Finally, (iii) the Coulomb logarithm, $\ln \Lambda$, is not constant but a function of the galactocentric distance and density profile which itself becomes influenced by the SMBH.

Once the secondary SMBH approaches the gravitational influence radius of the primary black hole, DF gradually loses its significance and becomes replaced by

---

[9]A velocity distribution is isotropic if all eigenvalues $\sigma_r, \sigma_\phi, \sigma_\theta$ of the velocity dispersion tensor, $\sigma_{ij}^2 = \overline{v_i v_j} - \overline{v}_i \overline{v}_j$, are equal.

another process. At scales of the influence radius, both SMBHs form a hard binary (Merritt, 2013). The velocity of the smaller SMBH starts to exceed the local velocity dispersion σ. This is the second regime. In this second phase the gravitational slingshot effect removes stars from the binary and reduces the separation between the two black holes. For the sake of completeness it should be mentioned that there are numerical investigations (Khan et al., 2014) indicating that this second binary evolution phase is absent in the evolution of over-massive black hole binaries with masses comparable to those of their host galaxies (e.g. NGC 4486B (Magorrian et al., 1998) or NGC 1277 (van den Bosch et al., 2012)). Nevertheless, for "typical" SMBH binaries the gravitational slingshot effect can be explained as follows. Stars can gain or lose energy during a gravitational encounter with the SMBH binary. If a star loses energy it will come even closer to the binary such that there will be a second, more violent gravitational interaction. This procedure can be repeated until a star gains enough energy to become unbound to the binary or even the whole galaxy. Depending on the degree of rotation of the galactic nucleus and orientation of the binary black hole, its eccentricity and alignment with respect to the angular momentum vector of the nucleus can change (Sesana et al., 2011; Gualandris et al., 2012).

In spherical host galaxies, the central SMBH binary depletes all stars which come close enough. This happens on a crossing timescale $T_{\text{cross}} \approx 40 \left(R_H^3 / M_{\text{GAL}} \right)^{0.5} \text{Myr}$ of the galaxy, where the half mass radius, R_H, is given in pc and the dynamical mass of the galaxy, M_{GAL}, in $\text{M}_\odot$. Disconnected from additional stellar supply, the binary would stall, unable to reduce its remaining angular momentum. This is known as the *final parsec problem*, although the stalling radius is not fixed to one parsec. This problem is claimed to be solved as long as the shape of the host galaxy deviates from spherical symmetry (Khan et al., 2013) due to a reservoir of stars on centrophilic orbits (§ 2.2.2) with large eccentricities. But see also Vasiliev et al. (2013) for a critical view.

SMBH binary evolution depletes the centers of galaxies by the preferential removal of galactic center stars and those on eccentric orbits from further out. Therefore, they transform cusps into shallow cores (Makino, 1997; Merritt & Poon, 2004; Kulkarni & Loeb, 2012) and decrease the amount of eccentric orbits, i.e. increase the tangential anisotropy. According to Kormendy & Bender (2009), the stellar mass/light deficit ($\equiv M_{\text{def}}$) correlates nearly linearly with the mass of the central black hole(s). Therefore, galaxies with the most pronounced cores are promising candidates for hosting the most massive black holes in the universe (§ 2.1.1). But not only the mass deficit, also the size of the core should be related to the influence radius and hence to the mass of the black hole. This was recently confirmed by Rusli et al. (2013) and McConnell et al. (2012). In the case of NGC 4889, the size of the core overlaps with the influence radius and the region where the velocity distribution is tangentially biased.

For the sake of this paragraph it is now assumed that stellar encounters successively reduce orbital momentum of the (binary) black holes so that they enter the gravitational radiation dominated phase. In this final phase angular momentum is radiated away in form of gravitational waves until coalescence. The energy and angular momentum which is carried away by gravitational waves depends on the semi-major axis, *a*, and

eccentricity, e. Following Peters (1964):

$$P_{\text{GW}} = \frac{\mathrm{d}E}{\mathrm{d}t} = -\frac{32G^4}{5c^5} \frac{(M_{\bullet 1}M_{\bullet 2})^2 (M_{\bullet 1} + M_{\bullet 2})}{a^5 (1 - e^2)^{\frac{7}{2}}} \left(1 + \frac{73}{24}e^2 + \frac{37}{96}e^4 \right). \tag{2.41}$$

Gravitational wave emission of SMBH binaries just before merging can easily exceed the brightest electromagnetic sources in the whole universe. The OJ287 system with a primary mass of $M_{\bullet 1} = 1.8 \cdot 10^{10}\,\text{M}_\odot$, secondary mass of $M_{\bullet 2} = 1.4 \cdot 10^8\,\text{M}_\odot$, eccentricity $e = 0.66$ and semi-major axis $a = 11500\,\text{AU}$ (Valtonen et al., 2008), generates $P_{\text{GW, OJ287}} \approx 2 \cdot 10^{48}\,\text{erg/s}$. This corresponds to $5 \cdot 10^4$ times the electromagnetic output of the Milky Way. Without taking GW emission into account, the outburst of the OJ287 system in 2007 would have occurred 20 days later than observed (Valtonen et al., 2008).

The last step is the final merger. All perturbations of the newly formed black hole are radiated away as it settles down into a Kerr-metric. Depending on the mass ratio and spin distribution of the progenitor holes, the gravitational waves are not emitted isotropically (Campanelli et al., 2007a; Pretorius, 2005; Brügmann et al., 2008; Sundararajan et al., 2010) and the spin axis can change. This phenomenon is called spin flip. In some extreme configurations, the newly formed black hole kicks out of the galactic center due to momentum conservation. The kick can exceed the escape velocity of the galaxy (Campanelli et al., 2007a). However, the received kick velocity might be lowered afterwards if the perturbed black hole emits gravitational waves in the opposite direction to its velocity vector (Rezzolla et al., 2010). The size of the stellar core can be further increased by dynamical heating and the lowering of the central potential (Gualandris & Merritt, 2008). Galaxies where such ejection scenarios are discussed are NGC 1275 (Shields & Bonning, 2013) and the BCG inside the Abell 2261 cluster (Postman et al. 2012, Figure 2.6)[10].

It is expected that in the near future the direct detection of low frequency gravitational waves with a pulsar timing array (Manchester et al., 2013) will directly probe the collision rate of massive black holes.

2.2.4. Loss Cone Refilling by Phase Space Smearing & Runaway Growth

The observable quasar luminosity function (§ 2.2.1) implies the bulk of SMBH growth to have occurred early on. In this section I want to present two new ideas concerning SMBH growth processes which might have been realized during the evolution of the first galaxies and their SMBHs. The first idea might explain over-massive black holes (§ 2.2.1) far in excess of the predictions of any known scaling relation due to an unregulated phase of SMBH growth. The other idea which was developed in Brockamp et al. (2014) might be relevant for the linear relationship between globular clusters and the mass of the black hole (§ 2.1.3).

---

[10]On the other hand the pronounced core inside A 2261 may signal the presence of an extraordinary massive black hole as indicated in a different context in Hlavacek-Larrondo et al. (2012)

The first idea shares similarities with simple toy models designed to infer SMBH mass accretion rates in infinite halos of constant density (Shapiro & Teukolsky, 1983; Hernandez & Lee, 2010). They rely on the accretion of unbound matter with respect to the SMBH, i.e. $E = E_{\text{kin}} - GM_\bullet/r > 0$ and they consider back-reaction effects due to the mass which becomes trapped by the SMBH. Under certain circumstances, a black hole can enter an unregulated growth mode which feeds upon itself. Following (Shapiro & Teukolsky, 1983; Hernandez & Lee, 2010), the mass accretion rate $\dot{M} = 16 \, (6\pi)^{1/2} G^2 M_\bullet^2 \rho_0 / (\sigma c^2)$ can be obtained by calculating the response of the mass density profile to the presence of the black hole and by using $\dot{M} \propto \rho A \sigma$. Here A is the cross section of the black hole for non relativistic particles (i.e. massive particles) which is corrected for gravitational focussing (relevant for unbound matter) and σ is the overall (constant) velocity dispersion. The mass accretion can be integrated to obtain (Hernandez & Lee, 2010):

$$M_\bullet (t) = \frac{M_{\bullet 0} c^2 \sigma}{c^2 \sigma - 16 \, (6\pi)^{1/2} G^2 \rho_0 M_{\bullet 0} t}, \tag{2.42}$$

where $M_{\bullet 0}$ the initial black hole mass and ρ_0 the unperturbed density. Evidently, $M_\bullet (t)$ diverges after some finite time, $t_{\text{div}} = c^2 \sigma / \left(16 \, (6\pi)^{1/2} \rho_0 M_{\bullet 0} \right)$. It seems questionable whether this runaway process yields a satisfactory approach for explaining over-massive black holes. It relies on constant density profiles and galaxies are not infinitely large and massive. Furthermore, the variable t in Equation 2.42 should not be extrapolated beyond a half mass crossing timescale of the galaxy/halo which is usually smaller than t_{div}.

However, this simple treatment illustrates that there can exist black hole accretion processes which feed upon themselves. The new idea can be understood as follows. Particle trajectories within a collapsing proto-galaxy ($2T_{\text{tot}}/|W_{\text{tot}}| < 1$) and without a seed black hole are determined by the mass distribution $M(\vec{r}, t)$. During collapse, the radial part of the velocity dispersion tensor σ_r dominates. Particles on mostly radial orbits pass through the center of the galaxy. $M(\vec{r}, t)$ evolves and settles down into a static configuration under the influence of violent relaxation. The situation might behave differently if this galaxy harbors an initial seed black hole which traps matter. The presence of the black hole causes a *relocation of mass*. The *relocation of mass* implies that objects on particular orbits would have to response to the increase of enclosed mass, $M(r, t) + M_\bullet(t)$. This is the case when matter on highly eccentric trajectories but from further out becomes trapped by the black hole. Objects which are affected in this way would enter even more eccentric orbits and the likelihood for a SMBH capture increases. In addition to that, gravitational focussing being relevant for unbound particles effectively increases the black hole cross section to $A = 4\pi \, (c/v_\infty)^2 \, r_s^2 \approx 4\pi \, (c/\sigma)^2 \, r_s^2$ (Novikov & Frolov, 1989) and enhances its accretion rate. The mass accretion in turn quadratically increases the cross section $A \propto r_s^2$ as $r_s \propto M_\bullet$. Both processes, the *relocation of mass* and the quadratical increase of the black hole cross section fuel each other and under the right circumstances a black hole might enter a runaway growth mode. It has to be investigated whether this process works in reality and if it is related to the presence of over-massive black holes in small compact

galaxies like NGC 1277 (§ 2.2.1). However, the (prospective) quantitative investigation of this process is numerically challenging, due to the immense difficulty of handling dynamical processes operating at scales of a few Schwarzschild radii up to the size of the galaxy (a few kpc).

The second proposed SMBH growth channel is related to eroding star and globular clusters (GCs). Currently, it is debated whether the linear $N_{\mathrm{GC}} - M_{\bullet}$ relationship (§ 2.1.3) is a consequence of GCs being actively involved in the growth of SMBHs or not (Rhode, 2012; Capuzzo-Dolcetta & Vicari, 2005; Gnedin et al., 2014). Brockamp et al. (2014) found evidence that eroding GCs might contribute to loss cone refilling processes, albeit quantitative accretion rates have to be obtained in future studies. During the first few orbits, a significant fraction of GCs becomes eroded due to strong tidal fields close to the galactic center. This episode is called a *tidal disruption dominated phase* (TDDP). The internal energy of the cluster increases through tidal shocking and they start to lose mass. Former cluster stars become trapped by the galactic potential but they still follow the overall path of the GC. However, these stars dilute over the phase space as time proceeds, like a shot charge which disperses. Most clusters which are disrupted during the TDDP are on highly eccentric orbits (Brockamp et al., 2014). Escaped cluster stars might repopulate loss cone trajectories. Although quantitative numbers are missing, the rapid evolution of the *TDDP* is compatible with the fast mass accretion episodes of SMBHs in the early universe. See also § 5.1 where the first steps are taken in order to carry out systematically such a loss cone study.

Part II

Own Publications

Chapter 3 is based on

Brockamp, M., Baumgardt, H., & Kroupa, P. 2011, MNRAS, 418, 1308

Chapter 4 is based on

Brockamp, M., Küpper, A. H. W., Thies, I., Baumgardt, H., & Kroupa, P. 2014, MNRAS, 441, 150

Chapter 3

Tidal Disruption Rate of Stars by SMBHs

As described in depth in the previous Chapter 2.2, there exist several SMBH feeding processes. Black holes grow through the accretion of gas, SMBH mergers and, depending on their mass, through tidal disruption or swallowing of whole stars. This chapter which is based on Brockamp et al. (2011) examines in much greater detail the flux of stars which are driven by relaxation processes onto loss cone orbits[11]. I concentrate on the least massive black holes where relaxation driven effects are enhanced due to small relaxation timescales. The disruption rate of stars by SMBHs is calculated numerically with a modified version of Aarseth's NBODY6 code. A detailed description of NBODY6 can be found in the Appendix A.1. The effects of other loss cone refilling processes like centrophilic orbits in non-symmetrical potentials or massive perturbers are neglected. There exist several different approaches to obtain the relaxation driven tidal disruption rate of stars by SMBHs. Each method has its own advantages and disadvantages. One great advantage of direct N-body integrations is their ability to take dynamical processes like the wandering of the black hole, dynamical cluster heating and cusp formation into account.

The whole Chapter 3 is based on Brockamp et al. (2011). Compared with Brockamp et al. (2011), three modifications are made: (i) The abstract and the first appendix of Brockamp et al. (2011) have been removed and some formulations have been improved, (ii) the second appendix can be found at the end of this thesis, see Appendix B. (iii) The third appendix of Brockamp et al. (2011) is partially implemented into this chapter.

To eliminate any confusion with the overlapping topic of my Diploma thesis, it must be explicitly stated that for this PhD study (i) all computations were recalculated with the NBODY6 software and that (ii) much larger N-body computations containing up to $(2.5 - 5) \cdot 10^5$ particles were included. Furthermore (iii), I used a different extrapolation method for scaling these models to astrophysical systems including new estimates for the tidal disruption rate and (iv) I performed a much more sophisticated analysis as well as interpretation of the results.

---

[11]This chapter has been published, apart from minor changes which are described in the text, in the MNRAS journal (Vol. 418, pp. 1308-1324).

3.1. Introduction

The evolution of supermassive black holes (SMBHs) and their host galaxies is at present one of the key problems of astrophysics. Motivated by empirically found scaling relations between properties of galaxies in terms of velocity dispersion σ (Gebhardt et al., 2000; Ferrarese & Merritt, 2000; Gültekin et al., 2009), luminosity L (Kormendy & Richstone, 1995; Ferrarese & Ford, 2005), bulge mass M_{Bulge} (Magorrian et al., 1998; Häring & Rix, 2004), central light deficit L_{def} (Lauer et al., 2007; Kormendy & Bender, 2009; Hopkins & Hernquist, 2010), total number of globular clusters N_{GC} (Burkert & Tremaine, 2010) and the mass of their central black holes $M_\bullet$, there is a substantial need to understand the related evolution of both SMBHs and their hosts. In order to constrain galaxy formation models and to answer the question as to what powers the growth of SMBHs over cosmic times, all forms of matter which are accreted must be taken into account. This becomes more urgent as recent studies have found evidence for deviations from the general scaling relations for the most-massive and for the least-massive black holes (Lauer et al., 2007; Gebhardt et al., 2011; Kormendy et al., 2011).

Gas accretion is thought to be the most dominant driver of SMBH growth (Soltan, 1982). Modern studies (Yu & Tremaine, 2002) estimate the black hole mass density from the spatial distribution and from the measured stellar velocity dispersions in elliptical galaxies in combination with the $M_\bullet - \sigma$ relation. The SMBH mass density is then compared with the observed quasar luminosity function in order to yield constraints on the accretion efficiency parameter ϵ as well as on the growth history. In order to make these studies even more accurate, the impact of other feeding modes like merging supermassive black holes and stellar captures must also be taken into account. Simultaneously the luminous gas accretion history of low-mass SMBHs ($M_\bullet \approx 10^5 - 10^7 \, \text{M}_\odot$) is harder to measure especially at large redshifts as they never approach luminosities comparable to those of quasars. It is even plausible that low-mass SMBHs gain most of their mass by tidal disruption events (Milosavljević et al., 2006). Therefore, it is important to infer the stellar capture rate for as many astrophysical systems of interest as possible, for all relevant SMBH masses using both theoretical and when possible numerical approaches. In order to avoid confusion regarding the terminology of the capture and disruption rate we note that the former expression is used for the general number of stars/particles which are either swallowed as a whole or disrupted outside the event horizon in a given time, i.e. independent of the mass of the SMBH. The latter one is explicitly used for situations in which stars are tidally disrupted before they would enter the event horizon.

In this paper we present the disruption rate of stars by SMBHs with masses in the lower range up to $M_\bullet \lesssim 10^7 \, \text{M}_\odot$ (Graham & Spitler, 2009) embedded inside realistic stellar density profiles. These results are obtained by self-consistent direct N-body integrations and increase the hitherto probed region of direct numerically inferred disruption rates. Pioneered by Baumgardt et al. (2004a,b); Baumgardt et al. (2006) for intermediate-mass black holes (IMBHs) at the centers of globular clusters, our calculations can be applied to a larger sample of systems. Our findings should

be regarded as complementary to other contributions (Duncan & Shapiro, 1983; Magorrian & Tremaine, 1999; Amaro-Seoane et al., 2004) where the impact of tidal disruption events is shown to be significant and therefore should not be neglected in considering the question of what powers the growth of black holes.

There are several mechanism by which stars are driven into the loss cone of a black hole. In spherical stellar distributions, where the relaxation time T_{rel} is comparable to or smaller than the present age of the universe (Freitag et al., 2008)[12], t_0, two-body relaxation induces a steady change in the angular momentum space distribution of stars such that some of them will drift to very eccentric orbits with pericentre distances smaller than the black hole capture radius (Frank & Rees, 1976; Lightman & Shapiro, 1977). In much larger systems like the most-massive elliptical galaxies which are thought to be triaxial in shape (Kormendy & Bender, 1996), stars on box orbits can cross the central region arbitrary close to the SMBH (Binney & Tremaine, 2008) such that they become disrupted or swallowed as a whole for the case of a very massive SMBH. Merritt & Vasiliev (2011) concluded that the feeding mode of very massive SMBHs, like M87 (Gebhardt & Thomas, 2009), is currently dominated by stellar captures. The true rates could be even higher since their analysis takes only stellar orbits within the black hole influence radius r_H into account, whereas stars within the loss cone but from much further away should reach the black hole, too, as long as the critical radius r_{crit} (a quantity which is defined in Eq. 3.45) remains larger than r_H. Norman & Silk (1983); Poon & Merritt (2001, 2002); Merritt & Poon (2004); Berczik et al. (2006) provide additional information on the dynamics of SMBHs and stellar capture rates in triaxial potentials.

Observed disruption events (Ulmer 1999; Komossa 2002; Halpern et al. 2004; Komossa et al. 2004; Esquej et al. 2008; Gezari et al. 2008; Cappelluti et al. 2009; Gezari et al. 2009; Komossa et al. 2009; van Velzen et al. 2011 and references therein), support the view that tidal disruptions contribute to the growth history of SMBHs. To which magnitude this is the case is a major aspect of this study.

The paper is organized as follows. In § 3.2 we will shortly explain the concept by which stars are driven by angular momentum diffusion into the "loss cone" of the SMBH. This formalism is applied to spherical stellar distributions with arbitrary slope parameters of the density profile. § 3.3 describes the NBODY6 code that we used. We will specify the scale-free models and motivate the very large set of performed simulations required to obtain the disruption rate of stars by SMBHs in the nuclei of galaxies. The results will be given in § 3.4 while more detailed information regarding the dynamics of the simulations will be part of § 3.5. In § 3.6 the procedure how to scale the obtained results to realistic astrophysical systems as well as the number of expected tidal disruption events will be specified. A critical discussion of potential error sources in § 3.7 is followed by a summary of our main findings in § 3.8.

---

[12]For the purposes of this study we do not discriminate between t_0 and one Hubble time H_0^{-1} and assume $H_0^{-1} \approx t_0 = 13.7 \cdot 10^9$ yr (Komatsu et al., 2009).

3.2. Theory

Frank & Rees (1976) calculate that massive black holes can grow not only by swallowing stars which lose their energy via dynamical relaxation, but also by swallowing stars on very eccentric orbits. The change of the stellar distribution in angular momentum space is expected to progress much faster than the change in energy space. The velocity vectors of stars must lie close together as long as they have pericentre distances which are smaller than the capture radius of the SMBH. This narrow region in velocity space is defined to be the loss cone. The symmetry axis of the loss cone angle, θ_{lc}, points towards the SMBH. Within the influence radius of the black hole, where the velocity distribution is Keplerian ($\propto r^{-0.5}$), θ_{lc} is defined to be

$$\theta_{lc} \propto \left(\frac{2r_{cap}}{3r} \right)^{\frac{1}{2}} \tag{3.43}$$

according to Frank & Rees (1976). For $r \geq r_H$, a different formula is required. In the following discussion we leave it unspecified if stars are swallowed or disrupted at the capture radius. A general capture radius, r_{cap}, can be specified for all purposes (Novikov & Frolov, 1989; Binney & Tremaine, 2008). Without dynamical relaxation, a full loss cone in a spherical galaxy would be emptied within a crossing time scale, t_{cross}. However, dynamical relaxation changes permanently the angular momentum distribution of stars. These gravitational two-body deflections give rise to changes in the velocity vectors by small amounts θ_{Diff} per crossing time (Frank & Rees, 1976):

$$\theta_{Diff} \propto \left(\frac{t_{cross}}{t_{rel}} \right)^{\frac{1}{2}}. \tag{3.44}$$

At the critical radius, r_{crit}, drifts of the velocity vector equal the loss cone angle, θ_{lc}:

$$\left. \frac{\theta_{lc}}{\theta_{Diff}} \right|_{r=r_{crit}} = 1. \tag{3.45}$$

Assuming a number density profile[13] $n(r) = n_0 r^\alpha$ within $r_{crit} \leq r_H$ and considering equal mass stars, an expression for the critical radius

$$r_{crit} \propto \left(\frac{r_{cap} M_\bullet^2}{M_\star^2 n_0} \right)^{\frac{1}{4+\alpha}} \tag{3.46}$$

is obtained by inserting Eq. 3.43 and Eq. 3.44 into Eq. 3.45. Spitzer's relaxation formula (Spitzer & Harm, 1958; Spitzer, 1987) is used for the relaxation time t_{rel}. The Coulomb logarithm is neglected.

The stellar capture rate can be derived by using eq. 17 from Frank & Rees (1976)[14]:

$$\dot{C} \propto \left. \frac{\theta_{lc}^2 r^3 n(r)}{t_{cross}} \right|_{r=r_{crit}} = \left. \frac{\theta_{Diff}^2 r^3 n(r)}{t_{cross}} \right|_{r=r_{crit}}, \tag{3.47}$$

---

[13]The parameter n_0 can be substituted by $n_0 = n_c r_H^{-\alpha}$ into the more common number density n_c at the influence radius r_H.

[14]We replace $v(r) \propto \frac{r}{t_{cross}}$.

For a density profile $n(r \leq r_{\text{crit}}) = n_0 r^\alpha$ the stellar disruption rate $\dot{C}$ is obtained by substituting $r = r_{\text{crit}}$:

$$\dot{C} \propto G^{\frac{1}{2}} M_\bullet^{\frac{1}{2}} r_{\text{cap}} n_0 \left(\frac{r_{\text{cap}} M_\bullet^2}{M_\star^2 n_0} \right)^{\frac{0.5+\alpha}{4+\alpha}} . \tag{3.48}$$

For the case of very massive SMBHs the critical radius exceeds the influence radius and Eq. 3.46 must be modified according to Frank & Rees (1976):

$$r_{\text{crit}} \propto \left(r_{\text{cap}} r_H n_0 \right)^{-\frac{1}{1+\alpha}} . \tag{3.49}$$

We assume the velocity dispersion to be $\sigma^2 \propto \frac{GM(r)}{r} \propto G n_0 M_\star r^{2+\alpha}$ and use the same formalism (Eq. 3.47) to derive Eq. 3.49. The capture rate for $r_{\text{crit}} > r_H$ becomes

$$\dot{C} \propto r_{\text{cap}} r_H n_0^{\frac{3}{2}} G^{\frac{1}{2}} M_\star^{\frac{1}{2}} \left(r_{\text{cap}} r_H n_0 \right)^{-\frac{2+3\alpha}{2(1+\alpha)}} . \tag{3.50}$$

For simplicity we adopt the number density profile to be $n(r \leq r_{\text{crit}}) = n_0 r^\alpha$ and thus assume α to remain constant. Real galactic nuclei with SMBHs more massive than $10^7 \, \text{M}_\odot$ can deviate from pure power-law profiles at radii $r \leq r_{\text{crit}}$, whereas the inner density profiles of large elliptical galaxies are nevertheless well approximated by simple power-law profiles (Trujillo et al., 2004). Eq. 3.50 is valid for $-3 < \alpha < -1$.

These equations which are derived from the very general angular momentum diffusion concept of Frank & Rees (1976), will lose their applicability for systems where the stellar phase space is not well-occupied with sufficient amounts of low angular momentum stars. Gaps in the phase space distribution, for example carved out by binary-SMBH evolution must first be repopulated, whereas the relaxation driven refilling process may take longer than one Hubble time H_0^{-1} for large elliptical galaxies. Hence for these systems the two-body relaxation driven capture rate will be strongly suppressed (Merritt & Wang, 2005).

3.3. Description of the N-body Models

In the following sections the computations and results will be specified. We make use of conventional N-body units (Heggie & Mathieu, 1986). For readers being unexperienced with these units, a very short overview is given below.

3.3.1. N-body Units

The set of N-body units is defined by

$$G = M = 1 \tag{3.51}$$

where G is the gravitational constant and M the total mass. In a gravitationally bound system which is in virial equilibrium ($r_{\text{vir}} = 1$), the total energy E is $E = -\frac{1}{4}$. N-body timescales which are used as the time base for the computations are defined to be $\frac{t_{\text{cross}}}{2\sqrt{2}}$. Here $t_{\text{cross}} = \frac{2r}{\sigma}$ is the crossing time of the particles at $r = r_{\text{vir}}$. The 3D half mass radius

($\approx$ 1.35 times the half light radius r_e) for a constant $\frac{M}{L}$-ratio is usually scaled to equal $r_{\text{vir}} = 1$. It is of the order of kpc scales in physical units for real elliptical galaxies. For example one N-body timescale would correspond to $t = 7.8 \cdot 10^6$ yr in physical units for a spherical bulge or galaxy of Sérsic type (n=4, see § 3.3.2) with a half mass radius of 0.65 kpc and total stellar mass $M = 10^9 \, M_\odot$. In § 3.6.1 and Appendix B the detailed procedure how the computational results are transformed from N-body to physical units is given.

3.3.2. Generation of the Models

The observed surface brightness profiles $I_n(r)$ of bulges and elliptical galaxies are well approximated by the following Sérsic law (Sersic, 1968; Caon et al., 1993):

$$I_n(r) = I_e \exp \left\{ -b_n \left[\left(\frac{r}{r_e} \right)^{\frac{1}{n}} - 1 \right] \right\}. \tag{3.52}$$

The parameter n, also known as the Sérsic index, specifies the strength of light concentration towards the center of the galaxy. $I_e = I(r_e)$ corresponds to the surface brightness at the half light radius, whereas b_n is defined in a way that half of the total light is emitted within r_e (Ciotti & Bertin, 1999). The 2D density profile is obtained from the surface brightness profile by using a mass-to-light ratio, which for our purposes is assumed to be constant along the radial distance to the center of the galaxy.

A Sérsic density profile is chosen for the initial state of the models. These N-body models are set up using the same method as described in Hilker et al. (2007). First, the 2D Sérsic models are deprojected into 3D density distributions using Abel's integral equation. From the 3D density profile, $\rho(r)$, the potential, $\phi(r)$, can be deduced. By assuming an overall isotropic velocity distribution, the velocities of the particles are derived with the help of eq. 4.46a from Binney & Tremaine (2008). The program is modified by adding a $1/r$-potential of the black hole of mass $M_\bullet = 0.01$ in N-body units (Heggie & Mathieu, 1986)[15]. This step guarantees that the N-body models are in equilibrium. The cut off radius for the models is chosen to be 20 times the half mass radius.

3.3.3. Nbody6 Numerical Dynamics Software

The up to date version of NBODY6 (Aarseth, 1999, 2003) with Graphical Processing Unit (GPU) support is used for the direct N-body integrations. A black hole is added by a SMBH particle of mass $M_\bullet = 0.01$. It is implemented into the models at the center of mass while being initially at rest. Particles which fall below the limit of the capture radius $r_{\text{cap}}^{\text{sim}}$ are removed from the simulations while their masses are added to the SMBH particle. The capture radius $r_{\text{cap}}^{\text{sim}}$ remains constant[16]. To ensure correct dynamics, the SMBH particle receives the center of mass velocity after the capture event.

---

[15]The differences between a $1/r$-potential and a realistic Schwarzschild or Kerr black hole potential are completely insignificant for distances of several hundred r_{cap} away from the black hole. This is typically the distance where the innermost particles are located.

[16]In reality the capture radius would change as well as the total number of capture events. However in order to simplify our extrapolation formalism to realistic galaxies and due to the fact that the mass
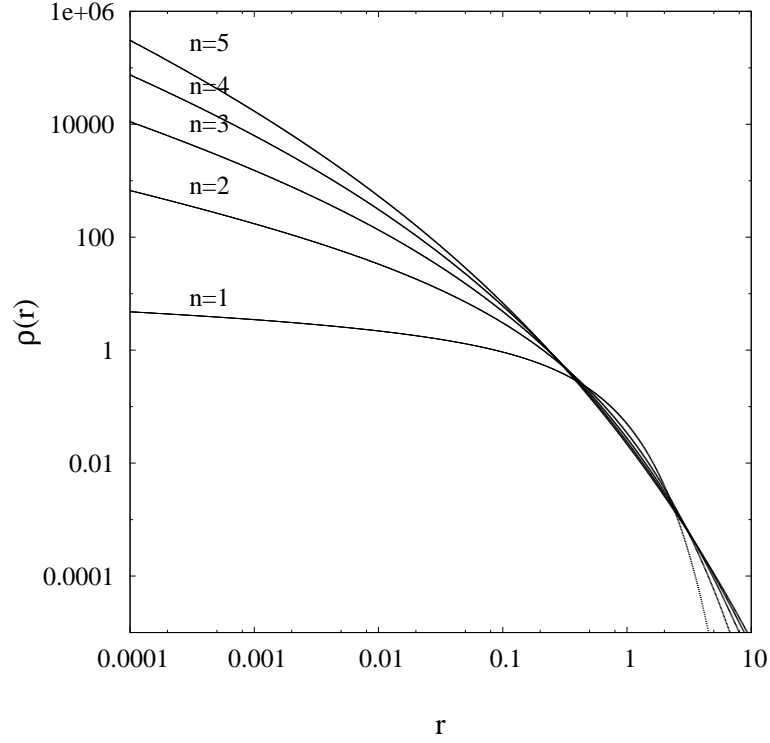
Figure 3.8.   Scale-free density profiles of different Sérsic models.

3.3.4. The Need for a Large Set of Simulations

In order to extrapolate many scale-free models to astrophysical systems which contain some orders of magnitudes more stars than are possible to be simulated with direct *N*-body integration methods on modern GPUs, the relaxation driven effects in angular momentum and energy space as well as every other *N* dependent systematic effect (see § 3.5.1 & § 3.5.2) must be determined. This can be achieved by simulating models with different numbers of particles but otherwise identical physical parameters. In doing so several particle models following a Sérsic $n = 4$ density profile are generated. It is desirable to simulate these models for as many different black hole configurations as possible in order to use the formalism in § 3.6.1 for the extrapolation to the black hole of interest, hence increasing the computational effort considerably. The masses of the particles $m_i = N^{-1}$ are always scaled to ensure $\sum_i m_i = 1$ in *N*-body units (Heggie & Mathieu, 1986). N=15×1 k, 15×2 k, 10×5 k, 5×10 k, 5×25 k, 2×50 k, 2×75 k and one model containing each 100 k, 150 k, 250 k and 500 k particles are generated and simulated. All these models are simulated forward in time up to 100 *N*-body timescales for three different black hole capture radii $r_{\mathrm{cap}}^{\mathrm{sim}} = 2, 4, 8 \cdot 10^{-7}$. Energy values and relative energy errors $|\Delta E| = \left| \frac{E(t_n) - E(t_{n-1})}{E(t_{n-1})} \right|$ are evaluated directly with the NBODY6 software and controlled every new *N*-body timescale. The relative energy errors usu-

---

gain of the black hole within $T = 100$ NBODY timescales is limited to the order of a few percent, it is assumed to be constant.

ally not exceeded values of $|\Delta E| = 10^{-8} - 10^{-4}$. A few models had to be discarded afterwards as they suffered from repetitive energy errors in excess of $|\Delta E| = 10^{-2}$. To guarantee unbiased capture rates we also discarded models in which the position of the black hole was offset by a distance $d \geq 0.1$ from the density center of the particle distribution. The statistical significance of the low N models is increased by simulating as many models as possible. The required time for the computations of all simulations exceeds a timespan of seven months on five modern GPUs.
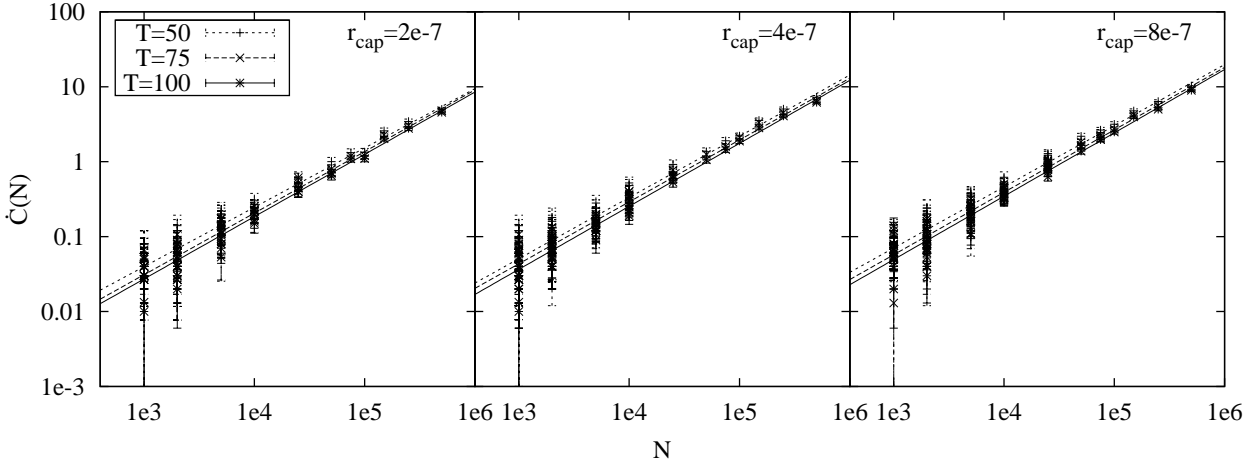
3.4. Results

Figure 3.9. The capture rates per one N-body time unit for the three computed black hole capture radii, evaluated from the total amount of swallowed particles within the timespan of $T = 50, 75$ & 100 N-body time units. These values are best fitted by the power-law function $\dot{C}(N) = aN^b$, here N refers to the total number of simulated particles.

For each capture radius, $r_{cap}^{sim} = 2, 4, 8 \cdot 10^{-7}$, the number of swallowed particles is plotted in Fig. 3.9 as a function of the total number of particles. Moreover, the capture rate per N-body timescale is obtained by dividing the total number of captured particles within $T = 50, 75, 100$ N-body integration times by these values. The number of captures averaged over all runs are then approximated by a power-law function

$$\dot{C}(N) = aN^b \tag{3.53}$$

with the help of the *Marquardt-Levenberg* minimization method and independently by a grid scanning algorithm minimizing the Chi-square error statistics. The parameters a, b must be positive and the boundary condition $\dot{C}(N)|_{N=0} = 0$ requires no offset. To reduce the correlation between the parameters a and b to zero, we normalize the power-law function $\dot{C}(N) = a' (N/\bar{N}_L)^b$ during fitting. The denominator $\bar{N}_L$ refers to the logarithmic mean. The resulting effect can be seen in Fig. 3.10. These uncorrelated values[17] are used for the extrapolation to realistic values. The justification for using

---

[17]To simplify the extrapolation formalism, the renormalized constant of proportionality a' and its error is afterwards transformed back to $a = \frac{a'}{\bar{N}_L^b}$. This does not affect the correlation coefficient $\rho = 0$ between a, b.

T	$r_{\text{cap}}^{\text{sim}}$	$a(10^{-5})$	b	χ_μ	Q
50	$2 \cdot 10^{-7}$	16.76 ± 3.11	0.79 ± 0.02	0.82	0.79
	$4 \cdot 10^{-7}$	17.95 ± 2.89	0.82 ± 0.01	1.06	0.36
	$8 \cdot 10^{-7}$	25.08 ± 3.92	0.82 ± 0.01	1.41	0.02
75	$2 \cdot 10^{-7}$	10.63 ± 1.95	0.82 ± 0.02	1.01	0.45
	$4 \cdot 10^{-7}$	14.46 ± 2.09	0.83 ± 0.01	1.13	0.25
	$8 \cdot 10^{-7}$	18.15 ± 2.51	0.83 ± 0.01	1.41	0.02
100	$2 \cdot 10^{-7}$	8.73 ± 1.33	0.83 ± 0.01	0.83	0.79
	$4 \cdot 10^{-7}$	10.98 ± 1.49	0.84 ± 0.01	1.12	0.26
	$8 \cdot 10^{-7}$	14.41 ± 1.97	0.85 ± 0.01	1.57	0.01

Table 3.1. Fit parameters of the power-law approximation (Eq. 3.53) for the simulated Sérsic $n = 4$ models. The black hole capture radii and timescales T are given in N-body units. $\chi_\mu = \chi^2/\mu$ corresponds to the reduced Chi-Square values, μ are the degrees of freedom and $Q = \Gamma(0.5\mu, 0.5\chi^2)$ the χ^2-probability function which estimates the likelihood of the power-law fit.

a power-law approximation for the capture rate $\dot{C}(N)$ from the simulations comes from Eq. 3.48 when replacing $n_0 = N\rho_0$ and $M_\star = N^{-1}$. Poisson square root errors $\sqrt{N_c}$ are assumed for all values and N_c is the total number of captured particles. The results can be found in Table 3.1. Additionally, the reduced Chi-Square values χ_μ and the χ^2-probability function $Q(\mu, \chi^2)$ are calculated in order to test the validity of a power-law approximation for the capture rate. Given the values in Table 3.1, the hypothesis of a power-law function seems to be a reasonable assumption. However, for the determination of the error values of parameters a, b the square root errors $\sqrt{N_c}$ are rescaled slightly by the values $\sqrt{\chi_\mu}$ from Table 3.1 to obtain $\chi_\mu = 1$. Otherwise the quoted error values would be underestimated for the case of $\chi_\mu \geq 1$ (Press et al., 1992)[18].

The advantage of numerical simulations over analytical expressions like Eq. 3.48 are given in the ability to take dynamical aspects like cusp formation, dynamical heating (§ 3.5.1) and a wandering SMBHs (§ 3.5.2) into account. These depend strongly on time and on the total number of particles and may influence the capture rate $\dot{C}(N)$. The predicted power-law index of Eq. 3.48 is therefore not expected to exactly match the value obtained from the simulations. In fact Eq. 3.48 would only predict $\dot{C}(N) \propto N^{\frac{4.5+2\alpha}{4+\alpha}} \approx N^{0.6}$ for $\alpha \approx -1.5$ compared to $\dot{C}(N) \propto N^{0.83}$ from the computations. The difference is caused by stronger dynamical evolution and cluster heating in low number particle simulations accompanied by a decrease in the total number of particles falling into the black hole. Models containing many more particles have much smoother potentials and relaxation driven effects (notably cluster heating) need longer to influence (decrease) the capture rate (Fig. 3.11). Consequently the exponent b of the power-law function which approximates the number of captured particles of the total set of simulations becomes larger than expected from Eq. 3.48. These dynamical processes are reflected by the values of a, b at different timescales. The constant of proportionality a decreases in time, whereas the slope parameter b is consistent with a small increase from $b \approx 0.80$ at time $T = 50$ up to $b \approx 0.83$ at time $T = 75$. Thus the exponent of the power-law function which approximates the capture rates becomes
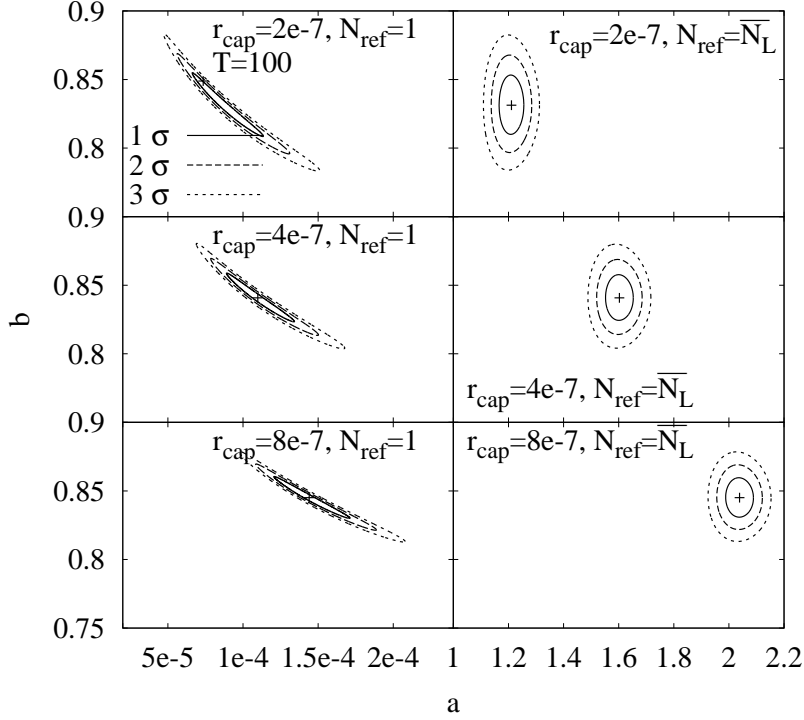
---

[18]Chapter 15.1

Figure 3.10. The error ellipses for the models after $T = 100$ before (left) and after (right) renormalization. The shape of the error ellipses becomes nearly circular which proofs the parameters to be uncorrelated.

slightly larger, whereas the constant of proportionality decreases. Moreover, the $T = 50$ values may still be influenced by initial conditions. There are minor changes in b from $T = 75$ to $T = 100$.

For the purpose of this study the rate $\dot{C}$ is assumed, within the statistical uncertainty, to remain unchanged when extrapolated to larger values of N. This assumption can only hold if the phase space is already well occupied with sufficient amounts of low angular momentum stars. This is a necessary condition for the steady diffusion process of stars into the loss cone. The capture rates of the Sérsic $n = 4$ models are found to be maximal at the beginning of the simulations in contrast to Sérsic $n = 2$ models with their much shallower density profiles (Fig. 3.11). This demonstrates the above assumption to be credible, at least for galactic nuclei containing SMBHs less massive than $10^7 \, \mathrm{M_\odot}$. In such galaxies the diffusively refill of any small gap with radius $r_{\mathrm{gap}} << r_H$ would anyway occur on a timescale shorter than a Hubble time (Merritt, 2005). Additionally, one can show that the inequality

$$T_{\mathrm{refill}} = \theta^2 T_{\mathrm{rel}} << H_0^{-1} \tag{3.54}$$

is fulfilled up to SMBHs of order $10^7 \mathrm{M_\odot}$ and hence our result, $\dot{C} \propto N^{0.83}$, should yield realistic values when extrapolated to such black holes: By assuming the radius r at which particles can enter loss cone orbits without being scattered away through interactions with other stars to be $r_{\mathrm{crit}} \approx r_H\big|_{M_\bullet = 10^7 \mathrm{M_\odot}}$, the loss cone angle θ can be
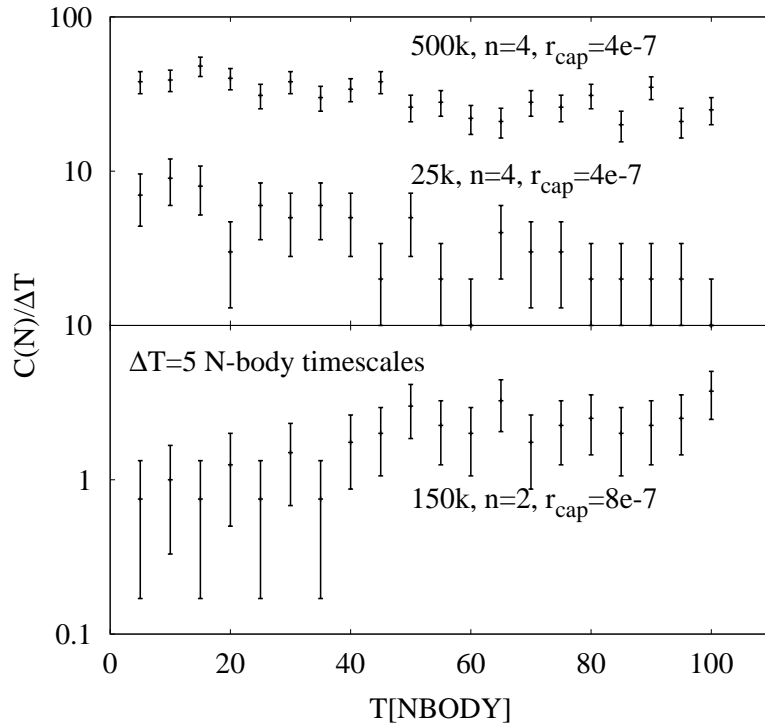
Figure 3.11. Time evolution of the capture rates for Sérsic $n = 4$ & $n = 2$ models. The statistical significance of the latter ones is increased by averaging over three simulations.

evaluated from Eq. 3.43. For the constant of proportionality f we use $f = 2$ in accordance with Frank & Rees (1976). By assuming $r \approx r_H$, $M_\star \approx 1 M_\odot$, the relaxation time to be $T_{\text{rel}} \approx H_0^{-1}$ (Freitag et al., 2008) and estimating all other relevant parameters from the $M_\bullet - \sigma$ relation (Ferrarese & Ford, 2005), one obtains the desired result $T_{\text{refill}} \approx 4 \cdot 10^{-6} \cdot H_0^{-1} << H_0^{-1}$. The observed strong N dependence (b=0.83) may become irrelevant or absent for black holes more massive than $10^7 M_\odot$, especially if they have core profiles. For these systems the loss cone refilling timescale $T_{\text{refill}} \approx \theta_{\text{lc}}^2 T_{\text{rel}}$, becomes very long. Once the initially filled loss cone becomes emptied within a few crossing times, the capture rate $\dot{C}$ would stagnate at insignificant values as long as there is no re-population mechanism more efficient than angular momentum diffusion (Merritt & Wang, 2005; Merritt, 2005).

This effect can be illustrated by simulating Sérsic $n = 2$ models. These have a slower dynamical evolution, a different cusp and cluster heating timescale and a reduced population of low angular momentum stars compared to the Sérsic $n = 4$ models. In this way, qualitative limitations on the number of capture events for core-type galaxies with shallow central density profiles (Fig. 3.8) can be obtained. Even though the extended outer profiles of the most-massive elliptical galaxies are conform with a large Sérsic index n, the 'depleted' core-type central regions (this is where the relevant black hole physics take place) are more similar in their appearance to the shallow

centers of low n models[19]. A strongly reduced disruption rate in comparison to the Sérsic $n = 4$ models is evident in these computations. The enlarged radius of influence r_H and therefore the difference in the extrapolation formalism to realistic galaxies can not compensate these differences. Moreover, in the largest simulated Sérsic $n = 2$ models, the capture rate stagnate first around insignificant values. It starts increasing (Fig. 3.11) afterwards, accompanied by the relaxation driven formation of a cusp and a population of stars with sufficiently low angular momentum. If we assume this behaviour to persist unchanged up to even larger numbers of particles, i.e. to large core-type galaxies where no cusps can form on timescales shorter than H_0^{-1}, these numerical findings confirm analytical predictions (Wang & Merritt, 2004) in a qualitative way. The capture rate of stars in large core-type galaxies is very low, as long as the diffusive refill of the angular momentum space with a sufficient number of stars, i.e. the cusp formation timescale, takes longer than a Hubble time.

Finally the here performed simulations of the Sérsic $n = 4$ models strongly support the scenario of Frank & Rees (1976) in which stars are driven into SMBHs via diffusion in angular momentum space and not only by diffusion in energy space. From the most elementary considerations of energy diffusion and by assuming the two-body relaxation time to be $T_{\mathrm{rel}} \propto \frac{N}{ln(N)}$, one would expect $\dot{C}(N) = \frac{\mathrm{d}N}{\mathrm{d}t} \propto N \cdot T_{\mathrm{rel}}^{-1} \propto \ln(N)$. Such a small increase of the capture rate with N is incompatible with our results.

3.5. Dynamics & Scaling Issues

The capture rate is influenced by several dynamical processes which are described below.

3.5.1. Cusp Formation and Cluster Expansion

The process of relaxation strongly influences the dynamics of stars around a SMBH. In Bahcall & Wolf (1976) the relaxation driven evolution of the stellar density profile near a SMBH is determined. It is found that the energy which some stars loose through near encounters is balanced by an outgoing flux of energy if the slope of the density profile is $\alpha = -1.75$. The required time to form such an equilibrium density B&W profile strongly depends on the relaxation time which becomes larger the smoother a gravitational potential is (Spitzer, 1987).

The $\alpha = -1.75$ profile is compatible with the present N-body models only up to $N = 25 - 50\,\mathrm{k}$ where relaxation is strongest and the statistical scatter is large. The $N > 50\,\mathrm{k}$ models, which allow a more precise measurement of α, are found to be in the developing stage towards more cuspy profiles. In Fig. 3.12 the time dependent

---

[19]This is also one reason which complicates the discrimination between 'true' cores, formed by the dynamical evolution of massive binary black holes and those in which only the outer envelopes are modified by near encounters. In the latter case the outer profile extrapolated to inwards radii would suggest the existence of a core (Hopkins & Hernquist, 2010). The binary black hole mechanism may also be accompanied by other processes lowering the central stellar density (Merritt & Vasiliev, 2011; Schawinski et al., 2006).
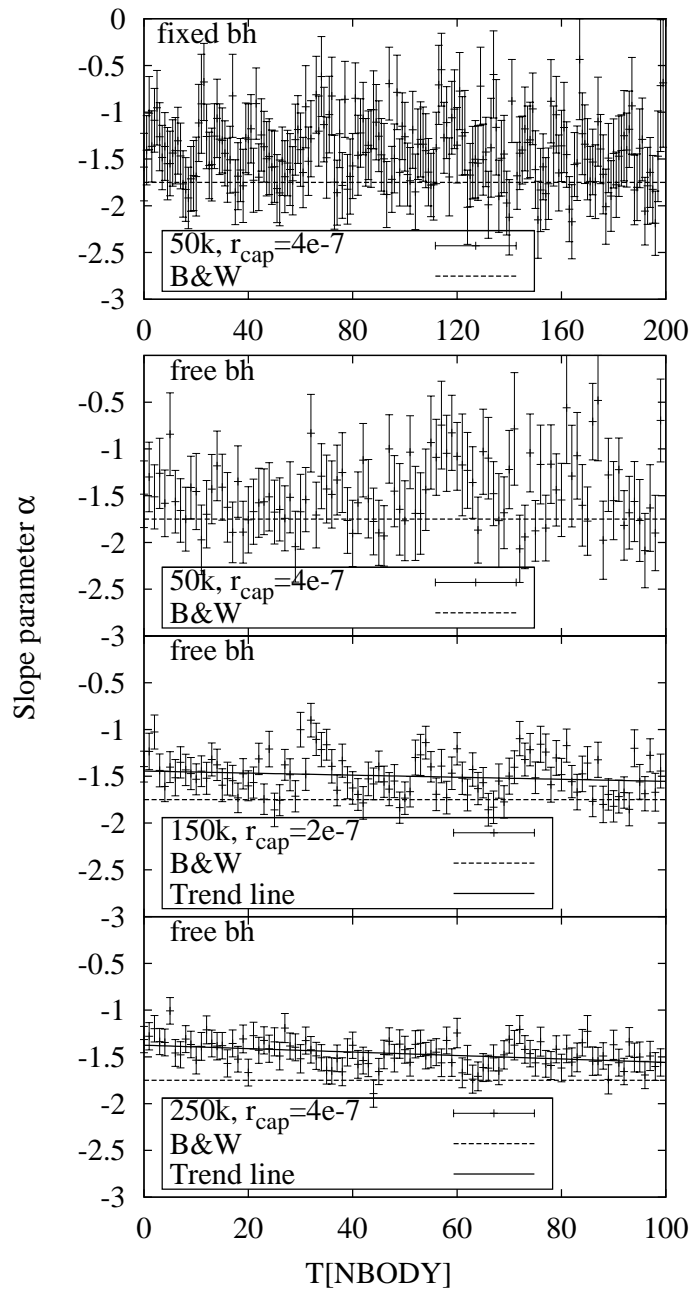
Figure 3.12. Time evolution of the central slope parameter α plotted for the 50 k, 150 k and 250 k models. The linear trend (solid line) is only drawn for the 150 k and 250 k models, while the first one (fixed black hole) was simulated forward in time up to $T = 200$.

central slope parameter α within $r = 0.004$ is plotted for some models. The radius r is chosen to be 20% smaller than the time and model-averaged black hole influence radius[20] in order to ensure that the slope parameter is not determined for radii larger

---

[20]See Appendix B for information regarding the determination of r_H.

than r_H at the beginning of the simulation when the mass and influence radius of the black hole is smallest. In order to obtain the central slope parameter α, it is inappropriate to calculate the density profile $\rho(r) \propto r^\alpha$ from given shells of thickness Δr and densities $\rho(r + \Delta r)$. Unfilled shells, especially in low N models, would strongly bias the determination. In order to circumvent this difficulty, the cumulative mass function $M(r) \propto r^\beta \propto \int_0^{r'} r^2 \rho_0 r^\alpha dr$ is calculated and the density slope parameter $\alpha = \beta - 3$ (equating coefficients) is determined from the measured β. This approach is tested by Monte-Carlo simulations in which several thousand models of particles following a $\rho \propto r^{-1.75}$ distribution are realized. For each of these models the central slope parameter α within $r = 0.004$ is calculated. The models are scaled such that the number of particles within $r = 0.004$ is equal (within the statistical scatter) to those of the 25 k, 50 k, 75 k, 150 k and 250 k simulations. The standard deviation σ from the obtained normal distribution[21] of central slope parameters is then taken as a reasonable estimate for the statistical error in addition to the one obtained from the fit itself. In Fig. 3.13 the time evolution of the mass profiles of two models are plotted.

In order to estimate the dependence of a wandering black hole on cusp formation processes and finally the capture rate, simulations of fixed black holes are desirable. Such simulations are realized by making use of a modified NBODY1 code (see §3.5.3 for more details regarding the capture rates). Within the large statistical errors, no significant difference in the density profiles between the free floating and fixed black hole is identified for the 50 k model. This is not an unexpected finding since the most bound particles, which are also the particles with the highest probability of being captured, are expected to follow the motion of the black hole. However a rigorous statistical evaluation is beyond the scope of this study.

While the capture rate is increased by cusp formation, dynamical heating counteracts by reducing the central density. The cluster starts to expand by decreasing the absolute value of its binding energy due to increasingly more strongly bound particles which are losing energy by relaxation. These particles, which may finally be swallowed by the black hole, are transferring their kinetic energy to other particles. This heating is illustrated by the time evolution of the Lagrange radii (Fig. 3.14). As a consequence the capture rate is expected to depend strongly on the density profile close to the black hole (Eq. 3.48).

In reality mass segregation of heavier bodies being relevant for multi-mass systems (Alexander & Hopman, 2009; Baumgardt et al., 2004b; Morris, 1993; Preto & Amaro-Seoane, 2010), stellar collisions (Bailey & Davies, 1999; Dale et al., 2009), a significant fraction of primordial binary stars (Hopman, 2009), torques from anisotropic matter distributions acting as massive perturbers (Perets et al., 2007), star formation by gas inflow (Hopkins & Quataert, 2010) and the possible presence of IMBHs (Baumgardt et al., 2006) would complicate the dynamics of stars close to a

---

[21] Actually very small particle numbers within $r = 0.004$ bias the power-law density-approximation and the distribution of central slope parameters becomes asymmetric with a tail towards very large values. This may partially account for some extreme outliers especially in low N models, whereas for larger models the distribution becomes more symmetric and the expectation values μ center around $\alpha = -1.75$.
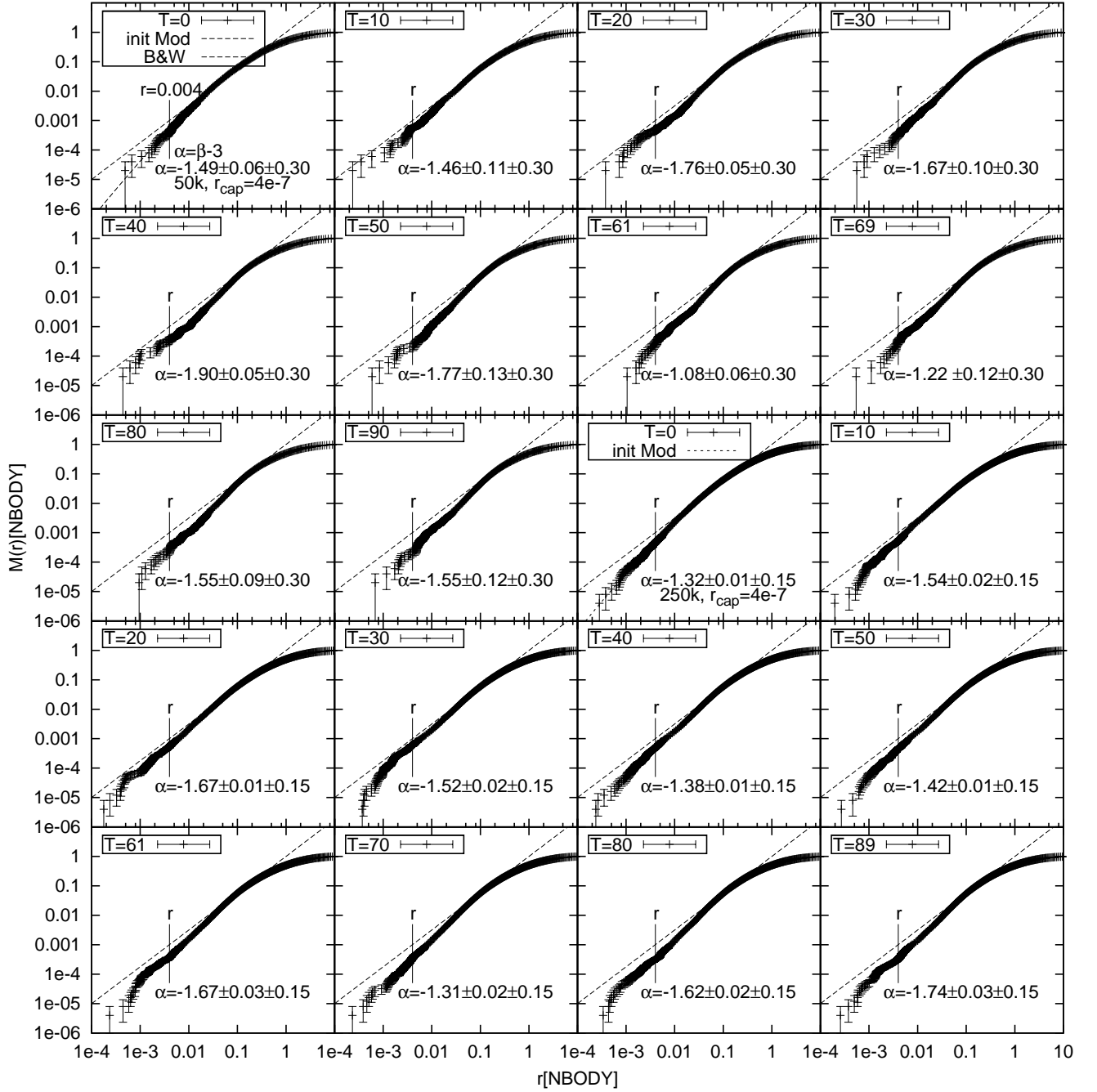
Figure 3.13. Mass profiles of two models. The thin dashed black line represents the gradient of the B&W profile while the thick dashed black line (only drawn for T=0) displays the unaltered Sérsic $n = 4$ model. The first error on α corresponds to the fitting error while the second one to the statistical error inferred from Monte Carlo simulations. The profiles and thus α are evaluated for radii $r \leq 0.004$. For more informations see the text below.

SMBH even more. These effects are also expected to accelerate the dynamical evolution and to enhance the number of stellar disruption events. Newly formed stars may

Figure 3.14. A comparison between the time evolution of several Lagrange radii for three different simulated models. As expected from theory, the Lagrange radii evolve faster to larger values in simulations containing fewer particles. The fluctuations are statistical in nature. The position of the black hole is used as the reference center.

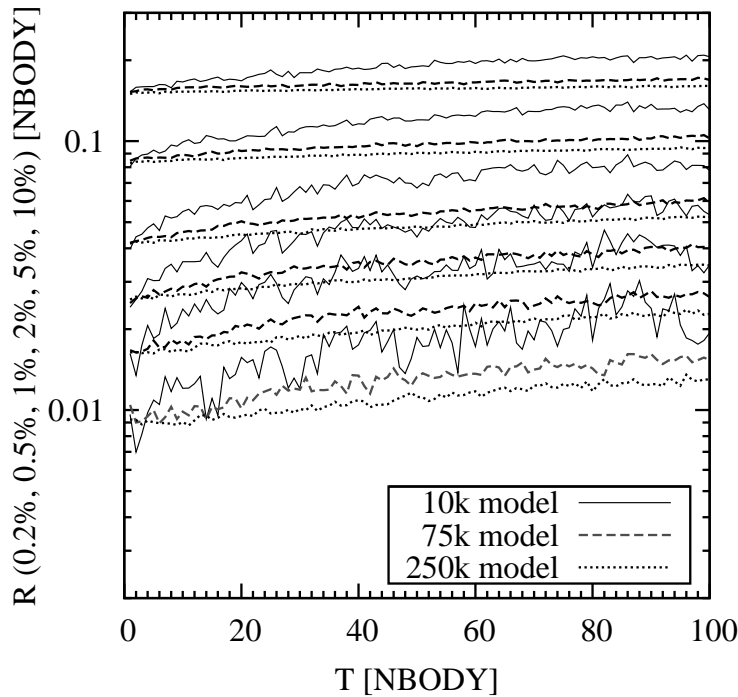replace those lost by tidal disruptions while tidal torques from IMBHs or a second SMBH are expected to refill the loss cone efficiently. Recoiled black holes should also enforce a burst of stellar disruptions (Stone & Loeb, 2011). In nature the relaxation driven B&W cusp formation takes very long and is expected to exceed one Hubble time H_0^{-1} for black hole masses larger than $10^7 \, \mathrm{M}_\odot$ (Freitag et al., 2008).

3.5.2. Wandering Black Hole

In the simulations the SMBH particle responds to the interaction with other particles which causes the SMBH to wander. This might affect the formation of a density cusp and influence the capture rate (Baumgardt et al., 2004a). Chatterjee et al. (2002) gives a very detailed overview of the relevant forces acting on a SMBH. They are summarized below.

The here performed simulations differ only in two ways from the *N*-body simulations done by Chatterjee et al. (2002). The black hole is allowed to swallow particles and the forces are unsoftened. The SMBH moves around the common center of mass due to the gravitational interaction with particles bound to it, whereas unbound particles are forcing the black hole to wander in a way which resembles the Brownian

motion of molecules. The latter process is the dominant contribution to the wandering of the black hole (see Fig. 3.15).

The situation is now complicated by the possible occurrence of violent three body encounters, e.g the interaction between the black hole, a strongly bound particle in orbit around it and another one. Recoil events force the black hole and its surrounding particles to move outwards. The mass fraction, $\frac{m}{M_\bullet}$, is usually orders of magnitudes larger in any performed N-body simulation than it is in a realistic nucleus of a galaxy. And, because the recoil effect becomes stronger for a larger fraction $\frac{m}{M_\bullet}$ and for smaller capture radii $r_{\text{cap}}^{\text{sim}}$, wandering of the SMBH in the N-body models is expected to modify the processes leading to the formation of a cusp. Consequently, the simulated capture rate may become affected. If the recoil kick of the SMBH particle is strong enough to eject it out of the density center or even from the whole cluster, the capture rate would drop significantly. This is expected, due to obvious reasons, to happen more likely in simulations with low particle numbers. As a consequence the extrapolated N-dependent capture rate would be strongly biased and the best fitted slope parameter, b, may be too large. Therefore, the actual position of the SMBH particle is compared to the density center of the matter distribution for every simulated model and at every new N-body time unit. The black hole particle is not considered in the calculation of the density center which is determined by the method described in Casertano & Hut (1985). If the position of the black hole and the density center are offset from each other by $d = 0.1$ in N-body units, the simulation is removed and replaced by a different one. In nearly all simulations this offset is smaller than $10^{-3} - 10^{-2}$. This guarantees that the results are not biased by displaced black holes in the low N models.

But even by removing those few models where "unnatural" kicks and displaced black holes are observed, the wandering of the black hole itself might affect the capture rate. The wandering radius can be determined by the standard deviation of the normal distribution (Fig. 3.15). It is found to be comparable in size to the influence radius $r_H = 0.005$ (for the 250 k model) and becomes gradually smaller for larger particle numbers i.e. smaller mass fractions $\frac{m}{M_\bullet}$.

A first clue about the degree to which the wandering black hole affects the results can be obtained by a closer look at the energies of accreted particles. If only particles are swallowed which are strongly bound i.e. have the most negative energies, the effect of Brownian motion on the capture rate is expected to be rather small, since the cloud of strongly bound particles moves together with the black hole. In Fig. 3.16 the initial energy distribution for two models is shown. Also plotted is the fraction of the accreted particles to the total number of particles within a given energy bin. Evidently only the most strongly bound particles are captured. If the energy $E = -\frac{M_\bullet m}{r} + 0.5mv_m^2 + 0.5M_\bullet v_{M_\bullet}^2$ of the particle of mass m and black hole is negative, shortly before it enters the capture radius and is removed, the particle is gravitationally bound to the SMBH. In our models the vast majority of particles are gravitationally bound to the black hole, e.g. the fraction of bound particles centers around 100% in the low-N models and 85 - 95% in the largest-N models.
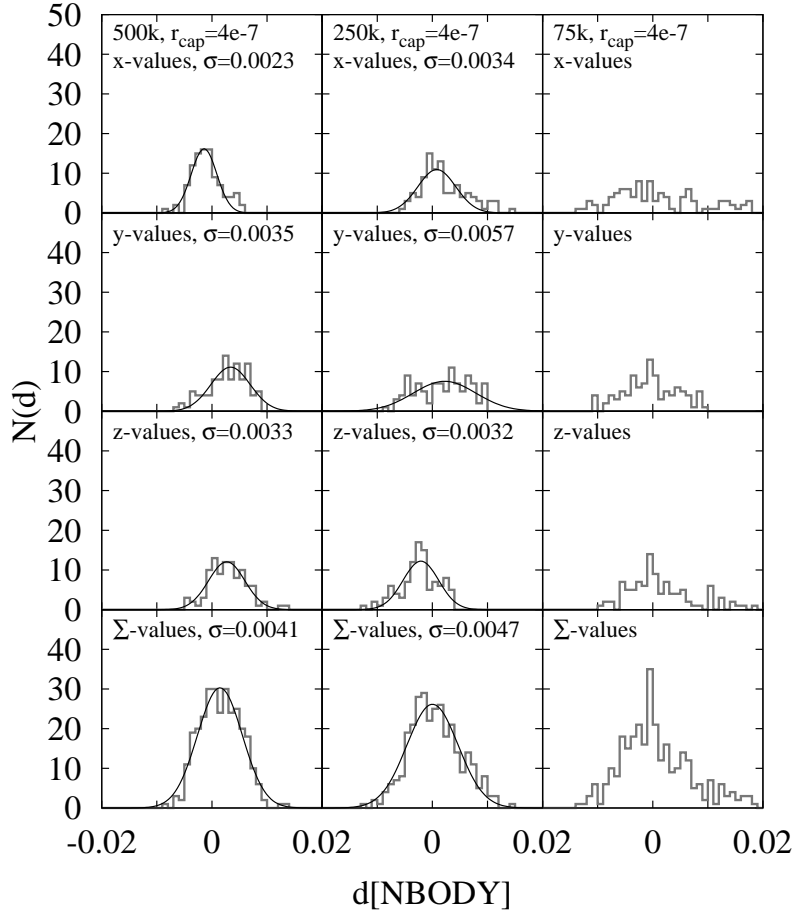
Figure 3.15. The 100 binned ($\Delta d = 0.001$) x, y, z-positions of the SMBH particle with a capture radius $r_{cap}^{sim} = 4 \cdot 10^{-7}$ for the 500 k, 250 k and 75 k model. In the last row the sum of these values is plotted and approximated by a normal distribution. The probability distributions are well approximated by a Gaussian underlining the character of the Brownian motion. The relevant length scale d is given in units of the virial radius $r_{vir} = r_e = 1$. The SMBH particle in the 75 k model experienced a minor kick during the integrations.

We therefore conclude that a wandering black hole does not bias the capture rate in a way that would make it unrealistic when extrapolated to real IMBHs and SMBHs. The performed simulations automatically contain the gradual change in the number of accreted particles which are influenced by the wandering of the black hole. Our largest N-computations already approach realistic IMBHs embedded in globular clusters. To resolve all doubts that the steep dependence on N of the capture rate, $\dot{C} \propto N^{0.83}$, is not caused by the systematics of the wandering black hole, especially in low N models, direct *N*-body simulations with fixed black holes (§ 3.5.3) are performed. For completeness it should also be mentioned that the *N*-body models include two additional effects: (i) A restoring force which arises between the black hole and the overall potential of the stellar distribution, especially if it has a cuspy density center, and (ii) a dynamical frictional force when the black hole passes through the cloud of particles (Chandrasekhar, 1943; Chandrasekhar, 1943b,c; Chatterjee et al., 2002).
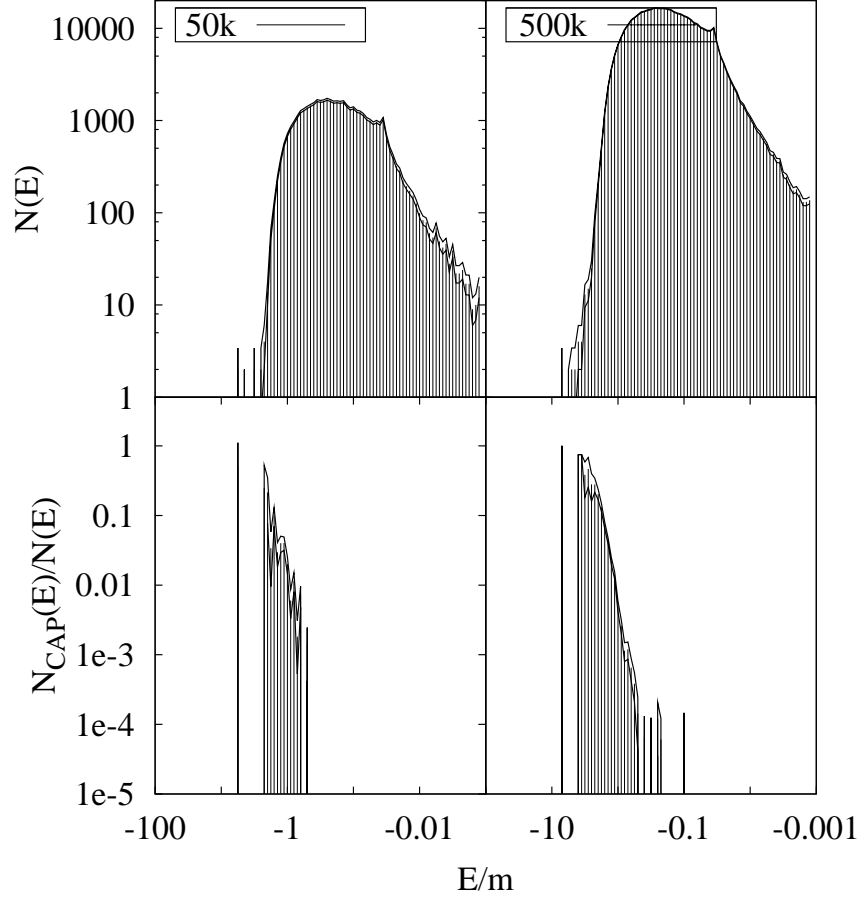
Figure 3.16. In the upper two figures the binned specific energy $\frac{E}{m}$ distributions of the 50 k, $r_{\text{cap}}^{\text{sim}} = 4 \cdot 10^{-7}$ and 500 k, $r_{\text{cap}}^{\text{sim}} = 4 \cdot 10^{-7}$ models are plotted. The lower diagrams depict the ratio of captured particles to total number of particles within the given energy bins. Evidently only the particles with the most negative energy i.e. the most strongly bound particles are accreted as expected from theory. The upper and lower (black) lines represent the error uncertainties.

3.5.3. Fixed Black Hole

Simulations with fixed black holes are realized by using NBODY1. Unfortunately it is impossible in NBODY6 to fix the SMBH particle to a specific location while simultaneously using all of its computational benefits. On the other hand the usage of an independent *N*-body software implementation reduces the possibility of systematic errors. The NBODY1 simulations are performed on special-purpose, GRAPE-6A boards (Fukushige et al., 2005) at the stellar Populations and Dynamics Research Group in Bonn. The black hole is mimicked by an (unsoftened) external $\frac{1}{r}$ potential which is directly implemented into the code. Particles which cross the capture radius are removed, while their masses are added to the mass of the black hole. To circumvent collisions between field particles, a small softening parameter $\epsilon = 10^{-4}$ is used. Additionally, some
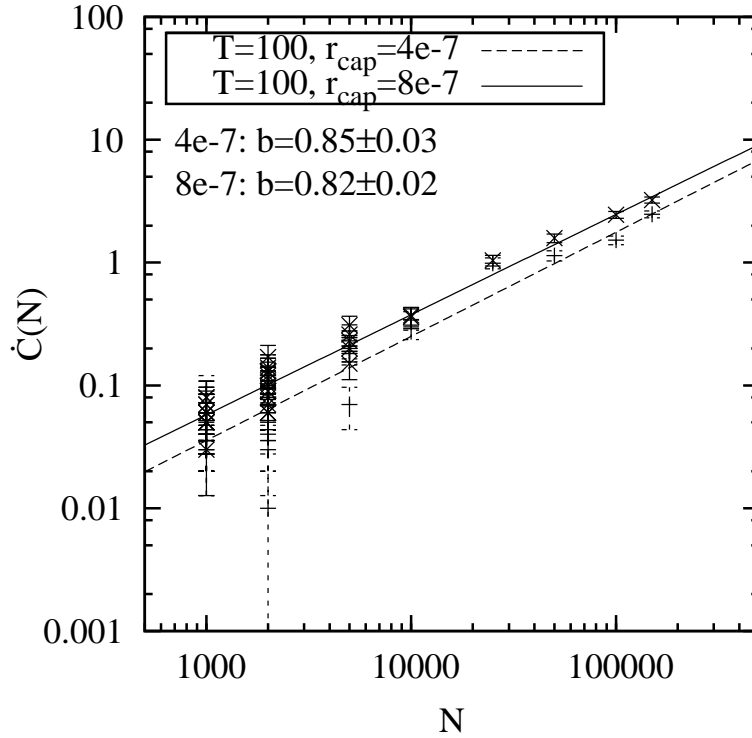
Figure 3.17. Results of the simulations with a fixed black hole. Strongly bound particles which needed to be removed artificially to prevent slow downs or a computational crash are not considered in the evaluation of the slope. Note the excellent agreement with the results obtained for the more realistic NBODY6 computations (Fig. 3.9).

strongly bound particles around the external potential are erased artificially (the number corresponds to roughly 30% of the total number of "true" capture events) in order to prevent gradual slow downs, large energy errors and/or the complete crash of the simulations. The energies of all removed particles are handled carefully to ensure a correct energy output. Due to these limitations and the much smaller sample of simulated models, the NBODY1 computations are not used for the extrapolation to realistic galaxies but only for a rough comparison to the much more advanced NBODY6 simulations. In Fig. 3.17 the results are plotted. Despite the large simplifications of the NBODY1 computations, the power-law index b of the capture rate, $\dot{C} \propto N^b$, agrees, within the statistical uncertainties, closely with the index obtained with the much more sophisticated NBODY6 simulations with free moving SMBHs. As a consequence a (strongly) wandering black hole particle does not bias the low N results in a way which would be dangerous when extrapolating these to astrophysical systems harboring many more stars than particles in our simulations. Of course this behaviour may change for initial black hole masses different from the one $M_{\bullet}(t = 0) = 0.01$ used in these computations.

3.6. Discussion

3.6.1. Scaling to Realistic Galaxies

The so-far presented results must be scaled to astrophysical systems in order to infer the rates at which stars are disrupted by central, supermassive black holes. From the following relation

$$\left.\frac{r_{\text{cap}}}{r_H}\right|_{\text{sim}} = \left.\frac{r_{\text{cap}}}{r_H}\right|_{\text{astro}}, \tag{3.55}$$

which must be necessarily fulfilled, the capture radii, r_{cap}, for the corresponding black holes of interest must be determined. In order to scale to astrophysical systems, we use the $M_\bullet - \sigma$ relation from Schulze & Gebhardt (2011),

$$\left(\frac{M_\bullet}{M_8}\right) = 1.51 \left(\frac{\sigma}{200\text{km s}^{-1}}\right)^{4.32}, \tag{3.56}$$

and the expression for the radius of influence,

$$r_H = \frac{GM_\bullet}{\sigma^2}, \tag{3.57}$$

to calculate r_H for a SMBH of given mass,

$$r_H \approx 13.1 \left(\frac{M_\bullet}{M_8}\right)^{0.54} \text{[pc]}. \tag{3.58}$$

Here M_8 corresponds to $10^8 M_\odot$ and for reasons of computational feasibility we neglected the intrinsic scatter of the $M_\bullet - \sigma$ relation. This is useful when dealing with averaged quantities like the impact of stellar disruptions for the growth history of the majority of SMBHs. Some studies may instead be interested in individual systems and the extrapolation formalism can easily be replaced by direct measurements of $M_\bullet, r_H$ and σ instead of using the values from the $M_\bullet - \sigma$ relation. This also holds for the choice of the relevant tidal disruption radius,

$$r_{\text{cap}} = g r_\star \left(\frac{M_\bullet}{M_\star}\right)^{\frac{1}{3}}, \tag{3.59}$$

where g is a parameter depending on the stellar polytrope, mass, spin of the SMBH and trajectory of the star. Black holes below $10^7 M_\odot$ and solar like stars are well approximated by $g \approx 1$ (Kochanek, 1992).

The relevant astrophysical timescale is obtained through the computation of the crossing time $t_{\text{cr}}(r_H) = \frac{2r_H}{\sigma(r_H)}$ at the influence radius r_H of the black hole in comparison with that of our numerical integrations. The number of disruption events within the given timescale is obtained from the derived capture rate [22] $\dot{C}(N, r_{\text{cap}}^{\text{sim}}) = a(r_{\text{cap}}^{\text{sim}})N^b$.

---

[22]The capture rates $\dot{C}(N)$ from the numerical computations are normalized to one N-body time unit and must be scaled down to one crossing time-scale at the influence radius in order to become synchronized with the astrophysical timescale t_{cross}.

Here N refers to the total number of (real) stars with the averaged mass $M_\star$ in the bulge component or whole elliptical galaxy. It is assumed to be $N = \frac{100M_\bullet}{M_\star}$ in accordance with our numerical integrations, whereas $a(r_{\rm cap}^{\rm sim})$ is extrapolated to the black hole mass of interest by using the $T = 100$ values for the parameters a[23]. The parameter b is assumed to be unrelated to the capture radius and is hence taken to be constant at $b = 0.83 \pm 0.01$. In fact Eq. 3.48 predicts the slope parameter b to be unrelated to the capture radius. Nevertheless a minor change in b towards smaller vales of $r_{\rm cap}^{\rm sim}$ cannot be rejected given the b values of Table 3.1 at $T = 100$. This might be explained by a combination of timing issues, simplified assumptions of our analytical approach or is purely statistical in nature. Therefore, the parameter b is extrapolated (by linear and power-law regressions) down to the required values of $r_{\rm cap}^{\rm sim}$ in order to test its impact on the capture rates. The impact is found to be moderate because $r_{\rm cap}^{\rm sim}$ has to be extrapolated down to $r_{\rm cap}^{\rm sim} = (0.06 - 0.07) \cdot 10^{-7}$ (depending on the used $M_\bullet - \sigma$-relation) for the largest black hole with $10^7 M_\odot$. While the capture rate would be unaffected for the least-massive black holes, it would drop by a factor of 2 for the most-massive ones. Increasing uncertainties of these values due to the propagation of error analysis strongly overlaps with those of fixed b. For the purposes of this study we therefore assume the parameter b to be independent of $r_{\rm cap}^{\rm sim}$ and refer the reader to § 3.7 for a more critical discussion on that topic as well as of the improvements left for future work.

Finally for an individual galactic nucleus hosting a SMBH of mass $M_\bullet$, with a radius of influence r_H, velocity dispersion $\sigma(r = r_H)$, capture radius $r_{\rm cap}$ and a stellar population with the mean mass $M_\star$, a very general expression for the capture rate inferred from the numerical integration can be obtained by applying Eq. 3.57:

$$\dot{C}_{\rm astro} = 0.00061 \left(\frac{M_\bullet}{M_\star} \right)^{0.95} r_H^{-1.36} r_\star^{0.36} g^{0.36} \sigma \tag{3.60}$$

The validity of Eq. 3.60 covers the parameter range of IMBHs as well as SMBHs up to $M_\bullet \approx 10^7 \, M_\odot$. In the following section we explicitly make use of the $M_\bullet - \sigma$ relation and assume only solar like stars as well as $g = 1$.

3.6.2. Disruption Rates of IMBHs & SMBHs

By applying the extrapolation formalism from section §3.6.1, the integrations yield the following expression for the capture rate of real astrophysical galaxies:

$$\dot{C}(M_\bullet) = 6.29 \cdot 10^{-8} \left(\frac{M_\bullet}{M_\odot} \right)^{0.45} \left[{\rm yr}^{-1} \right]. \tag{3.61}$$

For comparison the results are also extrapolated according to an older version of the $M_\bullet - \sigma$ relation from Ferrarese & Ford (2005) to illustrate the dependence of the capture

---

[23] At least three different capture radii must be simulated to allow for non linear extrapolation of the parameter $a(r_{\rm cap}^{\rm sim})$. This is required for the extrapolation to different black hole sizes/masses.

rate on systematic black hole mass determinations:

$$\dot{C}(M_\bullet) = 3.54 \cdot 10^{-7} \left(\frac{M_\bullet}{M_\odot} \right)^{0.35} \left[\text{yr}^{-1} \right].\tag{3.62}$$

These results holds for nonrotating isotropic galaxies or globular clusters with cuspy inner density profiles $\rho(r) \propto r^\alpha$, where the density power-law index is $\alpha \approx -1.5$. Eq. 3.61 and 3.62 should not be applied to black holes with masses larger than $10^7 M_\odot$. The uncertainties correspond to about 50% of the values (see Table 3.2). The interested reader is referred to Appendix B for a much more detailed description of how the numerical results are extrapolated to realistic galaxies. The astrophysical disruption rates of stars (including the statistical uncertainties) for some exemplary black holes are summarized in Table 3.2. We also calculate the disruption rates for IMBHs in order to compare them with previous simulations (Baumgardt et al., 2004a).

The expected number of tidal disruption events in galactic nuclei containing black holes of 10^6 to $10^7 M_\odot$ inferred from the numerical integrations are in good agreement with recent optical based surveys (van Velzen et al., 2011)[24]. While their study yields the rate for tidal flares per galaxy to be $\dot{C} = 3\left(^{+4}_{-2}\right) \cdot 10^{-5} \text{yr}^{-1}$, the results obtained from the present simulations give $\dot{C} = 3.0(\pm 1.4) - 8.3(\pm 4.2) \cdot 10^{-5} \text{yr}^{-1}$ for black holes in the mass range 10^6 to $10^7 M_\odot$.

The simulations also offer some clues about the growth of IMBHs and SMBHs in the lower mass range. We observe only a modest impact of the black hole mass on the capture rate. For a mass range over four orders of magnitude, the capture rate increases only by a factor 25-60 depending on the used scaling relation. The relaxation driven growth of massive black holes by stellar disruptions is thus only important for IMBHs and SMBHs up to several $10^5 M_\odot$. IMBHs should easily double their mass within a few Gyr in perfect agreement with earlier studies (Baumgardt et al., 2004a). More massive black holes must have grown by different processes rather than the relaxation driven infall of stars, in good agreement with the findings of Yu & Tremaine (2002) and gas accretion and feedback models (Silk & Rees, 1998; Fabian, 1999; Murray et al., 2005)[25].

Our findings exclude any relevance for establishing the $M_\bullet - \sigma$ relation from stellar disruptions in density profiles similar to those of the simulations. This is due to the relatively small capture rate and hence large doubling times ($T_{2D} > H_0^{-1}$) for black holes more massive than $10^6 M_\odot$. If for example the initial mass of a SMBH is strongly under-massive with respect to the $M_\bullet - \sigma$ relation, the feeding from tidal disruptions events alone might not be sufficient enough to bring it close to the observed relation for galaxies at $z \approx 0$. On the other hand if stellar disruptions dominate the growth of the least-massive black holes there is no obvious reason why these black holes should follow the $M_\bullet - \sigma$ relation. By now assuming the $M_\bullet - \sigma$ relation to be established for a primordial gas rich globular cluster (or galactic nucleus), which nowadays remains in isolation and without gas to drive new star formation, the resulting IMBH (or SMBH,

---

[24] ArXiv Version V1 for actual TD rate.

[25] The growth of the very early population of SMBHs may also be dominated by stellar disruptions in isothermal cusps (Zhao et al., 2002). See the information in the text below.

Schulze & Gebhardt (2011)			
$M_\bullet(10^6 M_\odot)$	$\dot{C}(10^{-5} yr^{-1})$	$T_{2D}(H_0^{-1})$	$\bar{L}(erg s^{-1})$
0.001	0.14 ± 0.06	0.11 ± 0.05	$3.9 \pm 1.7 \cdot 10^{39}$
0.01	0.38 ± 0.17	0.39 ± 0.18	$1.1 \pm 0.5 \cdot 10^{40}$
0.05	0.8 ± 0.4	0.9 ± 0.4	$2.2 \pm 1.0 \cdot 10^{40}$
0.1	1.1 ± 0.5	1.4 ± 0.7	$3.0 \pm 1.4 \cdot 10^{40}$
0.25	1.6 ± 0.8	2.3 ± 1.1	$4.5 \pm 2.2 \cdot 10^{40}$
0.5	2.2 ± 1.0	3.4 ± 1.6	$6.2 \pm 3.0 \cdot 10^{40}$
1	3.0 ± 1.4	4.9 ± 2.4	$8.4 \pm 4.1 \cdot 10^{40}$
2	4.0 ± 2.0	7.3 ± 3.6	$1.1 \pm 0.6 \cdot 10^{41}$
4	5.5 ± 2.7	11 ± 5	$1.6 \pm 0.8 \cdot 10^{41}$
10	8.3 ± 4.2	18 ± 9	$2.4 \pm 1.2 \cdot 10^{41}$

Ferrarese & Ford (2005)			
$M_\bullet(10^6 M_\odot)$	$\dot{C}(10^{-5} yr^{-1})$	$T_{2D}(H_0^{-1})$	$\bar{L}(erg s^{-1})$
0.001	0.40 ± 0.17	0.04 ± 0.02	$1.1 \pm 0.5 \cdot 10^{40}$
0.01	0.90 ± 0.40	0.16 ± 0.07	$2.6 \pm 1.2 \cdot 10^{40}$
0.05	1.6 ± 0.7	0.46 ± 0.21	$4.5 \pm 2.1 \cdot 10^{40}$
0.1	2.0 ± 0.9	0.72 ± 0.34	$5.8 \pm 2.7 \cdot 10^{40}$
0.25	2.8 ± 1.3	1.3 ± 0.6	$8.0 \pm 3.8 \cdot 10^{40}$
0.5	3.6 ± 1.7	2.0 ± 1.0	$1.0 \pm 0.5 \cdot 10^{41}$
1	4.6 ± 2.2	3.2 ± 1.5	$1.3 \pm 0.6 \cdot 10^{41}$
2	5.8 ± 2.8	5.0 ± 2.5	$1.7 \pm 0.8 \cdot 10^{41}$
4	7.4 ± 3.7	7.9 ± 3.9	$2.1 \pm 1.0 \cdot 10^{41}$
10	10.3 ± 5.2	14 ± 7	$2.9 \pm 1.5 \cdot 10^{41}$

Table 3.2. The expected number of stellar disruption events $\dot{C}$ for solar like stars by supermassive black holes up to $M_\bullet \leq 10^7 M_\odot$. For comparison our numerical results are extrapolated according to an older version of the $M_\bullet - \sigma$-relation (Ferrarese & Ford, 2005) and the most recent one (Schulze & Gebhardt, 2011). Within a factor of two they agree with each other. T_{2D} is the time needed to double the initial mass of the black hole in units of the Hubble time H_0^{-1}. Only one half of the stellar mass is assumed to become accreted by the black hole (Rees, 1988). Finally the time averaged mean luminosity $\bar{L} = 0.5\epsilon \dot{C} M_\odot c^2$ of these black holes is calculated by assuming the efficiency parameter of matter to energy conversion to be $\epsilon = 0.1$. The motivation behind is to compare these energies with potentially detectable left overs of relativistic outflows which may become deposited into the surrounding medium after tidal disruption events (Crocker & Aharonian, 2011; van Velzen et al., 2011). However the deposited energy strongly depends on the formation rate of relativistic jet outflows and may be significantly overestimated by us (Bower, 2011). Nevertheless these deposited energies might be relevant for studies aiming to make a robust detection of dark matter annihilation signals in galactic bulges, dwarf galaxies or globular clusters hosting a central black hole. These results have relevance for galaxies with cuspy density profiles with slope parameters $\alpha \approx -1.5$ within the inner most few pc.

at least if it is not too massive) should nowadays be more massive than expected from the $M_\bullet - \sigma$ relation due to subsequent tidal disruption events. It is very tempting to connect these results to the case of ω-Centauri (Noyola et al., 2010). Tidal disruption events might therefore have implications for the search and existence of IMBHs in globular clusters. Of course in order to proof its relevance for IMBHs, the use of the $M_\bullet - \sigma$ relation in the extrapolation formalism from numerical simulations to galactic

nuclei (Appendix B) must be replaced by more direct observational data because the extrapolated values strongly depend on the validity of this scaling relation. Tidal disruption events complicate the understanding of the relevant processes which drive the evolution of galaxies and their central black holes. Especially as the impact of disruption events for the mass growth of black holes strongly depends on their initial mass.

In spite of this it might be interesting to relate these findings to a recent study Kormendy et al. (2011) in which observational evidence for secular growth processes of black holes in disks and pseudobulges is found. The capture rate for rotation-supported models like rotating bulges or pseudo bulges should be enhanced compared to nonrotating models. These objects are expected to form from rotating bar instabilities (Kormendy & Kennicutt, 2004) and the relative velocities between two or more particles are generally lower. Therefore, two-body relaxation processes would be even stronger.

However the overall picture of black hole growth across cosmic times by tidal disruptions might be complicated even more due to the dynamical evolution of the density profile and a variable fraction of the initial stellar mass which finally becomes accreted by the black hole. Our conclusions regarding the growth history of IMBHs and SMBHs events should only hold for density profiles resembling those of our simulations and by assuming that a fraction of one half (or more) of the initial stellar mass becomes accreted by the black hole (Rees, 1988). In fact some effects can considerably reduce this fraction and complicate the efforts to estimate the significance of tidal disruption events for the overall growth history of black holes. Recent hydrodynamical simulations suggest that for loss cone stars on nearly parabolic orbits, most of the stellar matter is ejected within the first orbit and then later on due to powerful shocks which may be energetic enough to ignite thermonuclear reactions unbinding large amounts of stellar mass (Brassart & Luminet, 2008; Guillochon et al., 2009). Secondly and especially relevant for black holes in the lower mass range, accretion luminosities far in excess of the Eddington limit (Strubbe & Quataert, 2011) may blow away most of the remaining gas. In the end the growth of these black holes due to tidal disruption events may be insignificant even for very large capture rates of several events per 10^6yr.

3.7. Critical Discussion and Outlook for Future Work

To the best of our knowledge this study reports for the first time the expected tidal disruption rate of stars by SMBHs up to $10^7 M_\odot$ obtained by direct *N*-body integrations. *N*-body computations offer a large amount of advantages over analytical studies. They can handle several physical effects simultaneously while most analytical studies are forced to simplify at least some of the dynamics. On the other hand direct *N*-body integrations aiming to infer astrophysically relevant numbers of stellar disruption events are confronted by their own limitations and difficulties. In this section we will critically review limitations of our own simulations as well as improvements and ideas left for future work.

1. In Table 3.2 we calculate among other values the required timescale T_{2D} for doubling the mass of a black hole of given initial mass. This timescales is computed from the total number of captures averaged over 100 N-body time units (see Table 3.1). We recommend the reader to regard the doubling time T_{2D} only as some reference guide. When expressed in physical time, our simulations last only a fraction of one H_0^{-1} (between several 10^7 and one 10^9 years) and may not represent much longer time episodes. Moreover, we assumed one half of the disrupted star to be accreted by the black hole. There exist two effects that can reduce the amount of stellar matter which finally becomes swallowed by the black hole. First, if the tidal stripping occurs from a nearly parabolic orbit, hydrodynamical simulations suggest one half of its mass to be lost within its first path (Guillochon et al., 2009) and large quantities of the remaining mass to be blown away by shocks and thermonuclear reactions later on (Brassart & Luminet, 2008). Second, very small black holes might temporarily generate luminosities far in excess of the Eddington limit (Strubbe & Quataert, 2011) and most of the remaining matter may finally be blown away instead of being swallowed by the black hole. This would invalidate our conclusions regarding the growth history of small black holes where we assumed one half of the stellar mass to be accreted. Nevertheless the inferred capture rate should be valid for all galaxies or stellar clusters with density profiles comparable to our simulated ones.

2. With current generations of GPUs it is unthinkable to simulate galaxy models with realistic numbers of stars with direct N-body integration methods. The only way to obtain stellar disruption rates for SMBHs in the centers of galaxies is to simulate as many models as possible to infer all relevant N-dependent systematics affecting this rate. Afterwards, the results can be extrapolated. However it is important not to do this for only one given black hole capture radius but for many black hole configurations. Therefore, all these simulations must be repeated for several capture radii r_{cap}^{sim} in order to extrapolate them according to the formalism in § 3.6.1 to the black hole of interest. We calculate the capture rate for black hole masses in the range $10^{3-7}\,M_\odot$. Due to the highly nonlinear Eq. 3.56 we had to extrapolate parameter r_{cap}^{sim} from Table 3.1 down to $r_{cap}^{sim} \approx 0.07 \cdot 10^{-7}$. The usage of three different black hole capture radii is thus the minimal requirement to obtain useful values under the assumption that the parameter $a(r_{cap}^{sim})$ from Eq. 3.53 follows a power-law distribution[26] with positive parameters and no offset.

There is no question that future studies must redo these simulations for different capture radii to constrain $a(r_{cap}^{sim})$ even more precisely. However this is a very time consuming task. The complete set of our Sérsic $n = 4$ simulations took more than seven months to compute on five modern GPUs. Despite the large amount of needed computing power, direct integration methods like NBODY6 may exceed their limitations when the capture radius falls significantly below 10^{-7} in N-body units, especially if the mass of the black hole particle is of the

---

[26]$a(r_{cap}^{sim})$ is specified in Eq. B.3.

order of one percent or more of the total mass[27]. In addition to that the statistics may worsen (due to a limited number of capture events) and must be balanced by even more simulations.

In our computations no severe $r_{\text{cap}}^{\text{sim}}$ dependence of the parameter b is evident, in accordance with theoretical considerations (Eq. 3.48 & 3.50)[28]. Therefore, we assumed it to be constant. However we cannot exclude per se any deviation at very small capture radii. A systematic decrease in the parameter b for even smaller values of $r_{\text{cap}}^{\text{sim}}$ would only reduce the tidal disruption events of the more massive SMBHs in our sample. We plan to tackle this problem as well as to constrain the parameters $a(r_{\text{cap}}^{\text{sim}})$ and b even more precisely in the future.

3. In this study effects from general relativity are neglected. The relevant tidal disruption radius of a SMBH for solar like stars is several times larger than its Schwarzschild radius and relativistic effects should become strongly suppressed for radii $r \gg r_s$. This makes our assumption of neglecting GR credible. Nevertheless a fully relativistic treatment of a black hole potential yields a deeper gravitational potential than a purely Newtonian one, thus being more attractive for compact bodies like stars to be captured by the SMBH. On the other hand particle scattering by a relativistic potential may result in stronger deflection, perhaps powerful enough to reject some stars from the immediate vicinity of the black hole thereby decreasing the capture rate. The next generation of N-body integrators is expected to be sophisticated enough to address these aspects (Aarseth, 2007).

   Kerr black holes, i,e, rotating spacetimes with angular momentum, $J_\bullet$, should be taken into account as well. Depending on their spin parameters, $j = \frac{J_\bullet}{M_\bullet}$, as well as the trajectories of stars, the likelihood for a capture event is not equally distributed as the Kerr-metric is not invariant under angular coordinate transformation. A Kerr black hole inside a nonrotating (pressure-supported) stellar distribution might lose angular momentum. This effect might lower the spin parameter over time.

4. A crucial quantity for extrapolating our numerical results to astrophysical systems is the black hole radius of influence r_H. For its evaluation we use the kinematic determination (Appendix B). We observe this radius to be roughly five to six times smaller than the dynamical radius r_g. This is the radius at which the mass in stars/particles equals the mass of the black hole. If interested readers plan to rescale our models by replacing the $M_\bullet - \sigma$ relation by directly measured data of r_H for some galaxies, it is very important that they also use the same influence radii as the ones used in our simulations and not the dynamical radii.

5. The capture rate from our numerical results should not be applied to SMBHs above $10^7 M_\odot$. The refill of the loss cone takes a timespan of the order $T_{\text{refill}} \approx$

---

[27]Private communication with Sverre Aarseth.

[28]According to the theory of angular momentum diffusion, parameter b only depend on the slope parameter of the density profile.

$\theta_{lc}^2 T_{rel}$. The refill of the loss cone is much faster in N-body integrations than in nature, since the potentials are more cuspy and relaxation times are shorter than in reality. Therefore, our simulations have only relevance for galactic nuclei where the loss cone refilling times are much shorter than H_0^{-1}. For black holes significantly more massive than $10^7 M_\odot$, i.e. with very large particle numbers and very smooth potentials, the critical radius exceeds the size of the influence radius and Eq. 3.48 has to be replaced by Eq. 3.50. The latter one predicts a different behavior for $\dot{C}(N)$ such that the numerically found capture rate should not be extrapolated to black holes in excess of $10^7 M_\odot$. By inserting the relevant values from or computational findings to the systems of interest, Eq. 3.48 predicts the critical radius not to exceed the influence radius for black holes less massive than $10^7 M_\odot$, thus showing our simulations to be governed by processes $r_{crit} < r_H$.

6. One could even criticize the black hole mass $M_\bullet(t = 0) = 0.01$ used for our numerical computations to be too high as the black hole mass fraction in realistic galaxies is a factor of a few smaller (Magorrian et al., 1998). Nevertheless most of the relevant dynamics happens at distances of the order of the influence radius r_H whereas we use the radius of influence for the extrapolation to realistic galaxies. The choice of $M_\bullet(t = 0) = 0.01$ is therefore not expected to change the capture rate significantly. In this context the usage of different capture radii instead of different initial masses $M_\bullet(t = 0)$ for the extrapolation to the wide set of astrophysical SMBHs should be justified, too. The strict relation between mass and capture radius of a black hole enables variation of the latter one while keeping the former one constant in the scale-free N-body simulations. The great advantage of this strategy is given in equal black hole influence radii, crossing times, cusp formation timescales etc. simplifying the extrapolation formalism considerably. The same holds true for the overall Sérsic $n = 4$ profiles. Not every outer bulge component or elliptical galaxy profile resembles that of a Sérsic $n = 4$ i.e. de Vaucouleurs profile. Mostly relevant for the direct number of capture events is the density profile close to r_H. For relaxation times smaller than one H_0^{-1} the formation of a cusp (up to $\alpha = -1.75$) is expected. Such a gradual change of the density profile is also found in the numerical simulations. Hence our simulations cover a large space of isotropic, nonrotating density profiles for black hole masses up to $10^7 M_\odot$.

7. We only treat single-mass systems while galactic cores are known to be multiple-mass systems featuring additional processes like mass segregation, star formation, binary evolution, torques from anisotropic matter distributions, resonances etc. Stellar remnants like neutron stars would not be disrupted outside the event horizon and could probe much deeper potentials than solar like stars, thus complicating the gravitational dynamics and making relativistic correction terms inescapable. They would also disappear without any visible counterpart when finally captured.

8. Finally our numerical simulations should only be regarded as a first (very) limited approach to a systematical scan of capture rates in galaxies. It would be important to extent these studies by simulating the same models for even

smaller capture radii r_{text} and longer timescales in order to reduce the need of extrapolation. It would be important to take into account rotating and triaxial stellar density profiles around the SMBH and to decrease the still rather large uncertainties. Direct N-body simulations of isothermal $\rho(r) = \frac{\sigma^2}{2\pi G r^2}$ spheres, which might represent the initial phases of elliptical galaxies and bulges best, should be performed as well. Zhao et al. (2002) found evidence for strong black hole growth in isothermal cusps. By assuming $r_{\text{cap}} \propto r_s = \frac{2GM_\bullet}{c^2}$, rewriting Eq. 3.47 to $\dot{C}(r) \propto \rho(r) r^2 \sigma \theta_{lc}^2$ by using $r_H = \frac{GM_\bullet}{\sigma^2}$ and $\theta_{lc}^2 = \frac{2r_{\text{cap}} r_H}{r^2}$ for very massive SMBHs, one obtains $\dot{C}(r) \propto \frac{\sigma^5}{Gc^2} \cdot \left(\frac{r_H}{r}\right)^2$. Under the assumption that the capture rate is dominated by stars from r_H, the r dependence cancels out and the final mass of the black hole is $M_\bullet(t_f) = \int_{t=0}^{t=t_f} \dot{C}(r = r_H) \mathrm{d}t \approx 10^8 \mathrm{M}_\odot \cdot \left(\frac{\sigma}{200\mathrm{kms}^{-1}}\right)^5 \left(\frac{t_f}{H_0^{-1}}\right)$. This relation is indeed in very close agreement to the observed $M_\bullet - \sigma$ relation (Zhao et al., 2002). Therefore, stellar captures might contribute significantly to the growth of SMBHs in the past, especially if the loss cone refill is enhanced by mergers and/or triaxial stellar distributions.

Despite some of the details stated above, the here reported simulations represent (the first) systematic estimate for the capture rate by SMBHs of stars in galaxies with cuspy inner density profiles. This work should be followed up by simulating different capture radii $r_{\text{cap}}^{\text{sim}}$ as well as density profiles, taking relativistic correction terms into account, and by trying to find ways to infer the numbers of disruption/capture events for SMBHs with mass $> 10^7 \, \mathrm{M}_\odot$.

3.8. Conclusion

We performed direct N-body simulations to obtain the number of disruption events of stars by SMBHs which are presumed to exist in the centers of most galaxies. A modified NBODY6 code was used. All computations were processed by several GPUs over several months integration time. The initial density profiles of the models were chosen to follow nonrotating isotropic Sérsic $n = 4$ profiles. We calculated numerous models with different particle numbers but otherwise equal physical parameters in order to ensure good statistics. This is required because all systematic effects depending on the total number of particles must be specified in order to extrapolate the simulations to realistic galaxies by using the formalism presented in § 3.6.1. The rates at which stars are captured are found to be nearly independent of the mass of the black hole. Thus only the growth over cosmic times of IMBHs and of the least massive SMBHs may be dominated by stellar disruptions. The expected tidal disruption rate is a few events every 10^5 years per galaxy for black holes in the mass range up to $10^7 \, \mathrm{M}_\odot$. The feeding by stars from density profiles similar to the ones computed here bears no implications for establishing scaling relations between very massive black holes and their host galaxies. This is in agreement with conventional gas accretion/feedback models. On the other hand the growth history of the least massive black holes might be governed by more than one feeding mode (gas and star accretion). This might have implications for the search and existence of potential IMBHs in globular clusters and minor galaxies. As-

suming these scaling relations (e.g. the $M_\bullet - \sigma$ relation) to be established shortly after their primordial gas rich phase billions of years ago, the nuclear black holes would continue their growth by the subsequent disruption of stars. Depending on the initial conditions, the black hole masses could nowadays lie well above the predicted values of the $M_\bullet - \sigma$ relation as long as the globular cluster remains in isolation[29]. On the other hand the continuous monitoring and search for tidal disruption events in globular clusters (e.g. in the Virgo Cluster) should constrain the fraction of those clusters hosting a central IMBH. By assuming 25000 globular clusters with a central black hole in the mass range $M_\bullet = 10^3 - 10^4 M_\odot$ in the Virgo Cluster of galaxies, there should be one disruption event every $10 - 25$ years. Finally the performed computations indicate that the growth history of IMBHs and low mass SMBHs is diverse and not only governed by one process, i.e. gas accretion. However it needs to be pointed out that there exist effects which might reduce the fraction of stellar matter which finally becomes accreted by the black hole. We assumed one half of a captured star's mass to be swallowed (Rees, 1988), whereas a smaller fraction would result in even slower growth rates. Thus our conclusions regarding the growth history may change if small black holes gather only tiny fractions of the total initial stellar mass. Future studies can use the reported capture rate $\dot{C}(M_\bullet)$ to deduce more realistic growth rates $\dot{M}(M_\bullet)$ by taking more appropriate values for the fraction of accreted matter into account. It would also be interesting to extend these studies to the most-massive black holes as well as constraining the capture rate for different profiles.

---

[29]The relevant velocity dispersion σ should therefore not increase.

Chapter 4

Erosion of Globular Cluster Systems by SMBHs

Globular clusters belong to the oldest fossils of galaxies. The origin of the empirical linear relationship between the number of globular clusters and the mass of the central black hole (§ 2.1.3) is under debate. It is even not clear to what degree globular clusters or more generally star clusters influenced the growth of SMBHs. Vice versa one could ask the question to what degree the globular cluster distribution is influenced by the presence of a central SMBH. In this Chapter 4 which is based on Brockamp et al. (2014), I describe a new computer program that was designed to answer some of these questions[30]. It is named MUESLI, which stands for Multi-Purpose Elliptical Galaxy SCF + Time-Transformed Leapfrog Integrator. Like a real muesli, it consists of several well chosen ingredients which can easily be replaced, modified, omitted or added. The integral components of this software were developed in collaboration with Andreas Küpper, Ingo Thies, Holger Baumgardt and Pavel Kroupa. Inasmuch as erosion processes of GCs are complex and do not only depend on the presence of a central SMBH, all relevant internal and external effects (e.g. stellar evolution, relaxation and dynamical friction) were incorporated into the software. By applying MUESLI to a representative sample of elliptical galaxies, it is found that the GC number density profiles are centrally flattened in less than a Hubble time. In addition to that I discovered that by using different threshold mass/luminosity scales in observations of the GC number density profile, the erosion based flattening scenario can be directly tested. The inferred erosion rate depends primarily on a galaxy's mass, half-mass radius (i.e. its averaged density) and the initial velocity distribution. Ultimately, the absence of GCs around M 32 could be explained and entirely new phenomena like the *tidal disruption dominated phase* have been uncovered.

   Chapter 4 is based on Brockamp et al. (2014). Compared with Brockamp et al. (2014) two modifications were made: (i) The abstract has been removed and (ii) the appendix is implemented as a new section into this chapter. Finally, I would like to mention that primary software testing, the development of analysis tools as well as programs required for model generation were the most time intensive part of this PhD study.

---

[30]This chapter has been published, apart from minor changes which are described in the text, in the
   MNRAS journal (Vol. 441, pp. 150-171).

However, only a small fraction of all the performed software tests, namely those which are of scientific interest, are documented in this thesis. Moreover, a detailed description of two essential parts of the MUESLI software, namely the SCF and the TTL integration method are described in the Appendices A.2 and A.3.

4.1. Introduction

Globular clusters (GCs) are among the oldest objects in galaxies. They can provide a wealth of information on the formation and evolution histories of their host galaxies as well as on cosmological structure formation (Searle & Zinn, 1978; Marks & Kroupa, 2010; Harris et al., 2013). This paper is a first step in connecting and understanding properties of GC systems, their host galaxies and their central supermassive black holes.

Surveys of elliptical galaxies show radial GC profiles to be less concentrated when compared to the galactic stellar light profiles (Harris & Racine 1979; Forbes et al. 1996; McLaughlin 1999; Capuzzo-Dolcetta & Mastrobuono-Battisti 2009 and references therein). An impressive example is the 10 kpc core in the spatial distribution of GCs in NGC 4874, one of the two dominant elliptical galaxies inside the Coma cluster (Peng et al., 2011). Two competing scenarios attempt to explain these cored distributions. In one scenario, the core originated from processes operating at the onset of galaxy formation in the very early universe (Harris, 1986, 1993). The other scenario assumes that GCs were formed co-evally with the field stars with a cuspy distribution, i.e. comparable to the galactic stellar light profile. In this second scenario, the observed cores in the GC distributions are caused by the subsequent erosion and destruction of globular clusters in the nucleus of the galaxy itself (Capuzzo-Dolcetta, 1993; Baumgardt, 1998; Vesperini, 2000; Vesperini et al., 2003). It is this scenario we would like to shed light on with this study.

However, taking all the relevant processes that affect the GC erosion rates in elliptical galaxies into account is numerically challenging. This is due to the fact that there are several internal and external processes acting simultaneously on the dissolution of globular clusters, such as two-body relaxation, stellar mass loss and tidal shocks (Gnedin & Ostriker, 1997; Vesperini & Heggie, 1997; Fall & Zhang, 2001; Baumgardt & Makino, 2003; Gieles et al., 2006). In this study, we present a new code named MUESLI to investigate several processes that dominate cluster erosion: (i) tidal shocks on eccentric GC orbits and relaxation driven dissolution, and their dependence on the anisotropy profile of the GC population, (ii) tidal destruction of GCs due to a central super-massive black hole (iii) stellar evolution and (iv) orbital decay through dynamical friction. That is:

(i) GCs lose mass when stars get beyond the limiting Jacobi radius, r_J, and become unbound to the cluster. Two-body relaxation will cause any GC to dissolve with time. The dissolution time depends on the mass and extent of the GC as well as the strength of the tidal field (Baumgardt & Makino, 2003). GCs on very eccentric orbits are particularly susceptible for disintegration within a few orbits owing to the strong tidal

forces near the galactic center. In radially biased velocity distributions, large fractions of orbits are occupied by such eccentric, i.e. low angular momentum orbits, and the overall destruction rate of globular clusters is strongly enhanced over the isotropic case. The same holds for triaxial galaxies when GCs move on box orbits (Ostriker et al., 1989; Capuzzo-Dolcetta & Tesseri, 1997; Capuzzo-Dolcetta & Vicari, 2005).

(ii) The gradient of the potential which is relevant for the destruction of GCs is increased by the presence of supermassive black holes. SMBHs are commonly found in the cores of luminous galaxies (Magorrian et al., 1998; Lauer et al., 2007) and the connection between SMBHs and globular clusters is of particular interest. Burkert & Tremaine (2010) and Harris & Harris (2011) found empirical relations between the total number of GCs and the mass of the central black hole. The origin of this linear $M_\bullet - N_{GC}$ relation is under debate. See Harris et al. (2014) for a most recent version of the $M_\bullet - N_{GC}$ relation and comparison to other globular cluster/host galaxy relations. There is some evidence that $M_\bullet$ and N_{GC} are indirectly coupled over the properties of their host galaxies (Rhode, 2012), however a direct causal link cannot be ruled out owing to the difficulty of studying the growth of SMBHs from accreted cluster debris.

(iii) Another effect is mass loss by stellar evolution (SEV). SEV decreases the globular cluster mass most significantly during an initial phase of roughly 100 Myr. In this period, O and B stars lose most of their mass through stellar winds and supernovae (e.g. de Boer & Seggewiss 2008). Over a Hubble time, a stellar population loses about 30-40% of its mass due to stellar evolution (Baumgardt & Makino, 2003).

(iv) Finally, massive objects like globular clusters lose energy and angular momentum due to dynamical friction (DF) when migrating through an entity of background particles. GCs will gradually approach the center of the galaxy where they are destroyed efficiently as described above. In low-luminosity spheroids ($L \approx 10^{10} L_\odot$), decaying GCs might also merge together and contribute to the growth of nuclear star clusters (Tremaine et al., 1975; Agarwal & Milosavljević, 2011; Antonini, 2013; Gnedin et al., 2014). Among other quantities, the efficiency of DF depends on the departure of the host galaxy from spherical symmetry (Peñarrubia et al., 2004), and becomes largest for low angular momentum orbits (Pesce et al., 1992; Capuzzo-Dolcetta & Vicari, 2005).

Like a real muesli, our Multi-Purpose Elliptical Galaxy SCF + Time-Transformed Leapfrog Integrator (MUESLI) consists of several well-chosen ingredients. MUESLI has a high flexibility and is designed for computing GC orbits and erosion rates in live galaxies. It can handle spherical, axisymmetric and triaxial galaxies with arbitrary density profiles, velocity distributions and central SMBH masses for which no analytical distribution functions exist. Since the potential of the galaxy is computed self-consistently, the code can handle time evolving potentials due to e.g. the interaction of the galaxy and a central black hole (Merritt & Quinlan, 1998) or even non-virialized structures.

MUESLI is designed to constrain the field-star and GC formation efficiencies in the early universe. This can be done by relating the computational outcomes with observations of the GC specific frequency, S_N, which is the number of observed globular clusters normalized to total mass/luminosity of the host galaxy (Georgiev et al., 2010; Harris et al., 2013; Wu & Kroupa, 2013). The U-shaped S_N distribution, being highest for the least massive and most massive galaxies, traces the impact of feedback processes operating in different galactic environments. However, the quantitative examination of these processes requires knowledge about the total fraction of GCs eroded over time.

In this first paper, we provide detailed information about the code and about N-body model generation, and we show results from the code testing. We apply our code to erosion processes of GCs inside spherical galaxies with Hernquist and Sérsic profiles, isotropic and radially biased velocity distributions and central SMBHs. This is done for four representative galaxies. These galaxies cover a wide range of masses ($M_{\mathrm{GAL}} \approx 10^9 - 10^{12} \mathrm{M}_\odot$), sizes ($R_e \approx 10^2 - 10^4 \mathrm{pc}$) and central SMBH masses ($M_\bullet \approx 10^6 - 10^{10} \mathrm{M}_\odot$). Erosion rates in axisymmetric and triaxial galaxies, as well as nuclear star cluster and SMBH growth processes by cluster debris are reserved for later publications.

The present paper is organized as follows. The MUESLI code and the dynamics governing globular cluster dissolution and disruption processes are specified in § 4.2. At the end of this section we introduce the initial conditions of the GCs and discuss the generation of the underlying galaxy models. Extensive tests of the code are carried out in § 4.3. Results are presented in § 4.4, followed by a critical discussion (§ 4.5). The main findings are summarized in § 4.6.

4.2. Method

In the following, we briefly describe the main ingredients of MUESLI. These ingredients can easily be modified, exchanged or upgraded, making MUESLI a versatile platform for the study of GC dynamics in elliptical galaxies and related problems.

4.2.1. SCF Integration Method and Scaling Issues

The computations are performed with the self-consistent field (SCF) method (Hernquist & Ostriker, 1992). The SCF algorithm uses a basis-function approach to evaluate an expression for the potential ϕ from the underlying matter configuration. The orders n, l of the radial and angular expansion terms can be adjusted to match the type of galaxy. In the underlying study we restrict ourselves to spherically symmetric galaxies. The usage of $l > 0$ in spherical galaxy models can result in inhomogeneities and unphysical drifts of the angular momentum vectors. Therefore, $n = 30, l = 0$ is adopted for the main computation of the spherical galaxies of this study, while $n = l \geq 10$ is chosen for axisymmetric and triaxial galaxies. Tests are performed in § 4.3.1 and § 4.3.2.

The particle trajectories are integrated forward in time with the time-transformed leapfrog (TTL) scheme (Mikkola & Aarseth, 2002) combined with an iteration method to account for the inclusion of external (velocity-dependent) forces. These forces are the dynamical friction force (§ 4.2.2) and post-Newtonian forces allowing us to mimic general relativistic effects arising from the central SMBH. Post-Newtonian terms are not relevant for GC destruction processes as they occur on distances much larger than event horizon scales where GR effects are negligible and so we do not consider them for this study.

While the code uses conventional model units, $M_{\mathrm{GAL}} = R_H = G = 1$, the relevant globular cluster quantities (§ 4.2.3) as well as the dynamical friction force (§ 4.2.2) are defined in physical dimensions. The scaling of time, mass and size is performed during computations.

4.2.2. GC Dissolution Mechanisms

We aim at quantifying the relevance of internal and external effects like stellar evolution, relaxation driven evolution of GCs in tidal fields, tidal disruption through shocks and dynamical friction for shaping a cored GC distribution.

Stellar Evolution and Two-Body Relaxation

Stellar evolution reduces the cluster mass most significantly during an initial phase of roughly 100 Myr. During this period, the most massive stars lose mass through stellar winds and supernovae (e.g. de Boer & Seggewiss 2008). We implemented the combined scheme for stellar evolution and energy-equipartition driven evaporation in tidal fields from Baumgardt & Makino (2003). Compared to the long-term dynamical evolution, SEV decreases the initial cluster mass nearly instantaneously by 30% (Baumgardt & Makino 2003, their Fig. 1). Therefore, initial SEV can be taken into account by using a constant GC mass correction factor of 0.70 (Baumgardt & Makino 2003, their Equation 12).

On the other hand, two-body relaxation causes a more continuous mass loss (Hénon, 1961; Baumgardt & Makino, 2003; Heggie & Hut, 2003). Due to two-body encounters, stars gain enough energy so that they can leave the cluster. In the long term, this process leads to the dissolution of any star cluster. The process of relaxation-driven mass loss is accelerated when globular clusters are embedded in the external tidal field of a host galaxy as the potential barrier for escape is lowered (Chernoff & Weinberg, 1990; Baumgardt & Makino, 2003). In this case, a star may separate from the GC when passing beyond a characteristic radius, commonly known as the Jacobi radius, r_J (e.g. King 1962; Spitzer 1987). When the cluster moves on a non-circular orbit the tidal field strength varies with time, and so does the Jacobi radius. With growing eccentricity of the cluster's orbit, the extrema between the Jacobi radius at perigalacticon, where it is smallest, and apogalacticon increase (see e.g. Küpper et al. 2010b; Webb et al. 2013).

Baumgardt & Makino (2003) suggests that the time dependent mass loss rate of GCs in tidal fields can be approximated by a linear function. A few modifications were added to account for arbitrary galactic density profiles and changing GC orbits caused by dynamical friction. This is done by first computing the galactocentric distance, r_G, and velocity, $v_G = \sqrt{a \cdot r_G}$, where $a = |\vec{a}(\vec{r})|$ is the acceleration at the position of the globular cluster. Then, the dissolution time is calculated using Eq. 7 of Baumgardt & Makino (2003),

$$\frac{t_{\text{DISS}}}{[\text{Myr}]} = \beta \left(\frac{N_0}{\ln(0.02N_0)} \right)^\gamma \frac{r_G}{[\text{kpc}]} \left(\frac{v_G}{220\text{km/s}} \right)^{-1}, \qquad (4.63)$$

for every cluster individually. The two parameters β and γ depend on the concentration of the globular clusters. We chose values of $\beta = 1.91$ and $\gamma = 0.75$ for our main computations (as well as $\beta = 1.21$ and $\gamma = 0.79$ for a particular model), which have been found to reproduce the mass evolution of clusters with a King density profile and a W_0 of 5.0. This is typical density profile among Milky-Way globular clusters (e.g. McLaughlin & van der Marel 2005). Depending on the density profile of the respective globular cluster, β and γ can change. The initial number of globular cluster stars, N_0, is approximated by $N_0 = m_{\text{GC}}(t = 0)/0.547$ (Baumgardt & Makino, 2003). We assume that mass is lost linearly with time, so after each timestep, Δt, the GC mass is reduced by an amount $\Delta m = \Delta t \cdot m_{\text{GC}}(t = 0)/t_{\text{DISS}}$. The galactocentric distance used in Eq. 4.63 gets updated at each peri- or apocenter passage and we use the last pericenter or apocenter distance for r_G. In this way, our method reproduces the $(1 - \epsilon)$ scaling of the lifetimes found by Baumgardt & Makino (2003) without having to calculate orbital parameters.

In galaxies where the circular velocity v_G varies with radius, we use an average of the pericenter and apocenter velocity $\overline{v} = \left(v_{r_{apo}} + v_{r_{peri}} \right)/2$ to account for the varying circular velocity. Once the mass of a cluster is less than $m_{\text{GC}} = 10^2 \text{M}_\odot$, it is assumed to be dissolved.

Tidal Shocks

The variation of the tidal field does not only enhance the overall mass loss rate but also increases the cluster's internal energy (Gnedin & Ostriker, 1997; Gnedin, Hernquist & Ostriker, 1999b). If the pericentre distance to the galactic center is small, the energy input through tidal variation acts like a tidal shock and the energy gain of the cluster is significant (Gnedin & Ostriker, 1999a; Küpper et al., 2010a; Webb et al., 2013; Smith et al., 2013). In these cases, mass loss of the cluster gets driven by tidal shocks leading to quick cluster dissolution (Vesperini & Heggie, 1997; Gnedin & Ostriker, 1997; Gnedin, Hernquist & Ostriker, 1999b; Peñarrubia, Walker & Gilmore, 2009; Küpper et al., 2010b). We found that by using a second disruption criterion in addition to § 4.2.2, we can compensate for the underestimated mass-loss rate for clusters on very eccentric orbits within strong tidal fields and obtain better fits to direct NBODY6 integrations. This criterion is derived below:
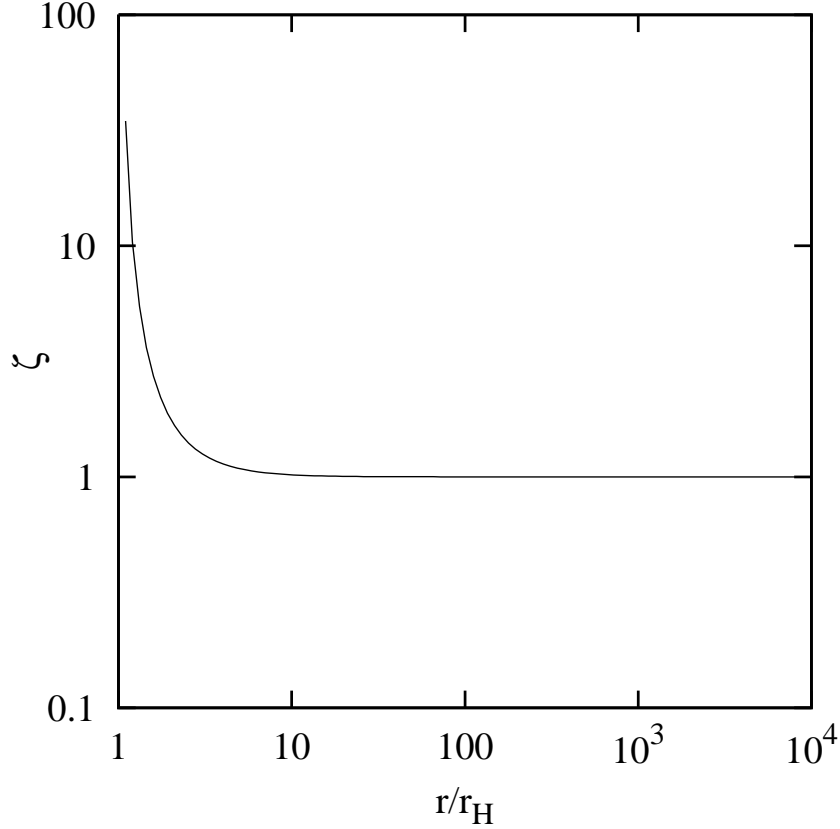
Figure 4.18. The ratio $\zeta = \frac{a(r+r_H)-a(r-r_H)}{2r_H} \big/ \left(\frac{\partial^2 \phi}{\partial r^2}\right)^{-1}$ plotted for a $\phi \propto -\frac{1}{r}$ potential. The distance r is given in GC half-mass radii, r_H. The approximation $\frac{\partial^2 \phi}{\partial r^2} \approx \frac{a(r+r_H)-a(r-r_H)}{2r_H}$ is accurate down to a few r_H and is almost exact for mass configurations with less steeply varying gradients.

For quantifying the strength of tidal shocks we calculate the Jacobi radius, r_J, following King (1962):

$$r_J = \left(\frac{Gm_{\text{GC}}}{\Omega^2 - \frac{\partial^2 \phi}{\partial r^2}}\right)^{\frac{1}{3}}. \tag{4.64}$$

Here, $\Omega = \frac{|\vec{r} \times \vec{v}|}{r^2}$ is the cluster's orbital galactocentric angular velocity. We approximate the second spatial derivative of the galactic potential in Eq. 4.64 by

$$\frac{\partial^2 \phi}{\partial r^2} \approx \frac{a(r+dr) - a(r-dr)}{2dr}, \tag{4.65}$$

where $a(r)$ is the acceleration at galactocentric radius r and $dr << r$ is a sufficiently small distance away from the cluster center. We choose $dr = r_H$ to be the 3D half-mass radius[31] of the respective globular cluster. This approximation works well even for the quickly declining $1/r$ potential close to the central SMBH (see Figure 4.18). If a GCs

---

[31] For galaxy specific quantities like the half mass radius, R_H, we use capital letters.
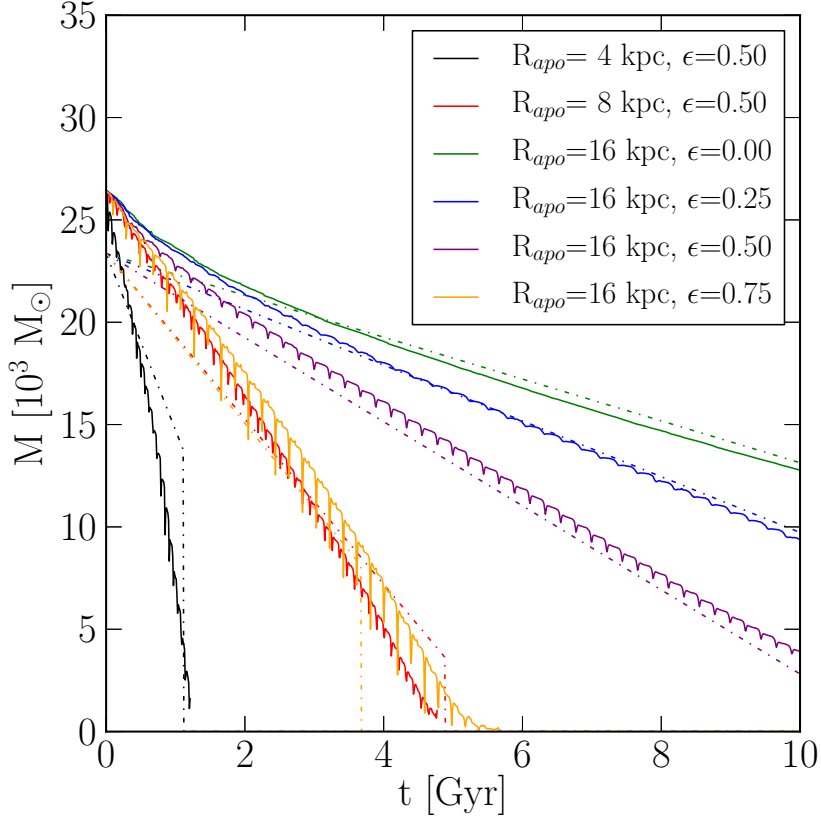
Figure 4.19. Temporal evolution of the cluster mass. The data were taken from a set of direct *N*-body experiments of a number of star clusters on orbits with different eccentricities in the tidal field of a galaxy. Clusters evolve from their initial masses of $\approx 3 \times 10^4 M_\odot$ towards dissolution. The clusters which are affected by the strongest tidal shocks (solid black, orange and red lines) are subject to fast dissolution even though their initial values $x = r_{H0}/r_J$ started below $x = 0.5$. The theoretically predicted mass evolutions as described in § 4.2.2 are shown with dashed lines.

falls below the galactic center distance $r = 2r_H$, r_J is taken to be the r_J at $r = 2r_H$. Equation 4.64 is valid for star clusters on eccentric orbits in arbitrary spherical potentials (see also, e.g. Spitzer 1987; Read et al. 2006; Just et al. 2009; Küpper et al. 2010a; Renaud, Gieles & Boily 2011; Ernst & Just 2013). It has been compared to *N*-body simulations of dissolving star clusters and found to well reproduce the radius at which stars escape from the star cluster into the tidal tails (Küpper, Lane & Heggie, 2012).

We assume that a cluster is disrupted if its ratio $x = \frac{r_H}{r_J}$ is larger than $x = 0.5$ at any point during its orbit[32]. This approach yields a safe lower limit on the disruption rate as some cluster would be confronted with tidal fields even in excess of $x = 0.5$ at perigalacticon. The motivation behind using the limit $x = 0.5$ is subject to (i) observations of GCs in the Milky Way and (ii) direct *N*-body computations. The majority of GCs in

---

[32] Furthermore, we assume that GCs passing a SMBH within their 3D half mass radii, r_H, are disrupted as well.
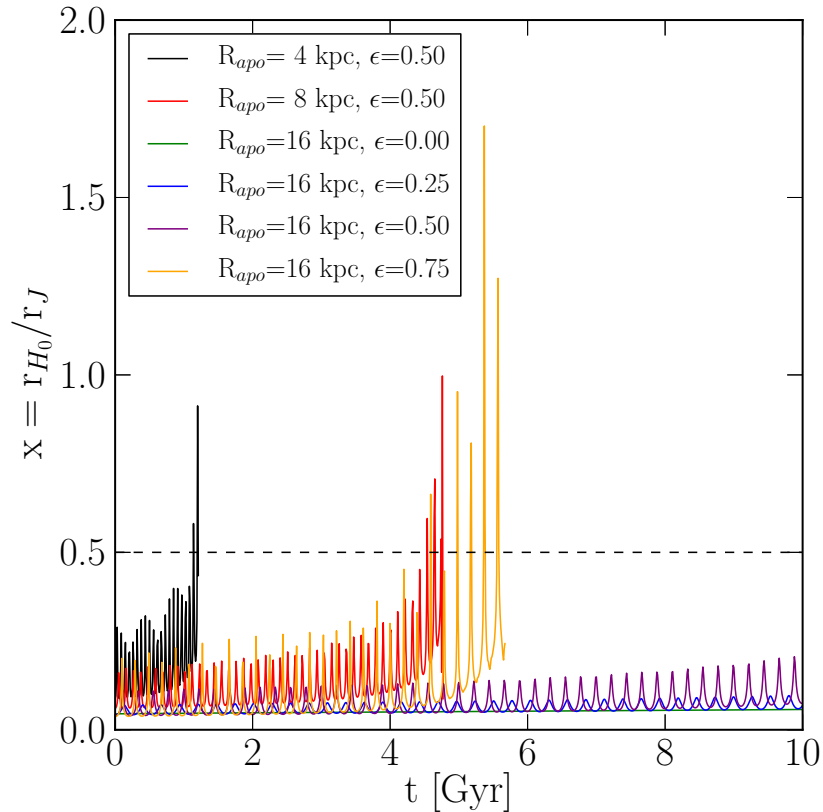
Figure 4.20. Ratio of initial half-mass radius $r_{H0} = 4$pc over Jacobi radius r_J versus time t for the models shown in Fig. 4.19. Depending on their orbits, the ratio x may temporarily reach values of $x > 0.5$, but those clusters are subject to quick dissolution. Surviving clusters stay well below our disruption threshold of $x = 0.5$ (dashed line) for the simulation length of 10 billion years.

the Milky Way are on eccentric orbits (Dinescu, Girard & van Altena, 1999). Most of them have ratios, x, well below 0.2, while only one GC has $x > 0.5$ (Baumgardt et al., 2010; Ernst & Just, 2013). The one cluster with $x \approx 0.55$ is the low-mass globular cluster Pal 5, which is thought to be in the very final stages of dissolution due to its pronounced tidal tails (Odenkirchen et al., 2003; Dehnen et al., 2004). Observations therefore suggest a limit of $x = 0.5$ to be reasonable. In addition to that we also performed direct *N*-body computations with the NBODY6 code (Aarseth, 1999, 2003) on the GPU computers of the SPODYR group at the AIfA, Bonn. We ran 32 simulations of compact and massive star clusters ($m_{GC} > 10^4 M_{\odot}$) on a range of orbits within a galactic tidal field. We followed their dynamical evolution for 10 billion years or until total dissolution, skipping the first 1 Gyr in which the clusters' evolution is dominated by the SEV processes and expansion as a consequence of rapid mass loss. See Fig. 4.19 for a representative sample. Also shown in Fig. 4.19 is the theoretically predicted mass evolution using Eq. 4.63 and the disruption criterion $x = 0.5$. Our model clusters lie in between a King profile with $W_0 = 5.0$ and $W_0 = 3.0$ so we had to use $\beta = 1.21$ and
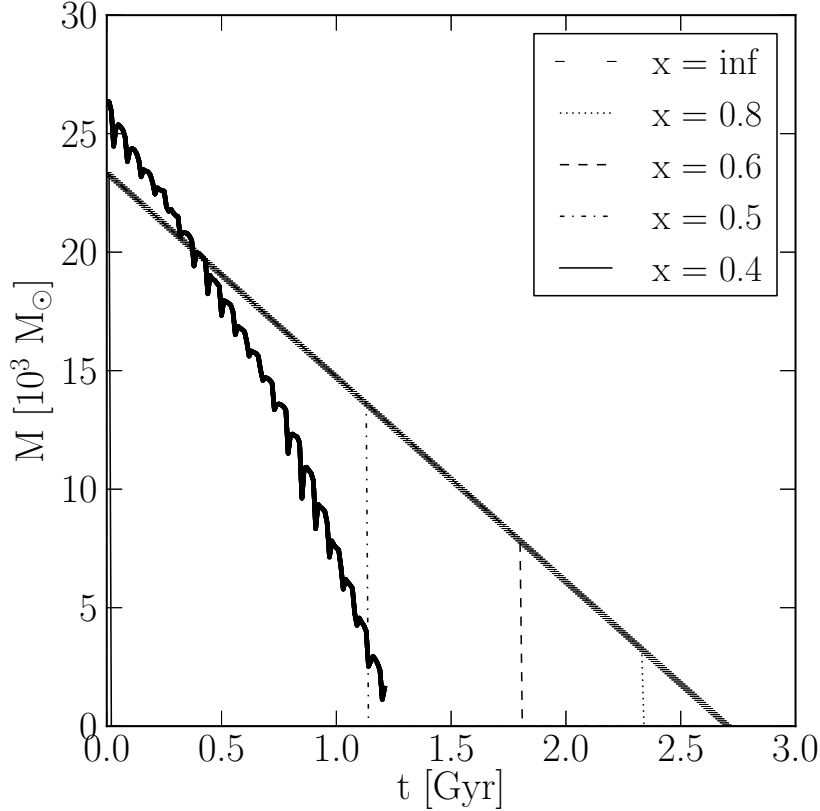
Figure 4.21. Mass evolution of a cluster with an apogalactic distance of 4 kpc and an orbital eccentricity of 0.5 (thick solid line). Also shown are the theoretical mass evolutions for different values of x. If x is chosen too small, the disruption by tidal forces is overestimated, if it is chosen too large, the cluster survives for too long.

$\gamma = 0.79$ for this comparison[33].

As can be seen in Fig. 4.20, some of the clusters evolve from initial ratios $x = \frac{r_{H0}}{r_J} = \frac{4\text{pc}}{r_J} \approx 0.3$ quickly to $x = 0.5$ where they are destroyed very rapidly. Only clusters with ratios well below $x = 0.5$ have a chance to survive for more than a Hubble time. Similar results have also been found by Trenti, Heggie & Hut (2007) and Küpper, Kroupa & Baumgardt (2008). Hence, N-body computations also suggest that a value of $x_{\text{crit}} = 0.5$ is a conservative limit for our computations. This criterion shows in a clear manner which areas in the phase space cannot be stably populated by clusters of a given mass. Even more so, because we neglect in our treatment of disruption processes that the half-mass radius grows with time when the clusters are initially tidally underfilling (Gieles et al., 2010; Madrid, Hurley & Sippel, 2012; Webb et al., 2013). In addition to that, it should be noted that the present study investigates GC dissolution and disruption processes in spherical galaxies. Here the angular momentum of cluster orbits, apart from dynamical friction, is a conserved quantity. A single GC not being

---

[33]To quantify the dependence of the overall GC system erosion rate on internal cluster profiles, computations with $\beta = 1.91$ and $\gamma = 0.79$ (i.e. $W_0 = 5.0$) and $\beta = 1.21$ and $\gamma = 0.79$ (green line in Figure 4.26) were performed.

fully disrupted once the tidal field strength exceeds $x = 0.5$ would be destroyed within the next few orbits.

As can be seen in Fig. 4.21, increasing x allows clusters on very eccentric orbits and deep within the tidal field of their host galaxy to survive longer than for $x = 0.5$ and longer than found in direct N-body simulations. Thus, we may then overestimate the number of surviving clusters in the central part of the host galaxies. A value smaller than 0.5 on the other hand may be too weak. Therefore, computations with more restrict criteria ($x = 0.8$ and $x = \infty$ i.e. no tidal disruption) but otherwise identical physical properties are performed as well. Our additional simulations allow us to constrain the systematics introduced by our second disruption criterion.

Dynamical Friction

Massive objects moving through a background of particles will decelerate and lose orbital energy by dynamical friction (DF) (Chandrasekhar, 1943). This effect may have profound implications for the orbital evolution and, hence, the fate of globular clusters. Our MUESLI code is designed to obtain the impact of DF on the destruction of GCs in galaxies with isotropic and anisotropic velocity distributions as well as axisymmetric and triaxial galaxies.

The equation of motion of a massive object like a globular cluster in a galaxy with DF, is:

$$\vec{a}_{\mathrm{GC}}\left(\vec{r}\right) = -\vec{\nabla}\phi(\vec{r}) + \vec{a}_{\mathrm{GC,\,DF}}\left(\vec{r}\right). \tag{4.66}$$

Here, $\vec{a}_{\mathrm{GC}}$ is the total acceleration of the globular cluster, $-\vec{\nabla}\phi(\vec{r})$ is the acceleration due to the combined galactic and SMBH potential, while $\vec{a}_{\mathrm{GC,\,DF}}$ describes the deacceleration due to DF. Chandrasekhar's dynamical friction formula has been extended to account for ellipsoidal velocity distributions by Pesce et al. (1992) and $\vec{a}_{\mathrm{GC,\,DF}}\left(\vec{r}\right)$ has the form:

$$\vec{a}_{\mathrm{GC,\,DF}}\left(\vec{r}\right) = -\,\gamma_1\left(\vec{r}\right)\tilde{v}_1\left(\vec{r}\right)\vec{e}_1 - \gamma_2\left(\vec{r}\right)\tilde{v}_2\left(\vec{r}\right)\vec{e}_2 \tag{4.67}$$
$$-\,\gamma_3\left(\vec{r}\right)\tilde{v}_3\left(\vec{r}\right)\vec{e}_3\,,$$

where the dynamical friction coefficients $\gamma_i\left(\vec{r}\right)$ can be written as:

$$\gamma_i(\vec{r}) = \frac{2\sqrt{2\pi}\rho\left(\vec{r}\right)G^2 m_{\mathrm{GC}}\ln\Lambda}{\sigma_1^3\left(\vec{r}\right)} \tag{4.68}$$
$$\times \int_0^\infty \frac{\exp\left(-\frac{\tilde{v}_1^2(\vec{r})/\left(2\sigma_1^2(\vec{r})\right)}{1+u} - \frac{\tilde{v}_2^2(\vec{r})/\left(2\sigma_2^2(\vec{r})\right)}{\epsilon_2^2+u} - \frac{\tilde{v}_3^2(\vec{r})/\left(2\sigma_3^2(\vec{r})\right)}{\epsilon_3^2+u}\right)}{\left(\epsilon_i^2+u\right)\sqrt{\left(1+u\right)\left(\epsilon_2^2+u\right)\left(\epsilon_3^2+u\right)}}\,du.$$

The function Λ that appears in the Coulomb logarithm, $\ln\Lambda$, can be obtained for bodies with a finite size (Binney & Tremaine 2008, their Equation 8.2) by:

$$\Lambda = \frac{b_{\mathrm{max}}}{\max\left(r_H, G m_{\mathrm{GC}}/v_{\mathrm{typ}}^2\right)}. \tag{4.69}$$

The maximum impact parameter b_{max} is approximated by the galactocentric distance r. This approach yields a more realistic treatment than by assigning a constant value for the Coulomb logarithm (Hashimoto et al., 2003; Spinnato et al., 2003). The validity of Eq. 4.69 is restricted to $\Lambda > 1$ in order to prevent unphysical acceleration by DF. The characteristic velocity is $v_{\mathrm{typ}}^2 \approx G M_{\mathrm{GAL}}/R_{\mathrm{H}}$. Here M_{GAL} and R_H correspond to the total mass and half mass radius of the galaxy. The parameter ϵ_i^2 which appears in Eq. 4.68 is given by the ratio of the eigenvalues $\sigma_i^2\left(\vec{r}\right)/\sigma_1^2\left(\vec{r}\right)$ of the velocity dispersion tensor $\sigma_{ij}^2 = \overline{v_i v_j} - \overline{v}_i \overline{v}_j$. For convenience, the velocity dispersion component with the largest eigenvalue of σ_{ij}^2 is defined to be $\sigma_1^2\left(r\right)$. The integral is evaluated numerically for each integration timestep by using the Gauß-Legendre integration method in combination with logarithmic mapping. The density $\rho\left(\vec{r}\right)$ is obtained directly from the SCF algorithm. The velocity components $\tilde{v}_i\left(\vec{r}\right) = \cos\theta_i\left|\vec{v}_{\mathrm{GC}}\left(\vec{r}\right)\right|$ with $\cos\theta_i = \frac{\vec{e}_i\cdot\vec{v}_{\mathrm{GC}}(\vec{r})}{|\vec{e}_i|\cdot|\vec{v}_{\mathrm{GC}}(\vec{r})|}$ are obtained by the projection of the GC velocity vector $\vec{v}_{\mathrm{GC}}$ on to the normalized eigenvectors $\vec{e}_i$ of the velocity dispersion tensor σ_{ij}^2. The position dependent eigenvalues σ_i and eigenvectors $\vec{e}_i$ are calculated in hundreds of cubic segments which are part of a 5x5x5 mesh with logarithmically increasing resolution towards the center (see Fig. 4.22 for illustration). This is achieved by replacing the inner 27 out of 125 cubes by a second 5x5x5 grid. The procedure is repeated $G_{\mathrm{depth}} \in \mathbb{N}$ times. The innermost resolution scale is $R_{\mathrm{res}} = 0.2 R_{\mathrm{max}} 0.6^{G_{\mathrm{depth}}}$. The size R_{max} of the outermost grid is chosen to encompass the whole galaxy. In this way a variable DF force acting on GCs in an elliptical galaxy is handled. The underlying galaxy models are specified in Section 4.2.3.

Grid based calculations are always affected by discontinuities/jumps in combination with discreteness noise subject to finite number of cells and particles. In order to counterbalance these systematics we apply the inverse distance weighting (IDW) method (Shepard, 1968). Irregularities are smoothed out by first calculating the center of mass of the particles in a box (which is used as the position of the box), local eigenvalues and eigenvectors of σ_{ij}^2. Boxes containing only few particles are left out of consideration. For the spatial interpolation only cells within a radius corresponding to the galactocentric distance of an orbiting GC are taken into account. To guarantee that the contribution of the nearest box dominates, the weighting parameter p (also known as the power parameter) is calibrated in many N-body experiments to be $p = 64$. For testing issues we refer to § 4.3.3. The eigenvalues and eigenvectors are calculated at the beginning of the computations and for each time-scale the potential becomes updated by the SCF algorithm.

4.2.3. Initial Conditions

Globular Cluster Mass and Size Distribution

The present-day GC mass spectrum, $\mathrm{d}N/\mathrm{d}m \propto m^{-\beta}$, can be characterized as a power-law distribution with different exponents for characteristic mass scales (McLaughlin, 1994). Usually, it is well approximated by the exponents $\beta = 0.2$ below and $\beta = 2$ above a threshold mass of $m_{\mathrm{TH}} = (1-2) \cdot 10^5 M_\odot$. This two-component power-law distribution resembles a bell-shaped function when expressed in terms of the number of globular clusters, $\mathrm{d}N$, per constant logarithmic cluster-mass interval, $\mathrm{d}\log_{10} m$. For
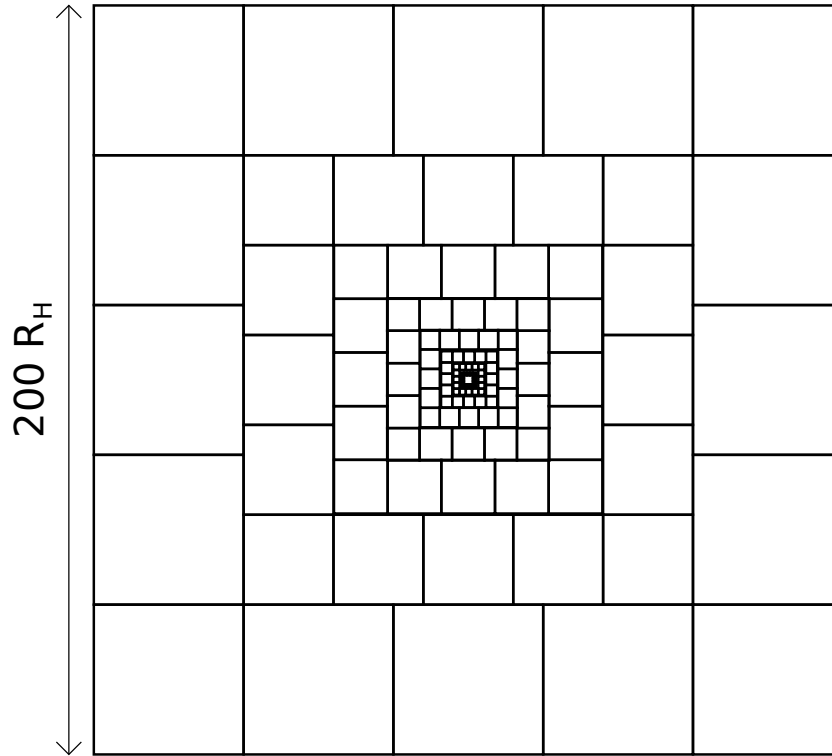
Figure 4.22. A 2D illustration of a 5x5x5 grid. The eigenvectors of the velocity dispersion tensor are calculated in each cell. Grid cells are logarithmically refined towards the inner part of a galaxy to guarantee sufficient resolution. The size of the outer grid is chosen to be 200 times the size of the galactic half mass radius R_H to encompass the whole galaxy.

the initial cluster mass function, we are using the single power-law distribution,

$$\frac{\mathrm{d}N}{\mathrm{d}m} \propto m^{-2}. \tag{4.70}$$

It finds support by observations of young, luminous clusters in starburst galaxies where the mass spectrum monotonically follows a (single) power-law profile with slope $\beta \approx 2$ (Battinelli et al., 1994; Zhang & Fall, 1999)[34].

It is our aim to investigate whether dissolution of low mass clusters is responsible for turning a power-law mass function into a bell shaped mass function (see also Baumgardt 1998; Fall & Zhang 2001; Vesperini et al. 2003; McLaughlin & Fall 2008; Elmegreen 2010) by cluster disruption processes, relaxation driven mass loss in tidal fields and dynamical friction. Scenarios involving gas expulsion (Kroupa & Boily, 2002; Parmentier & Gilmore, 2007; Baumgardt et al., 2008) are not considered in our main computations (with the exception of one model) and will be added in later publications. The overall GC mass range is chosen to be $m_{GC} = 10^4 - 10^7 M_\odot$. Clusters

---

[34]Recent investigations (Larsen, 2009) found that the initial mass distribution is also compatible with a Schechter-type mass function with a particular turn-down mass in the high GC mass regime. However, for simplicity we use a single power-paw mass function here, as the differences will be limited to the high-mass end where only relatively few clusters are found.

below10^4M$_\odot$ are not considered, because in galaxies with an age of several Gyr, they would have lost most (if not all) of their initial mass by energy-equipartition driven evaporation (Baumgardt & Makino, 2003; Lamers et al., 2010).

Observations find no strong correlation between half-mass radius and mass for GCs which are less massive than 10^6M$_\odot$ (Haşegan et al., 2005; Dabringhausen et al., 2008). The median 3D half-mass radius of GCs in typical early-type galaxies centers around $\overline{r_H} = 4$pc (Haşegan et al., 2005; Jordán et al., 2005)[35]. The situation changes when the clusters become more massive than a particular mass scale which is of the order of 10^6M$_\odot$(Dabringhausen et al., 2008). Hence, we assume that they follow a trend given by:

$$r_H = \begin{cases} 4\text{pc} & : \quad m_{\text{GC}} \lesssim 1.0 \cdot 10^6 \text{M}_\odot \\ 4 \left(\frac{m_{\text{GC}}}{10^6 \text{M}_\odot} \right)^{0.6} \text{pc} & : \quad m_{\text{GC}} \gtrsim 1.0 \cdot 10^6 \text{M}_\odot \end{cases} \tag{4.71}$$

The influence of other primordial size relations for GC erosion processes is not considered in this paper.

Spatial Distribution of GCs

Having defined cluster masses and sizes, the GC space and velocity vectors have to be distributed within the galaxies by making five underlying assumptions[36]:

1. The initial GC phase space distribution equals the one of the underlying galaxy model

2. Initial GC masses and sizes do not depend on the distance to the galactic center

3. Accumulation of GCs through mergers or subsequent formation in star-forming events is neglected.

4. The overall dynamics of the host galaxy are not influenced by globular cluster evolution processes

5. All galaxy models are virialized and remain in isolation

For this study we created several realistic base models. We assume that the stars follow a Sersic model (Sersic, 1968) with concentration $n = 4$ and constant mass-to-light ratio, Υ. They were generated by the deprojection of 2D Sérsic profiles into 3D density profiles. Afterwards, the density, potential and distribution function was calculated on a logarithmically spaced grid configuration of size $r \in \left[10^{-4}, 10^2 \right]$ in model units, $G = R_H = M_{\text{GAL}} = 1$. The distribution function for an anisotropic Osipkov-Merritt velocity profile (Osipkov, 1979; Merritt, 1985) was calculated by making use of Equation (4.78a) from Binney & Tremaine (2008). Here the velocity anisotropy parameter has the form $\beta(r) = \left(1 + R_A^2/r^2 \right)^{-1}$ and R_A is the anisotropy radius. The particle positions were distributed according to the density profile, while the normalized cumulative

---

[35]For the conversion $r_e = 0.75 r_H$ (Spitzer, 1987) of the projected half light radius, r_e, to the 3D half-mass radius, r_H, the mass-to-light ratio, $\Upsilon(r)$, is assumed to be constant.
[36]The code allows for individual adjustment of these aspects.

distribution function was used to allocate particle velocities. It was evaluated by the transformation of the double integral into a single integral according to the substitution described in Merritt (1985)[37]. Central SMBHs of mass $M_\bullet$ were implemented by adding the term $\phi_{BH} = -M_\bullet/r$ to the potential of the underlying mass distribution. Afterwards, all particles were inverted (and doubled) through the origin. In this way the center of mass and density center were located at the point of origin and the model stays at rest during computations. We also created galaxies following Hernquist (Hernquist, 1990) and Jaffe (Jaffe, 1983) models. Scale factors $a = \left(1 + \sqrt{2}\right)^{-1}$ for Hernquist and $a = 1$ for Jaffe models were used in order to fix the half mass radius to one.

Finally, we generated an additional triaxially shaped model (required for testing issues of the dynamical friction routine) with a central core and outer Sérsic $n = 4$ profile from cold collapse computations (Lynden-Bell, 1967; Aarseth & Binney, 1978; van Albada, 1982; McGlynn, 1984; Merritt & Quinlan, 1998). A spherical distribution with a $\rho \propto r^{-1.5}$ density profile and virial ratio $2T/|W| = 0$ was set up for $0 < r < 2$. It collapsed and settled down into a strongly triaxial configuration with $T = \left(a^2 - b^2\right)/\left(a^2 - c^2\right) = 0.53$ within its half mass radius. Here T is the triaxiality parameter and a, b, c are the three main axes of the ellipsoidal configuration. It was evolved forward in time with the NBODY6 (Aarseth, 1999, 2003) code until virialization. The density center was shifted to the center of origin and the model was rescaled to $R_H = 1$. Models generated from collapse simulations are isotropic in their centers and radially biased at large galactocentric distances.

In the scenario of hierarchical structure formation (but see also Samland 2004), where smaller structures merge to build up larger objects such as elliptical galaxies (Toomre, 1977; White & Rees, 1978; Kauffmann et al., 1993; Steinmetz & Navarro, 2002), violent relaxation causes the merger products to be centrally isotropic and radially biased at large radii (Lynden-Bell, 1967). Our models agree with these cosmological predictions.

Related to the fact that a systematic scan over the fundamental plane of elliptical galaxies is beyond the scope of this paper, we scaled our models to four representative elliptical galaxies. These are M 32, NGC 4494, IC 1459 and NGC 4889. While M 32 is a compact dwarf galaxy which is gravitationally bound to M 31, NGC 4889 is the most massive and extended galaxy in our sample. It is a brightest cluster galaxy (BCG) and defines together with NGC 4874 the gravitational center of the Coma cluster. The four galaxies were chosen because they cover the full mass range of elliptical galaxies from small compact dEs to giant BCGs. They lie (within $10\% - 45\%$ scatter) on the $R_e - M_{\rm GAL}$ relation (Dabringhausen et al. 2008, their Equation 4) for low redshift bright elliptical galaxies, bulges and very compact dwarf elliptical galaxies. We note that our results concerning globular cluster erosion processes in M 32 like compact galaxies should not be extrapolated to much more extended dwarf spheroidal galaxies with weaker tidal fields (see Fig.2 in Dabringhausen et al. (2008) and § 4.4.1 in this paper). Complementary to the galactic mass range, our representative galaxies host central SMBH

---

[37]Their Equation 11.

Model	Galaxy Example	$M_{\mathrm{GAL}}[10^9 M_\odot]$	$R_e[\mathrm{pc}]$	$R_H[\mathrm{pc}]$	$M_\bullet[10^9 M_\odot]$	Ref.
MOD1	M 32	0.8	125	170	0.0025	1,2,3
MOD2	NGC 4494	100	3715	5000	0.065	4,5,6
MOD3	IC 1459	300	6000	8050	2.6	7,8
MOD4	NGC 4889	2000	25000	34000	20	9,10

Table 4.3. Adopted parameters for the simulated galaxies. $R_H = 1.35 R_e$ is used to calculate the 3D half mass radius R_H from the effective radius R_e. **References:** (1) Magorrian et al. (1998); (2) Rose et al. (2005); (3) Karachentsev et al. (2004); (4) Lauer et al. (2007) for R_e and M_{GAL} by assuming $Y = 3$; (5) Bender et al. (1994); (6) McConnell et al. (2011) black hole mass from $M_\bullet - \sigma$ relation; (7) Häring & Rix (2004), (8) Cappellari et al. (2002), (9) McConnell et al. (2012), (10) McConnell et al. (2011)

with masses in the range of a few $10^6 M_\odot$ (MOD1, i.e. M 32) up to $10^{10} M_\odot$ (MOD4, i.e. NGC 4889). The number of observed globular clusters ranges from 0 (M 32, Harris et al. 2013) to about 11.000 GCs (NGC 4889, Harris et al. 2009). The physical properties of all four galaxy models are summarized in Table 4.3.

4.3. Testing

4.3.1. Discreteness Noise

When the potential becomes updated in time intervals Δt_{up} by the SCF algorithm, fluctuations in the overall particle distribution give rise to irregular oscillations of the virial ratio (Hernquist & Ostriker, 1992). Additionally, improper selection of the expansion coefficients, especially the angular expansion order leads to multipole induced precession.

We inferred the magnitude of these fluctuations, which inversely ($\propto N^{-0.5}$) depend on the particle number, by the computation of spherical and axisymmetric Sérsic $n = 4$ and Hernquist profiles. All models were evolved forward up to 100 N-body time units. We varied the particle number ($N = 2 \cdot 10^5$ and $N = 4 \cdot 10^6$), the timescales of potential evaluation ($\Delta t_{\mathrm{up}} = 1$ and $\Delta t_{\mathrm{up}} = 100$) as well as the radial and angular expansion order (between $l = 0$ and $l = 20$). In this way we were able to estimate the fluctuations and their relevance for the accuracy of orbit integrations of elliptical galaxy models. For testing purposes (only), the axisymmetric models were generated by simply reducing the z-components by factors of two. Without adjusting particle velocities properly, axisymmetric models generated in such a way are dynamically unstable. The only reason for using them instead of existing virialized axisymmetric models generated from cold collapse computations was subject to more controlled conditions required for the evaluation of discreteness noise effects. Orbits in axisymmetric models were therefore computed in fixed potentials i.e. by using $\Delta t_{\mathrm{up}} = 100$.

Ideally, a test particle with zero velocity in z-direction has to orbit the galaxy without changing its z-component. Hence, the maximal drift of the angular momentum vector $\vec{L}$, i.e. the maximal angle α_m between $\vec{L}_{t_0}$ and $\vec{L}_{t_i}$, was used as one criterion for the accuracy of orbit integration. As an additional criterion we have used the standard

Hernquist	N	Δt_{up}	n	l	σ_c(r=0.1,1,10)	α_m(r=0.1,1,10)
spherical	$2 \cdot 10^5$	1	30	0	0.002/0.006/0.003	0/0/0
spherical	$2 \cdot 10^5$	100	30	0	0.0001/0.0001/0.0004	0/0/0
spherical	$2 \cdot 10^5$	1	10	10	0.008/0.01/0.003	1.8/0.1/0.001
spherical	$2 \cdot 10^5$	100	10	10	0.003/0.002/0.007	1.8/0.08/0.002
spherical	$2 \cdot 10^5$	100	10	5	0.003/0.002/0.006	1.9/0.07/0.0006
axis-sym.	$2 \cdot 10^5$	100	12	1	—	0/0/0
axis-sym.	$2 \cdot 10^5$	100	12	2	—	0.06/0.008/0.0001
axis-sym	$2 \cdot 10^5$	100	12	5	—	0.3/0.008/0.0007
axis-sym	$2 \cdot 10^5$	100	12	10	—	0.1/0.02/0.001
axis-sym	$2 \cdot 10^5$	100	20	20	—	0.09/0.03/0.003
spherical	$4 \cdot 10^6$	1	30	0	0.0009/0.002/0.0005	0/0/0
spherical	$4 \cdot 10^6$	100	30	0	0.00001/0.00002/0.00009	0/0/0
spherical	$4 \cdot 10^6$	1	10	10	-/0.005/0.0003	-/0.01/0.0001
spherical	$4 \cdot 10^6$	100	10	10	0.0001/0.0003/0.0003	1.4/0.02/0.0003
spherical	$4 \cdot 10^6$	100	10	5	0.0001/0.0002/0.0003	1.4/0.01/0.0005
axis-sym.	$4 \cdot 10^6$	100	12	1	—	0/0/0
axis-sym.	$4 \cdot 10^6$	100	12	2	—	0.01/0.001/0.00002
axis-sym	$4 \cdot 10^6$	100	12	5	—	0.03/0.001/0.0001
axis-sym	$4 \cdot 10^6$	100	12	10	—	0.3/0.002/0.0001
axis-sym	$4 \cdot 10^6$	100	20	20	—	0.3/0.003/0.0003
Sérsic $n = 4$	N	Δt_{up}	n	l	σ_c(r=0.1,1,10)	α_m(r=0.1,1,10)
spherical	$2 \cdot 10^5$	1	30	0	0.001/0.0004/0.002	0/0/0
spherical	$2 \cdot 10^5$	100	30	0	0.00003/0.00005/0.0002	0/0/0
spherical	$2 \cdot 10^5$	1	10	10	0.005/0.02/0.003	1.7/0.03/0.002
spherical	$2 \cdot 10^5$	100	10	10	0.001/0.002/0.01	0.4/0.04/0.001
spherical	$2 \cdot 10^5$	100	10	5	0.001/0.002/0.01	0.3/0.08/0.0006
axis-sym.	$2 \cdot 10^5$	100	12	1	—	0/0/0
axis-sym.	$2 \cdot 10^5$	100	12	2	—	0.03/0.02/0.0004
axis-sym	$2 \cdot 10^5$	100	12	5	—	0.01/0.02/0.0004
axis-sym	$2 \cdot 10^5$	100	12	10	—	0.02/0.02/0.0005
axis-sym	$2 \cdot 10^5$	100	20	20	—	0.02/0.02/0.002
spherical	$4 \cdot 10^6$	1	30	0	0.0003/0.0009/0.0009	0/0/0
spherical	$4 \cdot 10^6$	100	30	0	0.000004/0.00004/0.0004	0/0/0
spherical	$4 \cdot 10^6$	1	10	10	0.002/0.002/0.02	0.6/0.009/0.0001
spherical	$4 \cdot 10^6$	100	10	10	0.00007/0.0005/0.02	0.5/0.02/0.0003
spherical	$4 \cdot 10^6$	100	10	5	0.00007/0.0005/0.02	0.5/0.02/0.0003
axis-sym.	$4 \cdot 10^6$	100	12	1	—	0/0/0
axis-sym.	$4 \cdot 10^6$	100	12	2	—	0.004/0.001/0.0001
axis-sym	$4 \cdot 10^6$	100	12	5	—	0.007/0.002/0.0004
axis-sym	$4 \cdot 10^6$	100	12	10	—	0.008/0.004/0.0005
axis-sym	$4 \cdot 10^6$	100	20	20	—	0.01/0.005/0.0005

Table 4.4. Parameters of the discreteness noise evaluation. N specifies the total number of particles and Δt_{up} is the characteristic timescale at which the overall potential becomes re-evaluated by the SCF algorithm. The parameters n, l correspond to the order of the radial and angular expansion terms. σ_c measures the standard deviation from circular motion at three different radii (r=0.1,1,10) and α_m traces the maximal angular deviation caused by multipole induced precession at the same radial distances. It is given in radians. There is no dipole moment induced precession (l=1) since all particles were initially inverted (and doubled) at the origin. The main computations are performed with five times higher particle numbers than the largest test models.

deviation $\sigma_c = \left(\frac{1}{N_l - 1} \sum_{i=1}^{N_l} (r_i - \bar{r})^2 \right)^{0.5}$ from circular motion at different galactocentric distances $r = 0.1, 1, 10$. This quantity reveals the magnitude of potential fluctuations.

Apparently, relaxation arising from discreteness noise is sub-dominant when performing integrations with high particle numbers ($N \geq 4 \cdot 10^6$) and by using low angular expansion terms i.e. $l = 0$ for the computation of spherical galaxies. In axisymmetric or triaxial galaxies torques from the overall matter configuration are orders of magnitudes larger than local anisotropies or discreteness noise. The integration inaccuracies are listed in the Table 4.4. On the basis of tabulated data, several trends can be obtained. The amplitude of discreteness noise effects are anti-correlated with the total number of particles. Torques induced by angular multipole expansion affect mostly trajectories with short orbital periods while the precession diminishes altogether by using lowest order (spherical) terms. Converging solutions of the underlying density profile are obtained with high radial order terms. For the parameter space of our main computation, radial orbit fluctuations correspond to only a few tens of parsec over timescales of several billion years when scaled to the proportions of giant elliptical galaxies like NGC 4889 (§ 4.2.3) and sub-parsec scales for the smallest galaxies.

4.3.2. The Conservation of the Space Phase Distribution

The order of the radial expansion coefficient, n, required to guarantee the conservation of the initial space phase distribution is investigated in more detail in this section. For that purpose we evolved spherical Hernquist, Jaffe and Sérsic models forwards in time up to 100 N-body timescales ($\Delta t_{\text{up}} = 1$). Several different values for the radial expansion coefficients, n, were chosen. Afterwards, we compared the numerical outcomes to the initial models in terms of density profiles, axis ratios at several Lagrange radii (1,2,5,10,25,50,60,70,80,90%), radial[38] and tangential velocity dispersion as well as velocity anisotropy parameter, $\beta(r) = \left(1 + R_A^2 / r^2 \right)^{-1}$. All profiles were found to be perfectly stable when represented by high radial $n = 30$ and lowest angular order ($l = 0$). This is in agreement with the results obtained in § 4.3.1. These are the coefficients adopted for the main computations[39]. For illustration the velocity dispersion profile of an anisotropic Hernquist model with scale length $a = \left(1 + \sqrt{2} \right)^{-1}$ is compared to the analytical profile in Fig. 4.23. The expansion coefficient evaluation of axisymmetric and triaxial models is postponed. Mesh effects and the dynamical friction routine (§ 4.2.2) are investigated and tested in the next section § 4.3.3.

4.3.3. Dynamical Friction and Grid Effects

The purpose of this section is two-fold. The DF routine itself has to be tested and compared with analytical predictions of idealized DF problems. Systematic effects caused by discreteness noise and grid selection effects have to be evaluated in isotropic and

---

[38]The radial velocity dispersion, σ_r^2, is a sensible indicator for model stability by tracing minuscule instabilities along r.

[39]The Hernquist base function of the SCF algorithm uses a different scale length a, hence a high radial order is required for these models as well.
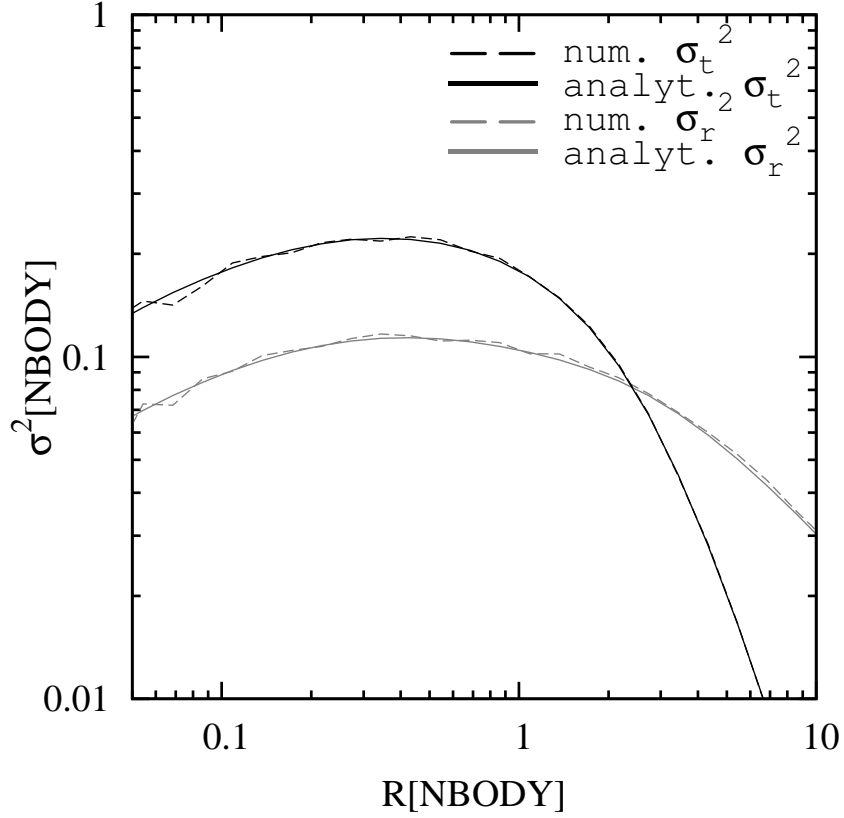
Figure 4.23. Radial and tangential velocity dispersion profile of an anisotropic Hernquist model ($R_A = R_H = 1, N = 4 \cdot 10^6$) which was dynamically evolved over 100 N-body timescales. Afterwards, we rescaled the model to $R_H = 1 + \sqrt{2}$ in order to compare it with the analytical velocity dispersion profile for anisotropic systems (Baes & Dejonghe, 2002). The usage of high radial order terms ($n = 30$) in combination with lowest order (spherical) angular terms ($l = 0$) yields accurate results.

anisotropic velocity distributions as well. In principle they can affect the computations and the calculus of the velocity dispersion tensor which is required for the generalized dynamical friction force (Eq. 4.67). We numerically evaluated the inspiral time t_{fric} of a GC on a circular orbit ($r = 5\mathrm{kpc}$) by using Equation 4.67 as well as Chandrasekhar's (standard) dynamical friction formula for a Maxwellian velocity distribution:

$$\vec{a}_{\mathrm{GC}} = -\frac{4\pi G^2 m_{\mathrm{GC}} \rho\left(\vec{r}\right) \ln\left(\Lambda\right)}{v_{\mathrm{GC}}^3} \times \tag{4.72}$$

$$\left[\mathrm{erf}\left(X\right) - \frac{2X}{\sqrt{(\pi)}}\exp(-X^2)\right]\vec{v}_{\mathrm{GC}}$$

Here $X = v_{\mathrm{GC}}/(\sqrt{2}\sigma)$ and $\sigma = \sqrt{\left(\sigma_1^2 + \sigma_2^2 + \sigma_3^2\right)/3}$ is the one dimensional velocity dispersion obtained from the eigenvalues of the local velocity dispersion tensor. The numerical outcomes were then compared with analytical predictions of a decaying ($m_{\mathrm{GC}} = 10^7 \mathrm{M}_\odot$) GC orbit and plotted in Fig. 4.24. The spherical galaxy had an isotropic velocity distribution, Jaffe density profile (Jaffe, 1983), total mass $M_{\mathrm{GAL}} = 10^{11}\mathrm{M}_\odot$
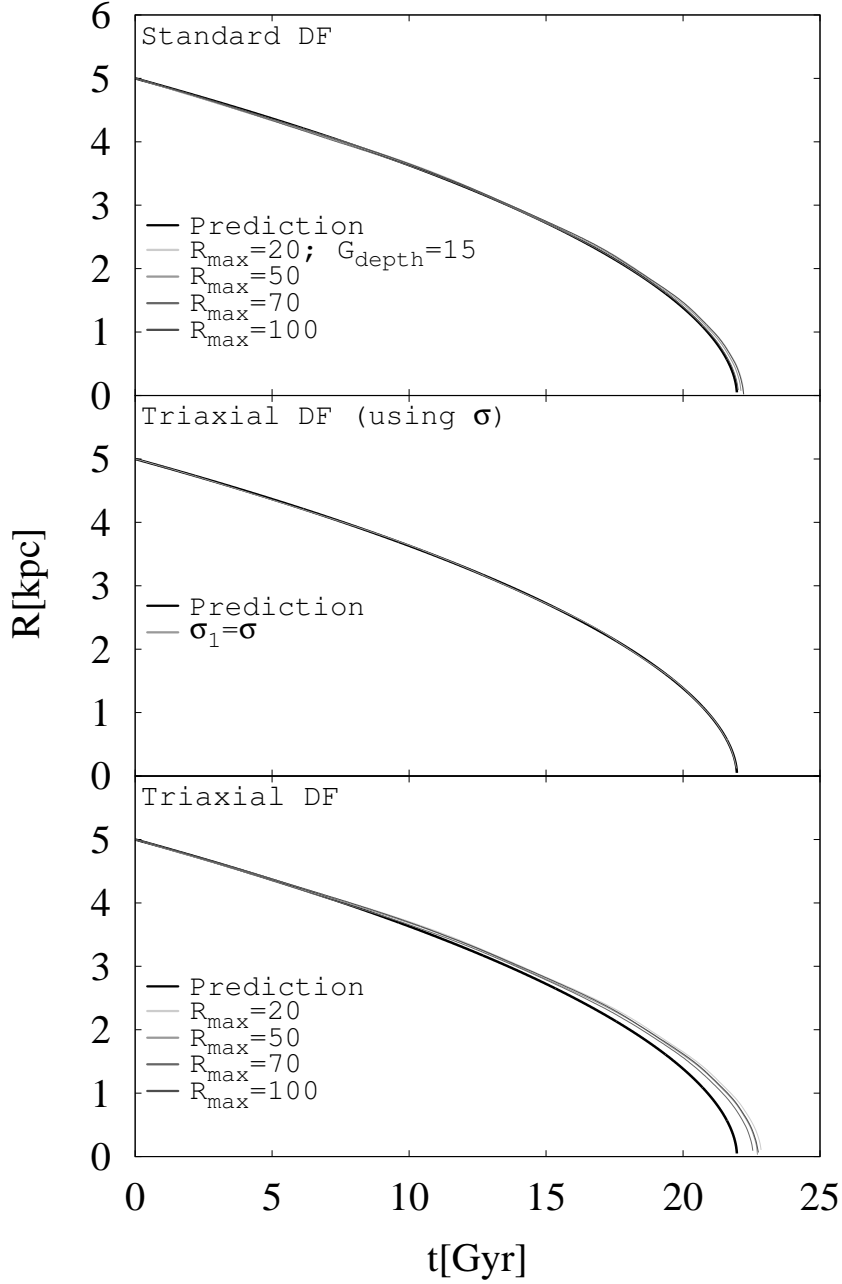
Figure 4.24. Decaying (circular) globular cluster ($m_{GC} = 10^7 M_\odot$) orbit as a function of different grid realizations and dynamical friction formulas. The standard DF computations match the predicted value within 1% accuracy (top) while the triaxial generalization formula yields slightly larger inspiral timescales t_{fric} (bottom). The reason for this are discreteness noise effects in the evaluation of the largest eigenvalue σ_1 in combination with the use of σ_1^3 in the denominator of Equation 4.68. By replacing σ_1 with the root mean square σ, which ideally should be equal in isotropic models, the triaxial DF formula matches the analytical prediction (middle). With regard to the difficulty of implementing highly nonlinear DF forces, a standard deviation of 1% from the predicted value, $t_{fric} \approx 22$ Gyr, for Chandrasekhar's (standard) formula and 4% for its triaxial generalization is an excellent result. Using even larger particle numbers than $N = 4 \cdot 10^6$ yields even more precise values.

and half mass radius $R_H = 5\text{kpc}$, similar to the properties of NGC 4494 (§ 4.2.3). We selected a Jaffe profile because of its analytical simplicity. Furthermore, it deviates from the underlying base model of the SCF algorithm. In this way the reliance on higher order base functions was automatically tested as well. We fixed the Coulomb logarithm to $\ln \Lambda = 6$ in order to ease the analytical calculation. Grid selection effects were investigated by carrying out integrations with $N = 4 \cdot 10^6$ particles and several realizations of the 5x5x5 grid (§ 4.2.2). Evidently Chandrasekhar's (standard) dynamical friction formula, its triaxial generalization and the analytical prediction yield (nearly) equal inspiral times t_{insp} despite the highly nonlinear character of DF (Fig. 4.24). Owing to the IDW interpolation method (§ 4.2.2), the chosen grid configuration does not have any visible systematic effect on t_{insp}. And indeed, the differences in t_{insp} caused by grid selection effects are only of the order of 200 million years, compared to $\approx$20 Gyr absolute integration time, or 1% in relative terms. Without the IDW interpolation method they are much bigger (of the order of 25%). The generalized triaxial DF routine (Eq. 4.67) yields slightly larger ($\approx$4%) inspiral times than the standard DF formula. The reason for this are discreteness noise fluctuations in the evaluation of the eigenvalues σ_i in combination with the systematic use of σ_1^3 in the denominator of Equation 4.68. By replacing (for test purposes in isotropic velocity distributions only) the denominator σ_1^3 with σ^3, the curve matches the analytical prediction (Fig. 4.24). Nevertheless, in axisymmetric or triaxial galaxies, the anisotropic velocity distribution greatly overwhelms discreteness noise fluctuations.

To further explore mesh and discreteness noise effects in anisotropic velocity distributions, we performed a second test. The orbits of 10,000 globular clusters in a strongly triaxial galaxy with a cored density profile and a radially biased velocity distribution at large distances ($\beta \approx 1$) were evolved forward in time under the influence of the generalized dynamical friction force (Eq. 4.67). The generation of this particular model is described in § 4.2.3. Total mass and scale of the galaxy were assumed to be identical to the test before. For this test we restrict to tidal disruption processes from Eq. 4.64 and neglect the long term energy-equipartition driven evaporation. The cluster masses and sizes were distributed according to the single power law mass spectrum (Eq. 4.70) and present day half mass relation (Eq. 4.71). Discreteness noise and mesh effects were artificially enhanced by computing a small number $N = 5 \cdot 10^5$ model over 200 N-body timescales ($\approx$ 3.5 Gyr). Moreover, the overall potential was frequently updated by the SCF algorithm in $\Delta t_{\text{up}} = 1$ intervals. We then compared the timescales until given fractions of GCs were destroyed in computations with identical physical properties apart from different grid size realizations. In this way mesh effects were isolated and analyzed. The numerical outcomes are shown in Figure 4.25. Evidently, the IDW interpolation method narrows grid effects down to insignificant values. The implemented DF routines yield credible results with insignificant errors.

4.3.4. Potential Fluctuations and their Relevance for GC Disruption

Finally, the performance of the disruption routine (§ 4.2.2) has to be evaluated. Notwithstanding that the base functions as well as their derivatives are continuous, summing up these functions might lead to wiggles along the radial direction. It may therefore
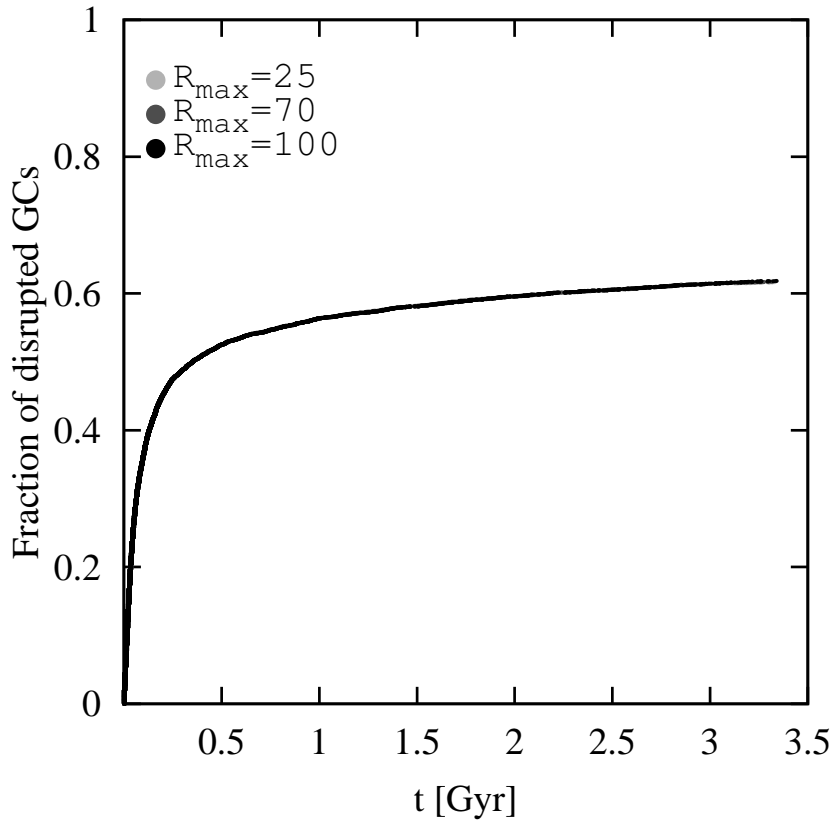
Figure 4.25. Owing to the IDW interpolation method, different grid configurations no longer have any discernible effects on the cluster tidal disruption rate. R_{max} is the outermost mesh size which affects the positioning of the inner grid cells.

be possible that the radial acceleration $a_r(r)$ as well as the evaluation of the Jacobi radius (Eq. 4.64) are affected and a cluster is incorrectly assumed to be destroyed by tidal forces. To guarantee computational outcomes free of biased GC disruption rates, we performed several test integrations by considering tidal disruption processes only, i.e. by neglecting the long term relaxation driven mass loss. Isotropic Hernquist models ($N = 10^6, n = 30, l = 0, \Delta t_{\mathrm{up}} = 1$) with 5,000 randomly distributed clusters were evolved forward in time. They were scaled to the physical properties of MOD1 (M 32) and MOD4 (NGC 4889, Table 4.3), the two galaxies in our sample with the most extreme GC-to-galaxy half mass ratios, r_H/R_H. For each of these models the Jacobian radius was evaluated directly from the SCF algorithm as well as by using an analytical expression for the radial acceleration. The differences in the total number of disrupted clusters N_{dis} were below 0.05% (M 32) and 0.3% (NGC 4889). This corresponds to absolute discrepancies of two and one globular cluster(s) respectively. Being so small in magnitude, these fluctuations can be neglected, particularly because the main computations are performed with twenty times higher particle numbers and without re-evaluation of the potential.

4.4. Results

In this section the main results of our computations are presented. They are divided into three major parts. In § 4.4.1 we discuss general aspects of the globular cluster erosion rate in various galaxies. We present evidence for a new phase in the evolution of globular cluster systems. In the following section (§ 4.4.2) we discuss the formation of cores in globular cluster systems. Finally, in § 4.4.3 we investigate the evolution of the cluster mass function.

4.4.1. Globular Cluster Erosion Rate

In order to evaluate the importance of the various processes for the dissolution of GCs, we performed 48 main computations plus additional 18 models which are required to uncover more systematical effects. Each of these models consists of $2 \cdot 10^7$ stellar particles and 20,000 GCs, distributed according to a power-law mass distribution as given by Eq. 4.70 and the present-day half mass radius relation (Eq. 4.71). We chose to model 20.000 GCs in order to obtain a good statistical significance of our results. The GCs in all computed models (with one exception) have King density profile with concentration parameters $W_0 = 5$. This is a common quantity among globular clusters (§ 4.2.2). For this study we assumed that the overall dynamics of the host galaxy are not influenced by globular cluster evolution processes (§ 4.2.3) and hence all results can be scaled to different total GC numbers. For each of the four representative galaxies shown in Table 4.3 we calculated models with and without central SMBHs, two different density profiles (Hernquist and Sérsic $n = 4$ models)[40] and three different velocity anisotropies ($R_A/R_H = 0.25; 1; \infty$), leading to 12 models per galaxy in total. We chose $R_A/R_H = 0.25$ as the most radially biased model since below this limit galaxies become unstable due to a lack of tangential pressure (Merritt & Aguilar, 1985). The models with $R_A/R_H = \infty$ represent the isotropic case. The central SMBHs masses were adopted from Table 4.3.

We evolved all models for 10 Gyr under the influence of the generalized dynamical friction force. As described in § 4.2.2, clusters were assumed to be destroyed if: (i) the strength of the tidal field, $x = \frac{r_H}{r_J}$, exceeded $x = 0.5$, (ii) relaxation driven mass loss in tidal fields (and SEV) decreases their masses below the limit $m_{GC} = 100 M_\odot$. The temporal evolution of the globular cluster destruction rate is plotted in Fig. 4.26 and absolute numbers of destroyed GCs after 10 Gyr evolution are summarized in Table 4.5.

Tidal Disruption Dominated Phase

We want to emphasize the strong chronological aspect in the evolution of whole globular cluster systems which can be observed in our computations (Fig. 4.26). Significant numbers of GCs are being torn apart early on, i.e. within a few crossing timescales of the galaxy at its half mass radius, $T_{\text{cross}} = 42.26 \left(R_H^3 / M_{\text{GAL}} \right)^{0.5} \text{Myr} \ll T_{\text{Hubble}}$,

---

[40]While at large radii both models agree well with each other, Sérsic $n = 4$ models are centrally more concentrated.
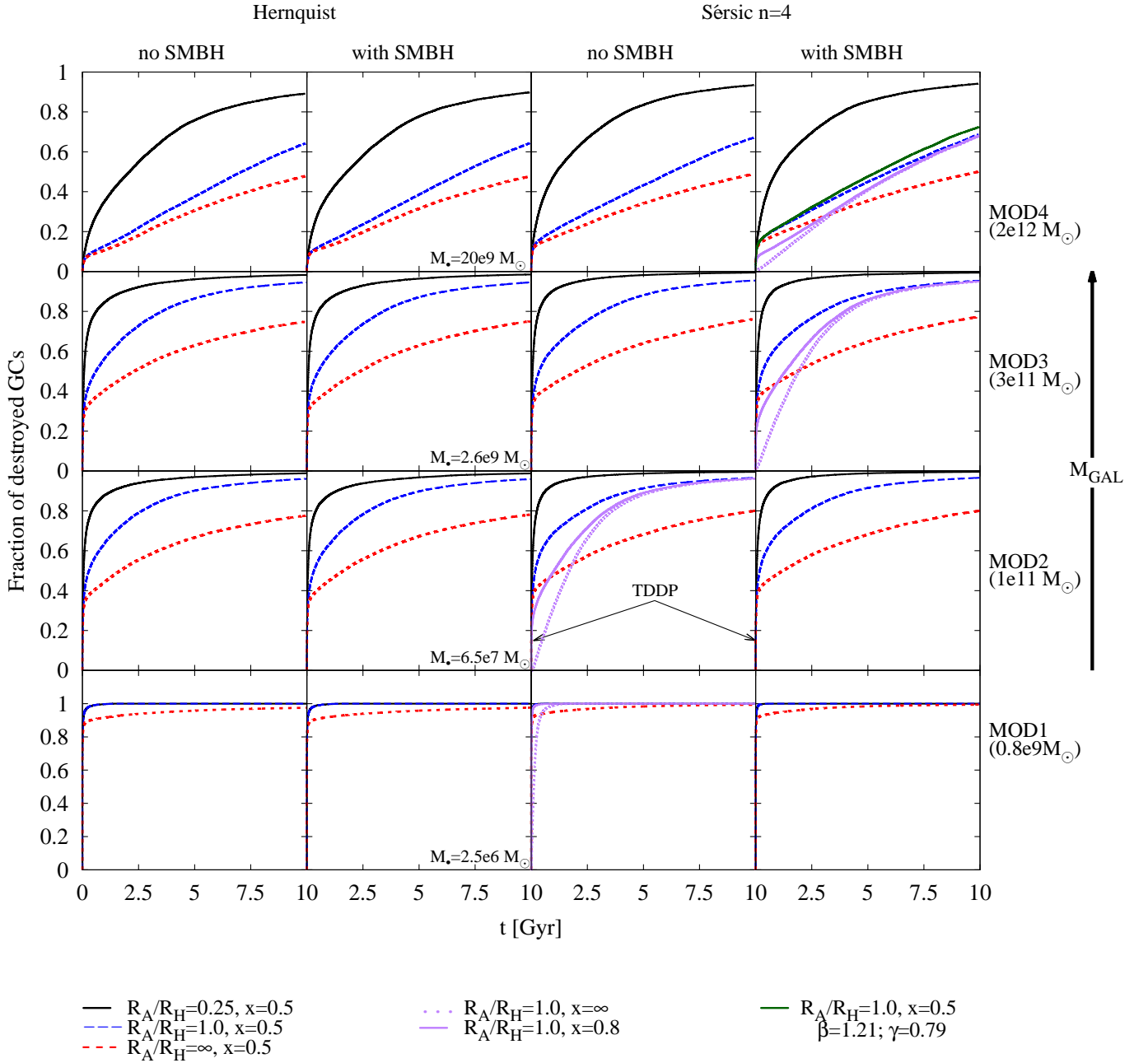
Figure 4.26. The temporal evolution of the fraction of destroyed globular clusters. Most of the destruction occurs at early times. Hence, we call this period the *tidal disruption dominated phase (TDDP)*. It is followed by a relaxation-driven dissolution phase. The destruction rate rises up to 100% in models representing the least massive and compact galaxies (MOD1), independent of their velocity distribution. The rate decreases to 50% in the most luminous and extended galaxies (MOD4) with an isotropic velocity structure. The different colors (i.e. black solid, blue long & red short dashed lines) represent the degree of radial anisotropy characterized by the anisotropy radius R_A of the Osipkov-Merritt models. Purple lines represent computations with more stringent criteria for GC destruction through tidal shocks (§ 4.2.2). Even by using $x = 0.8$ or $x = \infty$ there is a *TDDP* in the most compact models (MOD1). With the exception of one model (green solid line, upper right panel) GCs were assumed to have King profiles with a concentration parameter $W_0 = 5.0$. The green solid line illustrates the difference to a cluster population having parameters between $W_0 = 3.0$ and $W_0 = 5.0$, or more precisely by using $\beta = 1.21$ and $\gamma = 0.79$ in Equation 4.63 (§ 4.2.2).

Model	Example Galaxy	Profile	$M_\bullet[10^9M_\odot]$	$\chi_{0.25}$	χ_1	χ_∞
MOD4	NGC 4889	Hernquist	0	0.89 ± 0.01	0.64 ± 0.01	0.48 ± 0.01
MOD4	NGC 4889	Hernquist	20	0.90 ± 0.01	0.64 ± 0.01	0.48 ± 0.01
MOD4	NGC 4889	Sérsic n=4	0	0.93 ± 0.01	0.67 ± 0.01	0.49 ± 0.01
MOD4	NGC 4889	Sérsic n=4	20	0.94 ± 0.01	0.69 ± 0.01	0.50 ± 0.01
MOD3	IC 1459	Hernquist	0	0.98 ± 0.01	0.95 ± 0.01	0.75 ± 0.01
MOD3	IC 1459	Hernquist	2.6	0.98 ± 0.01	0.95 ± 0.01	0.75 ± 0.01
MOD3	IC 1459	Sérsic n=4	0	0.99 ± 0.01	0.95 ± 0.01	0.76 ± 0.01
MOD3	IC 1459	Sérsic n=4	2.6	0.99 ± 0.01	0.95 ± 0.01	0.77 ± 0.01
MOD2	NGC 4494	Hernquist	0	0.99 ± 0.01	0.96 ± 0.01	0.78 ± 0.01
MOD2	NGC 4494	Hernquist	0.065	0.99 ± 0.01	0.96 ± 0.01	0.78 ± 0.01
MOD2	NGC 4494	Sérsic n=4	0	$1.00 \pm^{0.00}_{0.01}$	0.97 ± 0.01	0.80 ± 0.01
MOD2	NGC 4494	Sérsic n=4	0.065	$1.00 \pm^{0.00}_{0.01}$	0.97 ± 0.01	0.80 ± 0.01
MOD1	M 32	Hernquist	0	$1.00 \pm^{0.00}_{0.01}$	$1.00 \pm^{0.00}_{0.01}$	0.98 ± 0.01
MOD1	M 32	Hernquist	0.0025	$1.00 \pm^{0.00}_{0.01}$	$1.00 \pm^{0.00}_{0.01}$	0.98 ± 0.01
MOD1	M 32	Sérsic n=4	0	$1.00 \pm^{0.00}_{0.01}$	$1.00 \pm^{0.00}_{0.01}$	0.99 ± 0.01
MOD1	M 32	Sérsic n=4	0.0025	$1.00 \pm^{0.00}_{0.01}$	$1.00 \pm^{0.00}_{0.01}$	0.99 ± 0.01
TD & DF only						
MOD4	NGC 4889	Hernquist	0	0.37 ± 0.01	0.10 ± 0.01	0.06 ± 0.01
MOD4	NGC 4889	Hernquist	20	0.42 ± 0.01	0.13 ± 0.01	0.08 ± 0.01
MOD4	NGC 4889	Sérsic n=4	0	0.48 ± 0.01	0.17 ± 0.01	0.12 ± 0.01
MOD4	NGC 4889	Sérsic n=4	20	0.52 ± 0.01	0.20 ± 0.01	0.14 ± 0.01

Table 4.5. In this table the fraction of destroyed clusters (after 10 Gyr of evolution) defined by the parameter $\chi_{\frac{R_A}{R_H}} = \frac{N_{\text{dest}}(t_{\text{end}})}{N_{\text{GC}}(t_0)}|_{\frac{R_A}{R_H}}$ are listed. Their Poisson errors were rounded upwards. In the lower part of the table results from computations without energy-equipartition driven evaporation and without SEV are presented. In this way the SMBH contribution to the *TDDP* in very massive and extended galaxies like NGC 4889 is demonstrated.

which is $T_{\text{cross}} = 3.3$Myr for M 32 and $T_{\text{cross}} = 187$Myr for NGC 4889. This can be seen in form of the steeply rising slope of the fraction of destroyed clusters at very early times. Hence, we characterize it as the *tidal disruption dominated phase (TDDP)*. In isotropic galaxy models (MOD2-MOD4) with central SMBHs and Sérsic $n = 4$ density profiles, approx. 10% (MOD4) to 40% (MOD2) of all GCs are destroyed within the *TDDP*. During the *TDDP*, tidal shocks dominate cluster dissolution processes. It is subsequently followed by a long term relaxation driven dissolution phase in which surviving clusters lose mass more gently. The *TDDP* can be explained as follows. By assuming the initial GC phase space distribution to equal that of the stellar component of the host galaxy, significant numbers of clusters pass close to the galactic center within their first orbit. Here tidal shocks cause rapid mass loss and destruction of GCs. The creation of central cores in the radial globular cluster distribution proceeds rapidly (§ 4.4.2). Evidently, the fraction of destroyed GCs depends on the mass and size of the galaxy i.e. the tidal field. The *TDDP* is most pronounced in very compact and not so massive galaxies and less efficient in very extended galaxies. However, we note that M 32 (MOD1) is an extremely compact galaxy and should not be regarded as representative for common dSph galaxies. We note that there are dwarf elliptical galaxies with much larger spatial scales than that of M 32. See also Figure 2 in Dabringhausen et al. (2008). In such dEs the tidal field is much weaker and the fraction of destroyed GCs is
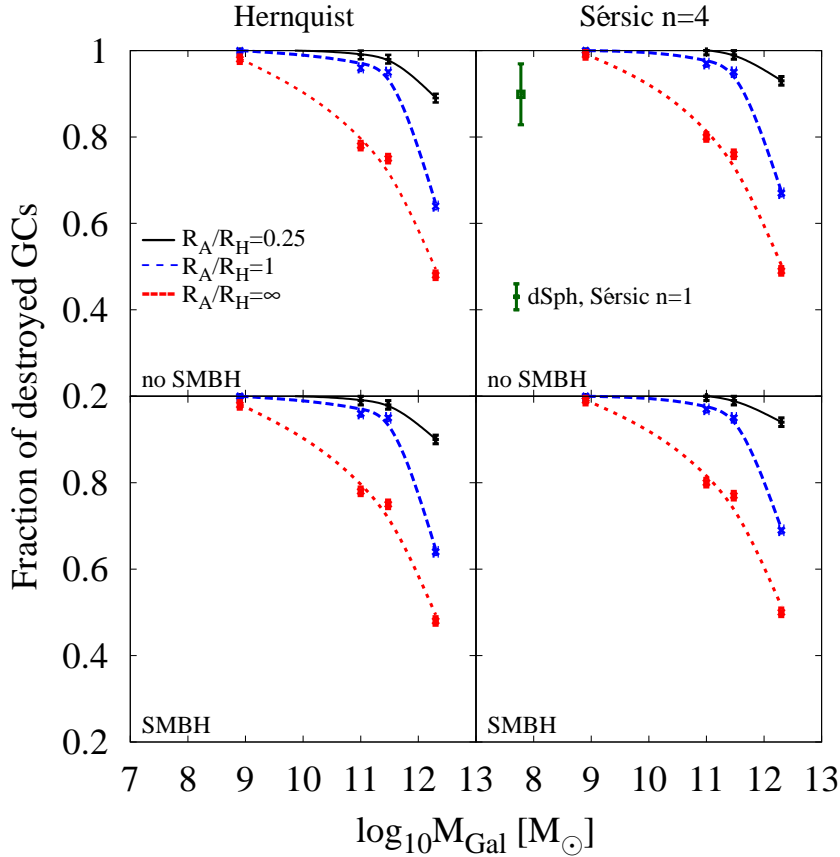
Figure 4.27. The fraction of destroyed clusters versus galaxy mass. The individual data points are listed in Table 4.5. The colored lines are obtained by a weighted cubic spline approximation. The fraction of eroded GCs decreases with increasing galaxy mass. For comparison, we also computed a dSph galaxy model ($M_{GAL} = 6 \cdot 10^7 \, M_\odot$, $R_H = 500 \, pc$) with a Sérsic n=1 density profile and an isotropic velocity distribution (green data point, right upper panel). The erosion rate after 10 Gyr in a dSph galaxy is strongly reduced compared to the more compact M 32 like models. We ran computations with and without dynamical friction. We then used the mean value for the fraction of destroyed clusters since DF has a substantial influence on the erosion rate in this model and the neglection of DF backreaction effects on the stellar density profile (§ 4.5, point vi) could lead to erroneous results.

strongly reduced. For comparison, we computed a dSph galaxy model with a Sérsic n=1 density profile and isotropic velocity distribution (Figure 4.27). In this model we found no indication for a pronounced *TDDP* but a strong contribution from dynamical friction. It drives large amounts of GCs to the center where they would merge together and form a nuclear star cluster.

To get a closer insight into the dynamics of the *TDDP*, we performed eight additional computations with more stringent criteria ($x = 0.8$ or $x = \infty$) for GC disintegration processes by tidal shocking. See the solid and dotted purple lines in Figure 4.26. Evidently, the number of destroyed clusters during the *TDDP* decreases and the overall slope rises less steeply. However, even by using $x = \infty$ there is evidence for the

occurrence of a *TDDP* in the most compact galaxy models MOD1. Interestingly, the *TDDP* does not change the total fraction of destroyed GCs after 10 Gyr but affects the temporal evolution/slope of disintegration processes. In § 4.5 we also critically review our assumptions of initial cluster sizes and galaxy models which affect the strength of the *TDDP*. In Section 4.4.1 we discuss the influence of secondary aspects like the central SMBH and galactic density profile on the *TDDP*.

The influence of the host galaxy on the cluster disruption/dissolution rate becomes also evident if we calculate the normalized arithmetic mean radius, $\overline{R_D}/R_H$. $\overline{R_D}/R_H$ is defined to be the averaged radius at which GCs in our computations were assumed to be destroyed, either by tidal shocks or relaxation driven dissolution. $\overline{R_D}/R_H$ anti correlates with the mass and size of the host galaxy and is largest in the compact M 32-like galaxy ($\overline{R_D}/R_H \approx 1.1$) and lowest in the most massive and extended galaxy, NGC 4889 ($\overline{R_D}/R_H \approx 0.15$).

The existence of a rapid phase in the evolution of GCs might be of strong relevance for the fast build-up of a galaxy's field-star population from eroding clusters. Furthermore, the existence of the *TDDP* might be relevant for SMBH growth processes in the very early universe as some fraction of the debris might enter loss cone trajectories and contribute to the feeding of the central black holes. Especially, as the majority of cluster debris is gravitationally unbound with respect to the black hole potential and gravitational focussing would enlarge its geometric cross section. Interestingly, the phase space distribution of the field stars originating from such a *TDDP* should be complementary to the phase space distribution of the surviving globular clusters which is discussed in § 4.4.2.

Radial Anisotropy

The overall fraction of destroyed globular clusters in spherical galaxies with an isotropic velocity distribution (and no central SMBH) depends on the mass and scale of a galaxy (Table 4.5). While up to 100% of all GCs are destroyed in compact dwarf galaxies like M 32, and $75 - 80\%$ in mid-size galaxies, no more than 50% are eroded over the course of 10 Gyr in the most massive and extended galaxies like NGC 4889 (MOD4). In Figure 4.27 the total fraction of dissolved GCs is plotted as a function of the mass of the galaxy. As can be seen, the initial orbital anisotropy has a considerable impact on the overall globular cluster erosion rate in massive elliptical galaxies. Compared to the specific isotropic galaxy model MOD4 with a Sérsic $n = 4$ and central SMBH, orbital anisotropy increases the fraction of destroyed clusters from 50% ($R_A/R_H = \infty$) to 70% ($R_A/R_H = 1$) and 95% ($R_A/R_H = 0.25$). Different formation or merger histories, and thus different degrees of radial anisotropy, may therefore be a reason for considerable scatter in the total number of surviving GCs in observed elliptical galaxies of similar size and mass.

The fraction of eroded GCs in compact dwarf elliptical galaxies like M 32 (MOD1) centers around 100%. This number is insensitive to the initial velocity distribution. Our computations naturally explain the absence of globular clusters around M 32. However,

early GC stripping by M 31 might have occurred as well.

Density Profile and SMBHs

Secondary aspects like the density profile or central SMBH exert their action only in very massive galaxies. On average the absolute erosion rate is 1-4% higher in the centrally more peaked Sérsic $n = 4$ models. The strongest impact is observed in the galaxy models MOD4 (Table 4.5). These differences can be explained by a higher initial number density of GCs inside the centrally more concentrated Sérsic $n = 4$ models and a steeper gradient of the tidal field.

The impact of SMBHs on the overall GC erosion rate after 10 billion years of evolution is insignificant. The increase of the total destruction rate compared to models without central SMBHs does not exceed the one percent level. This is of the same order as the assumed Poisson error related to statistics. However, this does not mean that SMBHs do not contribute to the exact sequence of GC dissolution processes inside galactic nuclei. It is irrelevant for the overall GC erosion rate (after 10 Gyr) if clusters were eroded continuously or disrupted by the central SMBH during a singe close passage. In order to isolate the impact of SMBHs during the *tidal disruption dominated phase*, computations without relaxation driven mass-loss and SEV were performed (lower part of Table 4.5). Evidently, the $M_\bullet = 2 \cdot 10^{10} M_\odot$ ultramassive black hole inside the reference galaxy MOD4, which has similar physical properties like the BCG NGC 4889, contributed significantly to the number of tidal disruptions.

Secondary aspects like the density profile or SMBH might also become relevant in low density dwarf or irregular galaxies in which the overall gradient of the potential as well as the fraction of tidally disrupted GCs are small.

Dynamical Friction

The influence of dynamical friction on the overall destruction rate in very massive elliptical galaxies is almost negligible. The reasons behind the sub-dominant impact of DF on the GC destruction rate are three-fold:

1. GC masses are distributed according to a single power-law GC mass function (§ 4.2.3). Most initial clusters masses are located at the low mass end of this distribution. Initial SEV further decreases their masses. However, the strength of de-acceleration by DF is proportional to cluster masses (Eq. 4.67 & 4.68). Figure 4.28 compares the influence of DF in models with a single and a double power-law initial cluster mass distribution but otherwise identical physical parameters. In the latter case, DF has a stronger influence on the overall GC erosion rate due to GCs being preferentially more massive. We chose the threshold mass, $m_{\text{TH}} = 2 \cdot 10^5 M_\odot$, with slopes $\beta = 0.2$ below and $\beta = 2$ above m_{TH}.

2. Low mass clusters are particularly susceptible for relaxation driven mass loss. In this way, their masses are continuously decreased so that dynamical friction gets less important
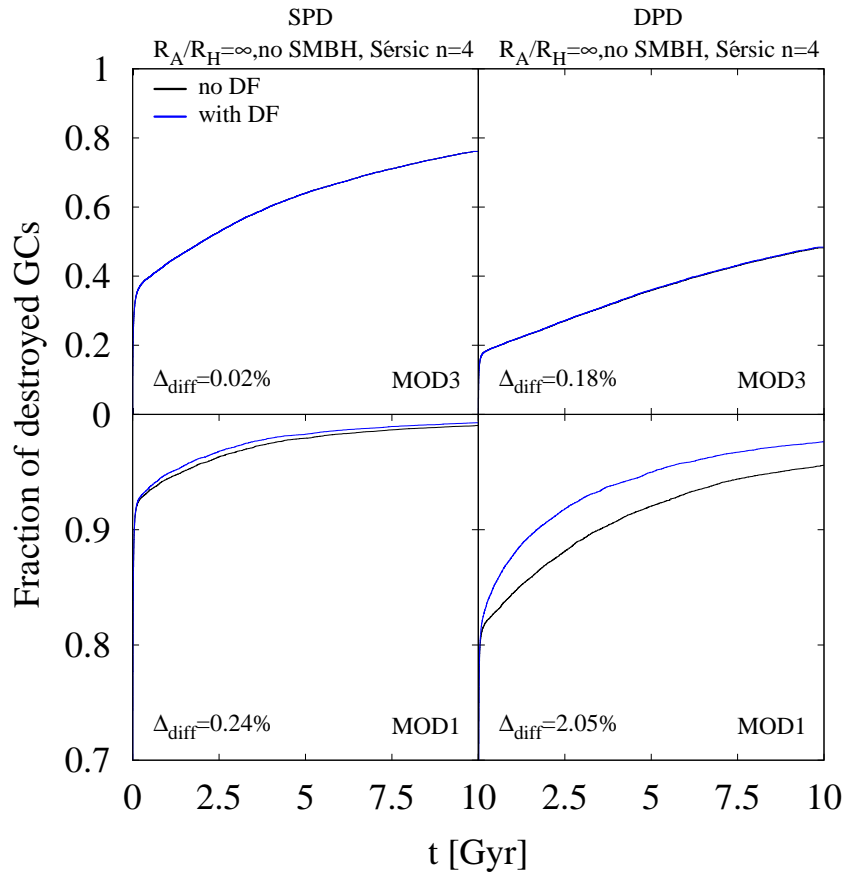
Figure 4.28. The fraction of destroyed clusters depends on the galaxy model, the initial cluster mass distribution (i.e. single (SPD) vs double power-law distribution (DPD)) and dynamical friction. The parameter Δ_{diff} quantifies the difference in the fraction of destroyed GCs after 10 Gyr between models including DF and those where it was ignored.

3. Finally, the strength of DF is proportional to the distance dependent Coulomb logarithm (Eq. 4.69) which becomes zero at small galactocentric distances.

The influence of DF on the overall destruction rate in models with a single power-law cluster mass function is only evident (up to the percentage level) in computations representing the dwarf compact elliptical galaxy M 32 (MOD1). But even in this galaxy, the tidal field strongly dominates GC erosion processes. The only exception where DF contributed significantly to GC erosion processes was observed in the dSph galaxy model (Figure 4.27).

4.4.2. GC Core Formation in Giant Elliptical Galaxies

Galaxy observations reveal the spatial globular cluster distribution to be centrally less peaked than that of the stellar light profile (Harris & Racine, 1979; Forbes et al., 1996; McLaughlin, 1999; Capuzzo-Dolcetta & Mastrobuono-Battisti, 2009). In this section the formation of core profiles as a consequence of globular cluster disintegration processes in tidal fields will be investigated. The initial and final (after 10 Gyr) 2D number den-

sity profiles are compared relative to each other. This is done for the representative galaxies MOD2 (NGC 4494), MOD3 (IC 1459) and MOD4 (NGC 4889) in our sample (§ 4.2.3). The initial population of 20,000 globular clusters was distributed according to the phase space distribution of Sérsic $n = 4$ models with an isotropic and a radially biased $R_A/R_H = 1$ velocity distribution and a central SMBH. The results are shown in Fig. 4.29 from which the following conclusions can be drawn:

1. In all galaxies the central globular cluster distribution becomes flattened by erosion processes. The outer GC number density profiles in isotropic distributions remain intact and it follows that GC distributions around the most massive and largest galaxies should have preserved their initial conditions. These results are in agreement with findings by Vesperini (2000). Cores are more extended in isotropic velocity distributions despite reduced numbers of destroyed clusters. The reason behind this apparent contradiction is related to the existence of the larger number of GCs on eccentric orbits in radially biased velocity configurations. GCs with large galactocentric distances also get close to the galactic center, where (at least) the less massive globular clusters are efficiently eroded. In this way clusters all along the radial distribution become affected over time while the overall shape (i.e. slope) of the number density distribution is conserved. This observation is also consistent with earlier studies (e.g. Vesperini et al. 2003, their figure 5). However, in velocity distributions of Osipkov-Merritt type with the most extreme value $R_A/R_H = 0.25$, mean pericentric distances of GC orbits decrease with increasing galactocentric distance, resulting in a steepening of the outer slope of the GC distribution. This effect is illustrated by means of independent Monte-Carlo Computations in Fig. 4.30. The final number density profile of such a radially biased Sérsic n=4 model with extreme anisotropy, $R_A/R_H = 0.25$, is plotted in Fig. 4.31. The profile shows a less pronounced core than the corresponding isotropic configuration (Fig 4.29). Although there are reports on galaxies in which the globular cluster system profiles at large radii are indeed steeper than the surface brightness profile of their host galaxies, e.g. NGC 4406 (M 86) (Rhode & Zepf, 2004; Capuzzo-Dolcetta & Mastrobuono-Battisti, 2009), such a highly radially biased (initial) GC configuration does not represent a plausible explanation, especially as the degree of radial anisotropy remains still very large at huge galactocentric distances. In the case of M 86 it was suggested by Rhode & Zepf (2004) that tidal truncation induced by M 84 or even the potential well of the Virgo cluster is responsible for the steep profile. The much flatter outer GCS profile of its companion M 84 might support this scenario (Capuzzo-Dolcetta & Mastrobuono-Battisti, 2009).

2. These observations have a profound impact for the study of GC systems. Efforts to compute the number of eroded GCs by simply integrating the central number deficit of clusters by comparison to the stellar light component might be biased. The inferred values should be corrected for the influence of radial anisotropy, mass and scale of the host galaxy.

3. A systematic study in which core sizes are obtained for comparison issues with actual data of real galaxies must also include a threshold mass scale in order to
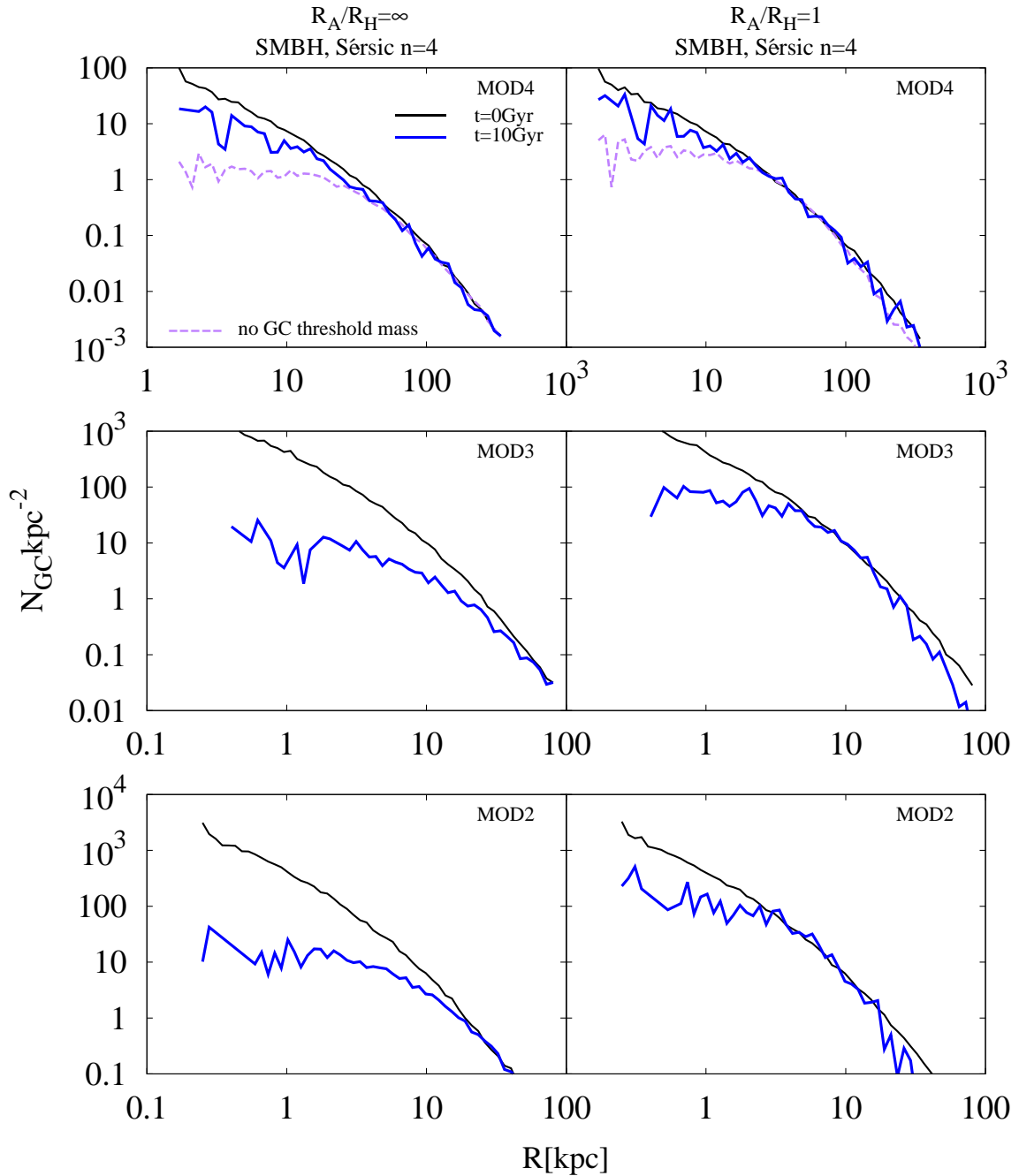
Figure 4.29. Projected 2D number density profiles of globular cluster systems with isotropic and radially biased ($R_A/R_H = 1$) velocity distributions. The slope of the initial GC configuration (solid black curve) also corresponds to the stellar light profile of its host galaxy. In all cases surviving globular cluster systems turn into centrally shallower configurations. Interestingly, central core profiles seem to be less pronounced in radially biased configurations provided they are compared to initial profiles (black lines). In anisotropic velocity configurations, GCs at large spatial scales are eroded more efficiently and the shape of the number density profile is less affected. Observational limitations are handled by using a GCs threshold mass ($M_{th} = 2 \cdot 10^5 M_\odot$ in MOD4, $M_{th} = 10^4 M_\odot$ in MOD3 and MOD2). Core sizes become more pronounced when all clusters are considered (purple curves with $M_{th} = 10^2 M_\odot$). However, core sizes in MOD3 and MOD2 are close to the unfiltered values as the number of GCs below $10^4 M_\odot$ is negligible (see the cluster mass distribution in Fig. 4.34). We note that for comparison issues the blue lines are rescaled by constant factors.
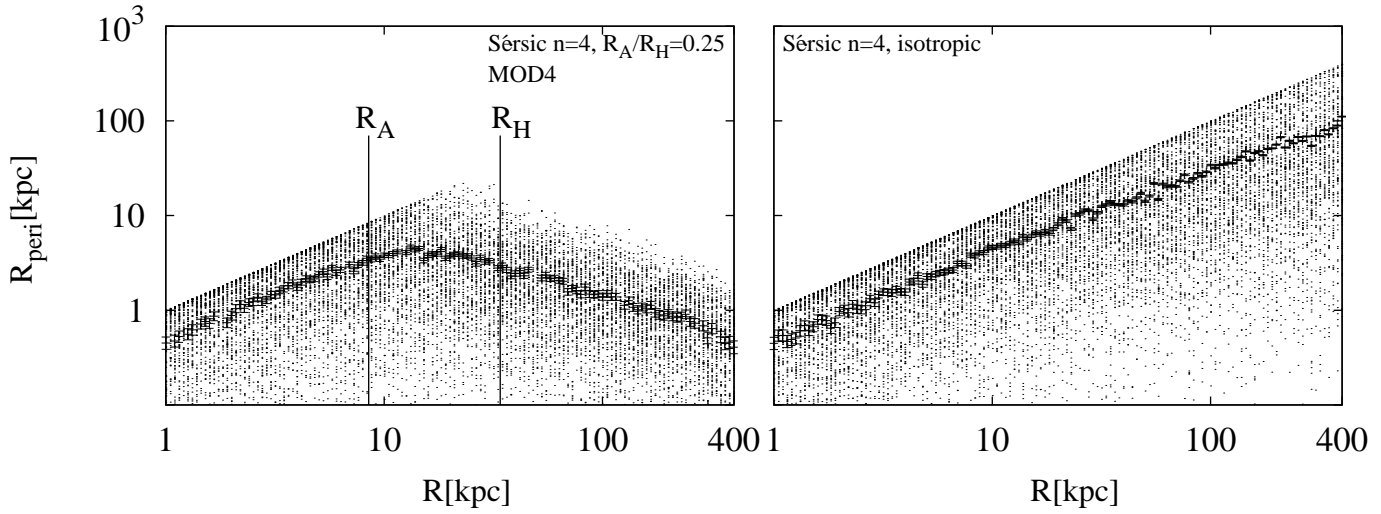
Figure 4.30. Monte-Carlo realizations of pericentre versus galactocentric distances of reference model MOD4 with a Sérsic n=4 density profile, central SMBH and a strongly radially biased (left panels) and isotropic (right panels) velocity distribution. The central (black) data points represents the arithmetic mean. A truncation in the strongly radially biased configuration is evident. It explains why the outer GC profiles in the $R_A/R_H = 0.25$ models are more strongly influenced beyond a characteristic radius being of the order of $R_A = 8.5$ kpc.
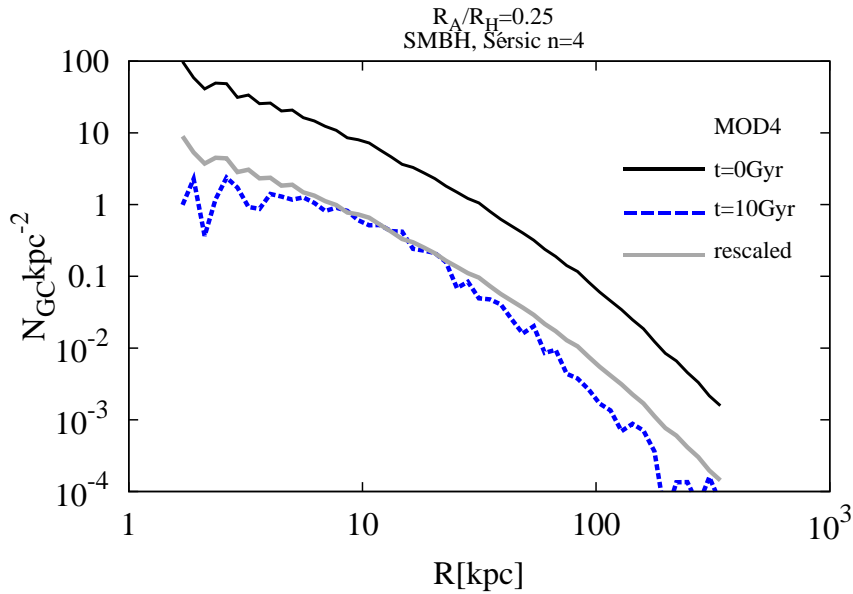
Figure 4.31. Number density profile of a radially biased Sérsic n=4 model with extreme anisotropy, $R_A/R_H = 0.25$. At some point, the slope becomes steeper than that of the initial distribution. There is no GC threshold mass and the gray line corresponds to the rescaled initial profile. The scaling factor is arbitrary and only serves for comparison issues.

mimic observational limitations. We found that core sizes depend on the imposed threshold mass, M_{th}. This is related to the fact that massive GCs are less affected by tidal fields. The effect is shown in Fig. 4.29 for the case of MOD4. Here the
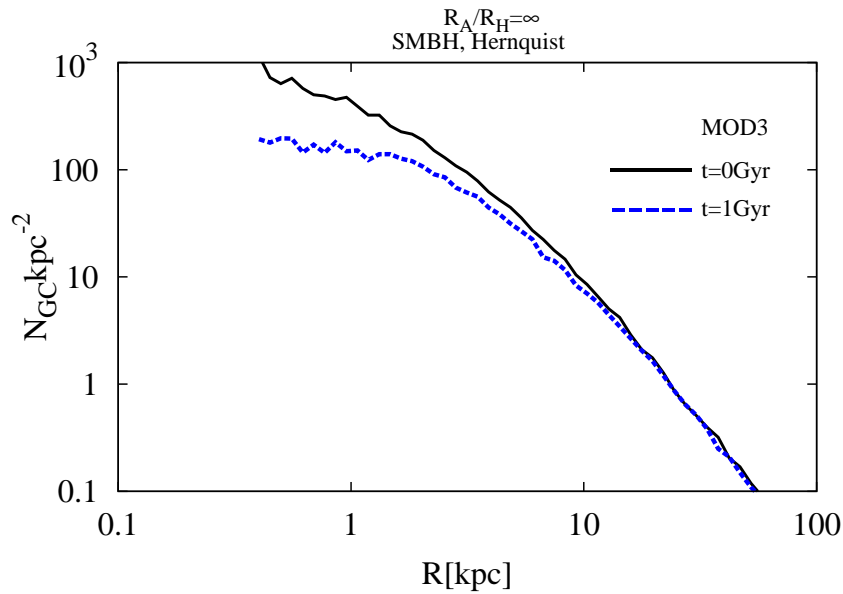
Figure 4.32. The central flattening of the GC number density profile progresses rapidly during the *TDDP*. The blue dashed line corresponds to the GC number density profile after one billion years of evolution. In order to emphasize the contribution from tidal shock driven cluster dissolution, mass loss through relaxation was neglected in this computation. The initial profile follows a Hernquist model.

fraction of surviving GCs is largest and the effect is most pronounced. The purple dashed lines represent the unfiltered number density profiles ($M_{th} = 10^2 \, M_\odot$) whereas the blue lines correspond to GCs in excess of $M_{th} = 2 \cdot 10^5 M_\odot$. This corresponds to the detection limit at the distance of NGC 4889. However, slope differences between unfiltered and those with $M_{th} = 10^4 M_\odot$ are small in MOD2 and MOD3, owing to a negligible fraction of GCs below $10^4 M_\odot$ (Fig. 4.34). The initial profiles (black solid lines) were rescaled to match the final profiles at large galactocentric radii. We take from this figure that the observation of a mass dependent core size of a globular cluster system might be proof of cluster dissolution as the origin of the core (§ 4.1).

4. Core formation occurs on short cosmological timescales. Shortly after the *TDDP* the GC number density profiles are centrally flattened (Fig. 4.32).

5. Despite the influence of radial anisotropy, cores are pronounced in less massive galaxies, as here the percentage of disrupted clusters as well as the ratio $\overline{R_D}/R_H$ is highest. However, spatially extended cores are also found in the most luminous galaxies in the universe, and our computational results indicate that observed GC profiles with central cores (Forbes et al., 1996) are created by disruption and dissolution processes. To see if our computations are in agreement with observations, we plotted GC number density profiles for NGC 4889 (MOD4, blue lines) by taking observational limitations into account. For a typical mass-to-V-band light ratio $Y_V = 1.5$ (McLaughlin & van der Marel, 2005), $m_{GC} = 2 \cdot 10^5 M_\odot$ corresponds to the threshold mass below a GC would be undetected at the distance
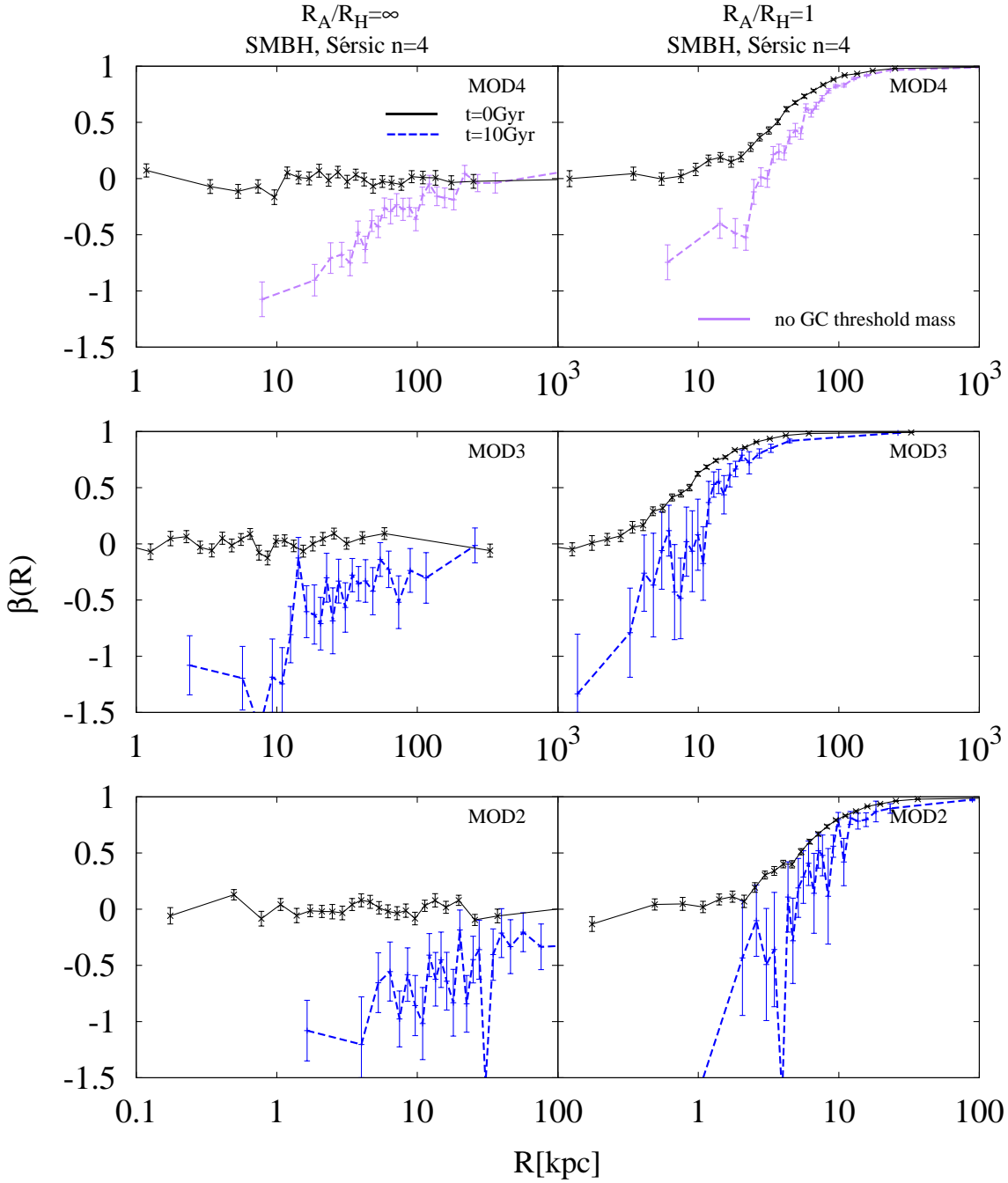
Figure 4.33. Final (3D) anisotropy profiles of the surviving GC population, $\beta = 1 - (\sigma_\theta^2 + \sigma_\phi^2)/2\sigma_r^2$, as a function of the galactocentric radius. The error values are obtained by the bootstrapping method. All GCs are weighted equally without discrimination of their mass/luminosity. In all computed models the central velocity distribution becomes tangentially biased. In configurations with initial radial anisotropy, the tangentially biased region develops within the 3D half mass radius. For MOD2 and MOD3 only clusters above the mass threshold $m_{GC} = 10^4 M_\odot$ are taken into account (blue dashed curves). Unfiltered values are plotted in MOD4.

of $D \approx 100$Mpc (Harris et al., 2009). As can be seen in Fig. 4.29, central flattening is compatible with our models within the central few kpc. This is in agreement with the inner parts of the galaxy $r \approx 3.5$kpc (figure 6 in Harris et al. 2009) where the GC number density profile becomes more shallow than the stellar light profile of NGC 4889. However, in a more realistic scenario, erosion is only partly responsible for the observed central shallow profiles, as in these galaxies' major merger events will also contribute to the spatial flattening of the radial GC density profiles (Bekki & Forbes, 2006).

6. Our computations also reflect the preferential destruction of GCs on elongated orbits and the consequences for the dynamics of the surviving globular cluster system. After 10 Gyr of evolution, the central regions of the plotted models (Figure 4.33) show strong signs of a tangential bias subject to the preferential survival of GCs on circular orbits. In models with initial radial anisotropy, a tangentially biased region develops within the 3D half mass radius. At large distances the radial anisotropy is reduced but still persists at significant levels.

Our computations demonstrate a relation between core sizes of globular cluster systems and the host galaxies mass and velocity distributions. A quantitative evaluation of this correlation will be an interesting task for a follow-up investigation.

4.4.3. Final Globular Cluster Mass Distribution

Fig. 4.34 shows the evolution of the globular cluster mass function (left-hand panels). Results are plotted for three galaxies with Sérsic $n = 4$ density profiles, central SMBHs and a radially biased velocity distributions. Evidently, a moderate degree of radial anisotropy ($R_A/R_H = 1$) transforms initial power-law distributions into bell shaped curves (upper and middle panels) with a peak at approx. 10^5M$_\odot$. However, the GC destruction rate in the most massive and extended galaxies (MOD4) is reduced owing to weak tidal fields. Here, the total fraction of dissolved GCs is not high enough to turn a power-law distribution into a bell shaped curve peaking at $2 \cdot 10^5$M$_\odot$. Stronger initial anisotropy or mass loss related to gas-expulsion (Kroupa & Boily, 2002; Baumgardt et al., 2008) might represent one solution to this discrepancy. Indeed, including gas expulsion during the gas rich cluster phase results in a bell shaped mass function after 10 Gyr of evolution. This is shown in Fig 4.34 in form of green shaded histograms. In order to mimic the effects of gas expulsion on the embedded cluster mass function, we applied Eq. 6,8,9 from Kroupa & Boily (2002). However, even by considering gas expulsion, the distribution peaks at a few 10^4M$_\odot$ instead of $2 \cdot 10^5$M$_\odot$. An additional effect which might naturally explain this discrepancy in the most massive and extended galaxies is related to the idea, that BCGs are partly grown from galaxy mergers of smaller constituents at high redshift. Furthermore, the progenitor galaxies of the most massive ones today were initially much more compact (see e.g. Trujillo et al. 2007, van Dokkum et al. 2008). Within these progenitor galaxies, the cluster mass functions quickly transformed into a bell shaped form before they merged together to form the BCG. Note the fast temporal evolution in Fig. 4.26 in the less massive but more compact galaxies.
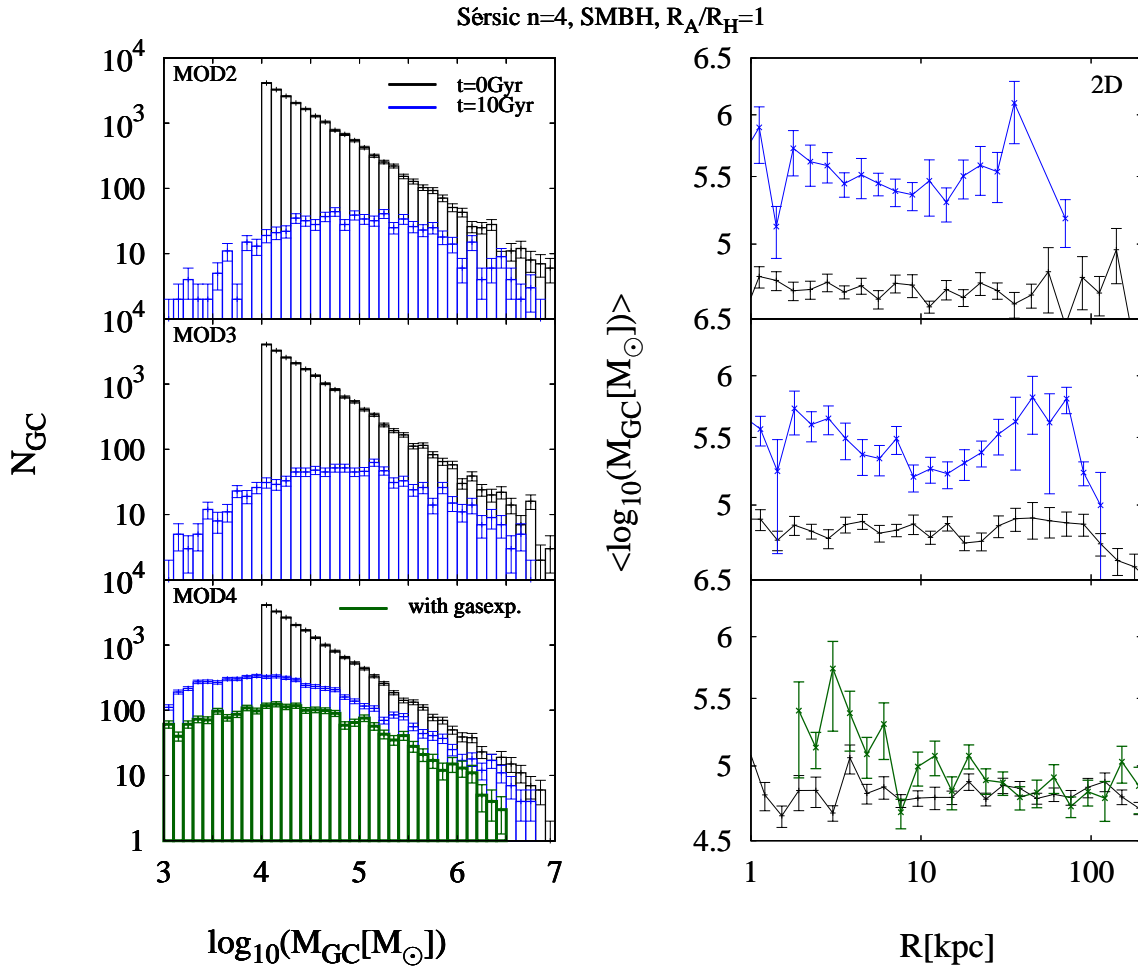
Figure 4.34. Left panels: Initial (black) and final (blue histograms) globular cluster mass functions. Error bars show Poisson uncertainties. A moderate degree of radial anisotropy ($R_A/R_H = 1$) transforms initial power-law distributions into bell shaped curves (MOD2 and MOD3). The inclusion of a primordial gas expulsion phase (green histograms and curve, MOD4) contributes to the shaping of a bell shaped mass function even in the most massive galaxies. Right panels: The globular cluster mean mass versus galactocentric distance obtained for 2D radial binning. Uncertainties were derived via bootstrapping. Despite a large degree of scatter MOD2 & MOD3 are compatible with a constant mean mass over a broad range of galactocentric distances (see text for more details). The mean mass centers around $(3-4) \cdot 10^5 M_\odot$ and is strongly affected by a small number of GCs more massive than a few $10^6 M_\odot$. By assuming a Schechter-type function for initial cluster masses with a particular turn-down mass in the high GC mass regime, the final mean mass might naturally lower to $2 \cdot 10^5 M_\odot$. At least in spiral galaxies in which the initial cluster mass distribution can be observed directly, it is compatible with such a Schechter mass function (Larsen, 2009).

The relations between GC mean masses and galactocentric distances are plotted in the right-hand panels of Fig. 4.34. Despite a large degree of scatter due to low number statistics of surviving clusters, models MOD2 & MOD3 are in agreement with the hypothesis of having a constant GC mean mass over a broad range of galactocentric distances. The residual slope b which is obtained from a linear regression in the

interval $r \in [1 - 200]$ kpc is of the order of the one sigma error bar ($b/\Delta b = 0.98$, MOD2) and ($b/\Delta b = 1.1$, MOD3) respectively. However, the hypothesis of a constant GC mean mass over a large galactocentric distance is rejected for MOD4 ($b/\Delta b = 2.8$). Our results imply that in order to reproduce observed GC properties of BCGs, their merger history from more compact progenitors should be considered.

Although our computations were not designed to reproduce GC characteristics of particular galaxies but instead to illustrate systematics, they already reproduce a lot of observed features: a bell shaped mass distribution, a nearly constant globular cluster mean mass over large galactocentric distances and shallow central number density profiles.

4.5. Critical Discussion and Outlook for Future Work

In this section we will critically review our assumptions and results. This will ease the efforts to identify potential weaknesses and help to improve follow-up studies.

1. The specific implementation of tidal shock and their relevance for disruption processes (§ 4.2.2) requires the orbital angular momentum to be conserved or decreasing due to dynamical friction. This is because a globular cluster does not necessarily become completely unbound by tidal shocks once the ratio of half mass radius to Jacobi radius exceeds $r_H/r_J = 0.5$. If the angular momentum is conserved or monotonically decreasing (which is the case in spherical galaxies), such a cluster will pass the same or an even stronger tidal field within the next crossing timescale until it would become eroded. In all computed galaxies the vast majority of crossing timescales is significantly below the total duration of the integrations, thus yielding safe lower limits on the number of disruptions. A more complicated situation emerges in galaxies deviating from spherical symmetry due to the existence of trajectories where the directional components of the angular momentum vector change in time. In such galaxies, a GC passing a region in which $r_H/r_J = 0.5$ might not repeat doing so for a long time. The criterion for disruption processes by tidal shocks in non-spherical galaxies represents a much more challenging task and will be part of future studies. We also note that our disruption criterion was adjusted by means of direct NBODY6 integrations in one particular galaxy model as well as by using one particular cluster model. However, in order to compensate these shortcomings we changed the parameter x to even higher values than $x = 0.5$ and discussed the systematics. We found no quantitative differences in the outcomes. In addition to that our SEV and relaxation driven dissolution implementation (§ 4.2.2) was calibrated in direct N-body computations (Baumgardt & Makino, 2003) which are based on a Kroupa IMF with lower and upper mass limits $0.1\,M_\odot$ and $15\,M_\odot$. The (initial) mass loss through stellar evolution would increase by using a higher upper mass limit. However, this would mostly affect the initial correction factor which has no influence on the shape of the single power-law GC mass distribution (§ 4.2.3).

2. In our computations GC half mass radii were distributed according to relation Eq. 4.71 and were then integrated by leaving their sizes unchanged. The strength

of tidal shocks and hence the efficiency of tidal disruption processes depends on the compactness (i.e. size) of globular clusters. Therefore, the percentage of disrupted GCs during the *tidal disruption dominated phase* depends on initial cluster sizes. If GCs would be much more compact after their rapid gas expulsion phase, the impact of the *TDDP* on the overall cluster erosion rate would be reduced. In future studies more realistic initial conditions as well as cluster size evolution should be included. However, the same criticism also applies to the used galaxy models which in this study were assumed to be non-evolving. van Dokkum et al. (2008) show that massive elliptical galaxies at high redshifts were more compact than today. In more compact progenitor galaxies, the *TDDP* on the other hand would be very pronounced and might quickly transform a single power-law cluster mass function into a bell shaped form. After (dry) merging processes these galaxies will inflate their sizes but the bell shaped cluster mass function should remain unaffected. In conclusion, the efficiency of the *TDDP* depends on cluster and galaxy size evolution.

3. Massive (elliptical) galaxies display a bimodal color distribution of globular clusters which have different metallicities, kinematics and number density profiles (Zepf & Ashman, 1993; Forbes et al., 1997; Brodie & Strader, 2006; Forbes et al., 2012). These cluster populations are leftovers of different star-formation events. The red and metal rich GC population is centrally more concentrated and follows the stellar light profile of its host galaxy, whereas the number density profile of metal poor GCs is flatter and dominates the GC system at large distances. Our computations address the evolution of the GC distribution which traces the galaxy light and we neglect GC populations which were formed (or accreted) later on.

4. The compact dwarf galaxy M 32 does not contain any globular clusters. Our computations indicate that they might have been eroded in the strong tidal field of this galaxy. The real stellar density profile of M 32 deviates at distances below 15 arcsec ($\approx 55\,\mathrm{pc}$) and above 100 arcsec ($\approx 370\,\mathrm{pc}$) from a Sérsic $n = 4$ profile (Kent, 1987) which we used in our computations. The central density inside M 32 is even higher than the corresponding density of a $n = 4$ profile (see Figure 4 in Kent 1987). This would result in an even stronger tidal field and an increase of the actual disruption rate. Therefore, our results concerning the erosion rate in compact M 32 like dwarf galaxies with Hernquist or Sérsic $n = 4$ density profiles should hold for M 32 itself. However, these results should not be applied to "more common" dwarf spheroidal galaxies (dSph) which are less massive, less dense and which have shallower density profiles (e.g. $n = 1$). The GC erosion rate in dSphs is reduced as indicated by the one computation with a Sérsic $n = 1$ density profile (Figure 4.27).

5. As already mentioned our computations are governed by the stellar density profiles specified in § 4.2.3. The next logical extension would be to use the cumulative density profiles from the stellar, dark matter and gas component. It has to be investigated whether the extended isothermal density profiles of DM halos would significantly alter the GC erosion rate which is dominated by tidal effects deep

within the galaxy where the stellar density dominates.

6. Dynamical friction (§ 4.2.2) is implemented as an external routine in the MUESLI code. While this is a commonly used strategy in numerical investigations, care has to be taken. By assuming GCs to be immune to dissolution processes, all of them would accumulate within given time periods near the center of the galaxy, driving the mass density upwards. In reality, DF is an energy conserving process and while compact objects spiral inwards, stellar mass is driven outwards. These back-reaction effects are not considered in this study. However, due to the sub-dominant role of DF in our computations, back-reaction processes will have a minor impact on the inferred results.

7. The main focus of this paper is about destruction rates of GCs by tidal shocks and relaxation driven mass loss in tidal fields of spherically symmetric galaxies. We kept it simple and neglected the fate of dissolving GCs and how their debris might affect internal dynamics of galaxies, e.g. by forming a nuclear star cluster (Tremaine et al., 1975; Agarwal & Milosavljević, 2011; Antonini, 2013; Gnedin et al., 2014). These issues as well as direct SMBH loss cone studies will be part of later studies. To handle them with our MUESLI code requires detailed understanding of GC dissolution mechanisms in evolving galaxies. Nevertheless, our computations already indicate a chronological aspect in the erosion of globular cluster systems which might be of relevance for the fast build-up of massive black holes in the early universe.

4.6. Conclusions

We developed a versatile code, named MUESLI, designed to investigate the dynamics and evolution of globular cluster systems in elliptical galaxies. It uses the self-consistent field method (SCF) with a time-transformed leapfrog scheme to integrate orbits of field stars and GCs. In this way, velocity-dependent forces like dynamical friction and post-Newtonian effects of central massive black holes can be handled accurately. In order to be able to treat spherical galaxies with anisotropic velocity distributions (as well as non-spherical galaxies), the code uses the ellipsoidal generalization of Chandrasekhar's dynamical friction formula (Pesce et al., 1992). The advantage of MUESLI lies in its flexibility to evaluate the impact of complex physical processes on the erosion rates of globular clusters (GC) in evolving galaxies.

In a first application, we have investigated if flat central cores in GC distributions around massive elliptical galaxies result from tidal disruption events (TDEs) and cluster dissolution processes through relaxation. Furthermore, we explored the question if the strong tidal field within the compact dwarf galaxy M 32 is responsible for lack of GCs in this galaxy.

We used a power-law distribution for the GC masses, and set the initial phase-space distribution of the GCs equal to the stellar phase-space distribution of the host galaxy. The rapid phase of gas expulsion was ignored with the exception of

one model. We assumed two cluster dissolution channels: (i) A slightly modified version of relaxation driven mass loss in tidal fields (which also handles SEV) from Baumgardt & Makino (2003) was implemented. Once a cluster mass becomes less than $m_{GC} = 100M_\odot$, it is assumed to be dissolved by relaxation. Additionally (ii), we identified a tidal disruption criterion in terms of the ratio of cluster half-mass radius, r_H, to Jacobi radius, r_J, in that no cluster was able to survive for a significant amount of time, when the ratio $x = r_H/r_J$ passed a threshold of $x = 0.5$. The condition for globular cluster disruption in tidal fields was calibrated by means of direct N-body experiments. For this purpose, we used the star cluster code NBODY6 to compute the evolution of massive clusters on various orbits within the tidal field of a host galaxy.

We found that, after 10 Gyr of evolution, all computed GC systems show signs of central flattening with the central core size depending in a non-trivial way on the mass, scale and anisotropy profile of the host galaxy and threshold GC mass. Galaxies with highly radially biased velocity distributions lose a significant fraction of clusters also at large galactocentric radii. As a result the cores, in their central density profiles are less pronounced than in galaxies with isotropic distributions. The primary factors which determine the disruption rate of GCs are the half-mass radius and mass of the galaxy and the initial degree of radial anisotropy of the GC system. For host galaxies with an isotropic velocity distribution, the fraction of disrupted globular clusters is nearly 100% in very compact, M 32-like dwarf galaxies.

The rate is lowest in the most massive and extended galaxies (50%) like NGC 4889. The arithmetic mean radius, $\overline{R_D}$, where most GC destruction occurred during the last 10 billion years, is roughly equal to the (3D) half-light radius R_H in compact dwarf ellipticals and drops to $0.15R_H$ in massive elliptical like NGC 4889. An isotropic initial velocity distribution is mostly preserved at large radius ($R > R_H$), while the GC velocity profile close to the galactic center become less radial or even tangentially biased. Different degrees of initial radial anisotropy may be the reason for a considerable scatter in the total number of GCs around more massive elliptical galaxies (see Table 4.5). In compact M 32-like galaxy models with radial anisotropy no single GC survived.

The influence of dynamical friction on the overall GC erosion rate in massive elliptical galaxies is insignificant as long as the initial cluster mass function follows a power-law distribution with slope $\beta = 2$. However, DF yields a small contribution in compact dwarf ellipticals like M 32. Secondary effects like the density profile or the presence of a central massive black hole manifest their influence only in the most massive and extended galaxies. An ultramassive black hole with a mass above ten billion solar masses inside a galaxy like NGC 4889 has a considerable impact on tidal disruption processes. Its presence increases the total fraction of destroyed GCs during the violent phase of tidal disruptions by 2% to 5% in absolute terms.

We also found that globular cluster erosion processes result in a bell shaped GC mass function and a nearly constant relation between GC mean mass and galactocentric distances as long as the galaxies are not too extended and radially biased. Observations

of bell-shaped GC mass functions in extended galaxies may indicate that their GC populations were formed in more compact building blocks of these galaxies, which later merged to form the present-day host.

Finally, our results show a strong chronological aspect in the evolution of globular cluster systems. That is, most tidal disruptions occur at early times, on dynamical timescales of the host galaxy. Hence, we call this a *tidal disruption dominated phase* in the evolution of globular cluster systems. Our simulations strongly suggest that the number of GCs in most galaxies was much higher at their formation. Therefore, depending on the fraction of stars in a galaxy which were born in globular clusters, the debris of the disrupted clusters should constitute a significant amount of a galaxy's field population. In the extreme case that all stars in galaxies were born in globular clusters, our study would imply that larger galaxies like NGC 4889 have to be the merger product of many smaller galaxies and/or that the progenitor galaxies were initially much more compact because otherwise 10-50% of its stellar mass would still have to be locked up in globular clusters (Fig. 4.26). Given the fact that only about 0.1% of all stars seem to be locked up in globular clusters nowadays, our study prefers building blocks of galaxies in the early universe to either have a small fraction of stars being born in very massive globular clusters, or being relatively compact like M 32, or having highly radially biased GC distributions.

Interestingly, we predict the field population coming from disrupted GCs to have complementary orbital properties to the phase space distribution of the surviving clusters. Moreover, we predict the centrally cored GC distributions around SMBHs to be tangentially biased, and thus parts of the field star population to have a pronounced radially biased component from cluster debris. The diffusion of this cluster debris in phase space (in combination with gravitational focussing relevant for unbound matter) might therefore contribute to the rapid growth of SMBHs in the early universe through the refilling of the black hole loss cone. To which degree will be subject to a future study.

Part III

Outlook & Conclusion

Chapter 5

<u>Outlook</u>

5.1. SMBH Loss Cone Refilling through Eroding Globular Clusters

The interaction between globular clusters, SMBHs and their host galaxies was investigated in Chapter 4. We uncovered the existence of a violent phase in the evolution of globular clusters which is called a *tidal disruption dominated phase* (TDDP). During this phase large fractions of clusters on low angular momentum, i.e. on eccentric orbits, were eroded owing to the presence of strong tidal fields near the galactic center. Two separate aspects indicate that there might also be a direct connection to the growth of SMBHs: (i) Field stars from eroding clusters are smeared over phase space but still populate highly eccentric orbits which are susceptible for gravitational capture by the black hole. (ii) The temporal evolution of the TDDP is comparable to the luminous quasar phase.

In the future it has to be investigated to which degree stellar mass objects contribute to the growth of SMBHs during the TDDP. If significant amounts of stars were accreted, this might help to explain the empirical $M_\bullet - N_{\mathrm{GC}}$ relation (see § 2.1.3). In addition to that, it might also help to yield insights into the (presumably) correlated growth of galaxies and SMBHs and the formation of field stars from eroding star clusters. In four separate steps, I will describe how a feasibility study of the aforementioned processes can be carried out.

5.1.1. Initial Conditions

In a first step a representative galaxy model including a central SMBH has to be selected and computed with MUESLI. It should conform with the properties of observed elliptical galaxies in the highly redshifted universe. These galaxies are compact i.e. they have effective radii of the order of 1-3 kpc but are still very massive ($M_{\mathrm{gal}} \approx 10^{11} M_\odot$) (Trujillo et al., 2007; van Dokkum et al., 2008). By assuming a given cluster phase space distribution one can use MUESLI to obtain the position and velocity vectors of clusters being eroded during the TDDP. For the sake of this feasibility study two modifications should be taken into account:

(i) The background potential which is usually evaluated from the particle distribution by means of a basis function approach, i.e. the SCF method, has to be replaced by an

analytical potential. In this way discreteness noise effects are suppressed and there is no need for time intensive testing. An analytical Hernquist profile (Hernquist, 1990) is already implemented into MUESLI. The density ρ and potential ϕ of a Hernquist model have the form:

$$\rho(r) = \frac{Ma}{2\pi r\,(r+a)^3}, \quad \phi(r) = -\frac{GM}{a+r}. \tag{5.73}$$

Here, M is the mass of the galaxy and $a = R_H / \left(1 + \sqrt{2}\right)$ is a scale length which depends on the (3D) half mass radius, R_H.

(ii) The position and velocity vectors of clusters which are destroyed (or significantly eroded) during their first orbits within the galactic nucleus have to be recorded at apogalacticon for reasons which will become obvious in Section 5.1.3. Peri- or apogalcticon passages can be identified by sign changes of the scalar product $\vec{r} * \vec{v}$ $(+ \rightarrow -$ pericenter passage, $+ \rightarrow -$ apocenter passage).

With the phase space distribution of eroded GCs at hand, the second step (§ 5.1.2) can be performed.

5.1.2. Modeling of a Relativistic SMBH

The central black hole potential in the original MUESLI code is approximated with a Keplerian $1/r$-Potential. This is a sufficient approximation as long as one is interested in the tidal destruction of GCs far away from the highly relativistic regime where the Newtonian treatment breaks down (§ 1.2). The situation is entirely different in loss cone studies where cluster debris (i.e. stars) can be swallowed by massive black holes in excess of $M_\bullet = 10^8 \mathrm{M}_\odot$. This is the typical SMBH mass in a massive ($M_{\mathrm{gal}} \approx 10^{11} \mathrm{M}_\odot$) elliptical galaxy. In the following paragraph I will describe the implementation of a relativistic black hole into the modified version of MUESLI.

The first step consists of approximating the Schwarzschild metric with an effective description in a flat space with a fixed global time i.e. the standart Cartesian framework which is used for ordinary N-body computations. There are several ways how this can be done: By making use of Modified-Newtonian potentials (MNPs) or alternatively by using Post-Newtonian (PN) accelerations terms. Both approaches are implemented into MUESLI. I will start with the description of the implemented Modified-Newtonian potentials. Afterwards, I will discuss the Post-Newtonian accelerations terms. All performed tests were conducted by making use of PN acceleration terms. The second step is the implementation of a generalized capture criterion.

Modified-Newtonian Potentials

Despite their mathematical simplicity, MNPs reproduce a lot of general relativistic effects like the relativistic precession of planets around the Sun or even the free-fall behaviour of test particle in the gravitational field of a massive black hole. Unfortunately, there is no MNP which traces all aspects of general relativity. For this reason I implemented four different MNPs (plus the Keplarian potential) into MUESLI. They are

labeled as $\phi_0 - \phi_4$ and can be individually selected depending to the requirement. In this way one can also compare the numerical results relative to each other and obtain a much higher confidence concerning the correct relativistic treatment of the black hole. The SMBH is assumed to be fixed, nonrotating and always located at the origin of the coordinate system. Hence one can write the acceleration of a test particle in the form:

$$\vec{a}(\vec{r}) = -\nabla\phi(\vec{r}) = a(r) \cdot \frac{\vec{r}}{r}. \tag{5.74}$$

The function $a(r)$ will be specified for all MNPs which are implemented into MUESLI. The gravitational radius, $r_g = 0.5r_s = \frac{GM_\bullet}{c^2}$, equals half the Schwarzschild radius, r_s.

1. **Newtonian Potential:**
$$\phi_0(r) = -\frac{GM_\bullet}{r} \tag{5.75}$$

$$a_0(r) = -GM/r^2 \tag{5.76}$$

The Newtonian case is useful for testing and comparing to direct N-body integrations.

2. **Paczynski-Wiita Potential**
$$\phi_1(r) = -\frac{GM_\bullet}{r - 2r_g} \tag{5.77}$$

$$a_1(r) = -\frac{GM_\bullet}{(r - 2r_g)^2} \tag{5.78}$$

This potential was derived by Paczyńsky & Wiita (1980) and is often used for accretion disks and N-body studies (e.g. Chen et al. 2011). Both the potential and the force diverge at $r \to r_s$.

3. **Artemova, Bjoernsson and Novikov Potential (A)**

$$\phi_2(r) = \frac{GM_\bullet}{r_g} \left(-1 + \left(\frac{r - 2r_g}{r} \right)^{\frac{1}{2}} \right) \tag{5.79}$$

$$a_2(r) = -\frac{GM_\bullet}{r^{\frac{3}{2}} \left(r - 2r_g \right)^{\frac{1}{2}}} \tag{5.80}$$

Here, the force diverges at the position of the horizon, i.e. $r \to r_s$ (Artemova et al., 1996).

4. **Artemova, Bjoernsson and Novikov Potential (B)**

$$\phi_3(r) = \frac{GM_\bullet}{2r_g} \ln \left(\frac{r - 2r_g}{r} \right) \tag{5.81}$$

$$a_3(r) = -\frac{GM_\bullet}{r(r - 2r_g)} \tag{5.82}$$

Both the force and the potential diverge at $r \to r_s$. It reproduces the correct free-fall acceleration of test particles at a given position (Artemova et al., 1996).

5. **Wegg Potential**

$$\phi_4(r) = -GM_\bullet \left(\frac{\alpha}{r} + \frac{(1-\alpha)}{r - \beta r_g} + \frac{\gamma r_g}{r^2} \right) \tag{5.83}$$

$$a_4(r) = -GM_\bullet \left(\frac{\alpha}{r^2} + \frac{(1-\alpha)}{(r - \beta r_g)^2} + \frac{2\gamma r_g}{r^3} \right) \tag{5.84}$$

The coefficients are $\alpha = -\frac{4}{3}\left(2 + \sqrt{6}\right)$, $\beta = \left(4\sqrt{6} - 9\right)$ and $\gamma = -\frac{4}{3}\left(2\sqrt{6} - 3\right)$. The potential and the force diverge at $r \to \beta r_g$. To a 1% accuracy this MNP reproduces the correct general relativistic particle precession in the far field limit (Wegg, 2012).

Post-Newtonian Correction Terms

The second strategy to account for relativistic effects is by making use of Post-Newtonian correction terms:

$$\vec{a} = \vec{a}_{PN0} + c^{-2} \cdot \vec{a}_{PN1} + c^{-4} \cdot \vec{a}_{PN2} + c^{-5} \cdot \vec{a}_{PN2.5} + \mathcal{O}(c^{-6}). \tag{5.85}$$

Here c is the speed of light and $\vec{a}_{PN0}$ is the acceleration of the Keplerian $1/r$ potential. The implementation of the PN1, PN2 and PN2.5 term is realized by using the well tested routine from the BHINT integrator (Löckmann & Baumgardt, 2008) which makes use of the Post-Newtonian correction terms presented in Blanchet (2006). The acceleration associated with the PN1 and PN2 terms is responsible for the relativistic perihelion shift whereas the PN2.5 term accounts for energy and angular momentum loss through gravitational wave emission.

Capture Condition

In order to evade problems with 'exploding' accelerations when particles approach horizon sized scales (especially when using MNPs), one has to effectively remove particles before they can enter the black hole. In all computations fully relativistic capture conditions can be used. A detailed derivation and description can be found in § 1.2.2:

$$\begin{cases} r < r_{\text{plunge}} = r_s \left[\tilde{L}^2 - \tilde{L}\sqrt{\tilde{L}^2 - 3} \right], & \tilde{L} = \left| \frac{m\vec{r} \times \vec{v}}{m r_s} \right| = \frac{1}{r_s} |\vec{r} \times \vec{v}| & : & \tilde{L} \geq \sqrt{3} \\ \vec{r} \cdot \vec{v} < 0 & & : & \tilde{L} < \sqrt{3} \end{cases} \tag{5.86}$$

Alternatively, an orbit averaged capture radius, $r_{\text{plunge}} = 4r_s$, can be used as well. In the next section I present two crucial tests which demonstrate the performance of the modified MUESLI code which can study SMBH growth processes.

Testing

To demonstrate the performance of the implemented relativistic black hole, two crucial test are performed. In both tests Post-Newtonian acceleration terms up to the PN2.5 order are used. The first test consists of reproducing the general relativistic contribution to the perihelion shift of the planet Mercury. Mercury fulfills 415 revolutions per

century and following Weinberg (1972), general relativity predicts a positive precession rate (i.e. precesses in direction of its motion) of its perihelion by:

$$\Delta\delta = 43.03 \text{ arcsec/century.} \tag{5.87}$$

The orbital precession rate is defined in radians as:

$$\Delta\delta = 2|\delta\left(r_p\right) - \delta\left(r_a\right)| - 2\pi. \tag{5.88}$$

The parameters r_p and r_a are the perihelion and aphelion. All other contributions to the observed perihelion shift of Mercury are neglected. These are gravitational perturbations induced by the other planets and the flattening of the Sun. As can be seen in Figure 5.35, the numerical outcomes of two computations with different accuracy parameters match the theoretical prediction of general relativity very well. It has to be noted that due to a discrete time resolution only the local minima of the blue and red curves have to match the analytical prediction (black curve).
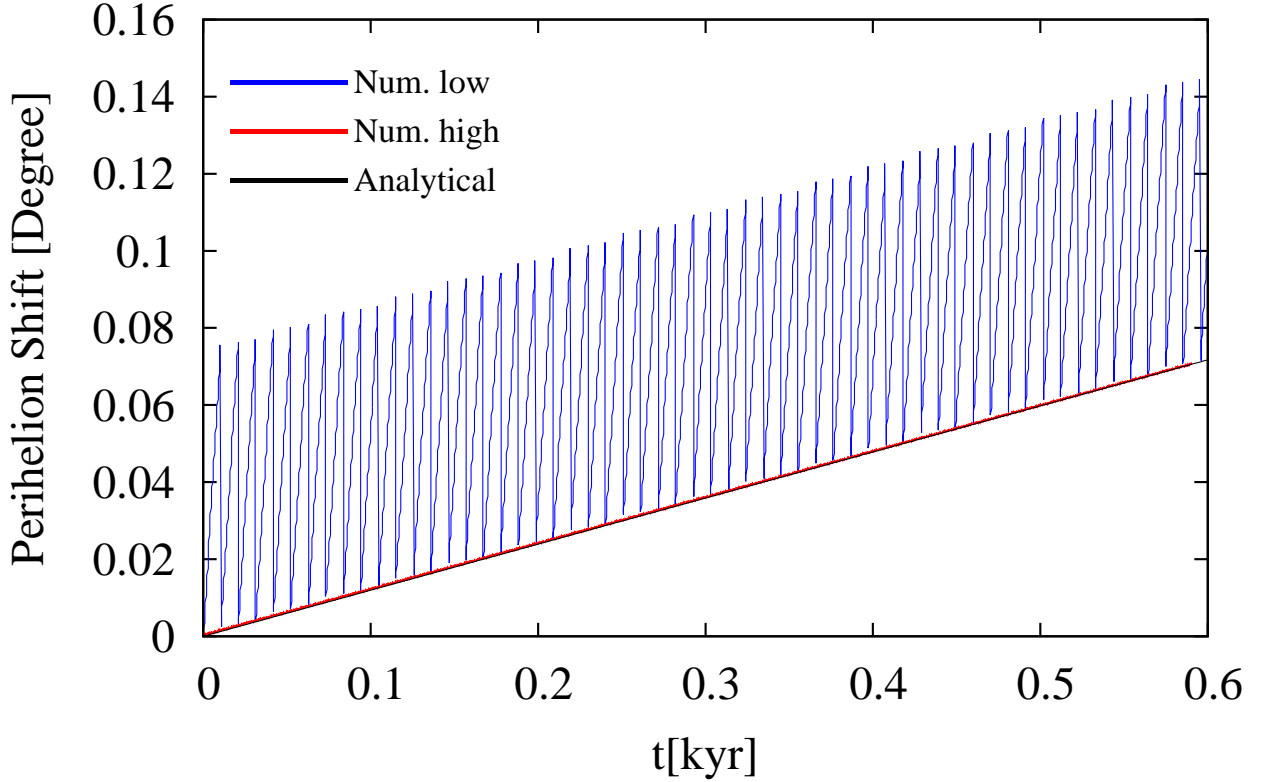

Figure 5.35. Numerical computations of Mercury's perihelion shift (blue and red curve) compared to the fully relativistic prediction (black curve). Owing to a discrete time resolution, the exact identification of the sign shift of the scale product, $\vec{r} * \vec{v}$, at the perihelion passage is not possible. Here, $\vec{r}$ is the position vector of Mercury and $\vec{v}$ is the velocity vector respectively. Therefore, the inferred angle is usually above the prediction and only the local minima of the numerically inferred $\Delta\delta$ values have to agree with the black curve.

The second test is numerically much more challenging and involves the dynamical evolution of a binary SMBH. It illustrates the performance of MUESLI when dealing
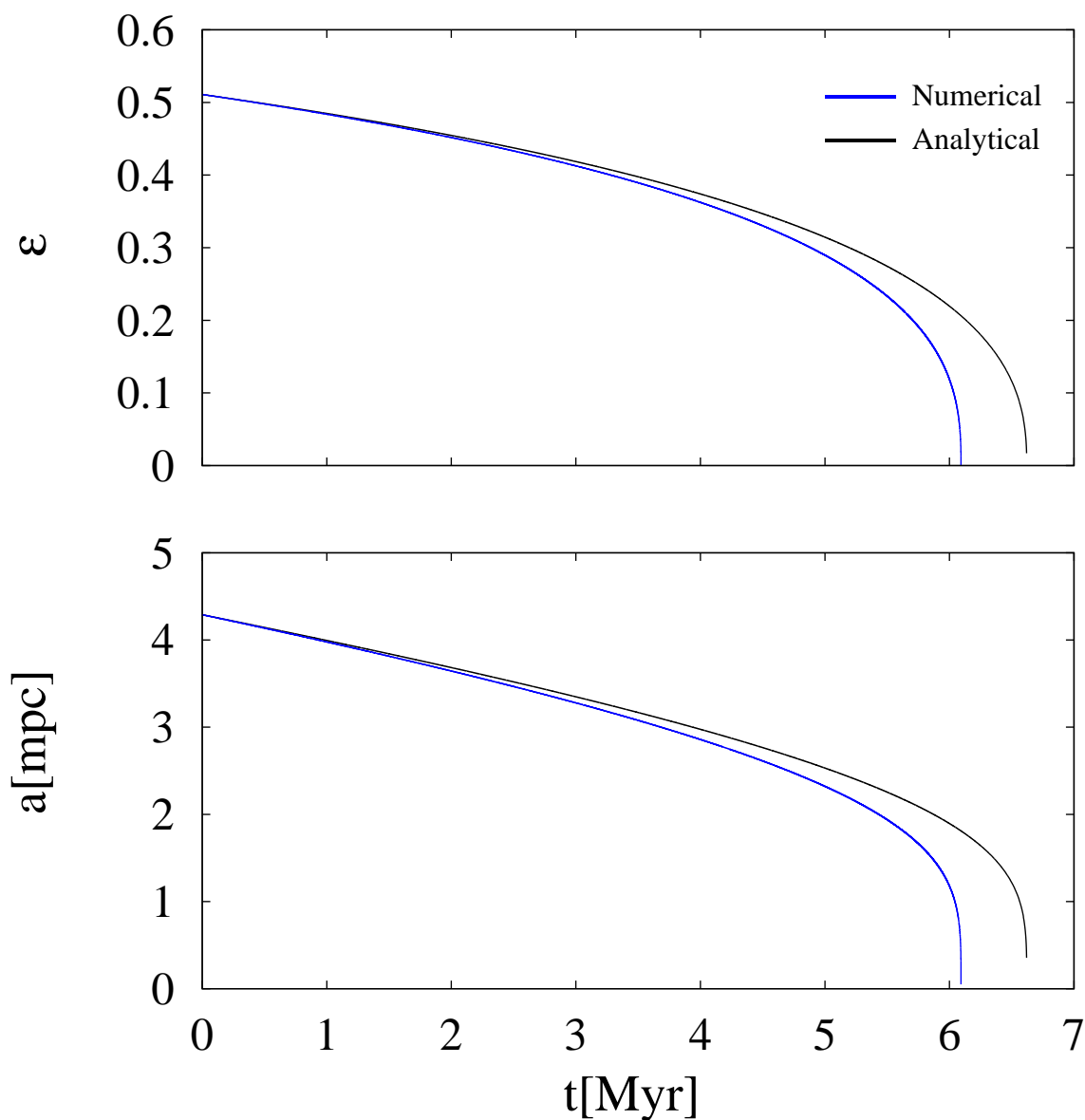
Figure 5.36. Orbital evolution of two bound black holes until coalescence. Black curve corresponds to the prediction of GR whereas the blue curve represents the MUESLI computation. The eccentricity (semi-major axis) evolution is plotted in the upper (lower) panel.

with highly relativistic orbits. The orbital separation between two black holes decreases through the emission of gravitational waves. In the PN description the PN2.5 term is responsible for the orbital decay. Without the PN2.5 term (or alternatively by using a zero mass for the secondary SMBH) the binary stalls and the eccentricity, ϵ, semi-major axis, a, and specific energy, E, are conserved. Indeed, a test computation with MUESLI (up to PN2.5 order) with a secondary SMBH mass, $M_{\bullet 2} = 0$, shows that ϵ and a were constants of motions even at the last (6th) decimal of the output. The binary was evolved forward in time over 10^4 orbital revolutions. This illustrates that the implemented TTL integration method (Appendix A.3) is far superior to most conventional integrators.

The real test, however, is to compute the inspiral of a SMBH into a more massive black hole. The starting point are two SMBHs ($M_{\bullet 1} = 10^8 M_\odot$ and $M_{\bullet 2} = 10^6 M_\odot$) with initial eccentricity $\epsilon \approx 0.5$ and a semi-major axis $a \approx 4.3 \cdot 10^{-3}$ pc. The numerical outcome (Figure 5.36) is compared to the relativistic prediction in form of two coupled differential equations which have to be solved numerically. These equations are derived in Peters (1964) by means of a Taylor expansion of the general relativistic field equations. Following Peters (1964), the differential equations which describe the evolution of the eccentricity and semi-major axis have the form:

$$\frac{d\epsilon}{dt} = -\frac{304\epsilon G^3 M_{\bullet 1} M_{\bullet 2} (M_{\bullet 1} + M_{\bullet 2})}{15c^5 a^4 (1 - \epsilon^2)^{5/2}} \left(1 + \frac{121}{304}\epsilon^2\right) \tag{5.89}$$

and

$$\frac{da}{dt} = -\frac{64\epsilon G^3 M_{\bullet 1} M_{\bullet 2} (M_{\bullet 1} + M_{\bullet 2})}{5c^5 a^3 (1 - \epsilon^2)^{7/2}} \left(1 + \frac{73}{24}\epsilon^2 + \frac{37}{96}\epsilon^4\right). \tag{5.90}$$

In Figure 5.36 the predicted evolution of ϵ and a (black curves) until SMBH coalescence is compared to the numerical outcome of MUESLI (blue curves). The curves agree within a 10% accuracy. The small but still present disagreement between the general relativistic prediction and the numerical outcomes of MUESLI is related to three fundamental and one technical problem:

1. The Post-Newtonian treatment (of PN2.5 order) of general relativistic effects faces limitations in strong gravitational fields $r \approx r_s$ and at very high velocities $v \approx c$.

2. Equations 5.89 and 5.90 do not represent exact solutions to the general relativistic field equations as they are derived from an approximation method as well.

3. MUESLI computes the orbital decay of the secondary SMBH in the potential of a fixed primary black hole. However, Equations 5.89 and 5.90 are relevant for binaries which evolve around a common center of mass, not a fixed one. MUESLI is not designed to compute the merger of nearly equal massive black holes. Instead it is designed to investigate the accretion of stars. Here, the situation is entirely different, as $M_\star << M_\bullet$. In this case the common center of mass lies at the position of the black hole.

4. Computations of SMBH in-spirals are very time intensive. Depending on the initial conditions, the secondary black hole usually goes through millions to billions of orbital revolutions before it plunges into the more massive one. In the computation presented in Figure 5.36, the black hole fulfilled more than $4.5 \cdot 10^6$ orbital revolutions. To compute such a huge number within a reasonable amount of time, the accuracy of integration should be as low as possible. However, a low accuracy might lead to inaccurate results. In Figure 5.37, the accuracy of orbital parameter evolution is plotted for different accuracy parameters. Only at the highest precision (brown and blue curves), the numerical outcomes converge and the agreement between prediction and numerical result improves. However, even with high accuracy, there is still a discrepancy between the prediction and the numerical outcomes as long as one computes the merger of two black holes which start already in the highly relativistic regime ($v(t = 0) \approx c$).
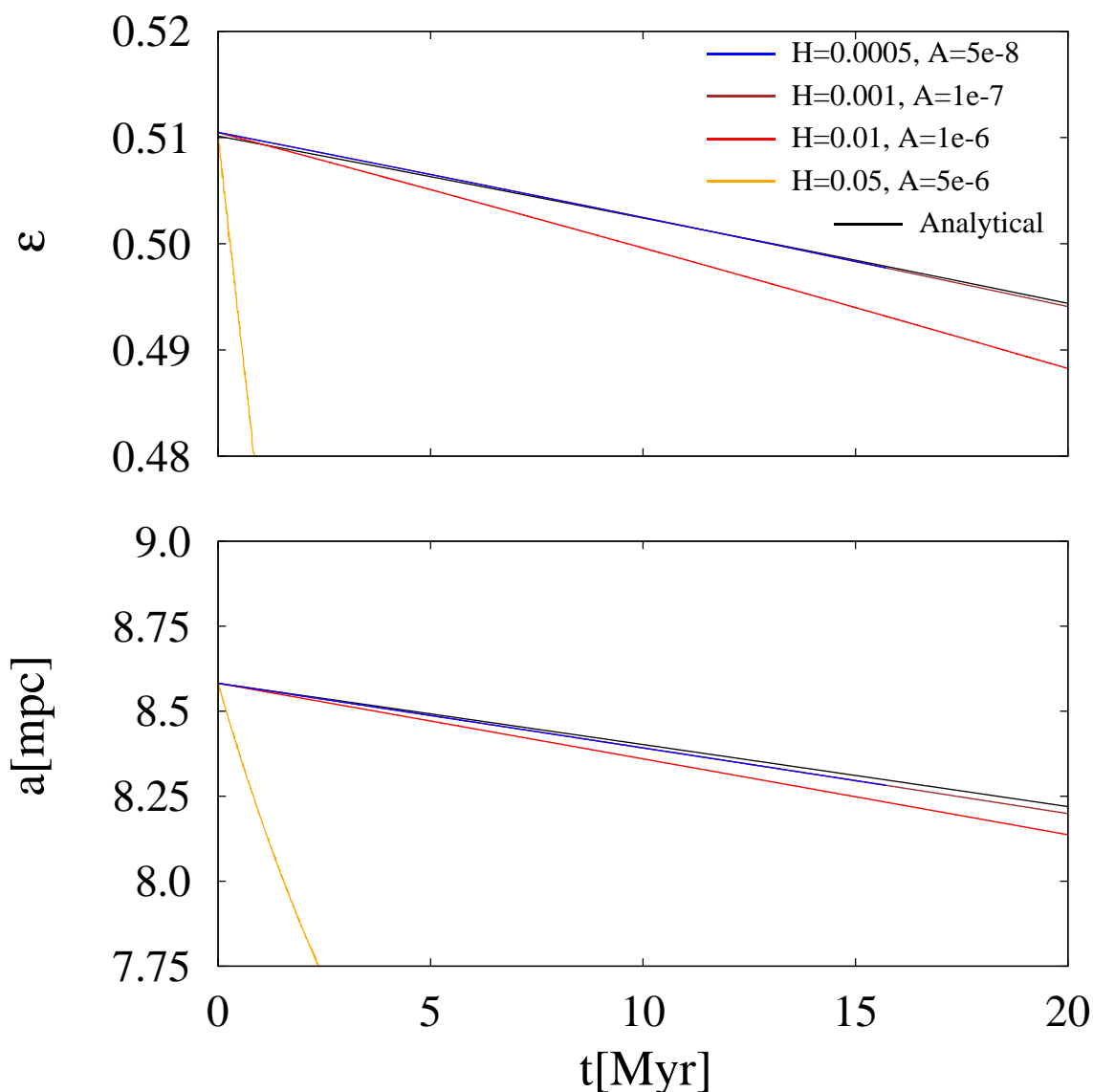
Figure 5.37. Depending on the accuracy, the numerical outcome converges (blue and brown curves). The parameter H is the maximal time step and A is the accuracy parameter (both quantities are given in N-body units).

MUESLI yields credible results (within an order of 10% accuracy) when performing SMBH merger computations. The merger of two SMBHs is an extreme scenario requiring the computation of millions to billions of orbits before coalescence. However, the proposed loss cone study of cluster debris is numerically less challenging and the performance of MUESLI is even better suited for this kind of study. This is related to two aspects: (i) The computation of a few (and not millions of) stellar orbital revolutions is sufficient. Stars which do not fall into the black hole will not do so at all. In the proposed feasibility study, effects like relaxation, tidal distortions of triaxial or axis-symmetrical galaxy potentials or massive perturbers (§ 2.2.2) are neglected. Hence, the angular momentum of a star is a conserved quantity and one has to compute only a

few crossing/orbital timescales. (ii) The center of mass is located at the position of the SMBH as $M_\star << M_\bullet$ and binary evolution around a common center of mass is no issue.

5.1.3. Direct N-body Studies of Eroding Clusters

The 3rd step of this feasibility study consists of computing the 6D phase space distribution of a representative (eroding) star cluster. The tidal field of the host galaxy must have identical physical properties like that used in step 1. The motivation behind using a Hernquist profile for the direct N-body computation is related to the fact that NBODY6 also features this background potential. The physical conditions of the cluster (in terms of $x = r_H/r_j$, see Eq. 4.64 for the definition of r_j) at perigalacticon must equal the disruption criterion which is used in the MUESLI computation for the overall cluster distribution. It makes sense to use a large ($x > 1$) value in order to ensure that a significant fraction of the total mass becomes separated from the potential well of the cluster. The output of the direct N-body computation has to be recorded after the critical pericenter passage at apogalacticon. This is important for the following reason: The smearing of cluster debris over phase space does not happen at the critical pericenter passage where it experiences a powerful tidal shock in excess of $x > 1$, it happens afterwards.

The velocities of all cluster stars have to be reduced by the amount of potential (cluster) energy. This is a necessary correction as the (individual) cluster potential is not considered in a MUESLI computation. Finally, the phase space distribution (i.e. velocity and position vectors) of a representative sample of stars (e.g. n=1000) with respect to the center of mass (of the cluster) have to be recorded.

5.1.4. SMBH Loss Cone Refilling by Eroding Cluster Debris

The 4th step is the final loss cone computation with the modified MUESLI code which includes the relativistic SMBH framework. For this purpose a particle model has to be created in which all destroyed GCs (evaluated in step 1) are replaced by the stellar phase space distribution (at apogalacticon) which was evaluated in step 3. Particle masses have to be weighed with respect to the former GC mass. In this way one can also determine which kind of cluster contributes most significantly to the growth of SMBHs. This is one big advantage compared to a simple loss cone study with equal mass particles and a given phase space distribution. Another improvement is the possibility to investigate the effect of dynamical friction. DF influences the trajectories of very massive GCs in the galactic center. Depending on the Coulomb logarithm, the orbits of very massive GCs might circularize before they are destroyed. In order to obtain meaningful statistics, thousands of eroded GCs have to be replaced by the obtained particle distribution from the direct N-body computation (step 3). This results in millions of particles which have to be integrated forward in time (with MUESLI) up to several crossing times at the half mass radius of the galaxy. The potential and mass of the galaxy (& SMBH) are the same as in step 1 and 3. By assuming that all stars form in

clusters (see e.g. Kroupa 2005) one can scale the inferred SMBH accretion rate properly to the mass of the galaxy to obtain the contribution of clusters to the growth of SMBHs in the early universe. Future studies should also investigate the influence of different velocity distributions and shapes of the galaxy on the growth rate.

5.2. Shape of the GC Specific Frequency versus Galaxy Luminosity Relation

Notwithstanding that the main topic of this PhD study is about the dynamics of SMBHs in galaxies, the developed MUESLI code can be applied to a broad sample of astrophysical problems which are unrelated to black hole physics. In Mieske et al. (2014) we investigated the influence of globular cluster erosion processes on the shape of the relation between specific frequency, $S_N = N_{GC} \cdot 10^{0.4(M_V + 15)}$, and host galaxies absolute V-band magnitude, M_V. We restricted ourselves to the case of elliptical galaxies only.

The specific frequency is not a constant function over M_V, but it has a u-shaped form (Forbes, 2005; Georgiev et al., 2010; Harris et al., 2013). It has a local minimum at intermediate galaxy luminosity $M_V = [-20.5 : -17.5]$ and increases for the least and most luminous (and massive) galaxies. This means that there is either a disproportionate large number of globular clusters in the least and most luminous galaxies or that there is a deficit of GCs in the intermediate mass regime. Two scenarios try to explain the observed u-shape: (i) An environment-dependent variation of the field star versus star cluster/globular cluster formation efficiency (Dekel & Birnboim, 2006) or (ii) subsequent tidal erosion processes which might be more efficient in intermediate mass galaxies. The latter idea dates back to Murali & Weinberg (1997) and Vesperini (2000).

In Brockamp et al. (2014) (i.e. Chapter 4) we found that the size and mass of a galaxy and therefore its averaged density, ρ, strongly affect the survival rate of globular clusters. This result can be explained intuitively. A typical crossing timescale at the half mass radius of a galaxy, R_H, is proportional to $\sqrt{R_H^3/M_{GAL}}$. Here M_{GAL} is the dynamical mass of the galaxy. The number of GC pericenter passages during a Hubble time is thus proportional to $\sqrt{\rho}$. Consequently, if the averaged density is large, the cluster has to survive more pericenter passages than a GC on a similar orbit in a less dense galaxy. In addition to that the Jacobi radius (Eq. 4.64) is smaller in a dense and compact galaxy. Interestingly, the average density of elliptical galaxies is not a constant function over the luminosity scale. It defines a similar u-shaped relation as the specific frequency relation (Misgeld & Hilker, 2011; Mieske et al., 2014). This has major implications for the shaping of S_N through GC erosion. Of course, the situation is complicated by the nonlinear dynamical friction force, the initial mass and size distribution of GCs, the galactic density profile and the initial velocity distribution. Nevertheless, by including all these effects, we found a nearly linear relation (in $f_s - \log(\rho)$ space) between the survival fraction of GCs, f_s, and the average density, $\rho \equiv M_{GAL}/R_H^3$. Therefore, our performed computations yield

strong support to a picture in which GC erosion has shaped S_N. Indeed, if the present S_N is corrected for the fraction of destroyed GC, the primordial relation becomes flatter. By assuming a radially biased initial GC velocity distribution, it becomes nearly flat. In summary, our results indicate that GC erosion strongly contributes to the present-day shape of the GC specific frequency relation and must be taken into account.

However, a lot more needs to be done in order to obtain a complete picture of the related evolution of galaxy and globular cluster systems in general, and its relevance for GC specific frequency in particular: (i) Future numerical studies must also take spiral and dSph galaxies into account. (ii) The diverse aspects which are already discussed in § 4.5 must be included in the analysis. (iii) Furthermore, more realistic settings including time evolving potentials (i.e. galaxy growth through merging or accretion) as well as GC distributions with different metallicities and kinematics (red and blue GCs) must be included as well. Additionally, the strong dependency of erosion processes on the averaged matter density should allow to perform a clean test of the dark matter (DM) paradigm. If the M/L ratio of dSph is really as high as it is usually claimed, the fraction of destroyed clusters should also be very large as they would fulfill more orbits within a given time interval. It must be investigated if the observed large value of S_N is compatible with dSph galaxies being fully dominated by DM or not.

Summary

Although their real power is unleashed within their horizon, massive black holes exert their influence on the dynamics of gas and dust up to distances of hundreds of kpc. Scaled down to an earth sized galaxy, the central black hole would not be bigger than a marble, albeit its accretion powered jet might reach continental dimensions. There is growing evidence that these compact objects have played (and are still playing) a very important role in the formation of structures, including galaxies, groups or even clusters of galaxies.

In the first part of this PhD thesis, I presented an outline of the present-day status of black hole related research. This includes empirical scaling relations (§ 2.1.3) which are important for theoretical model building and for constraining their limitations. For example, the $M_\bullet - R_{break}$ size relation yields useful information on the merger history of SMBHs. I discussed all major SMBH growth channels (§ 2.2) which include cold and hot gas accretion, stellar captures and SMBH merging, followed by two more hypothetical processes uncovered during this PhD thesis.

In the second part of this thesis my own work in form of published papers is presented. The first project (Chapter 3) calculated the (stellar) tidal disruption rate in spherical galaxies hosting central black holes which are less massive than $M_\bullet = 10^7 M_\odot$. Owing to the spherical symmetry of the host galaxy, the only contribution to the stellar accretion rate comes from the relaxation driven refill of the loss cone. By means of direct N-body computations with the NBODY6 software, the disruption rate is found to be nearly independent of the central SMBH mass. This bears implications for the SMBH growth history. While angular momentum diffusion of stars onto loss cone orbits would have no influence on the mass accretion rate of the most massive SMBHs, it might contribute to that of the least massive ones ($M_\bullet = 10^4 - 10^5 M_\odot$). We found that the Galactic Center black hole might tidally disrupt a star every 15000 to 35000 years.

The second project (Chapter 4) was more extensive. We developed a new software named MUESLI. MUESLI stands for Multi-Purpose Elliptical Galaxy SCF + Time-Transformed Leapfrog Integrator. It has a large flexibility and its physical routines can be easily replaced or upgraded. The code is designed to investigate the erosion processes of globular clusters systems in elliptical galaxies. The following initial conditions have an influence on the GC erosion rate and can be taken into account in computations with the MUESLI software. These are: the mass, scale, shape, density and velocity distribution of the host galaxy as well as its central SMBH, the initial mass and velocity distribution of the GCs as well as individual cluster aspects like their sizes, masses and concentration parameters. After selecting the initial conditions, individual

GCs are integrated forward in time. Several internal and external dissolution mechanism like (initial) gas-expulsion, stellar evolution, relaxation driven mass loss in tidal fields, tidal shocks and a form of triaxial dynamical friction act in combination on the cluster mass.

By applying Muesli to a representative set of elliptical galaxies, we were able to reproduce several observed features of these galaxies. (i) The shallow GC number density profiles in massive elliptical galaxies, (ii) tangentially biased velocity distributions in the central parts of a galaxy, (iii) the absence of GCs around M 32 and (iv) a final bell shaped cluster mass function. We also found strong indications for the existence of a rapid phase in the evolution of GC systems. We called this phase a *tidal disruption dominated phase* (*TDDP*). By assuming the initial GC phase space distribution to follow that of the galactic light, a large fraction of GCs passes close to the galactic center within their first orbit. Especially low mass clusters on eccentric (low angular momentum) orbits are destroyed quickly. The *TDDP* might therefore also contribute to SMBH growth in the early universe. If the tidal debris of a GC on a very eccentric orbit is smeared over phase space, some fraction of it might enter loss cone orbits.

The implementation and testing of a relativistic SMBH into the Muesli code is presented in the third part of this PhD study. This is a necessary step in order to perform the loss cone project of GC debris. Finally, I also discussed the contribution of cluster erosion processes for the observed u-shaped specific frequency distribution of GCs in elliptical galaxies.

Bibliography

Aarseth S. J., 1999, PASP, 111, 1333

Aarseth S. J., 2003, Gravitational *N*-body Simulations

Aarseth S. J., 2007, MNRAS, 378, 285

Aarseth, S. J., Tout, C. A., & Mardling, R. A. 2008, The Cambridge N-Body Lectures, 760,

Aarseth, S. J., & Binney, J. 1978, MNRAS, 185, 227

Abramowicz, M. A., & Fragile, P. C. 2013, Living Reviews in Relativity, 16, 1

Agarwal, M., & Milosavljević, M. 2011, ApJ, 729, 35

Ahmad, A., & Cohen, L. 1973, Journal of Computational Physics, 12, 389

van Albada, T. S. 1982, MNRAS, 201, 939

Alexander T., Hopman C., 2009, ApJ, 697, 1861

Allen, S. W., Dunn, R. J. H., Fabian, A. C., Taylor, G. B., & Reynolds, C. S. 2006, MNRAS, 372, 21

Amaro-Seoane P., Freitag M., Spurzem R., 2004, MNRAS, 352, 655

Andersson, L., van Elst, H., Lim, W. C., & Uggla, C. 2005, Physical Review Letters, 94, 051101

Antonini, F. 2013, ApJ, 763, 62

Artemova, I. V., Bjoernsson, G., & Novikov, I. D. 1996, ApJ, 461, 565

Baes, M., & Dejonghe, H. 2002, A&A, 393, 485

Bahcall J. N., Wolf R. A., 1976, ApJ, 209, 214

Bailey V. C., Davies M. B., 1999, MNRAS, 308, 257

Bak, J., & Statler, T. S. 2000, AJ, 120, 110

Battinelli, P., Brandimarti, A., & Capuzzo-Dolcetta, R. 1994, A&AS, 104, 379

Baumgardt, H. 1998, A&A, 330, 480

Baumgardt, H., & Makino, J. 2003, MNRAS, 340, 227

Bibliography

Baumgardt, H., Makino, J., & Ebisuzaki, T. 2004, ApJ, 613, 1133

Baumgardt, H., Makino, J., & Ebisuzaki, T. 2004, ApJ, 613, 1143

Baumgardt H., Gualandris A., Portegies Zwart S., 2006, MNRAS, 372, 174

Baumgardt H., Hopman C., Portegies Zwart S., Makino J., 2006, MNRAS, 372, 467

Baumgardt, H., Kroupa, P., & Parmentier, G. 2008, MNRAS, 384, 1231

Baumgardt, H., Parmentier, G., Gieles, M., & Vesperini, E. 2010, MNRAS, 401, 1832

Bekenstein, J. D. 1973, Phys. Rev. D, 7, 2333

Bekki, K., & Forbes, D. A. 2006, A&A, 445, 485

Bender, R., Saglia, R. P., & Gerhard, O. E. 1994, MNRAS, 269, 785

Berczik P., Merritt D., Spurzem R., Bischof H., 2006, ApJ, 642, L21

Binney, J., & Tremaine, S. 2008, Galactic Dynamics: Second Edition, Princeton University Press, Princeton, NJ, USA,

Blanchet, L. 2006, Living Reviews in Relativity, 9, 4

Blandford, R. D., & Znajek, R. L. 1977, MNRAS, 179, 433

Bondi, H., & Hoyle, F. 1944, MNRAS, 104, 273

Bondi, H. 1952, MNRAS, 112, 195

Bower G. C., 2011, ApJ, 732, L12+

Boylan-Kolchin, M., Ma, C.-P., & Quataert, E. 2004, ApJ, 613, L37

Braeck, S., & Grøn, Ø. 2013, European Physical Journal Plus, 128, 24

Brassart M., Luminet J.-P., 2008, A&A, 481, 259

Brenneman, L. 2013, Measuring the Angular Momentum of Supermassive Black Holes, SpringerBriefs in Astronomy. Laura Brenneman, 2013,

Brockamp, M., Baumgardt, H., & Kroupa, P. 2011, MNRAS, 418, 1308

Brockamp, M., Küpper, A. H. W., Thies, I., Baumgardt, H., & Kroupa, P. 2014, MNRAS, 441, 150

Brodie, J. P., & Strader, J. 2006, ARA&A, 44, 193

Brown, B. A., & Bregman, J. N. 2001, ApJ, 547, 154

Brügmann, B., González, J. A., Hannam, M., Husa, S., & Sperhake, U. 2008, Phys. Rev. D, 77, 124047

Burkert, A., & Tremaine, S. 2010, ApJ, 720, 516

Campanelli, M., Lousto, C., Zlochower, Y., & Merritt, D. 2007a, ApJ, 659, L5

Caon N., Capaccioli M., D'Onofrio M., 1993, MNRAS, 265, 1013

Cappellari, M., Verolme, E. K., van der Marel, R. P., et al. 2002, ApJ, 578, 787

Cappelluti, N., Ajello, M., Rebusco, P., et al. 2009, A&A, 495, L9

Capuzzo-Dolcetta, R. 1993, ApJ, 415, 616

Capuzzo-Dolcetta, R., & Tesseri, A. 1997, MNRAS, 292, 808

Capuzzo-Dolcetta, R., & Vicari, A. 2005, MNRAS, 356, 899

Capuzzo-Dolcetta, R., & Mastrobuono-Battisti, A. 2009, A&A, 507, 183

Carrasco, E. R., Gomez, P. L., Verdugo, T., et al. 2010, ApJ, 715, L160

Casertano S., Hut P., 1985, ApJ, 298, 80

Chandrasekhar, S. 1943, ApJ, 97, 255

Chandrasekhar S., 1943b, ApJ, 97, 263

Chandrasekhar S., 1943c, ApJ, 98, 54

Chatterjee P., Hernquist L., Loeb A., 2002, ApJ, 572, 371

Chen, X., Sesana, A., Madau, P., & Liu, F. K. 2011, ApJ, 729, 13

Chernoff D. F., Weinberg M. D., 1990, ApJ, 351, 121

Ciotti, L., & Bertin, G. 1999, A&A, 352, 447

Cenko, S. B., Krimm, H. A., Horesh, A., et al. 2012, ApJ, 753, 77

Crocker R. M., Aharonian F., 2011, Physical Review Letters, 106, 101102

Dabringhausen, J., Hilker, M., & Kroupa, P. 2008, MNRAS, 386, 864

Dale J. E., Davies M. B., Church R. P., Freitag M., 2009, MNRAS, 393, 1016

de Boer, K., Seggewiss, W., 2008, Stars and Stellar Evolution, EDP Sciences

de Zeeuw, T. 1985, MNRAS, 216, 273

Dehnen W., Odenkirchen M., Grebel E. K., Rix H.-W., 2004, AJ, 127, 2753

Dekel, A., & Birnboim, Y. 2006, MNRAS, 368, 2

Devecchi, B., & Volonteri, M. 2009, ApJ, 694, 302

Di Matteo, T., Springel, V., & Hernquist, L. 2005, Nature, 433, 604

Di Matteo, T., Khandai, N., DeGraf, C., et al. 2012, ApJ, 745, L29

Bibliography

Dinescu D. I., Girard T. M., van Altena W. F., 1999, AJ, 117, 1792

Doeleman, S., Agol, E., Backer, D., et al. 2009, astro2010: The Astronomy and Astrophysics Decadal Survey, 2010, 68

Doeleman, S. S., Fish, V. L., Schenck, D. E., et al. 2012, Science, 338, 355

Donoso, E., Yan, L., Stern, D., & Assef, R. J. 2013, arXiv:1309.2277

Dotan, C., Rossi, E. M., & Shaviv, N. J. 2011, MNRAS, 417, 3035

Dressler, A. 1979, ApJ, 231, 659

Dubois, Y., Gavazzi, R., Peirani, S., & Silk, J. 2013, MNRAS, 433, 3297

Duncan M. J., Shapiro S. L., 1983, ApJ, 268, 565

Edge, A. C. 2001, MNRAS, 328, 762

Elmegreen, B. G. 2010, ApJ, 712, L184

Emsellem, E. 2013, MNRAS, 433, 1862

Ernst A., Just A., 2013, MNRAS, 429, 2953

Esquej, P., Saxton, R. D., Komossa, S., et al. 2008, A&A, 489, 543

Faber, S. M., Tremaine, S., Ajhar, E. A., et al. 1997, AJ, 114, 1771

Fabian A. C., 1999, MNRAS, 308, L39

Fabian, A. C., & Rees, M. J. 1995, MNRAS, 277, L55

Fabian, A. C., Johnstone, R. M., Sanders, J. S., et al. 2008, Nature, 454, 968

Fabian, A. C. 2012, ARA&A, 50, 455

Fabian, A. C., Sanders, J. S., Haehnelt, M., Rees, M. J., & Miller, J. M. 2013, MNRAS, 431, L38

Fabian, A. C., Walker, S. A., Celotti, A., et al. 2014, MNRAS, 442, L81

Fall, S. M., & Zhang, Q. 2001, ApJ, 561, 751

Fasano, G., Bettoni, D., Ascaso, B., et al. 2010, MNRAS, 404, 1490

Feng, J. L. 2010, ARA&A, 48, 495

Forbes, D. A. 2005, ApJ, 635, L137

Forbes, D. A., Franx, M., Illingworth, G. D., & Carollo, C. M. 1996, ApJ, 467, 126

Forbes, D. A., Brodie, J. P., & Grillmair, C. J. 1997, AJ, 113, 1652

Forbes, D. A., & Kroupa, P. 2011, PASA, 28, 77

Forbes, D. A., Ponman, T., & O'Sullivan, E. 2012, MNRAS, 425, 66

Ferrarese, L., & Ford, H. 2005, Space Science Reviews, 116, 523

Ferrarese, L., & Merritt, D. 2000, ApJ, 539, L9

Finkelstein, D. 1958, Phys. Rev., 110, 965

Frank J., Rees M. J., 1976, MNRAS, 176, 633

Freitag M., Amaro-Seoane P., Kalogera V., 2006, ApJ, 649, 91

Freitag, M., Dale, J. E., Church, R. P., & Davies, M. B. 2008, IAU Symposium, 245, 211

Fukushige T., Makino J., Kawai A., 2005, PASJ, 57, 1009

Gebhardt, K., et al. 2000, ApJ, 539, L13

Gebhardt, K., & Thomas, J. 2009, ApJ, 700, 1690

Gebhardt, K., Adams, J., Richstone, D., et al. 2011, ApJ, 729, 119

Georgiev, I. Y., Puzia, T. H., Goudfrooij, P., & Hilker, M. 2010, MNRAS, 406, 1967

Gezari, S., Basa, S., Martin, D. C., et al. 2008, ApJ, 676, 944

Gezari, S., Heckman, T., Cenko, S. B., et al. 2009, ApJ, 698, 1367

Ghisellini, G., Foschini, L., Volonteri, M., et al. 2009, MNRAS, 399, L24

Ghisellini, G., Haardt, F., Della Ceca, R., Volonteri, M., & Sbarrato, T. 2013, MNRAS, 432, 2818

Gieles, M., Portegies Zwart, S. F., Baumgardt, H., et al. 2006, MNRAS, 371, 793

Gieles, M., Baumgardt, H., Heggie, D. C., & Lamers, H. J. G. L. M. 2010, MNRAS, 408, L16

Gillessen, S., Eisenhauer, F., Trippe, S., et al. 2009, ApJ, 692, 1075

Gnedin, O. Y., & Ostriker, J. P. 1997, ApJ, 474, 223

Gnedin O. Y., Ostriker J. P., 1999a, ApJ, 513, 626

Gnedin O. Y., Hernquist L., Ostriker J. P., 1999b, ApJ, 514, 109

Gnedin, O. Y., Ostriker, J. P., & Tremaine, S. 2014, ApJ, 785, 71

Graham, A. W., & Spitler, L. R. 2009, MNRAS, 397, 2148

Gualandris, A., & Merritt, D. 2008, ApJ, 678, 780

Gualandris, A., Dotti, M., & Sesana, A. 2012, MNRAS, 420, L38

Guillochon J., Ramirez-Ruiz E., Rosswog S., Kasen D., 2009, ApJ, 705, 844

Bibliography

Gültekin, K., Richstone, D. O., Gebhardt, K., et al. 2009, ApJ, 698, 198

Hairer E., Lubich C., Wanner G., 2003, Acta Numerica, 12, 399

Halpern J. P., Gezari S., Komossa S., 2004, ApJ, 604, 572

Hamilton, A. J. S. 2012, arXiv:1210.4541

Hamilton, A. J. S., & Lisle, J. P. 2008, American Journal of Physics, 76, 519

Häring, N., & Rix, H.-W. 2004, ApJ, 604, L89

Harris, W. E. 1986, AJ, 91, 822

Harris, W. E., & Racine, R. 1979, ARA&A, 17, 241

Harris, W. E. 1993, The Globular Cluster-Galaxy Connection, 48, 472

Harris, W. E., Kavelaars, J. J., Hanes, D. A., Pritchet, C. J., & Baum, W. A. 2009, AJ, 137, 3314

Harris, G. L. H., & Harris, W. E. 2011, MNRAS, 410, 2347

Harris, W. E., Harris, G. L. H., & Alessi, M. 2013, ApJ, 772, 82

Harris, G. L. H., Poole, G. B., & Harris, W. E. 2014, MNRAS, 438, 2117

Hashimoto, Y., Funato, Y., & Makino, J. 2003, ApJ, 582, 196

Hasinger, G., Miyaji, T., & Schmidt, M. 2005, A&A, 441, 417

Haşegan, M., Jordán, A., Côté, P., et al. 2005, ApJ, 627, 203

Hawking, S. W. 1974, Nature, 248, 30

Heggie, D. C., & Mathieu, R. D. 1986, The Use of Supercomputers in Stellar Dynamics, 267, 233

Heggie, D., & Hut, P. 2003, The Gravitational Million-Body Problem by Douglas Heggie and Piet Hut. Cambridge University Press, 2003, 372 pp.,

Hénon M., 1961, AnAp, 24, 369

Hernandez, X., & Lee, W. H. 2010, MNRAS, 404, L6

Hernquist, L. 1990, ApJ, 356, 359

Hernquist, L., & Ostriker, J. P. 1992, ApJ, 386, 375

Herrnstein, J. R., Moran, J. M., Greenhill, L. J., & Trotter, A. S. 2005, ApJ, 629, 719

Hlavacek-Larrondo, J., Fabian, A. C., Edge, A. C., & Hogan, M. T. 2012, MNRAS, 3158

Hicks, A. K., & Mushotzky, R. 2005, ApJ, 635, L9

Hilker M., Baumgardt H., Infante L., Drinkwater M., Evstigneeva E., Gregg M., 2007, A&A, 463, 119

Holley-Bockelmann, K., Mihos, J. C., Sigurdsson, S., Hernquist, L., & Norman, C. 2002, ApJ, 567, 817

Hopkins, P. F., Hernquist, L., Cox, T. J., Robertson, B., & Krause, E. 2007, ApJ, 669, 45

Hopkins P. F., Hernquist L., 2010, MNRAS, 407, 447

Hopkins P. F., Quataert E., 2010, MNRAS, 407, 1529

Hopman C., 2009, ApJ, 700, 1933

Ivanov P. B., Chernyakova M. A., 2006, A&A, 448, 843

Jaffe, W. 1983, MNRAS, 202, 995

Jahnke, K., & Macciò, A. V. 2011, ApJ, 734, 92

Johannsen, T., Psaltis, D., Gillessen, S., et al. 2012, ApJ, 758, 30

Jordán, A., Côté, P., Blakeslee, J. P., et al. 2005, ApJ, 634, 1002

Jorgensen, I., Franx, M., & Kjaergaard, P. 1996, MNRAS, 280, 167

Just A., Berczik P., Petrov M. I., Ernst A., 2009, MNRAS, 392, 969

Karachentsev, I. D., Karachentseva, V. E., Huchtmeier, W. K., & Makarov, D. I. 2004, AJ, 127, 2031

Kauffmann, G., White, S. D. M., & Guiderdoni, B. 1993, MNRAS, 264, 201

Kent, S. M. 1987, AJ, 94, 306

Khan, F. M., Holley-Bockelmann, K., Berczik, P., & Just, A. 2013, ApJ, 773, 100

Khan, F., Holley-Bockelmann, K., & Berczik, P. 2014, arXiv:1405.6425

Kelly, B. C., & Merloni, A. 2012, Advances in Astronomy, 2012,

Kelly, B. C., & Shen, Y. 2013, ApJ, 764, 45

Kerr, R. P. 1963, Physical Review Letters, 11, 237

Kesden, M. 2012, Phys. Rev. D, 85, 024037

King I., 1962, AJ, 67, 471

King, A. 2003, ApJ, 596, L27

Kochanek C. S., 1992, ApJ, 385, 604

Komatsu, E., Dunkley, J., Nolta, M. R., et al. 2009, ApJS, 180, 330

Bibliography

Komossa, S. 2002, Reviews in Modern Astronomy, 15, 27

Komossa, S. 2002, Lighthouses of the Universe: The Most Luminous Celestial Objects and Their Use for Cosmology, 436

Komossa, S. 2003, The Astrophysics of Gravitational Wave Sources, 686, 161

Komossa, S., Halpern, J., Schartel, N., et al. 2004, ApJ, 603, L17

Komossa, S., Zhou, H., Rau, A., et al. 2009, ApJ, 701, 105

Kormendy, J., & Richstone, D. 1995, ARA&A, 33, 581

Kormendy, J., & Bender, R. 1996, ApJ, 464, L119

Kormendy J., Kennicutt Jr. R. C., 2004, ARA&A, 42, 603

Kormendy, J., & Bender, R. 2009, ApJ, 691, L142

Kormendy J., Bender R., Cornell M. E., 2011, Nature, 469, 374

Kormendy, J., & Ho, L. C. 2013, ARA&A, 51, 511

Kroupa, P. 1998, MNRAS, 300, 200

Kroupa P., 2001, MNRAS, 322, 231

Kroupa, P., & Boily, C. M. 2002, MNRAS, 336, 1188

Kroupa, P. 2005, The Three-Dimensional Universe with Gaia, 576, 629

Kroupa, P. 2012, PASA, 29, 395

Kroupa, P. 2014, arXiv:1406.4860

Kulkarni, G., & Loeb, A. 2012, MNRAS, 2670

Küpper A. H. W., Kroupa P., Baumgardt H., 2008, MNRAS, 389, 889

Küpper A. H. W., Kroupa P., Baumgardt H., Heggie D. C., 2010a, MNRAS, 401, 105

Küpper A. H. W., Kroupa P., Baumgardt H., Heggie D. C., 2010b, MNRAS, 407, 2241

Küpper A. H. W., Lane R. R., Heggie D. C., 2012, MNRAS,420, 2700

Kustaanheimo, P., & Stiefel, E. 1965, Reine Angew. Math., 218, 204

Lai D., Rasio F. A., Shapiro S. L., 1994, ApJ, 437, 742

Lamers, H. J. G. L. M., Baumgardt, H., & Gieles, M. 2010, MNRAS, 409, 305

Larsen, S. S. 2009, A&A, 494, 539

Latif, M. A., Schleicher, D. R. G., Schmidt, W., & Niemeyer, J. C. 2013, MNRAS, 436, 2989

Latif, M. A., Schleicher, D. R. G., Schmidt, W., & Niemeyer, J. 2013, ApJ, 772, L3

Lauer, T. R., Ajhar, E. A., Byun, Y.-I., et al. 1995, AJ, 110, 2622

Lauer, T. R., Faber, S. M., Richstone, D., et al. 2007, ApJ, 662, 808

Lauer, T. R., Gebhardt, K., Faber, S. M., et al. 2007, ApJ, 664, 226

Lightman A. P., Shapiro S. L., 1977, ApJ, 211, 244

Liu, F. K., & Chen, X. 2013, ApJ, 767, 18

Löckmann, U., & Baumgardt, H. 2008, MNRAS, 384, 323

Löckmann U., Baumgardt H., Kroupa P., 2010, MNRAS, 402, 519

Lopez-Cruz, O., Anorve, C., Birkinshaw, M., et al. 2014, arXiv:1405.7758

Lynden-Bell, D. 1967, MNRAS, 136, 101

Machalski, J., Kozieł-Wierzbowska, D., Jamrozy, M., & Saikia, D. J. 2008, ApJ, 679, 149

MacLeod, M., Guillochon, J., & Ramirez-Ruiz, E. 2012, ApJ, 757, 134

Madrid J. P., Hurley J. R., Sippel A. C., 2012, ApJ, 756, 167

Magaña, J., & Matos, T. 2012, Journal of Physics Conference Series, 378, 012012

Magorrian, J., Tremaine, S., Richstone, D., et al. 1998, AJ, 115, 2285

Magorrian J., Tremaine S., 1999, MNRAS, 309, 447

Makino, J. 1997, ApJ, 478, 58

Malbon, R. K., Baugh, C. M., Frenk, C. S., & Lacey, C. G. 2007, MNRAS, 382, 1394

Maldacena, J., & Susskind, L. 2013, Fortschritte der Physik, 61, 781

Malin, D. F., & Carter, D. 1980, Nature, 285, 643

Manchester, R. N., Hobbs, G., Bailes, M., et al. 2013, PASA, 30, 17

Marconi, A., & Hunt, L. K. 2003, ApJ, 589, L21

Marks, M., & Kroupa, P. 2010, MNRAS, 406, 2000

Martizzi, D., Teyssier, R., & Moore, B. 2012, MNRAS, 420, 2859

Mathews, W. G., & Guo, F. 2011, ApJ, 738, 155

McConnell, N. J., Ma, C.-P., Gebhardt, K., et al. 2011, Nature, 480, 215

McConnell, N. J., Ma, C.-P., Murphy, J. D., et al. 2012, ApJ, 756, 179

McConnell, N. J., Chen, S.-F. S., Ma, C.-P., et al. 2013, ApJ, 768, L21

Bibliography

McConnell, N. J., & Ma, C.-P. 2013, ApJ, 764, 184

McDonald, M., Bayliss, M., Benson, B. A., et al. 2012, Nature, 488, 349

McGlynn, T. A. 1984, ApJ, 281, 13

McLaughlin, D. E. 1994, PASP, 106, 47

McLaughlin, D. E. 1999, AJ, 117, 2398

McLaughlin D. E., van der Marel R. P., 2005, ApJS, 161, 304

McLaughlin, D. E., & Fall, S. M. 2008, ApJ, 679, 1272

McLure, R. J., & Dunlop, J. S. 2002, MNRAS, 331, 795

McNamara, B. R., Nulsen, P. E. J., Wise, M. W., et al. 2005, Nature, 433, 45

McNamara, B. R., Kazemzadeh, F., Rafferty, D. A., et al. 2009, ApJ, 698, 594

McNamara, B. R., Rohanizadegan, M., & Nulsen, P. E. J. 2011, ApJ, 727, 39

Merritt, D. 1985, AJ, 90, 1027

Merritt, D., & Aguilar, L. A. 1985, MNRAS, 217, 787

Merritt, D., & Quinlan, G. D. 1998, ApJ, 498, 625

Merritt, D., & Valluri, M. 1999, AJ, 118, 1177

Merritt, D., & Ekers, R. D. 2002, Science, 297, 1310

Merritt, D., Milosavljević, M., Favata, M., Hughes, S. A., & Holz, D. E. 2004, ApJ, 607, L9

Merritt D., Poon M. Y., 2004, ApJ, 606, 788

Merritt, D. 2005, Growing Black Holes: Accretion in a Cosmological Context, 221

Merritt D., Wang J., 2005, ApJ, 621, L101

Merritt, D., Alexander, T., Mikkola, S., & Will, C. M. 2011, Phys. Rev. D, 84, 044024

Merritt, D., & Vasiliev, E. 2011, ApJ, 726, 61

Merritt, D. 2013, Dynamics and Evolution of Galactic Nuclei, by David Merritt. Princeton: Princeton University Press, 2013,

Michell, J. 1784, Philosophical Transactions of the Royal Society of London, 74, pp. 35

Mieske, S., Küpper, A. H. W., & Brockamp, M. 2014, A&A, 565, L6

Mikkola, S., & Aarseth, S. J. 1993, Celestial Mechanics and Dynamical Astronomy, 57, 439

Mikkola, S., & Aarseth, S. 2002, Celestial Mechanics and Dynamical Astronomy, 84, 343

Milgrom, M. 1983, ApJ, 270, 371

Milosavljević, M., Merritt, D., & Ho, L. C. 2006, ApJ, 652, 120

Misgeld, I., & Hilker, M. 2011, MNRAS, 414, 3699

Misner, C. W., Thorne, K. S., & Wheeler, J. A. 1973, San Francisco: W.H. Freeman and Co., 1973,

Morris M., 1993, ApJ, 408, 496

Mortlock, D. J., Warren, S. J., Venemans, B. P., et al. 2011, Nature, 474, 616

Mullaney, J. R., Daddi, E., Béthermin, M., et al. 2012, ApJ, 753, L30

Murali, C., & Weinberg, M. D. 1997, MNRAS, 291, 717

Murray N., Quataert E., Thompson T. A., 2005, ApJ, 618, 569

Narayan, R., & Fabian, A. C. 2011, MNRAS, 415, 3721

Narayan, R., & McClintock, J. E. 2008, New Astronomy Reviews, 51, 733

Narayan, R., & Quataert, E. 2005, Science, 307, 77

Norman C., Silk J., 1983, ApJ, 266, 502

Novikov I. D., Frolov V. P., 1989, Physics of black holes

Noyola, E., Gebhardt, K., Kissler-Patig, M., et al. 2010, ApJ, 719, L60

Odenkirchen M., et al., 2003, AJ, 126, 2385

Osipkov, L. P. 1979, Soviet Astronomy Letters, 5, 42

Ostriker, J. P., Binney, J., & Saha, P. 1989, MNRAS, 241, 849

Parmentier, G., & Gilmore, G. 2007, MNRAS, 377, 352

Paczyńsky, B., & Wiita, P. J. 1980, A&A, 88, 23

Page, M. J., Symeonidis, M., Vieira, J. D., et al. 2012, Nature, 485, 213

Papadodimas, K., & Raju, S. 2013, Journal of High Energy Physics, 10, 212

Peñarrubia, J., Just, A., & Kroupa, P. 2004, MNRAS, 349, 747

Peñarrubia J., Walker M. G., Gilmore G., 2009, MNRAS,399, 1275

Perets, H. B., Hopman, C., & Alexander, T. 2007, ApJ, 656, 709

Peng, E. W., Ferguson, H. C., Goudfrooij, P., et al. 2011, ApJ, 730, 23

Pesce, E., Capuzzo-Dolcetta, R., & Vietri, M. 1992, MNRAS, 254, 466

Bibliography

Peters, P. C. 1964, Physical Review, 136, 1224

Poon M. Y., Merritt D., 2001, ApJ, 549, 192

Poon M. Y., Merritt D., 2002, ApJ, 568, L89

Portegies Zwart, S. F., Baumgardt, H., Hut, P., Makino, J., & McMillan, S. L. W. 2004, Nature, 428, 724

Postman, M., Lauer, T. R., Donahue, M., et al. 2012, ApJ, 756, 159

Press, W. H., Teukolsky, S. A., Vetterling, W. T., & Flannery, B. P. 1992, Cambridge: University Press, —c1992, 2nd ed.,

Preto M., Amaro-Seoane P., 2010, ApJ, 708, L42

Pretorius, F. 2005, Physical Review Letters, 95, 121101

Quinlan, G. D., & Hernquist, L. 1997, New Astronomy, 2, 533

Rafferty, D. A., McNamara, B. R., Nulsen, P. E. J., & Wise, M. W. 2006, ApJ, 652, 216

Read J. I., Wilkinson M. I., Evans N. W., Gilmore G., Kleyna J. T., 2006, MNRAS, 366, 429

Rees M. J., 1988, Nature, 333, 523

Rees, M. J., & Volonteri, M. 2007, IAU Symposium, 238, 51

Renaud F., Gieles M., Boily C. M., 2011, MNRAS, 418, 759

Reynolds, C. S. 2013, Space Sci. Rev., 81

Rezzolla, L., Macedo, R. P., & Jaramillo, J. L. 2010, Physical Review Letters, 104, 221101

Rhode, K. L., & Zepf, S. E. 2004, AJ, 127, 302

Rhode, K. L. 2012, AJ, 144, 154

Rose, J. A., Arimoto, N., Caldwell, N., et al. 2005, AJ, 129, 712

Rusli, S. P., Erwin, P., Saglia, R. P., et al. 2013, AJ, 146, 160

Salpeter, E. E. 1964, ApJ, 140, 796

Samland, M. 2004, PASA, 21, 175

Schawinski et al. K., 2006, Nature, 442, 888

Schulze A., Gebhardt K., 2011, ApJ, 729, 21

Searle, L., & Zinn, R. 1978, ApJ, 225, 357

Sesana, A., Gualandris, A., & Dotti, M. 2011, MNRAS, 415, L35

Schmidt, M. 1963, Nature, 197, 1040

Shapiro, S. L., & Teukolsky, S. A. 1983, Research supported by the National Science Foundation. New York, Wiley-Interscience, 1983, 663 p.,

Shields, G. A., & Bonning, E. W. 2013, ApJ, 772, L5

Schulze, A., & Gebhardt, K. 2011, ApJ, 729, 21

Schwarzschild, K. 1916, Abh. Konigl. Preuss. Akad. Wissenschaften Jahre 1906,92, Berlin,1907, 1916, 189

Sersic J. L., 1968, Atlas de galaxias australes

Shannon, R. M., Ravi, V., Coles, W. A., et al. 2013, arXiv:1310.4569

Shepard, D. 1968, in Proceedings of the 1968 23rd ACM National Conference, ACM '68 (New York, NY, USA: ACM), 517–524

Silk, J., & Rees, M. J. 1998, A&A, 331, L1

Smith R., Fellhauer M., Candlish G. N., Wojtak R., Farias J. P., Blaña M., 2013, MNRAS, 1577

Soltan A., 1982, MNRAS, 200, 115

Spinnato, P. F., Fellhauer, M., & Portegies Zwart, S. F. 2003, MNRAS, 344, 22

Spitzer Jr. L., Harm R., 1958, ApJ, 127, 544

Spitzer, L. 1987, Princeton, NJ, Princeton University Press, 1987, 191 p.

Spitzer L., 1987, Dynamical evolution of globular clusters

Steinmetz, M., & Navarro, J. F. 2002, New Astronomy, 7, 155

Stone, N., & Loeb, A. 2011, MNRAS, 412, 75

Strubbe L. E., Quataert E., 2011, MNRAS, pp 696–+

Sundararajan, P. A., Khanna, G., & Hughes, S. A. 2010, Phys. Rev. D, 81, 104009

Toomre, A. 1977, Evolution of Galaxies and Stellar Populations, 401

Trakhtenbrot, B. 2014, ApJ, 789, L9

Tran, H. D., Tsvetanov, Z., Ford, H. C., et al. 2001, AJ, 121, 2928

Tremaine, S. D., Ostriker, J. P., & Spitzer, L., Jr. 1975, ApJ, 196, 407

Tremaine, S., Gebhardt, K., Bender, R., et al. 2002, ApJ, 574, 740

Trenti M., Heggie D. C., Hut P., 2007, MNRAS, 374, 344

Tristram, K. R. W., & Schartmann, M. 2011, A&A, 531, A99

Bibliography

Trujillo I., Erwin P., Asensio Ramos A., Graham A. W., 2004, AJ, 127, 1917

Trujillo, I., Conselice, C. J., Bundy, K., et al. 2007, MNRAS, 382, 109

Ulmer A., 1999, ApJ, 514, 180

Urry, C. M., & Padovani, P. 1995, PASP, 107, 803

Valtonen, M. J., Lehto, H. J., Nilsson, K., et al. 2008, Nature, 452, 851

van den Bosch, R. C. E., & de Zeeuw, P. T. 2010, MNRAS, 401, 1770

van den Bosch, R. C. E., Gebhardt, K., Gültekin, K., et al. 2012, Nature, 491, 729

van Dokkum P. G., et al., 2008, ApJ, 677, L5

van Raamsdonk, M. 2010, General Relativity and Gravitation, 42, 2323

van Velzen, S., Farrar, G. R., Gezari, S., et al. 2011, ApJ, 741, 73

van Velzen, S., Körding, E., & Falcke, H. 2011, MNRAS, 417, L51

Vasiliev, E., & Merritt, D. 2013, ApJ, 774, 87

Vasiliev, E., Antonini, F., & Merritt, D. 2013, arXiv:1311.1167

Vesperini, E., & Heggie, D. C. 1997, MNRAS, 289, 898

Vesperini, E. 2000, MNRAS, 318, 841

Vesperini, E., Zepf, S. E., Kundu, A., & Ashman, K. M. 2003, ApJ, 593, 760

Volonteri, M., & Rees, M. J. 2005, ApJ, 633, 624

Walker, S. A., Fabian, A. C., Russell, H. R., & Sanders, J. S. 2014, MNRAS, 442, 2809

Walsh, J. L., Barth, A. J., Ho, L. C., & Sarzi, M. 2013, ApJ, 770, 86

Wang, J., & Merritt, D. 2004, ApJ, 600, 149

Webb J. J., Harris W. E., Sills A., Hurley J. R., 2013, ApJ, 764, 124

Wegg, C. 2012, ApJ, 749, 183

Weinberg, S. 1972, Gravitation and Cosmology by Steven Weinberg, pp. 688. Wiley-VCH , July 1972.,

White, S. D. M., & Rees, M. J. 1978, MNRAS, 183, 341

Will, C. M. 2012, Classical and Quantum Gravity, 29, 217001

Wong, K.-W., Irwin, J. A., Yukita, M., et al. 2011, ApJ, 736, L23

Wu, X., & Kroupa, P. 2013, MNRAS, 435, 1536

Younger, J. D., Hopkins, P. F., Cox, T. J., & Hernquist, L. 2008, ApJ, 686, 815

Yu Q., Tremaine S., 2002, MNRAS, 335, 965

Zauderer, B. A., Berger, E., Soderberg, A. M., et al. 2011, Nature, 476, 425

Zepf, S. E., & Ashman, K. M. 1993, MNRAS, 264, 611

Zhang, Q., & Fall, S. M. 1999, ApJ, 527, L81

Zhao H., Haehnelt M. G., Rees M. J., 2002, New Astron., 7, 385

Appendices

A. N-body Methods

A.1. Nbody6

The NBODY6 software (Aarseth, 1999, 2003) is a versatile platform for investigating the gravitational dynamics of stellar systems. NBODY6 was designed as a direct summation code which means that every particle gravitationally interacts with every other particle. It solves the equation of motion of the underlying N-body system:

$$m_i \ddot{\vec{r}}_i = -G \sum_{j=1; j \neq i}^{N} \left(\frac{m_i m_j \left(\vec{r}_i - \vec{r}_j \right)}{\left| \vec{r}_i - \vec{r}_j \right|^3} \right). \tag{A.1}$$

Here, m_i and $\vec{r}_i$ is the mass and the position vector of the i$^{\text{th}}$ particle. NBODY6 is well suited for numerical investigations of stellar systems with relaxation timescales shorter than the time scale of interest. This applies to star clusters or even the most inner parts of galactic nuclei hosting the least massive SMBHs.

According to Aarseth et al. (2008), NBODY6 consists of three major elements:

1. Creating initial conditions

2. Integration of the Newtonian equation of motion

3. Data evaluation

In the following discussion I concentrate solely on part 2.

Due to the symmetry of gravitational forces and by assuming a model with N single particles, a direct summation method has to evaluate

$$\frac{1}{2} N(N-1) \sim N^2 \tag{A.2}$$

forces per time step. The quadratical increase of the required computing power poses a computational challenge. It effectively limits the usable particle number to be $N \lesssim 10^6$ (Heggie & Hut, 2003). However, there are two strategies which speed-up direct N-body integrations. Both are implemented into NBODY6: First of all (i), by assigning (synchronized) individual time-steps, h, to all particles. Near mass concentrations where accelerations are large, the step size becomes smallest. In the outer parts of a stellar system where the motion is governed by a low acceleration, a large step size is sufficient. The following time-step criterion is implemented into NBODY6 (Aarseth et al., 2008):

$$h = \left(\frac{\eta \left(\left| \vec{a}^{(0)} \right| \left| \vec{a}^{(2)} \right| + \left| \vec{a}^{(1)} \right|^2 \right)}{\left| \vec{a}^{(1)} \right| \left| \vec{a}^{(3)} \right| + \left| \vec{a}^{(2)} \right|^2} \right)^{\frac{1}{2}}. \tag{A.3}$$

A. N-body Methods

Here, η is the accuracy parameter which is usually 0.02 (Aarseth et al., 2008) and $\vec{a}^{(n)}$ is the time derivative of nth order of the acceleration. Secondly (ii), by making use of the Ahmad-Cohen neighbour scheme (Ahmad & Cohen, 1973). The basic idea behind the Ahmad-Cohen neighbour scheme is to group all forces which act on a particle into two regimes which are then recalculated in different time intervals. This includes the $N - 1$ direct forces as well as those from an additional IMBH/SMBH. Forces which belong to the first regime must be updated every new time step, h. These forces emanate from nearby particles (or a nearby IMBH/SMBH), within the so called neighbour radius. Relative particle positions from beyond the neighbour radius do not change as quickly and their force contribution can be updated in more extended time intervals. External forces from the potential of the host galaxy are treated like forces within the neighbour radius.

The particles themselves are integrated forward in time by making use of the Hermite integration scheme (Aarseth et al., 2008). The Hermite scheme is a predictor-corrector method[1]. This integration scheme is capable to calculate the position

$$\vec{r}_{n+1} = \vec{r}_n + ... + \vec{a}_n^{(3)} h^5 / 120 \tag{A.4}$$

and velocity,

$$\vec{v}_{n+1} = \vec{v}_n + ... + \vec{a}_n^{(3)} h^4 / 24, \tag{A.5}$$

up to the 5th and 4th order of a Taylor expansion series, respectively. However, it does not use brute force to calculate $\vec{a}_n^{(2)}$ and $\vec{a}_n^{(3)}$ directly. Instead, it first makes a predictor step

$$\vec{r}_{n+1} = \vec{r}_n + \vec{v}_n h + \frac{1}{2}\vec{a}_n^{(0)} h^2 + \frac{1}{6}\vec{a}_n^{(1)} h^3 \tag{A.6}$$

$$\vec{v}_{n+1} = \vec{v}_n + \vec{a}_n^{(0)} h + \frac{1}{2}\vec{a}_n^{(1)} h^2$$

in which $\vec{r}_{n+1}$ and $\vec{v}_{n+1}$ are calculated up to low order. Afterwards, expressions for $\vec{a}_n^{(3)}$ and $\vec{a}_n^{(2)}$ are evaluated from the predicted (at step $n + 1$) and old values (at step n). This is the corrector step:

$$\vec{a}_n^{(2)} = \frac{-6\left(\vec{a}_n^{(0)} - \vec{a}_{n+1}^{(0)}\right) - h\left(4\vec{a}_n^{(1)} + 2\vec{a}_{n+1}^{(1)}\right)}{h^2}$$

$$\vec{a}_n^{(3)} = \frac{12\left(\vec{a}_n^{(0)} - \vec{a}_{n+1}^{(0)}\right) + 6h\left(\vec{a}_n^{(1)} + \vec{a}_{n+1}^{(1)}\right)}{h^3} . \tag{A.7}$$

Finally, the high-order corrections are applied to the predicted values of $\vec{r}_{n+1}$ and $\vec{v}_{n+1}$ (Eq. A.6) in order to obtain the solution at the 5th and 4th order of the Taylor expansion (Eq. A.4 and A.5).

Hard binaries and strongly bound hierarchical systems, either in form of primordial binaries or emerged from dynamical interactions, require special care. Hard binaries

---

[1]See e.g. Aarseth et al. (2008) for a more detailed description of the Hermite scheme.

are handled with the KS regularization method (Kustaanheimo & Stiefel, 1965) which bases on a coordinate transformation of the 3D treatment into a 4D coordinate system with a new time coordinate. An example for another kind of regularization method can be found in Appendix A.3. The dynamical evolution of the binary itself is integrated forward in time with the KS method while its center of mass is numerically evolved with the ordinary scheme. Hierarchical systems (e.g. two gravitationally bound binaries) are treated with the chain regularization method (Mikkola & Aarseth, 1993). It can be summarized as a method which regularizes the strongest two body interactions and which adds the other force components as perturbations.

Additional physical processes that can be modelled with NBODY6 include a Post-Newtonian treatment, Roche lobe overflow of interacting binaries, physical collisions between stars, stellar mass loss, supernovae explosions and remnant formation as well as gas expulsion.

A.2. SCF Method

The SCF algorithm (Hernquist & Ostriker, 1992) evaluates the potential and density profile from a particle distribution, which itself can be taken, for example, from a cosmological large scale simulation. The SCF method allows to integrate these particles forward in time by calculating the acceleration vectors at arbitrary positions from the gradient of the obtained potential:

$$\vec{a}\left(\vec{r}\right) = -\nabla\phi(\vec{r}). \tag{A.8}$$

Depending on the numerical problem, the overall potential-density pair can be re-evaluated (i.e. updated) in arbitrary time intervals. In this way the SCF method handles time evolving galaxy potentials. In contrast to NBODY6 (Appendix A.1), the SCF algorithm is a collision-less method well suited for investigating dynamics of galaxies. The principle of the SCF algorithm and how it obtains an analytical expression for ϕ from the particle distribution, is explained below.

Every density, ρ, and potential, ϕ, which are square-integrable on the unit-sphere, can be expanded into radial and angular dependent functions. They form a complete (and orthogonal) basis and following Hernquist & Ostriker (1992) they have the form:

$$\rho\left(\vec{r}\right) = \sum_{nlm} A_{nlm}\rho_{nlm}\left(\vec{r}\right) \tag{A.9}$$

$$\phi\left(\vec{r}\right) = \sum_{nlm} A_{nlm}\phi_{nlm}\left(\vec{r}\right). \tag{A.10}$$

Here, n, l, m specify the order of the expansion. With the help of the Poisson equation:

$$\nabla^2\phi\left(\vec{r}\right) = 4\pi\rho\left(\vec{r}\right), \tag{A.11}$$

an explicit expression for these radial and angular dependent functions can be found. However, before solving the Poisson equation, one first needs to specify boundary conditions. Proper boundary conditions (for $n, l, m = 0$) should be selected by choosing

an underlying galaxy model which is already very close to the model one wishes to expand. The SCF formalism which is implemented into the MUESLI code uses a Hernquist density-potential pair (Hernquist, 1990) as boundary conditions. They have the form:

$$\rho_{000} = \frac{M_{\text{GAL}}a}{2\pi r \left(r + a\right)^3} \tag{A.12}$$

$$\phi_{000} = -\frac{GM_{\text{GAL}}}{r + a}. \tag{A.13}$$

Here, M_{GAL} is the total mass and $a = R_H / \left(1 + \sqrt{2}\right)$ is a scale length which is proportional to the 3D half mass radius, R_H. For convenience, $G = M_{\text{GAL}} = a = 1$ are scaled to model units.

The solution of Eq. A.11 incorporates spherical harmonics and Gegenbauer polynomials (Eq. 3.12 and 3.13 in Hernquist & Ostriker (1992)). Actually, the solution of the angular dependent part is straightforward to obtain as spherical harmonics already define an orthogonal and complete basis set. By having explicit expressions for $\rho\left(\vec{r}\right)$ and $\phi\left(\vec{r}\right)$, one can calculate the density-potential pair up to a given order $m, n, l \in \mathrm{N}_{>0}$ from all particles in the underlying model.

A.3. TTL Integrator

The simulation of few-body systems with arbitrary masses and separations is a great challenge in numerical astrophysics (Mikkola & Aarseth, 2002). Velocity dependent forces which occur e.g. in the PN treatment complicate these efforts. The reason for this is as follows: Non-symplectic integrators like the Runge-Kutta (RK) method usually do not preserve energy. A binary black hole system can artificially gain energy over time so that the separation between the holes enlarges. Moreover, a general mathematical criterion concerning energy conservation does not exist and in principle it has to be tested by calculating $\Delta E = |E - E_0|$ (during computations) for any problem individually.

In the case that the Hamiltonian, H, is also the energy of the system, energy errors are bounded from above in symplectic methods like the leapfrog integration technique. The following inequality was derived in Hairer et al. (2003) for the leapfrog integration method:

$$|H_n - H_0| \leq Ch^2 + C_n h^n t, \quad 0 \leq t = nh \leq h^{-N}. \tag{A.14}$$

Here N, C_1 and C_n are positive constants, h is the time step and t the time. However, a necessary condition for (accumulated) energy errors which are bounded from above (like in Eq A.14) is that forces do not depend on the velocity. This is not the case in relativistic scenarios or cases where dynamical friction is involved.

Mikkola & Aarseth (2002) found a regularization method which allows to accurately calculate the motion of objects with arbitrary mass ratios. It can also handle velocity dependent forces which are important in the immediate vicinity of SMBHs. This

method is the time-transformed leapfrog (TTL) scheme and is shortly presented below:

In the TTL scheme, the set of two first-order equations

$$\frac{d\vec{r}}{dt} = \vec{v}, \qquad \frac{d\vec{v}}{dt} = \vec{a}\,(\vec{r}) \tag{A.15}$$

is first transformed into a set of four first-order equations which can then be solved more efficiently (Mikkola & Aarseth, 2002). The transformation is done in two steps: (i) Through a substitution (i.e. time transformation) of the form:

$$ds = \Omega\,(\vec{r})\,dt. \tag{A.16}$$

Here, $\Omega\,(\vec{r})$ is a positive function which depends on the masses of the particles and their separations. And (ii), by introducing an additional variable $W = \Omega$. However, the auxiliary variable is not directly obtained from the value Ω. Instead, it is evaluated from the differential equation:

$$\frac{\partial W}{\partial t} = \frac{\partial \Omega}{\partial t} = \frac{\partial \Omega}{\partial t} \cdot \frac{\partial \vec{r}}{\partial \vec{r}} = \vec{v}\frac{\partial \Omega}{\partial \vec{r}}. \tag{A.17}$$

In this way one obtains four differential equations:

$$\text{(1.)} \; \frac{d\vec{r}}{ds} = \frac{\vec{v}}{W} \; \text{(2.)} \; \frac{d\vec{t}}{ds} = \frac{\vec{1}}{W} \; \text{(3.)} \; \frac{d\vec{v}}{ds} = \frac{\vec{a}}{\Omega} \; \text{(4.)} \; \frac{\partial W}{\partial t} = \vec{v}\frac{\partial \Omega}{\partial \vec{r}} \tag{A.18}$$

which are solved with the leapfrog integration method presented in Mikkola & Aarseth (2002) (their Equations 14-19). The additional effort involved in solving Eq. A.18, one now has to solve four differential equations instead of two, is balanced by the fact that one obtains a much more efficient and precise integration method which can handle arbitrary mass ratios.

B. Extrapolation to Astrophysical Galaxies

In the following part we give a more detailed description of the formalism by which the here obtained capture rates (Table 3.1) can be scaled up to realistic bulges of galaxies or elliptical galaxies.

1. From the relation

$$\left. \frac{r_{\text{cap}}}{r_H} \right|_{\text{sim}} = \left. \frac{r_{\text{cap}}}{r_H} \right|_{\text{astro}} \tag{B.1}$$

the required capture radius $r_{\text{cap}}^{\text{sim}}$ for a black hole of mass $M_\bullet$ must be obtained by using astronomical observations of individual galaxies or by making use of the $M_\bullet - \sigma$ relation from Schulze & Gebhardt (2011). If in the near future much larger samples of measured SMBH masses allow for more accurate values, it will be no problem to implement them into this formalism. By combining Eq. B.1 with the disruption radius $r_{\text{cap}} = g r_\star \left(\frac{M_\bullet}{M_\star} \right)^{\frac{1}{3}}$ and the expression for the radius of influence $r_H \approx 13.1 \left(\frac{M_\bullet}{M_8} \right)^{0.54}$ [pc] which is derived from the $M_\bullet - \sigma$ scaling relation, $r_{\text{cap}}^{\text{sim}}$ follows:

$$r_{\text{cap}}^{\text{sim}} \approx 4g \cdot 10^{-9} \left(\frac{M_\bullet}{M_8} \right)^{-0.2067}. \tag{B.2}$$

It specifies the required capture radius in the scale-free N-body integrations for the astrophysical black hole of interest. The function $a(r_{\text{cap}}^{\text{sim}})$ must be evaluated from the values in Table 3.1:

$$a(r_{\text{cap}}^{\text{sim}}) = 0.023(\pm 0.006) \left(r_{\text{cap}}^{\text{sim}} \right)^{0.363(\pm 0.020)} \tag{B.3}$$

yields a reasonable approximation[1] for the extrapolation of the parameter a from Eq. 3.53 to any desired $r_{\text{cap}}^{\text{sim}}$. For the purpose of this paper the slope parameter $b = 0.83$ is assumed to be independent of $r_{\text{cap}}^{\text{sim}}$. As already mentioned in § 3.6.1 the parameter g accounts for the stellar model and mass of the black hole. It is of the order of one (Kochanek, 1992; Lai et al., 1994; Ivanov & Chernyakova, 2006). For simplicity we use $g = 1$ which is a reasonable assumption for nonrotating black holes less massive than $M_\bullet = 10^7 M_\odot$ and solar mass stars. Eq. B.2 assumes all stars to be disrupted before entering the horizon.

2. The dynamical timescale t_{sim} of the N-body particles inside the sphere of influence r_H has to be calculated according to $t_{\text{sim}} = \frac{2r_H}{\sigma(r=r_H)} \approx 0.008$. It is used as a reference for timing issues when compared to the relevant astrophysical timescales t. To ease the extrapolation of the numerical results to astrophysical systems, we

---

[1] $Q = 0.89$ without rescaling $\chi_\mu = 1$. Afterwards, the uncertainties are taken directly from the covariance matrix. Renormalization induces the errors to be uncorrelated to each other.

compute the time averaged influence radius r_H. Representative for all models we calculate r_H and t_{sim} from the 25 k, 50 k, 75 k, 150 k and 250 k models. For the calculation of the radius of influence we bin the particles in cylindrical shells of thickness $\Delta r = 0.001$ and measure for each configuration the one dimensional velocity dispersion (line of sight velocity) $\sigma_i^2 = \frac{\sum_i v_{i,z}^2}{N_i}$ in order to obtain $\sigma(r)_{\text{sim}}^2$. Here N_i is the number of particles within each configuration. We choose the line of sight axis to be parallel to the z-axis. Afterwards, $\sigma_{\text{bh},i}^2 = \frac{M_{\bullet}(t)}{3N_i} \cdot \left(\sum_{i=1}^{N_i} \frac{1}{r_i} \right)$ is calculated for each cylindrical shell to obtain $\sigma(r)_{\text{bh}}^2$, here $r_i = \sqrt{x_i^2 + y_i^2 + z_i^2}$. The factor 3 in the denominator is used for the normalization to the relevant line of sight velocity inside the isotropic distribution. The radius of influence r_H is then calculated to be the radius at which $\frac{\sigma(r)_{\text{sim}}^2}{\sigma(r)_{\text{bh}}^2} = 2$. We note that in N-body units $G = 1$. The position of the black hole is used as the reference center and the mass gain of the black hole is taken into account. For the time averaged influence radius and velocity dispersion we obtain $r_H \approx 0.005$ and $\sigma(r = r_H) \approx 1.26$. The black hole influence radius is $5 - 6$ times smaller than the dynamical radius.

3. Afterwards, the astrophysical timescale $t_{\text{cr}}(r_H) = \frac{2r_H}{\sigma}\big|_{\text{astro}}$ of the mass distribution within the influence radius must be obtained for the black hole of given mass by using $r_H \approx 13.1 \left(\frac{M_{\bullet}}{M_8} \right)^{0.54}$ [pc] and $\sigma \approx 200 \left(\frac{M_8}{1.5135} \right)^{0.23}$ [kms^{-1}] from Schulze & Gebhardt (2011).

4. The number of stars N in the astrophysical galaxy must be specified. For simplicity we assume all stars having the same masses $\langle M_{\star} \rangle = 1 M_{\odot}$. A coarse estimate for the number of stars can be computed by:

$$N = \frac{100 M_{\bullet}}{\langle M_{\star} \rangle}. \tag{B.4}$$

The choice of $\langle M_{\star} \rangle = 1 M_{\odot}$ depends on the stellar mass function and seems to be a reasonable assumption for galactic nuclei where mass segregation is important (Freitag et al., 2006; Kroupa, 2001; Löckmann et al., 2010). The factor 100 accounts for the fraction of bulge mass to black hole mass in accordance with our simulations.

5. Finally the disruption rate of stars by massive black holes can be evaluated. In a first step the numerically inferred number of captures $\dot{C}(N)$ per N-body time unit (Table 3.1) must be normalized to the relevant crossing time $t_{\text{sim}} = 0.008$ (in N-body time units) at the influence radius of the black hole. This dimensionless number must afterwards be synchronized with the relevant timescale $t_{\text{cr}}(r_H)$ of the astrophysical galaxy. Consequently $\dot{C}(N) \cdot t_{\text{sim}}$ has to be divided by $t_{\text{cr}}(r_H)$ in order to obtain the number of disrupted stars within the desired physical time unit (e.g yr, Myr) for the black hole of interest:

$$\dot{C}_{\text{astro}} = \frac{0.008 \cdot a(r_{\text{cap}}^{\text{sim}}) N^b}{t_{\text{cr}}(r_H)}. \tag{B.5}$$

Our extrapolation formalism strongly depends on the $M_\bullet - \sigma$ relation. More accurate and numerous black hole measurements will improve this relation in the future. Moreover, we only treat errors from our simulations and neglected the intrinsic scatter of the $M_\bullet - \sigma$ relation for simplicity.